

UNIVERSITE D'AIX-MARSEILLE

ED 352 – Physique et Sciences de la Matière

CEA Cadarache – DER/SPRC/Laboratoire d'Etudes de Physique

Thèse présentée pour obtenir le grade universitaire de docteur

Discipline : Physique et Sciences de la Matière

Spécialité : Energie, Rayonnement et Plasma

Luca DIONI

Development of a Multi-purpose Fast Neutron Spectrometric Capability in the MASURCA Facility

Soutenue le 21/09/2017 devant le jury :

M. Arjan PLOMPEN	JRC - IRMM	Examineur
M. Imre PAZSIT	Chalmers University	Examineur
M. Bertrand PEROT	CEA Cadarache	Examineur
M. Mossadek TALBY	Aix-Marseille Université	Examineur
M. Mario CARTA	ENEA	Examineur
M. Elio TOMARCHIO	Università di Palermo	Examineur
M. Brian STOUT	Aix-Marseille Université	Directeur de thèse
M. Marco SUMINI	Università di Bologna	Directeur de thèse
M. Robert JACQMIN	CEA Cadarache	Invité
M. Vincent Gressier	IRSN Cadarache	Invité
M. Mourad AICHE	CENBG	Invité

Cette page est laissée blanche intentionnellement

Abstract

This doctoral thesis work is focused on the development of neutron spectroscopy techniques in mixed radiations fields for fast research reactor applications, especially for the MASURCA facility.

The first part of the thesis is dedicated to the study of special MASURCA configurations in which a radial channel is built to extract a continuous beam of intermediate-to-fast energy neutrons, tailorable to meet different needs. Operating MASURCA as a neutron beam facility would open up new possibilities of experiments, such as fast neutron attenuation and shielding experiments; measurements in standard (reference) fast neutron fields, development and calibration of fast neutron detection systems; fast neutron radiography; etc. The conclusion is that MASURCA has favorable characteristics for such an extension. Results of simulations show that it would be possible to extract a neutron beam having an intensity of up to $\sim 1 \times 10^8$ neutrons $\text{cm}^{-2} \text{s}^{-1}$ in the adjacent experimental room, with about 89 % (respectively 75 %) of the neutrons having energies above 10 keV (respectively 100 keV). The neutron-to-gamma flux ratio at the beam exit is estimated to be between 4 and 5.

The second part of the thesis is dedicated to the development of fast neutron spectrometric capabilities for the on-line characterization of the neutron energy distribution in the prospective beam configuration (ex-core) and in the traditional one (in-core), with an energy resolution better than 10%. Different candidate detector systems are compared. A “best compromise” spectrometer is shown to be a system combining proportional counters and organic scintillators. Such a system would be able to cover the neutron energy domain between 10 keV and 10 MeV, with an overlap region going from 400 keV to 1.5 MeV. The selected organic scintillator is a stilbene single crystal obtained by a recently developed solution-grown process, promising better performance than traditional organic scintillators. As no information was available on this new organic scintillator for research reactor applications, a prototype detector was built with a $\varnothing 25 \text{ mm} \times 25 \text{ mm}$ crystal and tested in reference fast neutron beams, in a zero-power critical reactor, and in a material irradiation port at a research reactor. For the tests in high-intensity neutron (and mixed gamma-ray) fields, the detector was coupled with a digital acquisition system. A Monte Carlo calculation procedure was developed for simulating the detector response. Various properties were investigated, including discrimination capability, linearity as a function of the applied high voltage, response anisotropy, etc. The results show that the new stilbene scintillator has a better neutron-gamma discrimination capability than traditional organic scintillators, and that it is able to cover a wider energy domain, which should be of interest to several research fields. Overall, it is concluded that a neutron spectrometer based on a solution-grown stilbene detector would be suitable for use in MASURCA and in other mixed radiations fields, and would perform better than traditional detector systems.

Résumé

Ce travail de thèse porte sur le développement de techniques de spectroscopie neutronique dans les champs de rayonnement mixte pour des applications liées aux réacteurs de recherche à neutrons rapides, en particulier l'installation MASURCA.

La première partie est consacrée à l'étude des configurations expérimentales spéciales de MASURCA dans lesquelles un canal radial est construit pour extraire un faisceau continu de neutrons d'énergie intermédiaires et rapides, adaptable à différents besoins. Exploiter MASURCA en tant qu'installation de faisceau de neutrons ouvrirait de nouvelles possibilités d'expériences telles que des expériences de protection et de transport de neutrons rapides, la production de champs neutroniques standards (de référence), le développement et étalonnage de systèmes de détection des neutrons rapides, la radiographie neutronique rapide, etc. La conclusion est que MASURCA a des caractéristiques favorables à une telle extension. Les résultats des simulations ont montré qu'il est possible de délivrer un faisceau de neutrons avec une intensité maximale d'environ 1×10^8 neutrons $\text{cm}^{-2} \text{s}^{-1}$ dans la salle expérimentale adjacente (à $P = 5$ kW), 89 % (respectivement 75 %) des neutrons ayant des énergies supérieures à 10 keV (resp. 100 keV). Le rapport entre les flux de neutrons et de rayons gamma à la sortie du faisceau est estimé entre 4 et 5.

La deuxième partie de la thèse est dédiée au développement d'une capacité de spectrométrie neutronique rapide pour la caractérisation en ligne de la distribution d'énergie neutronique dans une configuration prospective du faisceau (ex-cœur) et dans une configuration traditionnelle (in-cœur), avec une résolution en énergie inférieure à 10%. Différents types de détecteurs sont comparés. Le meilleur compromis pour ce spectromètre est un système combinant des compteurs proportionnels et des scintillateurs organiques. Ce système est capable de couvrir le domaine énergétique entre 10 keV et 10 MeV avec une région de chevauchement entre 400 keV et 1.5 MeV. Le scintillateur organique sélectionné est un monocristal de stilbène obtenu par un procédé "solution-grown" développé récemment, promettant de meilleures performances que les scintillateurs organiques traditionnels. Compte tenu qu'aucune information concernant l'utilisation du scintillateur organique pour les applications liées aux réacteurs de recherche n'était disponible, un prototype de détecteur a été construit avec un cristal $\varnothing 25 \text{ mm} \times 25 \text{ mm}$ et testé dans des faisceaux de neutrons rapides de référence, dans un réacteur critique à puissance nulle et à l'extérieur d'un réacteur d'irradiation. Pour les essais en champs neutronique à haute intensité, le détecteur a été couplé à un système d'acquisition numérique. Une procédure de calcul Monte Carlo a été développée pour simuler la réponse du détecteur. Diverses propriétés ont été étudiées, y compris la capacité de discrimination, la linéarité en fonction de la haute tension appliquée, l'anisotropie de la réponse, etc. Les résultats montrent que le nouveau scintillateur stilbène a une meilleure capacité de discrimination neutron-gamma que les scintillateurs organiques traditionnels et qu'il est capable de couvrir un domaine énergétique plus large, qui devrait intéresser plusieurs domaines de recherche. Au bilan, on conclut qu'un spectromètre à neutrons basé sur un détecteur de stilbène de type "solution-grown" serait adapté à une utilisation dans MASURCA et dans d'autres champs de rayonnement mixte et qu'il serait plus performant que les systèmes de détection traditionnels.

Riassunto

Questo lavoro di tesi di dottorato ha come soggetto le tecniche di spettroscopia per neutroni veloci in campi di radiazione mista. Le applicazioni principali sono quelle relative a MASURCA e, in generale, ai reattori di ricerca.

La prima parte è dedicata allo studio di configurazioni sperimentali speciali di MASURCA, nelle quali un canale radiale è costruito per estrarre un fascio di neutroni con energie intermedie e veloci, adattabile a differenti bisogni. Operare MASURCA come una sorgente di neutroni potrebbe aprire nuove possibilità in termini di applicazioni. Queste comprendono: esperimenti di trasmissione e schermaggio di neutroni veloci; la produzione di campi neutronici standard (di riferimento); ricerche su sistemi di rivelazione avanzati; studi degli effetti dell'irradiazione su materiali organici, semi-conduttori e metalli; radiografia neutronica veloce; etc. La conclusione è che MASURCA ha delle caratteristiche favorevoli per una tale estensione. Risultati di simulazioni hanno mostrato che è possibile produrre un fascio di neutroni con intensità massime dell'ordine di 1×10^8 neutroni $\text{cm}^{-2} \text{s}^{-1}$ ($P = 5$ kW), con circa l'89 % (risp. 75 %) dei neutroni con energie al di sopra di 10 keV (risp. 100 keV).

La seconda parte della tesi è invece dedicata allo sviluppo di una capacità di spettroscopia neutronica veloce per la caratterizzazione on-line della distribuzione in energia nella configurazione speciale proposta (ex-core) e tradizionale (in-core), con una risoluzione energetica migliore di 10%. Differenti detector sono stati analizzati e comparati. Il miglior compromesso è un sistema combinato basato su contatori proporzionali e scintillatori organici. Un tale sistema dovrebbe essere in grado di coprire il dominio energetico tra 10 keV e 10 MeV, con una regione sovrapposta tra 400 keV e 1.5 MeV. Lo scintillatore scelto è un mono-cristallo di stilbene ottenuto da un processo recentemente sviluppato (di tipo solution-grow), che promette performance migliori rispetto agli scintillatori organici tradizionali. Siccome nessuna informazione relativa all'utilizzo di tale scintillatore in applicazioni legate ai reattori di ricerca è stata trovata, un prototipo è stato costruito con un cristallo delle dimensioni $\varnothing 25 \text{ mm} \times 25 \text{ mm}$ e testato in fasci di neutroni di riferimento, in un reattore di ricerca a potenza nulla e all'esterno di un reattore di irradiazione. Per i test in ambienti caratterizzati da alti flussi neutronici, un sistema di acquisizione di tipo digitale è stato utilizzato. Diverse caratteristiche sono state studiate, incluse la capacità di discriminazione, la linearità della risposta in funzione dell'alta tensione applicata, l'anisotropia della risposta, etc. I risultati mostrano che lo scintillatore stilbene ha una miglior capacità di discriminazione (neutroni-gamma) rispetto a classici scintillatori organici e che è in grado di coprire un dominio energetico più ampio, di interesse per diversi ambiti di ricerca. In generale, la conclusione è che uno spettrometro di neutroni basato sullo stilbene di tipo solution-grown è adatto per usi in MASURCA e in altre campi di radiazione mista, con migliori performance rispetto a sistemi tradizionali.

INDEX

I. General Context and Introduction.....	1
II. Presentation of the Project.....	5
2.1 Starting Point and Evolution	6
2.2 MASURCA	6
2.2.1 Past Programs	6
2.2.2 Characteristics of MASURCA	8
2.3 Opportunity & Motivation	9
2.3.1 The Flexibility of MASURCA	9
2.3.2 Instrumentation	11
2.4 Objectives	12
III. MASURCA as a Multipurpose Facility - <i>Learn from history</i>	15
3.1 Fast Neutron Source Reactors	16
3.2 MASURCA Beam Configuration	20
3.3 Simulation Models	21
3.3.1 Flux and Criticality Evaluation	24
3.3.2 Neutron Spectrum and Intensity Evaluation	25
3.3.3 Gamma Spectrum and Intensity Evaluation	27
3.4 MASURCA Beam Configuration vs Fast Neutron Source Reactors	29
3.5 Conclusion about MASURCA as a Multipurpose Facility	30
IV. Fast Neutron Spectroscopy - <i>Invest time on basics</i>	31
4.1 Instrumentation for Fast Research Reactors	32
4.1.1 Fast Neutrons	32
4.1.2 Neutron Detectors for Fast Research Reactors	33
4.2 Intermediate-to-Fast Neutron Spectroscopy Techniques	34
4.3 Gas-filled Detectors	37
4.3.1 Regions of Operation	38
4.3.2 ³ He-filled Gas Detectors	40
4.3.3 Proton Recoil Proportional Counters	41
4.4 ⁶ Li Sandwich Detector	43
4.4.1 Principle of Operation	43
4.4.2 Main Features	45
4.5 Proton Recoil Telescopes	45
4.5.1 Gas Telescopes	46
4.5.2 Diamond Telescopes	47
4.6 Organic Scintillators	48
4.6.1 Principle of Operation	48

4.6.2 Main Features	50
4.7 Comparison and Pre-selection	51
V. The Stilbene Scintillator - <i>Know your limits & Together we are stronger</i>	53
5.1 The Spectral Project	54
5.1.1 Down-selection of Organic Scintillators	55
5.2 Organic Scintillators as Mixed Radiations Fields Spectrometers	57
5.2.1 PSD - Pulse Shape Discrimination	57
5.2.2 PHS - Pulse Height Spectrum	60
5.3 Stilbene	66
5.3.1 Features of Stilbene	68
5.3.2 Solution-grown Stilbene	74
5.4 Methodology for Simulating the Response of Organic Scintillators	78
VI. Experiments - <i>Make the most from opportunities</i>	81
6.1 Tests of the Solution-grown Stilbene Detector	82
6.1.1 Electronics	82
6.2 Description of the Experiments	84
6.2.1 Measurements at AIFIRA	84
6.2.2 Measurements at LVR-15	87
6.2.3 Measurements at LR-0	90
VII. Results & Discussion/Difficulties - <i>Be patient</i>	95
7.1 The Mono-energetic Neutron Fields of the AIFIRA Facility	96
7.1.1 Measurements at 5 MeV	96
7.1.2 Measurements at 565 keV	102
7.2 The Si-filtered Extended Neutron Beam Delivered by LVR-15	103
7.2.1 Effects of the Applied High Voltage	103
7.2.2 Measurements at Different Orientations	108
7.2.3 Simulation of the Detector Response	110
7.3 Neutron Spectra Measurements at the ZPR LR-0	111
7.3.1 B0	111
7.3.2 B1 & B2	114
7.4 Discussion/Difficulties	116
7.4.1 Anisotropy	117
7.4.2 Simulation	122
VIII. Conclusion & Perspectives.....	127
8.1 Conclusion	128
8.2 Perspectives	130
References.....	133
APPENDIX A. Simulations of the MASURCA Beam Configuration.....	147

APPENDIX B. Concepts and Quantities in Radiation Measurements.....	165
APPENDIX C. Simulation of the Organic Scintillator Response with MCNPX-PoliMi and MPPost.....	175
APPENDIX D. Contributions.....	195
Acknowledgements.....	199

List of Acronyms

ADC	Analog-to-Digital Converter
ADS	Accelerator Driven System
CC	Charge Comparison (method)
CVD	Chemical Vapor Deposition (diamond)
FA	Fuel Assembly
FNAA	Fast Neutron Activation Analysis
FoM	Figure of Merit
FP	Fission Product
FPGA	Field-Programmable Gate Array
GEN (I, ..., IV)	Generation (I, ..., IV)
LO	Light Output
LY	Light Yield
MOX	Mixed OXide (fuel)
NEEDS	Nucléaire, Energie, Environnement, Déchets et Société
NPP	Nuclear Power Plant
OffC	Off-Centered model
OffCIC	Off-Centered Inverted Cone model
OffCIC-LB	Off-Centered Inverted Cone - Low Background model
PH	Pulse Height
PHS	Pulse Height Spectrum
PMT	Photomultiplier
PR	Pilot Rod
PSD	Pulse Shape Discrimination
REF	Reference model
RR	Research Reactor
SFR	Sodium-cooled Fast Reactor
SPECTRAL	Spectrométrie neutronique rapide large bande

SR	Safety Rod
VVER	Water-Water Energetic Reactor
ZPR	Zero Power Reactor

I. General Context and Introduction

Experimental nuclear research reactors known as “Zero Power Reactors” (ZPRs) play a major role in support of R&D programs addressing the needs of the nuclear industry and research organizations such as CEA. ZPRs are designed and used to simulate a large variety of fission reactor core configurations representative of neutron physics phenomena of interest, with much flexibility and intrinsic provisions for local and global measurements. The “integral” experiments that can be performed in ZPRs are numerous and can serve different purposes [Bignan 2008]:

- The validation of basic nuclear data, neutron physics calculation methods and codes;
- Needs that arise from the operation of existing nuclear power plants (GEN II) and new ones (GEN III);
- The design studies and developments of advanced types of reactor cores, with improved characteristics for better use of uranium resources and fuel cycle management (GEN IV);
- The exploration of innovative systems and reactor concepts, such as hybrid systems, *e.g.* systems involving a sub-critical core coupled with an external neutron source produced by a particle accelerator;
- Safety;
- Nuclear instrumentation development and validation;
- Etc.

The majority of the ZPRs, like other nuclear research facilities, have been built in the 60’s and 70’s [Lesage 2001]. Since then, major changes in national energy policies and nuclear programs, combined with the ageing of the installations, the rising costs of operation, and increased safety requirements, have led to the progressive shutdown and non-replacement of many ZPRs. This is not the case for the MASURCA facility, a fast neutron research reactor which CEA considers essential for the development of the ASTRID [Astrid] demonstrator, an innovative GEN IV sodium-cooled fast reactor (SFR). However, in order to comply with new safety regulations, MASURCA has to undergo a refurbishment program, which includes reinforcements of the building support structure. The facility is expected to resume operation in 2021, after completion of this upgrading work.

The MASURCA building upgrade provides an opportunity for simultaneously investigating expanded experimental capabilities, which could be introduced as part of a new instrumentation when the facility is restarted. The motivation for this new instrumentation is twofold: (i) Complement or improve the current portfolio of physics measurement techniques; and (ii) Open up the possibility of using MASURCA for new, innovative applications, and attract new users in the process.

By design, ZPRs are very versatile facilities, the core structural subassemblies being made of small, easily repositionable “simulation elements”, not unlike Lego bricks. There is much open space around the core, and typical operating conditions are at room temperature. As neutron flux levels are kept to low values, there is little material activation and negligible irradiation, so that access to the core for placing various detectors or for remodeling is easy. MASURCA being air-cooled, this flexibility is even greater than that of sister water moderated ZPRs. A good illustration of this high flexibility is provided by the series of experiments performed in MASURCA as part of the MUSE-4 program in the 90’s. In this program jointly led by CEA and CNRS, a sub-critical neutron multiplying core was coupled to a D-T neutron source. The tritium target was placed near the core center. A beam of accelerated deuterons was created in an adjacent room and directed to the tritium target by means of an evacuated tube.

This particular context provided the stimulus for submitting a research grant application to the A*MIDEX funded 2014 Call labelled « Excellence Academy – PhD Collegium ». This application was successful, and resulted in the present PhD project jointly supervised by Aix-Marseille University and Bologna University, the work taking place at CEA Cadarache, where MASURCA is located. The research environment involved personnel from the CEA/DER Reactor Physics Division and Experimental Neutron Physics Division, the AMU Fresnel Laboratory, and the UNIBO Energy Engineering Department. As the project developed, it triggered interest among other groups who provided contributions, in particular the CEA/DTN Nuclear Measurement Section, the IRSN Neutron Metrology and Dosimetry Laboratory at Cadarache, the CNRS/IN2P3 Centre d'Etudes Nucléaires at Bordeaux-Gradignan (CENBG), and the Rez Research Center near Prague in the Czech Republic.

As part of this PhD project, it was decided to investigate the possibility of using MASURCA to extract an intermediate-to-fast energy neutron “beam” having some well-controlled properties. Indeed, MASURCA has several unique and favorable features, suggesting that it would lend itself well to such an extended use. Potentially interested fields of applications are: fast neutron shielding and transport experiments; delivery of standard (reference) neutron (and gamma) fields for detector calibration; validation of neutron detection systems for nuclear safeguards; neutron activation studies; investigations of neutron-induced damage on organic materials, semi-conductors and metals; fast neutron radiography; and so on.

Developing a neutron beam-type capability alone without appropriate consideration for the corresponding instrumentation would have limited interest. Therefore, the PhD project also included the objective of establishing (at the level of a proof of principle, plus a prototype-scale demonstration) that the extracted neutrons could be sufficiently well characterized in intensity and energy distribution (spectrum). This was immediately recognized as a challenge, as there is a general lack of neutron spectrometry techniques for covering the intermediate-to-fast energy range (10 keV to 10 MeV) in ZPRs. Classical techniques used at MASURCA and elsewhere rely on small fission chambers and activation measurements, combined with calculations, for unfolding a detailed energy structure. In order to avoid resorting to the usual off-line unfolding calculations, one needs detectors that would record the energy dependence of the neutrons on-line, with a reasonably good energy resolution (< 10%) so as to distinguish broad peaks and valleys in the spectra. These detectors would have to be small enough to be positioned in small radial and axial experimental channels (less than \varnothing 60 mm) without causing too big perturbations. They would also have to be sufficiently sensitive and efficient so as to operate in low flux levels, able to discriminate neutrons from gamma-rays, reliable without requiring frequent calibrations or complicated correction factors, easy to handle and to operate.

These introductory considerations explain why the PhD project was titled: “Development of a Multi-purpose Fast Neutron Spectrometric Capability in the MASURCA Facility.”

II. Presentation of the Project

2.1 Starting Point and Evolution

2.2 MASURCA

2.2.1 Past Programs

2.2.2 Characteristics of MASURCA

2.3 Opportunity & Motivation

2.3.1 The Flexibility of MASURCA

2.3.2 Instrumentation

2.4 Objectives

Introduction

In this chapter, the MASURCA facility and its instrumentation are first introduced, then the objectives for this research project are outlined.

2.1 Starting Point and Evolution

Fast neutron spectroscopy techniques for use in the MASURCA zero-power reactor are the starting point of this PhD project. MASURCA was selected because of its favourable characteristics, as well as for the opportunity provided by a planned upgrade of the facility. However, the research project rapidly developed into a more far-reaching neutron spectrometry project, having interest for other research reactors (RR) and even for applications other than reactors. Thus, the project evolved from a mostly reactor physics driven work to a multi-application driven work, the common denominator being the need for the spectral characterization of neutron fields in the intermediate to fast range, *i.e.* 10 keV to 1 MeV, in mixed radiation field (neutrons and gamma-rays) environments. This explains why different research groups and organizations got involved as the project developed.

Nevertheless, for this work, the starting context - neutron spectroscopy for RR applications - is highlighted, with the hope of providing a more consistent discussion without too many digressions on other domains.

Hereafter, the MASURCA facility is described. Subsequently, the initial motivations and objectives of this research project are presented.

2.2 MASURCA

MASURCA is a French acronym (*MAquette de SURgénérateur à CAdarache*) which stands for “mock-up facility for fast breeder reactor studies at Cadarache”. It is a “zero-power” (meaning actually very low power) critical facility that was built in the 1960’s for the purpose of studying experimentally the physics of fast neutron multiplying lattices and cores [Bignan 2008].

2.2.1 Past Programs

Until the early 1990’s, MASURCA was operated almost exclusively for validation studies of sodium-cooled fast neutron reactor cores. A complete list of the experimental programs in MASURCA is shown in [Cacuci 2010], among them:

- The RZ and PLUTO programs (1969-1975), devoted to the study of material buckling as a function of fuel enrichment (for Uranium and Plutonium cores);
- The PECORE program (1975), for the Italian PEC (fuel element testing) irradiation reactor project;
- The PRE-RACINE and RACINE programs (1976-1984), for the validation of the calculation tools to be applied to SUPERPHENIX;
- The BALZAC program (1985-1988), for the study of the control rod reactivity effects;
- The CONRAD program (1989-1992), for studying the physics of large cores;

- The BERENICE program (1993), an international Benchmark on the measurements of the effective fraction of delayed neutrons;
- The CIRANO program (1994-1997), devoted to the replacement of radial fertile UO_2 blankets by stainless steel reflectors.

Subsequent programs were directed towards nuclear waste transmutation physics, while similar facilities in Europe and in the USA were permanently shut down:

- The COSMO Program (1998-1999), for studying the physics of long lived fission product targets irradiated at the periphery of a fast neutron core;
- The MUSE Program (2000-2004), which involved a fast sub-critical lead-cooled core coupled with an external neutron source simulating the spallation source of an Accelerator Driven System. (Information about the MUSE-4 experiment is given in Section 2.3.1 below.)

These transmutation physics experiments, most notably the European Commission sponsored FP5/MUSE-4 program [Mellier 2005], attracted interest among European countries and were carried out as part of international collaborations.

The MASURCA facility (Figure 2.1) is currently undergoing a major multiyear refurbishment work in preparation for new programs to support the development of sodium-cooled fast neutron reactors, mainly the ASTRID demonstrator [Astrid].

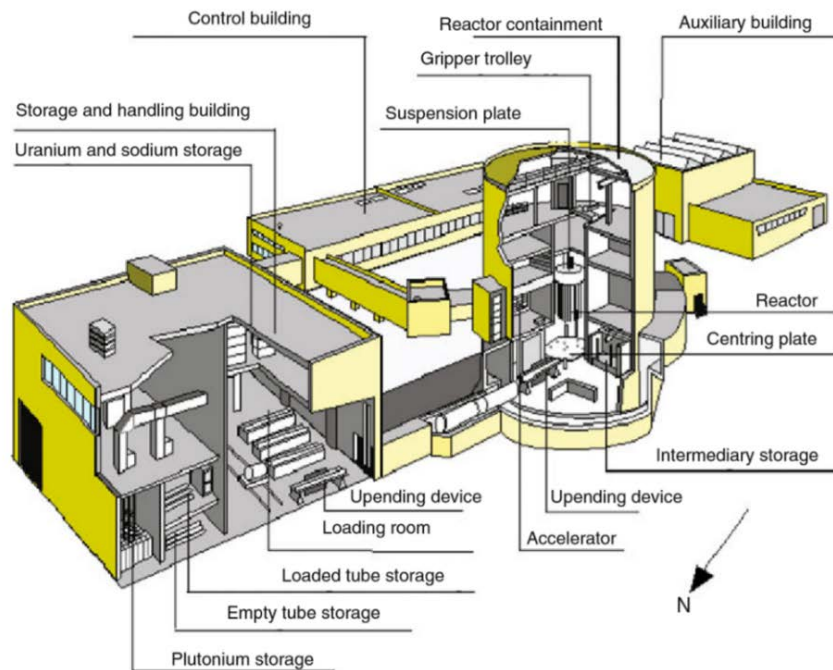


Figure 2.1. The MASURCA facility.

2.2.1 Characteristics of MASURCA

MASURCA (Figure 2.2) is a low-power, air-cooled research reactor having a rated maximum thermal power of 5 kW, which corresponds to a neutron flux level of about 10^{11} neutrons $\text{cm}^{-2} \text{s}^{-1}$ at the core centre [Chabre&Bonin].

Experimental configurations are constructed by loading subassemblies (called “tubes”), vertically, in a square lattice (Figure 2.3a). These stainless steel structure tubes have a 106 mm × 106 mm horizontal cross section and are about four meter long. They are filled with small rodlets or platelets (Figure 2.3b) of various types (fissile, fertile, structure, coolant, absorber, air, etc.), arranged in such a way as to represent average material concentrations and geometrical patterns of interest. Hundreds of such tubes can be loaded, allowing core diameters up to approximately 3.8 m. A typical experimental configuration consists of a quasi-cylindrical fissile core, radially surrounded by a fertile blanket or steel reflector, itself surrounded by shielding tubes. As a consequence of the large and diverse inventories of materials available at MASURCA, there is considerable flexibility in the configurations that can be simulated.

There are 40 pre-set Safety Rods (SRs) positions in the lattice and the shutdown mechanism is usually provided by four-to-eight SRs, depending on the characteristics and size of the core. A calibrated, low-worth, Pilot Rod (PR) is used to adjust the core reactivity near the critical state.

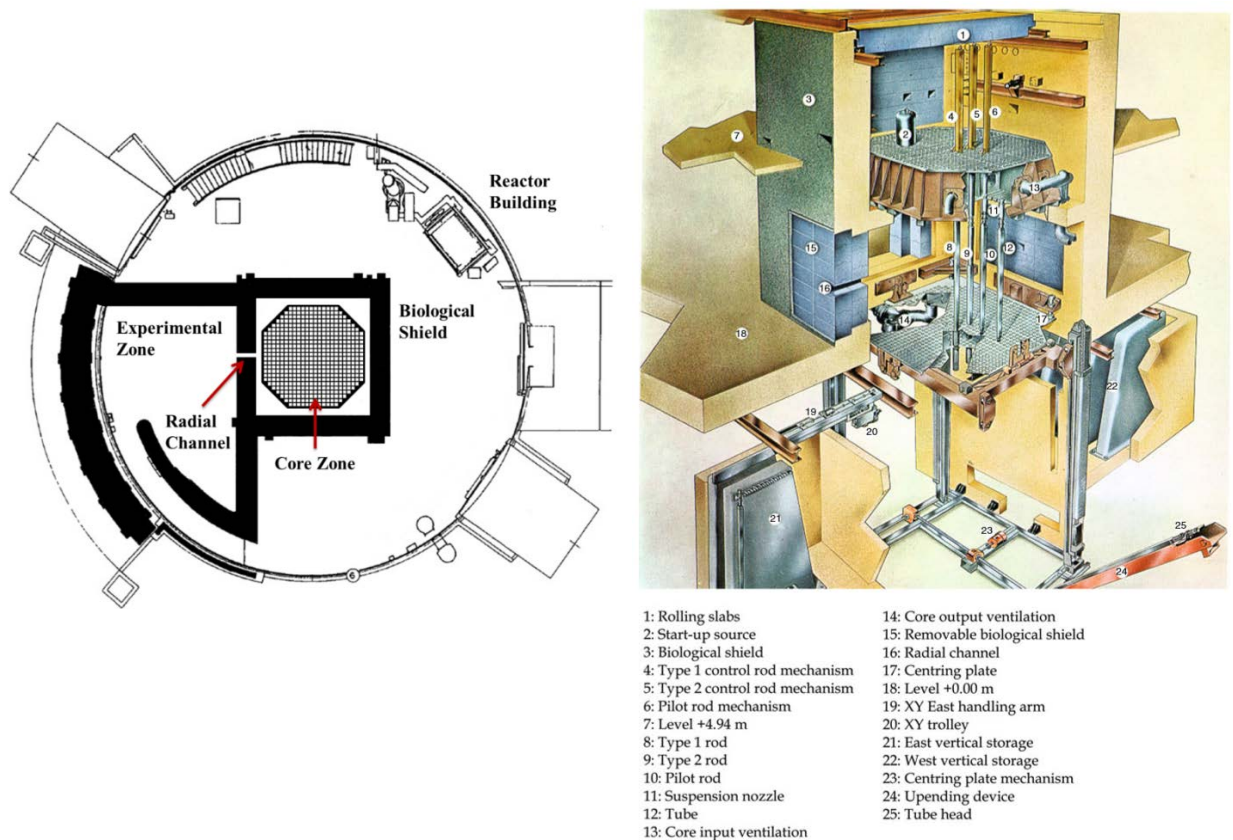


Figure 2.2. The MASURCA reactor building.

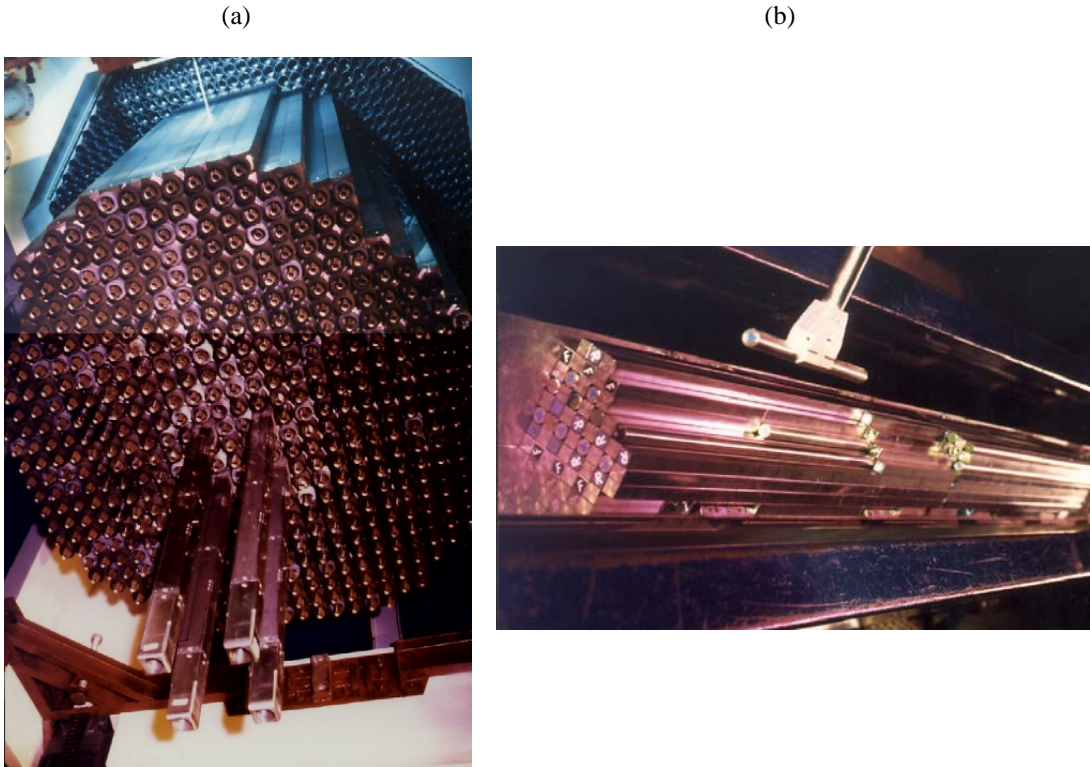


Figure 2.3. (a) A typical experimental configuration of MASURCA. (b) Rodlets and platelets loaded in a MASURCA tube.

Two radial measurement channels running across the core and several axial channels (one per tube) can be installed in the core. These experimental tubes have, typically, dimensions of 12.7 mm \times 12.7 mm. Bigger axial or radial channels, such as the radial tube employed in the MUSE-4 experiments (about 100 mm \times 100 mm in cross-sectional area) are less common, but can also be arranged for other types of measurements.

Local neutron flux measurements are usually obtained by moving small fission chambers through such channels, from the open space surrounding the biological shield. Other detection systems that have been extensively used are activation foils, for dosimetry purposes and thermo-luminescent detectors, for gamma-heating measurements. As always, such measurements are actually not “flux” measurements, but reaction rate measurements. If a sufficient number of such integral reaction rate measurements is available, then a spectral distribution can be inferred by using traditional unfolding techniques.

2.3 Opportunity and Motivation

2.3.1 The Flexibility of MASURCA

The high flexibility of MASURCA is best exemplified by the MUSE-4 program (2000-2004). In this series of experiments, a neutron source was generated by fusion reactions of deuterons impinging on a tritium (or deuterium) target placed at the centre of various sub-critical neutron multiplying media. This setup was used to investigate the physics of ADSs (Accelerator Driven Systems). The GENEPI variable-frequency pulsed deuteron accelerator and its associated high-voltage (250 kV) unit were conveniently located in the large open space provided by the “accelerator room”, an experimental zone on the North side of the reactor hall, which was already equipped with a biological shield (Figure 2.2). The deuteron beam was focussed and transported to the MASURCA core centre thru a vacuum guide tube running through a pre-arranged 100 mm × 100 mm radial channel, from an opening made in the reactor biological shield. Further advantage was taken of the large space available in the experimental zone to install an on-line beam monitoring instrument, facing the opening. This instrument was made of silicon detectors that detected the protons and alpha particles emitted at nearly 180° angle of the incident beam and returning thru the guide tube.

In keeping up with the spirit of the MUSE-4 experiments, which broadened the scope of the MASURCA activities and help initiate new collaborations, the current refurbishment period can be seen as an opportunity to look into the untapped potential of the facility, and to consider (or reconsider) innovative experimental configurations or setups, for the purpose of getting valuable new data from largely uncharted neutron physics territories.

The “accelerator room” (the name actually predates the MUSE experiments, as it dates back to the pioneers who designed MASURCA in the 60’s, which testifies to their visionary mind-set) could be used again, not for introducing an external source, but for extracting a fraction of the neutrons coming from the core thru a radial channel and a pre-arranged opening in the shield, in a beam-like configuration. The relative high fast neutron flux (for this type of facility) of 10^{11} neutrons $\text{cm}^{-2} \text{s}^{-1}$ (at 5 kW peak power) at the core center is sufficient for providing a neutron beam with fairly high intensity next to the core zone, at least for a short period. This time-continuous neutron beam will have energies distributed mainly in the intermediate-to-fast energy range, over a variable cross-sectional area thanks to an adjustable-size window in the biological shield. In doing so, one can take advantage of several favourable features of the reactor building and core characteristics to tailor the experimental configuration to the needs:

- i. Fast neutron spectrum, adjustable by modifying the core and reflector constituents, and also by inserting filtering materials;
- ii. Neutron flux intensity at the beam exit, adjustable by modifying the reactor thermal power and/or the distance between the core and the beam window;
- iii. Large and diverse inventories of simulation elements, combined with modular core, reflector and steel shield loadings, so that the neutron source spectrum can be tailored to different needs;
- iv. Small neutron attenuation thru air in experimental channels;
- v. Easy access to the reactor core from all sides;
- vi. A well-shielded, well-separated, experimental room adjacent to the core, large enough to house various spectroscopy instruments to monitor and characterize the beam in detail, and to house room-return attenuation materials (if necessary).

Such an extracted beam of intermediate-to-fast neutrons, adaptable in intensity, size and energy spectrum, assuming that it can be well-characterized and calibrated, could serve several purposes. Potential applications include nuclear physics experiments, shielding and transmission experiments, testing and validation of neutron detectors, neutron activation analyses, etc.

2.3.2 Instrumentation

In SFR physics validation studies, a major objective is the accurate determination of the detailed neutron energy distribution everywhere in and near the core. Acquiring the necessary experimental data is very difficult in an actual power plant, which has limited provisions for inserting measurement devices. This is why in typical MASURCA experiments, much attention is paid to the acquisition of neutron spectrum data, in various relevant situations and in representative conditions.

As already mentioned, the measurement techniques that are routinely used in MASURCA for local (in-core and near-core) flux characterization are activation foils and movable small-size fission chambers. These techniques have the advantage of not being very intrusive, they are particularly robust and precise, which makes them well suited to monitor the neutron flux, and perform radial and axial traverses (spectrum indices, reaction rates, neutron importance,...) throughout the core and in the surrounding reflector zones. Typical experimental uncertainties are in Table 2.1 [Assal 2012].

Table 2.1. Typical experimental uncertainties [Assal 2012].

Parameter	Uncertainty (1σ)
Critical Mass	few pcm
Reactivity Jump	$\Delta\rho < 1\text{\$}$: few pcm $\Delta\rho > 1\text{\$}$: 2 % to 4 %
Fission Rate	1 % to 2 %
Spectrum Index	2 % to 3 %
β_{eff}	2 %

However, these measurement techniques do not provide direct experimental access to the variation of the neutron spectrum typical of fast reactors, as the neutron energy information is simply integrated by the foil or the chamber. This shortcoming can be partly compensated by performing repeated measurements with different types of foils and chambers. The various measurements can then be combined with the corresponding calculated responses in a best-fit-plus-unfolding procedure to infer an estimate of the spectrum. However, the detailed energy spectrum derived from such a procedure is largely dependent on calculated quantities (as well as on the related errors and uncertainties), and on the prior knowledge of neutron cross section profiles as a function of energy.

As a result, such measurements, although very valuable, are not sufficient to form a complete set of experimental data for a comprehensive physics validation in which spectral errors cannot go unnoticed. This is particularly true in regions where neutron transport calculations are notoriously difficult, such as near material interfaces, along streaming paths or in preferential leakage directions, in low-density regions (an extreme case being a coolant voided situation following an accident), inside reflectors and shields where there are severe flux gradients, etc. For all such situations which are typical of SFR applications, there is therefore an incentive in developing non-intrusive spectrometric techniques capable of recording the local neutron energy over several decades, with a sufficient resolution (better than 10%), based on a detection process which can be calibrated using independent reactions (standards). Ideally, such a spectroscopy system should also be able to measure the neutron direction of travel selectively, but this is beyond the scope of this work.

2.4 Objectives

This PhD project has mainly two objectives. The first one is to establish the range of conditions under which a continuous beam of intermediate-to-fast energy neutrons could be extracted radially from MASURCA and used for a range of new applications. The second - correlated - objective is to develop a neutron spectrometric capability for the characterization of mixed radiations fields in this intermediate-to-fast energy domain, from tens of keV to tens of MeV. The spectrometer should be capable of producing high-quality data, having sufficient resolution so that they can be reliably used as validation data. The set goal is to develop a proof of principle and (ideally) a prototype to be tested, the technological feasibility and optimization of the spectrometer being outside the scope of this PhD project.

Regarding the first point, before definite statements can be made about the practical use of MASURCA as a beam facility for specific applications, several conditions must be met. These conditions relate to the beam characteristics in intensity, energy spectrum, neutron-to-gamma background at various positions along the channel, as well as to the sensitivity of these characteristics to changes in the source neutrons and in the general experimental setup. Such considerations are classical in the field of neutron beam physics. Already in 1962, K. H. Beckurts, P. A. Egelstaff and H. Goldstein [Beckurts 1962] wrote:

“There seems to be an almost universal need for basic information on how to ‘tailor’ neutron beams to meet particular requirements. These requirements depend of course on the type of experiment. The problem is usually to get a high intensity of neutrons in a certain energy range with as few neutrons of other energies and gammas as possible. Sometimes a sacrifice in the desired neutron intensity can be tolerated if the ordinary type of background radiation is sufficiently reduced.”

This will be the subject of Chapter III, devoted to the evaluation of MASURCA as a beam facility and as multi-purpose, physics installation.

The second objective is subdivided into two parts. The first part aims to evaluate the feasibility of neutron spectrum measurements:

- In or near the MASURCA core, mainly (but not only) for validating neutron transport calculations in high-leakage regions of SFR cores. This is a particular challenging task as the spectrometer would have to be quite small to fit in a confined space and to cause minimal perturbations;
- Out of the MASURCA core (and surrounding reflectors and shielding tubes), for beam-type applications. In this case, the adjacent experimental zone provides ample room for the spectrometer.

This will be further discussed in Chapter III, where the constraints imposed by the MASURCA environments on the detection system are examined.

The second part is the actual development of the fast neutron spectrometric capability. This is the core of this PhD and it will be covered from Chapters IV to VII. The starting point will be an assessment of the wanted characteristics, followed by a survey of fast neutron spectroscopy techniques, and the considerations which will lead to choosing a particular detection technique. It is worth noting that, thanks to a favourable development of this work, it was actually possible to assemble and test a real prototype detector.

III. MASURCA as a Multipurpose Facility

- 3.1 Fast Neutron Source Reactors
- 3.2 MASURCA Beam Configuration
- 3.3 Simulation Models
 - 3.2.1 Flux and Criticality Evaluation
 - 3.2.2 Neutron Spectrum and Intensity Evaluation
 - 3.2.3 Gamma Spectrum and Intensity Evaluation
- 3.4 MASURCA Beam Configuration vs Fast Neutron Source Reactors
- 3.5 Conclusion about MASURCA as a Multipurpose Facility

Introduction

The dwindling number of neutron research reactor facilities (ZPRs, source reactors, MTRs, hot labs, ...) requires to make the most efficient use of the remaining ones, while assuring that the needs of a broad physics community are covered. Those organizations that continue to maintain and operate ZPRs have therefore a special responsibility with respect to this research community. In the case of MASURCA and several other ZPRs, there are valuable lessons to be learned from the way they were originally designed, their evolution, and the many years of operation.

The first part of this chapter is dedicated to a review of past and present fast neutron “source reactors”, together with their experimental programs and researches. The second part is devoted to the evaluation of MASURCA as a beam facility, at the level of a scientific feasibility study: several simplifications are therefore made in describing the reactor core and the surrounding zones. The last part is a comparison between the characteristics of the fast neutron beams delivered by source reactors and those of a prospective MASURCA beam experimental configuration. The chapter concludes with a brief discussion of MASURCA as a multi-purpose facility.

This chapter is kept - purposely – short. However, there is a considerable legacy of scientific articles and technical documents, many of them dating back to the 1960-to-1990 period. Historical considerations relating to experimental neutron physics can be found in *Neutron Physics* (1964) by Beckurts and Wirtz, based upon the lectures given by Wirtz at the university of Göttingen since 1951; or in Part II of *Fast Neutron Physics* (1960) by Marion and Fowler and in *Fundamental Aspects of Reactor Shielding* (1959) by Goldstein. The previously mentioned volume 17, number 4/5 (1963) of *Journal of Nuclear Energy Parts A/B* dedicated to “SPECIAL BEAMS FROM REACTORS AND ACCELERATORS” is another interesting reading for the addressed theme. For more up to date reactor physics experiments, chapter 18 of *Handbook of Nuclear Engineering* (Cacuci, 2010): “Reactor Physics Experiments on Zero Power Reactors”, gives a well-rounded view of the R&D programs and techniques developed at the CEA (Commissariat à l’Energie Atomique) and elsewhere.

3.1 Fast Neutron Source Reactors

Fast neutron source reactors are extremely useful research tools for physicists and engineers. Versatility and flexibility are the main characteristics of such facilities.

A good example is the Tokyo University source reactor YAYOI (Figure 3.1) in Japan, a multi-purpose facility that was operated for various studies and aims [Oka 1998 (1)], such as:

- i. Fast neutron shielding and neutron transport researches [Oka 1998 (2), Oka 1980, Shin 1980, Oka 1981];
- ii. Standard neutron field and researches of advanced neutron detection systems [Nakazawa 1998];
- iii. Pulsed operation [Wakabayashi 1998];
- iv. Measurement of decay heat of fast neutron fission products [Akiyama 1998];
- v. Study of epithermal neutron column for boron neutron capture [Oka 1998 (3)];
- vi. On-line tritium recovery from fusion breeder materials [Tanaka 1998, Terai 1998];
- vii. Fast neutron radiolysis of water at elevated temperatures relevant to water chemistry [Katsumura 1998];
- viii. Fast neutron radiography [Yoshii 1998];
- ix. Measurements of neutron cross section for fast neutrons [Harada 2009];
- x. Other: studies of irradiation effects of organic materials, semi-conductors and metals, neutron noise, etc.;
- xi. Education.

As evidenced from the above list, YAYOI was constructed so as to meet the needs of many researchers. The core fuel is enriched uranium surrounded by a fuel blanket (depleted uranium), contained in a lead reflector. There are no moderating materials in the reactor and no thermal neutrons are produced: the neutron spectrum is hard. The gamma-rays associated with fission are well shielded by the thick lead reflector/shield around the fuel zone.

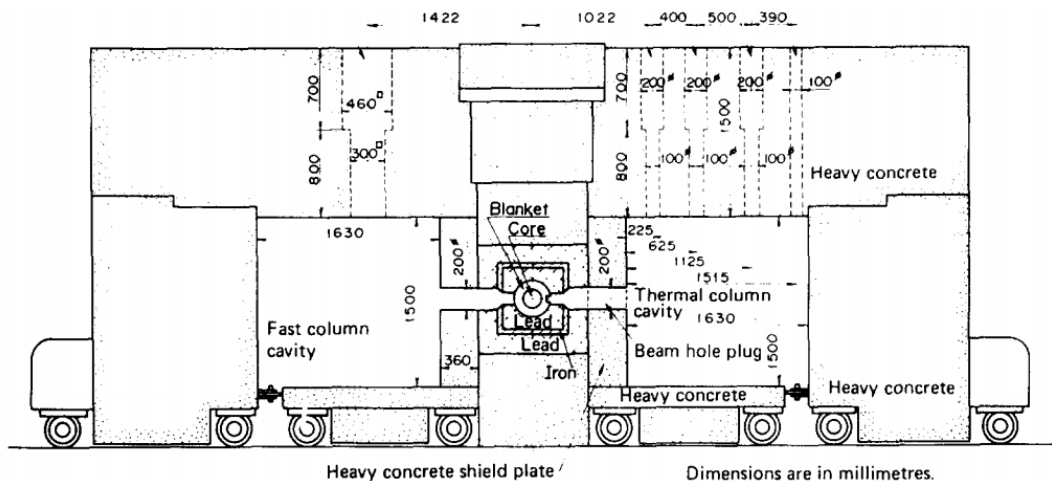


Figure 3.1. Fast neutron source reactor YAYOI [Oka 1998 (2)].

A series of experimental channels of different sections are available from the sides of the core, including the well-known Glory Hole and Grazing Hole. Movable concrete blocks allow further flexibility for neutron measurements. YAYOI attained its first criticality in 1971, but was permanently shut down in 2011.

TAPIRO (Figure 3.2), in Italy, is another facility capable of providing the means for several applications. The reactor went critical in 1969 and during its operational life performed thousands of irradiations for applications in different fields (nuclear physics, biological applications, damage studies, etc.). Examples of studies in TAPIRO are listed in the following:

- i. Irradiation experiments for studies of neutron damage [Angelone 1998, Salvatore 2007, Angelone 2010];
- ii. Propagation studies [De Caroli 1980, Carta 1982];
- iii. Nuclear data experiences [D'Angelo 1973];
- iv. Fast neutron activation analysis (FNAA);
- v. Experiments for codes validations;
- vi. Medical applications [Rosi 2004];
- vii. Radiological characterization;
- viii. Etc.

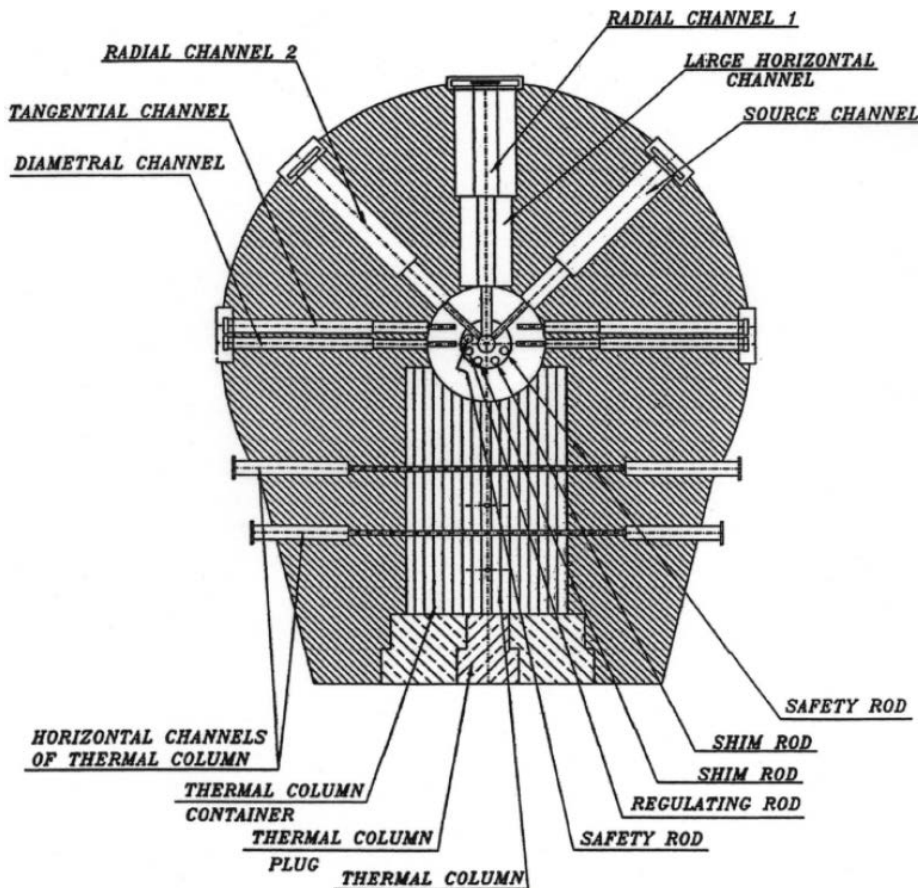


Figure 3.2. Fast neutron source reactor TAPIRO.

The TAPIRO reactor core is a highly enriched ^{235}U cylinder surrounded by a copper reflector. A biological shield of borate concrete separates the core from the reactor hall. A number of channels, of different dimensions, run across the reactor reflector and shield. Other experimental channels do not reach the core but are located at different distances from it. All these channels are able to host various types of detectors, allowing a good characterization of the different neutron spectra available.

TAPIRO is based on the concept of the AFSR (Argonne Fast Source Reactor), another fast source reactor defined, using the words of P.I. Amundson et al. [Amundson 1969], as:

“...a source of both fast and thermal neutron fluxes in convenient proximity, so that a variety of useful irradiation can be performed. Moreover, it is a “test bed” reactor in which many techniques can be developed and refined.”

AFSR (Figure 3.3) has been mainly used for the calibration of neutron detectors, such as ^6Li sandwiches and fission chambers, to use in ZPPR (Zero-Power Physics Reactor) [Lesage 2001].

In France, a reactor of this type has been constructed in Cadarache at approximately the same time: HARMONIE. Its characteristics are similar to those of the described fast neutron source facilities and, regarding applications, it played an important role in the first qualification tests of SFR shielding materials [Chabre&Bonin].

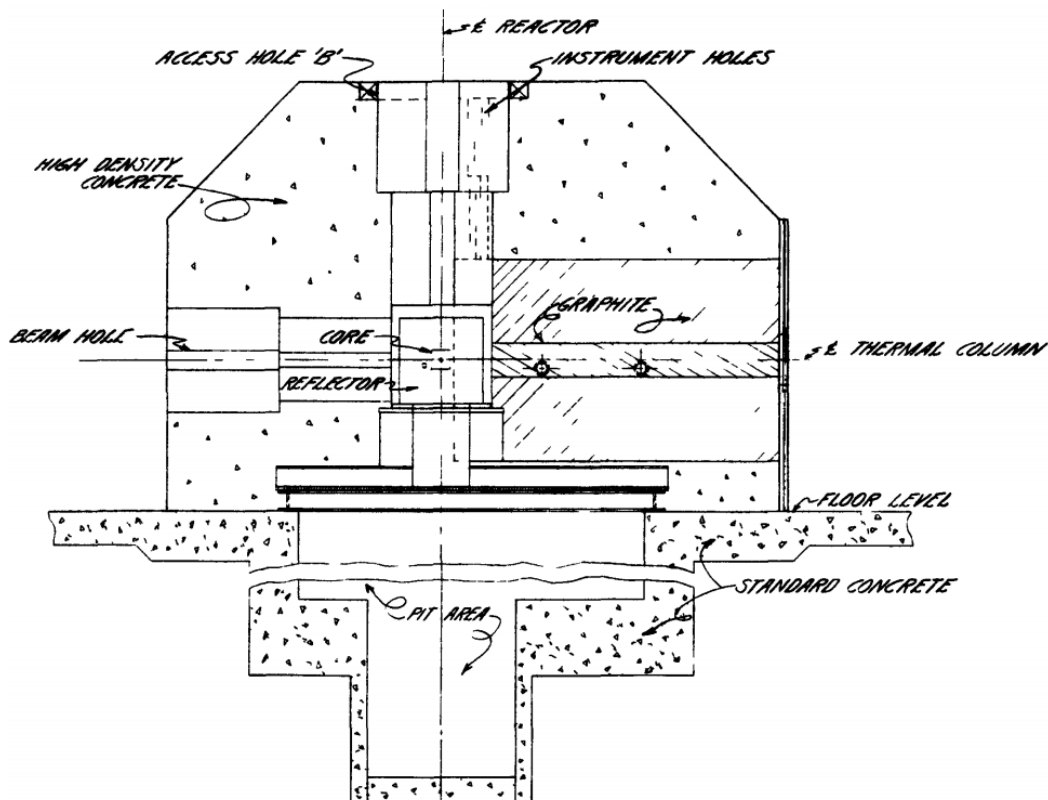


Figure 3.3. Fast neutron source reactor AFSR [Amundson 1969].

MASURCA does not strictly belong to this “source reactor” category, in which the reactor core remains always the same. In MASURCA, the core constituents and positions can be varied almost at will, the limits being the allowed safety envelope and the available material inventories. The large range of possible variations in simulation elements and subassembly loading patterns is an essential asset, as the physics studies of fast neutron lattices and cores require multiple parametric changes. However, as the saying goes, “he who can do more can do less”, MASURCA can also be seen as a source reactor each time a particular core configuration is loaded and remains unchanged for some time. This holds all the more as there is ample open space and quite easy access for experiments from all sides of the core, let alone the large “accelerator room”.

These considerations, combined with those of Chapter II, suggest that MASURCA could easily “bring on board” some of the capabilities of fast neutron source reactors. One such capability is the delivery of a fast neutron beam in the experimental zone thru prearranged radial channels. This could be of importance as there are very few facilities still in operation with such a capability. A sketch of the concept is shown in Figure 3.4.

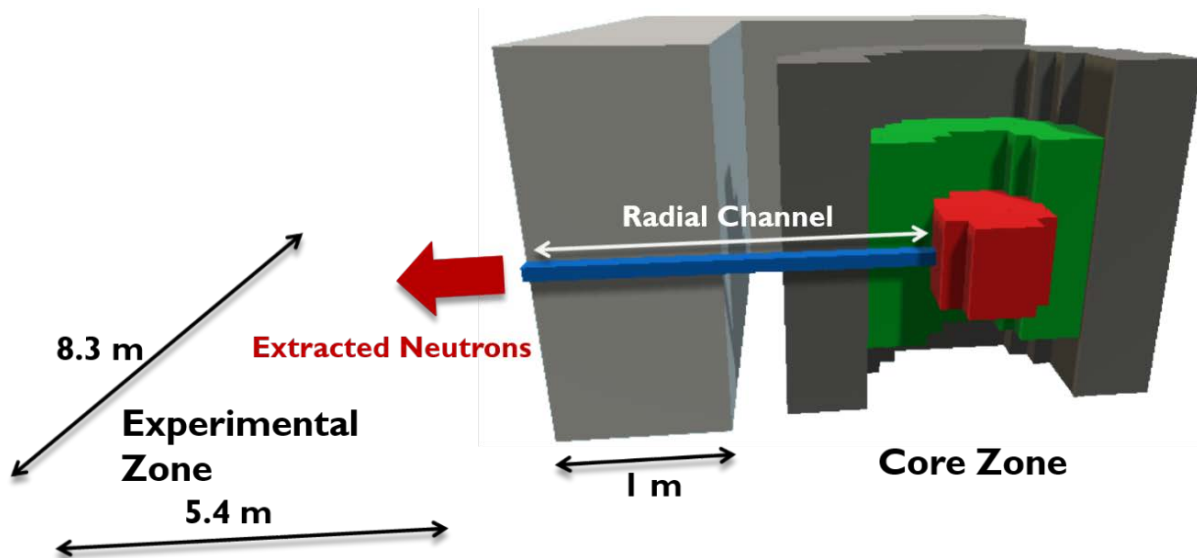


Figure 3.4. MASURCA beam experimental configuration.

Table 3.1 compares some of the facilities discussed previously and MASURCA. Regarding the characteristics of the core in terms of thermal power and neutron flux, they are very similar, although the structure of the MASURCA one is rather different. The maximum thermal powers are comparable in magnitude, from 1 to 5 kW, as well as the maximum neutron flux at the centre of the core (only TAPIRO is an order of magnitude greater). All source reactors have enriched uranium as fuel. On the other hand, MASURCA has the advantage of being able to use different types of fissile core materials: uranium and plutonium, mixed in variable proportions with natural or depleted uranium, and many other materials.

Table 3.1. Comparison between MASURCA and research reactors that operated also as a fast neutron sources [Oka 1998 (1)].

	MASURCA	YAYOI	TAPIRO	AFSR
Location	France	Japan	Italy	U.S.A.
1st Criticality	1966	1971	1969	1960
Status	Refurbishment	Shut Down	Refurbishment	Shut Down
Fuel	Variable	Enriched U	Enriched U	Enriched U
Blanket	Variable	Depleted U	None	Depleted U
Reflector	Variable	Lead	Copper	None
Cooling	Forced Air	Forced Air	Forced He	Forced Air
Max thermal power	5 kW	2 kW	5 kW	1 kW
Max neutron flux at centre (n cm⁻² s⁻¹)	3.0×10^{11}	8.0×10^{11}	3.0×10^{12}	5.7×10^{11}
Beam size (cm)	?	Ø 20.0	Ø 5.6	Ø 5.6
Beam intensity (n cm⁻² s⁻¹)	?	$\sim 10^6$ - 10^7	$\sim 10^8$ - 10^9	1.0×10^7
Type of spectrum (@ channel exit)	?	Intermediate-to-fast	Intermediate-to-fast	Intermediate-to-fast
n_{fast}/γ	?	-	-	-

Regarding the features of the extracted beams, as stated before, there are three significant requirements for fast neutron beam applications. The first one is to have a sufficiently intense neutron flux level at the beam exit; the second one is to have an appropriate (for a specific application) energy spectrum; and the last one is to have a good compromise in terms of (fast) neutron-to-background ratio.

In the next section, a feasibility study of the MASURCA beam configuration concept is carried out. The aim is to fill the missing data in Table 3.1 and thus being able to compare MASURCA with other source facilities which proved, during their operation time, the capability of performing a large number of useful applications.

3.2 MASURCA Beam Configuration

The survey performed on fast neutron source reactors suggests that a minimum beam intensity on the order of 10^7 - 10^8 neutrons cm⁻² s⁻¹ should be aimed for in order to keep as many applications and options open. An early estimation of the number of neutrons that reach the end of the extraction channel can be done with the following formula [Beckurts&Wirtz]:

$$J = \frac{\Phi F}{4\pi l^2} . \quad (3.1)$$

Where Φ is the neutron flux ($\text{n cm}^{-2} \text{s}^{-1}$) entering the front surface F (cm^2) of the beam hole, l is the length of the channel and J the neutron current density ($\text{n cm}^{-2} \text{s}^{-1}$) at the channel exit. Considering a MUSE-4-like radial channel, F is about 110 cm^2 and l about 290 cm . If Φ is in the order of $10^{11} \text{ neutrons cm}^{-2} \text{s}^{-1}$ (at 5 kW), J is found to be about $10^7 \text{ neutrons cm}^{-2} \text{s}^{-1}$. Thus, with only a coarse estimation, it is already possible to conclude that the potential of MASURCA as a beam facility is real.

Before proceeding with more accurate tools, such as Monte Carlo codes, another interesting evaluation (with this “*paper&pen*” approach), is to understand to what extent it is possible to increase this number and also, as an exercise, to establish the maximum “extractable” beam intensity. It is well known that the neutron attenuation goes with the square of the distance and thus the easiest way for increasing the beam intensity in the experimental zone is to shorten the path travelled by neutrons. In order to do this, the displacement of the core off-centre has been taken into consideration (as much as practically feasible towards the experimental zone). In fact, in MASURCA, the core can be moved inside the square lattice (Figure 2.2, core zone) along the x and y directions, with the only limitation sets by the SRs fixed positions. There are 40 pre-set SRs positions in the lattice and as long as the core is constructed in a place where the SRs can be located, no practical limit is broken. It is therefore possible to move the core off-centre by a maximum of about 100 cm along the x axis, in the direction of the experimental zone, as there are no pre-set SR positions past that point. By doing this, the length of the extraction channel is decreased to about 190 cm and the magnitude of J is approximately doubled. By taking into account also the partial enlargement of the radial channel section, maximum intensities in the order of $10^8 \text{ neutrons cm}^{-2} \text{s}^{-1}$ are expected.

Another important aspect is the composition of the neutron spectrum and the relative contribution of uncollided neutrons (*id est* the fraction of neutrons leaving the fuel region that directly reach the experimental zone through the radial channel) at the channel exit. Indeed, only a fraction of the neutrons leaving the fuel region directly reach the experimental zone through the radial channel, the other neutrons undergoing various collisions that alter their energy. For some applications, the uncollided neutrons will be the neutrons of interest, for instance if the objective is to study the beam sensitivity to the core fissile constituents [Dioni 2016 (1)]. Enlarging the beam diameter at the start of the channel could help increase this sensitivity. This is studied via simulations in the next section.

One way to tailor or optimize the neutron beam is by introducing filtering materials in the beam. In doing so, the fraction of low energy neutrons ($< 10 \text{ keV}$) can be significantly reduced without much altering the higher energy part, but at the expense of a lower intensity. This is discussed in [Dioni 2016 (2)] and in **APPENDIX A**.

3.3 Simulation Models

In this section, the simulation models and the corresponding results concerning the MASURCA beam configuration are described. All calculations have been done with the Monte Carlo code TRIPOLI-4® [Tripoli] or with the deterministic code ERANOS-2® [Eranos], using JEFF-3.1-based nuclear data [Jeff 3.1]. In practice, many calculations have been performed; only a subset of them are reported here, in order to illustrate the main findings.

As mentioned before, MASURCA principal activities were related to core physics studies and, at the beginning of this work, no models were available for studying this special configuration of MASURCA. A similar, in a way, set-up can be found in the MUSE-4 models, in the sense that a bigger radial channel (than the experimental ones), radially crossing a part of the core, was present.

A MUSE-4-like radial channel is taken as starting point for constructing the models, together with the following assumptions:

- i. to use only materials available in MASURCA;
- ii. to find an-almost-critical core configuration;
- iii. to make the model representative but otherwise simple enough, so as not to require too much computational time (Monte Carlo).

The backbone of these assumptions is the idea of performing a feasibility study for evaluating the intensity and the spectrum of an extracted fast neutron beam that is representative (of MASURCA) and simple (for the nature of this work). The representativeness takes the form of material and geometrical constraints, meanwhile the simplicity of homogenized core regions: fuel, reflector and shield region.

Mainly three models were set-up:

- 1) A reference, first of a kind for MASURCA, beam model: called ‘REF’, reference (schematically represented in Figure 3.5a);
- 2) A 100 cm off-centred model, for increasing the neutron beam intensity: ‘OffC’, Off-Centred (Figure 3.5b);
- 3) An off-centred model in which the channel is further modified for increasing the fraction of uncollided neutrons and the neutron intensity at the channel exit: ‘OffCIC’, Off-Centred Inverted Cone (Figure 3.5c);

The REF model is characterized by a typical centred core in the x - y horizontal plane, and by a ~ 2.9 m long radial beam channel having a constant section of 10.6 cm × 10.6 cm. As previously said, all material zones considered are homogenous: the fuel zone is made of metallic uranium fuel (~ 30 % ²³⁵U enriched) and sodium, the reflector zone of stainless steel and sodium, and the shield zone of stainless steel and absorbers (more information is provided in **APPENDIX A**). About one meter of air separates the core from a 90 cm thick biological shield made of concrete blocks. The radial beam channel is filled with air. The dimensions are chosen so that the configuration is nearly critical. The height of the fuel zone is 45 cm and the radii of the quasi-cylindrical core zones are reported in Figure 3.5a in units of cm.

The OffC model is identical to the REF model, except for the position occupied by the core in the horizontal plane. The core has been moved 100 cm away from the geometrical centre of the support

structures, along the x axis, in the direction of the experimental zone. Thus, the radial channel length is ~ 1.9 m.

In order to maximize the fraction of neutrons coming from the core edge and entering the channel, the area of the channel facing the fuel is increased fourfold ($20.7 \times 20.7 \text{ cm}^2$). This is the OffCIC model. It is identical to the OffC model, except for the shape of the radial channel (the total length is the same).

Different calculation approaches have been used for saving computing time: stepwise runs, source particle storage and restart, variance reduction methods, etc. Detailed information regarding these calculations can be found in **APPENDIX A**.

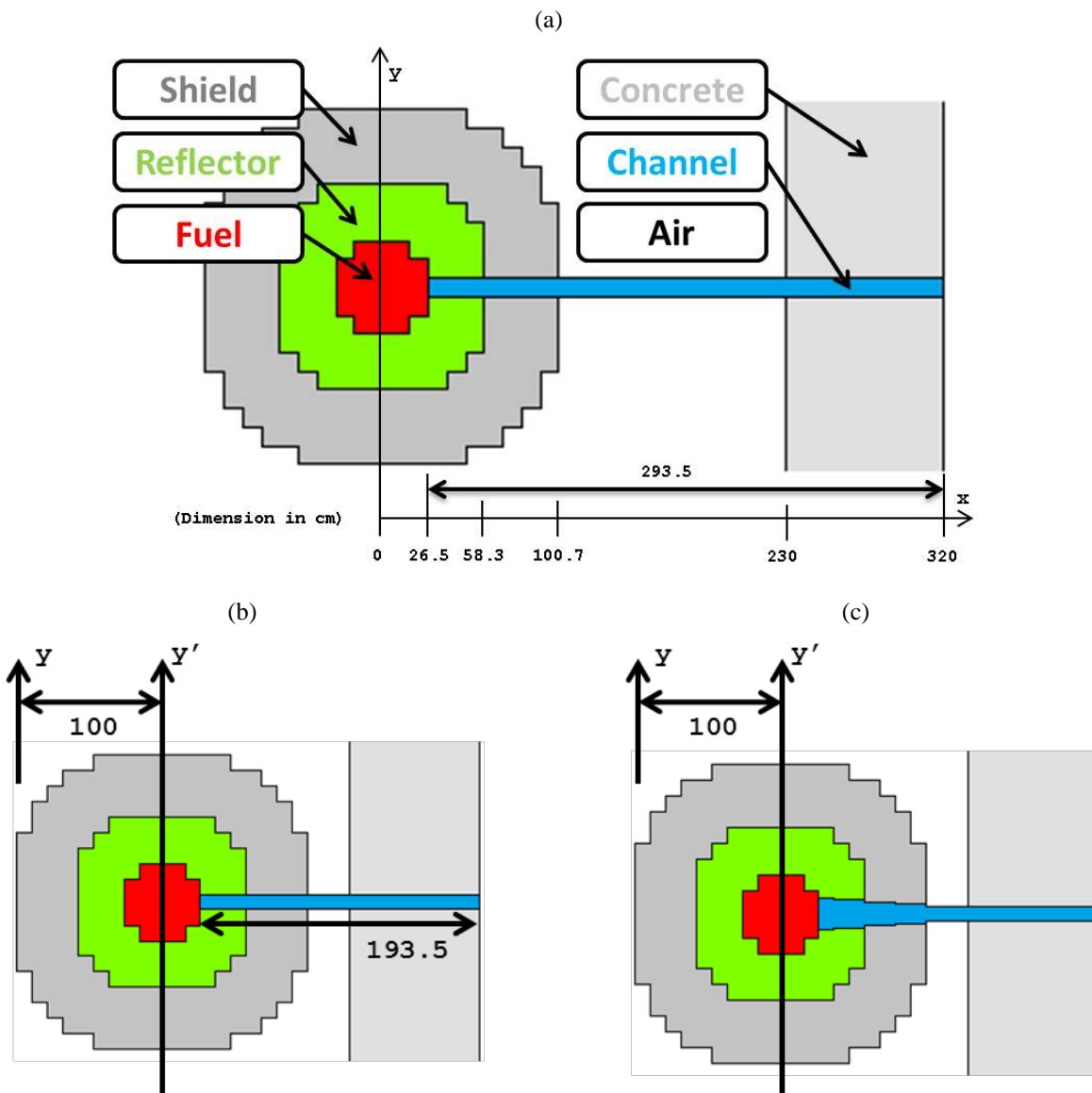


Figure 3.5. MASURCA (a) REF, (b) OffC and (c) OffCIC models.

The results presented hereafter were actually obtained from a two-step calculation: first, a criticality calculation for finding the k_{eff} of the system and the neutron source term; second, a shielding calculation for evaluating the neutron (and photon) intensity and spectrum at different positions along the beam channel. The validity of this two-step procedure was verified for one model by comparison with a (much longer running) single-step calculation.

3.3.1 Flux and Criticality Evaluation

In Table 3.2, a comparison of the computed k_{eff} values of the three models is made.

Table 3.2. Computed k_{eff} values for the three models.

	k_{eff}	1σ stat. unc.
REF	1.0141	5E-05
OffC	1.0139	5E-05
OffCIC	1.0055	5E-05

The small difference (20 pcm) between REF and OffC is due to neutron reflections on the concrete wall, which is nearer in the OffC case. The behaviour of the flux in the external region of the core, the shield, is also slightly different, since more neutrons come back in the shield in the OffC case, after being slowed down in the concrete wall. The shield is efficient at preventing these neutrons from returning to the fuel region, since the flux there is the same for the REF and OffC models. This difference can be seen in Figures 3.6a and b. These figures represent the same normalized neutron flux in a 33 energy bin structure, but with two different scales: log-lin and log-log. Regarding the flux in the radial channel crossing the reflector and the shield, a small fraction of low-energy neutrons contaminates the flux distribution. This can be seen in Figure 3.6c, “channel”, which shows a (total) flux traverse in the core at $z = 0$ and $y = 0$. Note that the coordinate x is not the absolute abscissa here but the relative position with respect to the centre of each core.

A fairly large difference of 840 pcm can be observed between the k_{eff} values of the OffC and OffCIC models. This is mainly due to the difference in shape between the two extraction channels: since the entry surface of the second one is larger, more neutrons leak out of the fuel region, and therefore fewer neutrons participate in the neutron chain reaction. Still, the spectra in the core fuel region remain almost the same, only a very small difference can be seen when the spectra are plotted in a log-log scale (Figure 3.6b), at low energies.

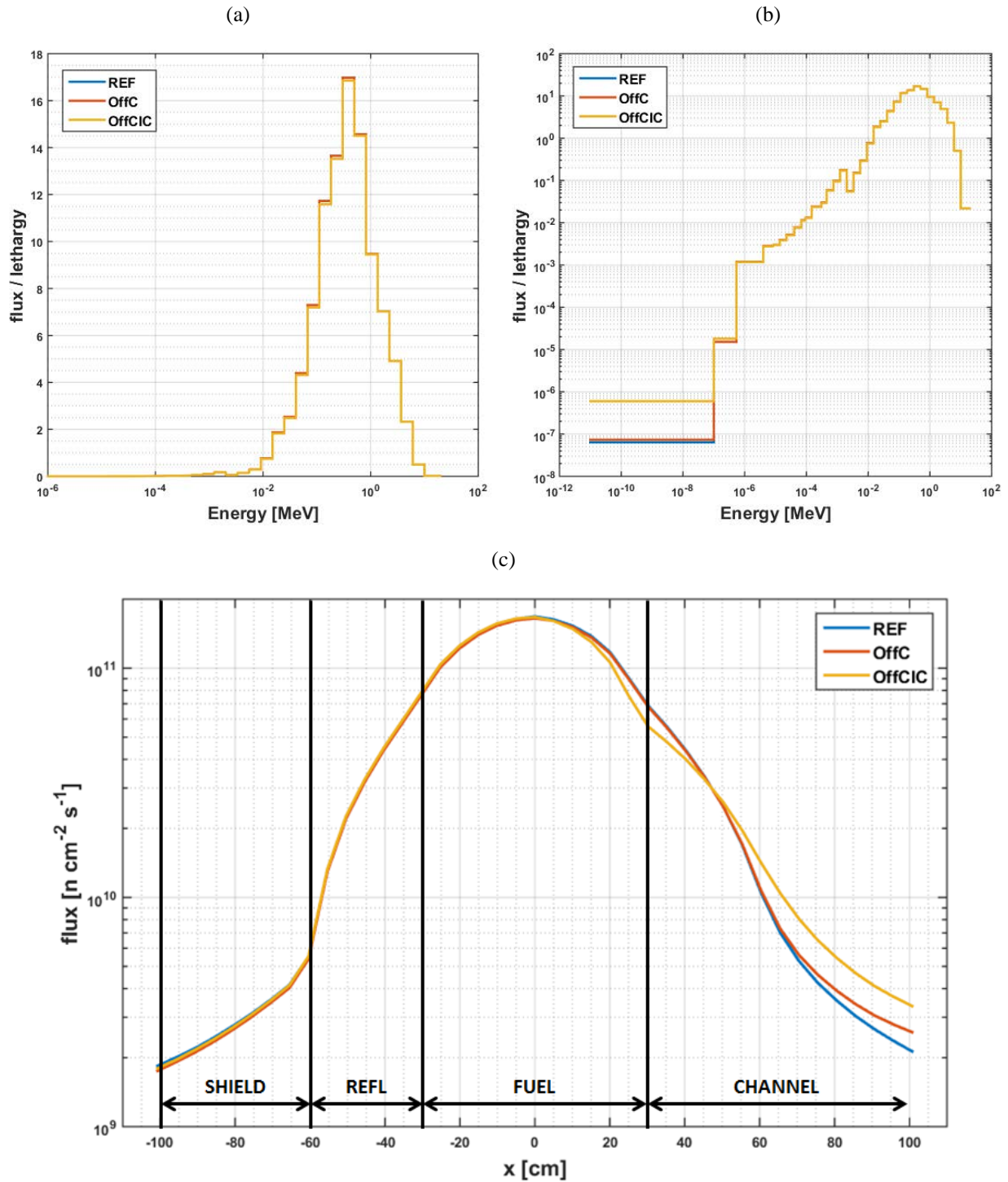


Figure 3.6. (a), (b) Neutron flux in the fuel region. (c) Flux traverse in the core at $z=0$ and $y=0$, as a function of relative x position (5 kW).

3.3.2 Neutron Spectrum and Intensity Evaluation

The results discussed in this section are all normalized to 5 kW total thermal power.

Figure 3.7a compares the total current intensities (neutrons $\text{cm}^{-2} \text{s}^{-1}$) as they attenuate along the radial channel. The curves represent Monte Carlo computed outgoing (i.e., directed towards $x > 0$) neutron currents that cross successive surface tallies in the extraction channel. Here, the x coordinate is the absolute position. In the REF model, the channel starts at $x=26.5$ cm, while in the other two models it starts at $x = 126.5$ cm.

A neutron beam intensity in the order of 10^7 (neutrons $\text{cm}^{-2} \text{s}^{-1}$) was estimated thanks to equation 3.1 and now is confirmed by Monte Carlo simulations, as well as that of a one meter shorter channel, which led to an intensity that is approximately doubled. With the geometry of the extraction channel used in OffCIC, it is possible to reach outgoing neutron currents in the order of $10^8 \text{ n cm}^{-2} \text{s}^{-1}$. These kinds of values were the objective set in order to keep as many applications as possible open (10^7 - $10^8 \text{ n cm}^{-2} \text{s}^{-1}$). Additional information of the total neutron beam intensity exiting the channel are presented in the first column of Table 3.3. By looking at the table, it is immediately clear how much the changes in the model configurations contributed to the rising of the beam intensity.

The computed neutron spectra of the outgoing current at the beginning and at the end of the channel are shown in Figure 3.7b and c. Table 3.3 also shows a macro-energy breakdown of the neutron energy spectrum at the channel exit. The impact of the one-meter shift and the change in the channel geometry (OffCIC) can be seen: the portion of the uncollided neutrons is higher and the fast-to-total neutron ratio is increased. In the OffCIC configuration, 89% of the neutrons have energies above 10 keV (respectively, 75% over 100 keV).

Table 3.3. Neutron current intensity and energy distribution at the channel exit (at 5 kW).

	Total ($\text{n cm}^{-2} \text{s}^{-1}$)	<0.5 eV	0.5 eV-10 keV	>10 keV	<100 keV	>100 keV
REF	3.65E+07	0.07	0.07	0.86	0.31	0.69
OffC	7.74E+07	0.07	0.08	0.85	0.31	0.69
OffCIC	1.32E+08	0.06	0.06	0.89	0.25	0.75

Note the big, well-defined, resonance “dip” in the neutron spectra, corresponding to the large scattering resonance of ^{56}Fe at 28 keV in Figure 3.7b and c. The mark is well preserved along the channel path. This is less the case for the ^{23}Na 2.8-keV resonance, which can be clearly seen at the beginning of the channel (Figure 3.7b) but is quite attenuated at the end (Figure 3.7c). In [Dioni 2017 (1)] is presented a study for evaluating to what extent changes in the reactor core constituents affect the fast neutron beam and how much the distinctive features of the neutron spectra are maintained as neutrons travel into the radial channel, until they reach the experimental zone. The general conclusion is that the neutron spectra at the end of the channel preserve much of the characteristics of the starting spectra above 10 keV. This is an incentive to try to develop a spectrometer capable of measuring the neutron spectrum at energies as low as 10 keV, in order to extract information on the MASURCA cores from the spectral signature at the channel exit.

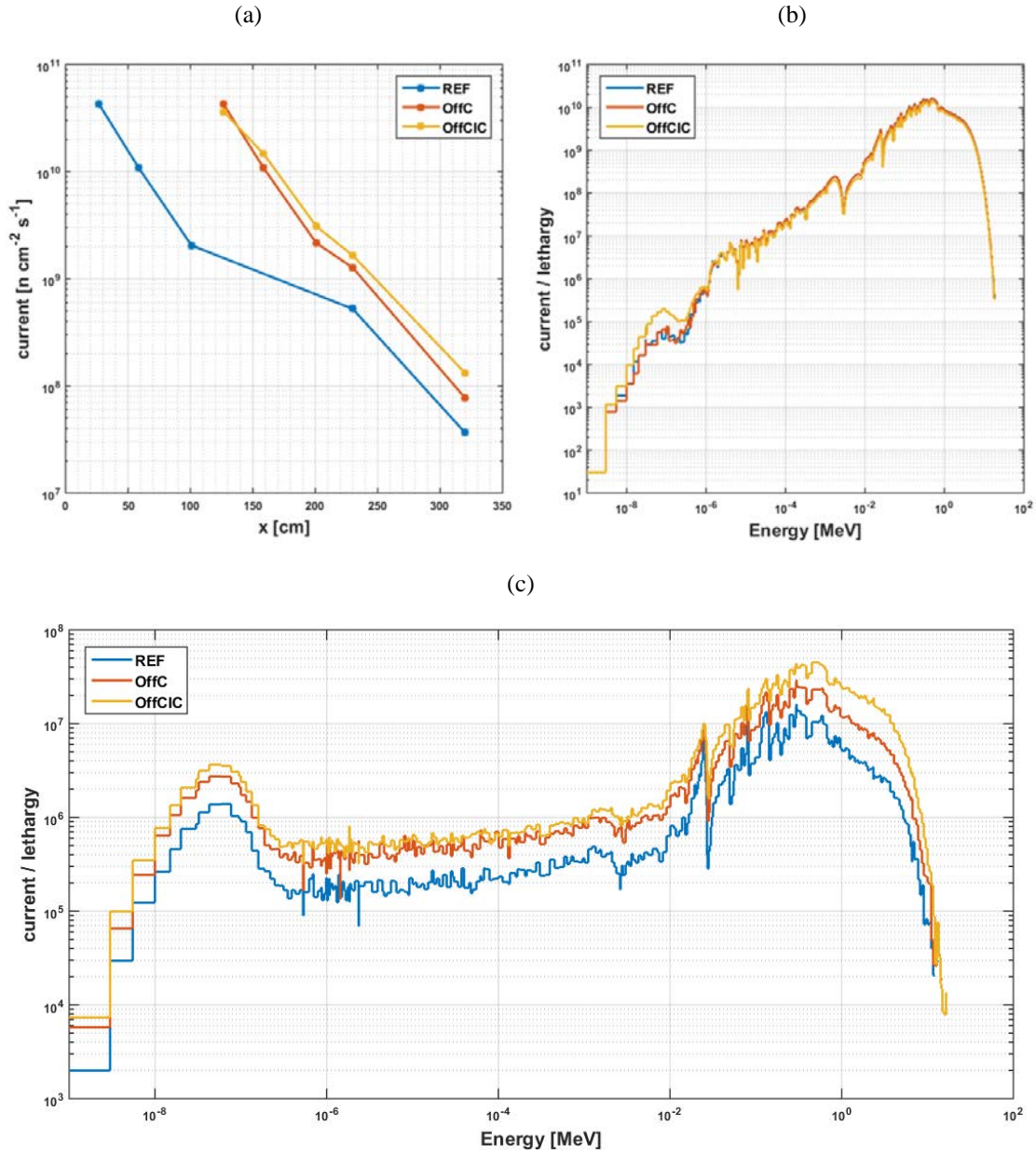


Figure 3.7. (a) Flux traverse in the core at $z=0$ and $y=0$, as a function of the relative x position, (b) neutron current spectrum at the beginning of the channel, and (c) neutron current spectrum at the beam channel exit.

3.3.3 Gamma Spectrum and Intensity Evaluation

As indicated in Chapter II, gamma-rays will inevitably contaminate the neutron beam. If too intense, they may complicate the neutron measurements, possibly limiting the types of neutron spectrometry techniques applicable, unless they are sufficiently attenuated before reaching the detector. On the other hand, measuring the spectrum of the non-attenuated gamma-rays directly emitted from the core could be of interest to nuclear physicists.

It is therefore important to estimate the gamma-ray yield and spectrum along the beam, in the same way as for the neutrons. This was done using the same data and code systems for the MASURCA models described previously.

A comparison of the neutron and gamma intensities is presented in Table 3.4. The fast neutron fraction is defined as the ratio between the intensity of neutrons with energies over 10 keV and the total intensity. The (fast) neutron-to-gamma ratio for the REF, OffC and OffCIC models is found to be in the 4-to-5 range.

Table 3.4. Total neutron and gamma intensity at the end of the channel (at 5 kW).

	Neutron Intensity (n cm ⁻² s ⁻¹)	Fast Neutron Fraction (>10 keV)	Gamma Intensity (γ cm ⁻² s ⁻¹)	n_{fast}/γ
REF	3.65E+07	86%	7.17E+06	4.38
OffC	7.74E+07	85%	1.54E+07	4.27
OffCIC	1.32E+08	89%	2.52E+07	4.66

As Figure 3.7a for neutrons, Figure 3.8a compares the total gamma-ray current intensities as they attenuate along the radial channel. As before, the x coordinate is the absolute position (REF channel starts at $x = 26.5$ cm, OffC and OffCIC at $x = 126.5$ cm). The shortening of the channel length leads to an increase in the total gamma-rays intensity of the same magnitude as for the neutrons.

The gamma spectrum entering the experimental channel is shown in Figure 3.8b. The majority of the gamma rays are in the 100 keV to 10 MeV energy range.

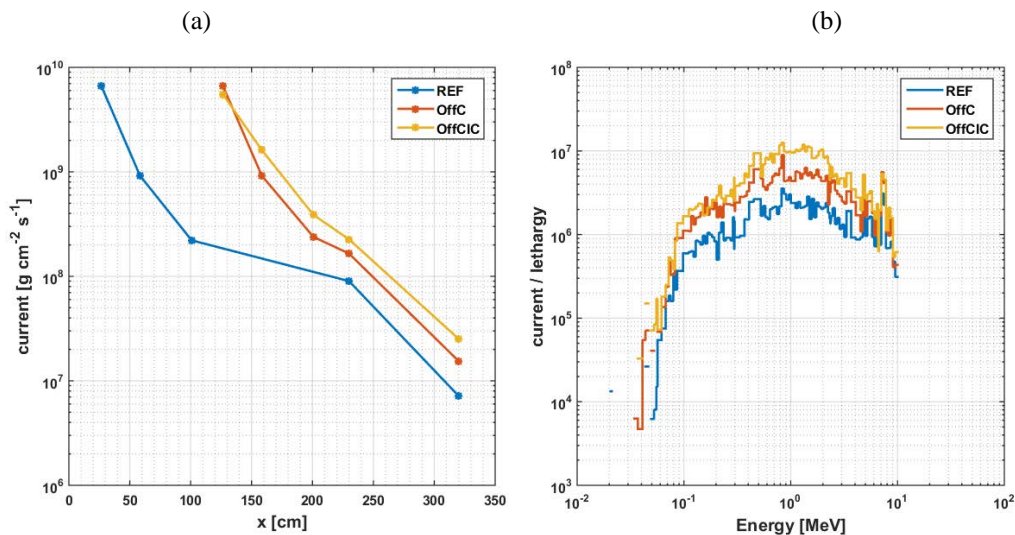


Figure 3.8. (a) Total gamma intensity loss along the radial channel as a function of absolute x position, and (b) gamma current spectrum at the beam channel exit.

3.4 MASURCA Beam Configuration vs Fast Neutron Source Reactors

Even though the above results provide only a preliminary indication of a possible extension of the MASURCA experimental capability, which will require further studies, they allow to compare the characteristics of the extracted beam to those of the fast neutron source reactors described at the beginning of the chapter. Missing data are added in Table 3.5.

Table 3.5. Comparison between MASURCA and other fast neutron research reactors (II).

	MASURCA	YAYOI	TAPIRO	AFSR
Location	France	Japan	Italy	U.S.A.
1st Criticality	1966	1971	1969	1960
Status	Refurbishment	Shut Down	Refurbishment	Shut Down
Fuel	Variable	Enriched U	Enriched U	Enriched U
Blanket	Variable	Depleted U	None	Depleted U
Reflector	Variable	Lead	Copper	None
Cooling	Forced Air	Forced Air	Forced He	Forced Air
Max thermal power	5 kW	2 kW	5 kW	1 kW
Max neutron flux at centre (n cm⁻² s⁻¹)	3.0×10^{11}	8.0×10^{11}	3.0×10^{12}	5.7×10^{11}
Beam size	10.16×10.16 cm ²	Ø 20.0 cm	Ø 5.6 cm	Ø 5.6 cm
Beam intensity (n cm⁻² s⁻¹)	$\sim 1.3 \times 10^8$ (max)	$\sim 10^6$ - 10^7	$\sim 10^8$ - 10^9	1.0×10^7
Type of spectrum (@ channel exit)	Intermediate-to-fast	Intermediate-to-fast	Intermediate-to-fast	Intermediate-to-fast
n_{fast}/γ	4-to-5	-	-	-

The MASURCA beam intensity and the spectrum properties compare favourably with those of the other facilities. A distinctive feature of MASURCA is the capability to change the core and surrounding materials to produce different spectra. These characteristics, together with the possibility of introducing filtering materials in the extraction channel, would make it possible to deliver different “reference” neutron fields for various purposes. Another interesting feature is the adjustable size and shape of the extraction channel, to adapt to the needs.

3.5 Conclusion about MASURCA as a Multipurpose Facility

The possible future use of MASURCA as a multi-purpose time-continuous beam facility has been evaluated by simulating a radial extraction channel, from the core edge to the adjacent (“accelerator”) experimental room, past the biological shield. The performance of this beam has been compared with that of fast neutron source reactors.

The conclusion is that the MASURCA beam configuration would be feasible and would make it possible to deliver continuous neutron beams of up to 10^8 neutrons $\text{cm}^{-2} \text{s}^{-1}$ in the experimental room, with a neutron-to-gamma ratio around 4, and an adjustable neutron spectrum.

From the preceding discussion, and from the knowledge of the studies already performed in YAYOI, AFSR, HARMONIE and TAPIRO, it is possible to conclude that the following applications should be feasible (even if it is in a limited form for some of them) in a MASURCA beam configuration:

- i. Fast neutron transport and propagation into shields;
- ii. Standard (reference) neutron fields for various uses, *i.e.* calibration of advanced neutron detection systems;
- iii. Measurement of decay heat of fast neutron fission products;
- iv. Fast neutron radiography;
- v. Measurements of fast neutron cross sections;
- vi. Studies of irradiation effects and neutron damage on organic materials, semi-conductors and metals, etc. ;
- vii. Neutron transport and shielding code validation;
- viii. Radiological characterization;
- ix. Education and training;

IV. Fast Neutron Spectroscopy

- 4.1 Instrumentation for Fast Research Reactors
 - 4.1.1 Fast Neutrons
 - 4.1.2 Neutron Detectors for Fast Research Reactors
- 4.2 Intermediate-to-Fast Neutron Spectroscopy Techniques
- 4.3 Gas-filled Detectors
 - 4.3.1 Regions of Operation
 - 4.3.2 ³He-filled Gas Detectors
 - 4.3.3 Proton Recoil Proportional Counters
- 4.4 ⁶Li Sandwich Detector
 - 4.4.1 Principle of Operation
 - 4.4.2 Main Features
- 4.5 Proton Recoil Telescopes
 - 4.5.1 Gas Telescopes
 - 4.5.2 Diamond Telescopes
- 4.6 Organic Scintillators
 - 4.6.1 Principle of Operation
 - 4.6.2 Main Features
- 4.7 Comparison and Pre-selection

Introduction

The basics for this work are fast neutron spectroscopy techniques and detection systems. The chapter addresses this topic at an intermediate level, some prior knowledge on radiation interactions with matter being necessary for a full understanding. The main concepts and quantities in radiation measurements are provided in **APPENDIX B**, as a short reminder.

The chapter begins with a brief discussion of the typical instrumentation employed in RRs and continues with the analysis of the desirable characteristics for the spectroscopy system to be implemented in MASURCA. Possible candidates are examined one by one. These are: gas-filled detectors, organic scintillators, solid-state detectors (semiconductors and diamonds) and proton recoil telescopes. In the last section, the pros and cons of every selected detector are compared and a conclusion on how to build a “best” neutron spectrum measurement system by combining different detection techniques is provided.

4.1 Instrumentation for Fast Research Reactors

4.1.1 Fast Neutrons

Typical neutron spectra found in MASURCA and in other fast (sodium-cooled) RR are those obtained by simulation in the previous chapter and are shown, again, in Figure 4.1. From this plot, it is possible to appreciate the great difference in magnitude between slow and fast neutrons.

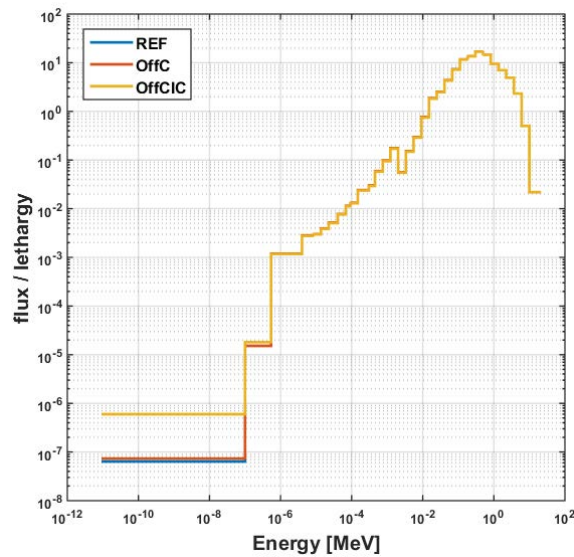


Figure 4.1. MASURCA fast neutron spectra.

Distinguishing low-energy (slow) from intermediate- and fast-energy neutrons is very important, mainly because the properties (cross sections) of materials interacting with neutrons differ significantly at low, intermediate and high incident neutron energies. This well-known fact is important not only for reactor physics, but also for detection purposes.

In this work, the somewhat-arbitrary convention specified in Figure 4.2 is adopted for designating slow, intermediate and fast neutrons.

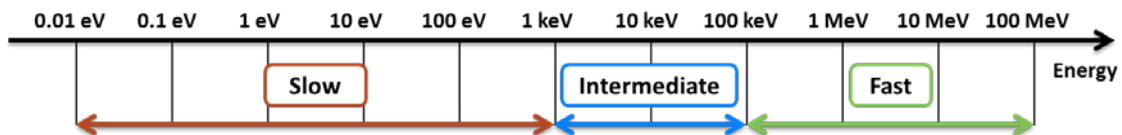


Figure 4.2. Energy convention.

4.1.2 Neutron Detectors for Fast Research Reactors

From the neutronics point of view, classical instrumentation for in-core fast research reactors mainly includes fission chambers and activation detectors [Harrer]. This instrumentation is used for determining the neutron flux and fluence, the neutron spectrum, and the power distribution.

Neutron activation techniques [Beckurts&Wirtz] exploit certain well-known nuclear reactions - such as $(n, 2n)$, *inelastic scattering* and some (n, p) and (n, α) reactions - that occur only when the neutrons have energies above a particular threshold energy. In many cases, these reactions induce activity in the material, which can be measured after the irradiation. An integral (spectrum weighted) measure of the neutron fluence can thus be inferred from the neutron induced activity and decay scheme (detection of γ -rays from decay). The material selection criteria are defined according to the needs.

Fission chambers (Figure 4.3), thanks to fission cross sections that have a marked step structure with thresholds in the early low MeV energy region, can also be used as (threshold) detectors for fast neutrons. They are characterized by a fissile deposit coating the interior of a cylindrical ionization chamber (see 4.3) and the ionization of the gas is induced by the fission products (FP).

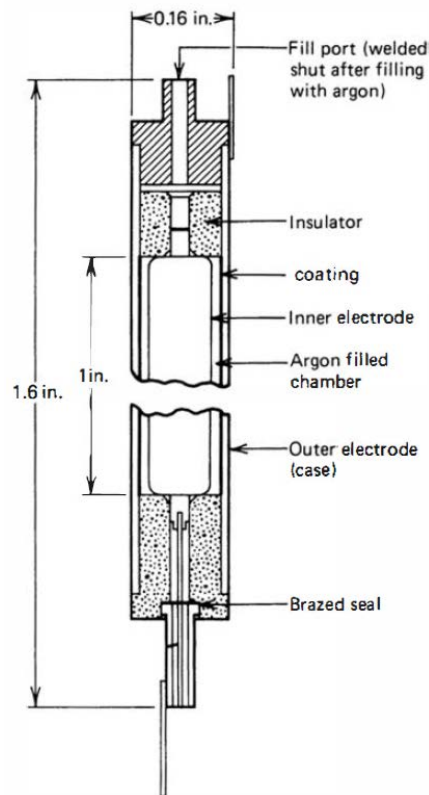


Figure 4.3. Fission Chamber [Knoll].

Fission chambers provide satisfactory operation in all three basic modes (**APPENDIX B**): pulse, current and Campbelling modes. They are thus suitable for source-range channel use, where pulse counting is required on account of low values of the neutron flux; in the intermediate range channels, where the Campbelling mode extends the operating range; and in the power range channels, where the current mode provides the appropriate operation for managing the high counting rate. For each of these modes, the optimum design is different with respect to size, materials, fill gas pressure, neutron sensitivity, etc.

Some examples of threshold reactions are shown below (Table 4.1).

Table 4.1. Some threshold reactions of interest for fast neutron detection.

Reaction	Threshold [MeV]	T_{1/2} daughter product
$^{58}\text{Ni}(n,p)^{58}\text{Co}$	2.6	71 days
$^{54}\text{Fe}(n,p)^{54}\text{Mn}$	2.8	312 days
$^{63}\text{Cu}(n,\alpha)^{60}\text{Co}$	6.2	5.27 years
$^{238}\text{U}(n,f)^{137}\text{Cs}$	1.8	30 years
$^{237}\text{Np}(n,f)^{137}\text{Cs}$	0.6	30 years

As stated in Chapter II (2.3.2), the purpose of this work is to investigate another category of detection systems, to complete the set of experimental data attainable with such detection techniques. The focus is on instrumentation which rely less on calculated quantities (as well as on the related errors and uncertainties), and on the prior knowledge of neutron cross sections for inferring the neutron spectrum. The detection system of interest should thus be capable of measuring the neutron energy in the intermediate-to-fast range, with a reasonably good resolution, for different types of measurements (flexible): in-core, near-core, and out-of-core. It should also be robust, operable on-line, easy-to-handle and easy to set up in MASURCA ZPR-type experimental configurations.

4.2 Intermediate-to-Fast Neutron Spectroscopy Techniques

Radiation spectroscopy is referred to as the measurement of the intensity of a radiation field with respect to its properties; *e.g.* its energy, momentum, angle of incidence and other related quantities. Of particular interest for different applications is the characterization of the energy distribution of these radiation fields, commonly denoted as the energy spectrum. The proper description of this quantity is essential in neutron beam applications, for guaranteeing the delivery of reference neutron fields; or in reactor physics measurements, where the spectral characterization of the

neutron flux in different positions inside and near the core is used - for example - for validating neutron transport codes. Other applications of interest include different nuclear physics measurements for nuclear data purposes, such as neutron shielding and transmission experiments or prompt and delayed neutrons measurements.

Different types of fast neutron spectroscopy techniques exist and almost all of them are based on the so-called “*method of the associated charged particle*”, in which neutrons have to first pass through an ‘intermediate’ interaction for producing or causing the motion of a secondary charged particle that can be detected. The reactions of interest are summarized in Figure 4.4a. In general, fast neutron spectroscopy techniques can be divided in several groups [Brooks & Klein 2002]:

1. Techniques in which the neutron is scattered and the energy of a recoiling nucleus is measured;
2. Techniques based on the measurement of the energy of a charged particle released in a neutron-induced nuclear reaction;
3. Techniques in which the neutron velocity is measured;
4. Threshold techniques;
5. Techniques in which the neutron energy distribution is determined by unfolding a set of readings of detectors (or detector geometries);
6. Techniques in which the time-distribution of the slowing down of a short burst of neutrons in a suitable media is measured.

Comprehensive reviews and surveys on fast neutron spectroscopy methods can be found elsewhere [Knoll, Beckurts&Wirtz, Marion&Fowler, Allen, Lyoussi], here only a subset of them is considered. The focus is on spectrometers with the following - desired - properties [Thomas & Klein 2003]:

- a. The spectrometer should ideally operate over a wide range of environmental conditions (in-core, near-core, out-of-core, beam-type applications, physics measurements);
- b. The spectrometer should ideally operate over a wide energy range, intermediate-to-fast neutron energy domain (10 keV - 10 MeV);
- c. Since it will work in mixed radiation field conditions (neutrons and gamma-rays), the spectrometer should be insensitive to the gamma component of the field, or should be capable of discriminating between the two types of radiations;
- d. An energy resolution of about 10% or better;
- e. Since it will often be employed in restricted areas, due to safety or radiation protection regulations, the spectrometer should be portable, robust and easy to set up and use;
- f. Because access time and spatial limitations at the measurement sites will be limited, the spectrometer should represent a good compromise between detection efficiency and size;
- g. An additional desirable property is the capability to operate on-line, so that a preliminary analysis of the spectrum can be done during the experiment, to identify any measurement problems and take rapid corrective action.

Techniques 4) and 5) consist of multiple measurements with the use of different detectors (for instance, different types of material for activation foils and geometries for Bonner spheres), they are robust and easy to set up, but they usually do not provide an on-line evaluation of the neutron spectrum. In addition, unfolding the neutron spectrum is not a straightforward operation.

Methods 3) and 6) are proper for measuring pulsed neutron sources, but do not fit well with direct measurement of continuous radiation fields.

For on-line measurements of (time-) continuous mixed radiation fields, the most suitable methods are 1) and 2), mainly based on one of the following reactions (Figure 4.4b and c): *elastic scattering* (usually with protons), ${}^3\text{He}(n,p)$ and ${}^6\text{Li}(n,\alpha)$.

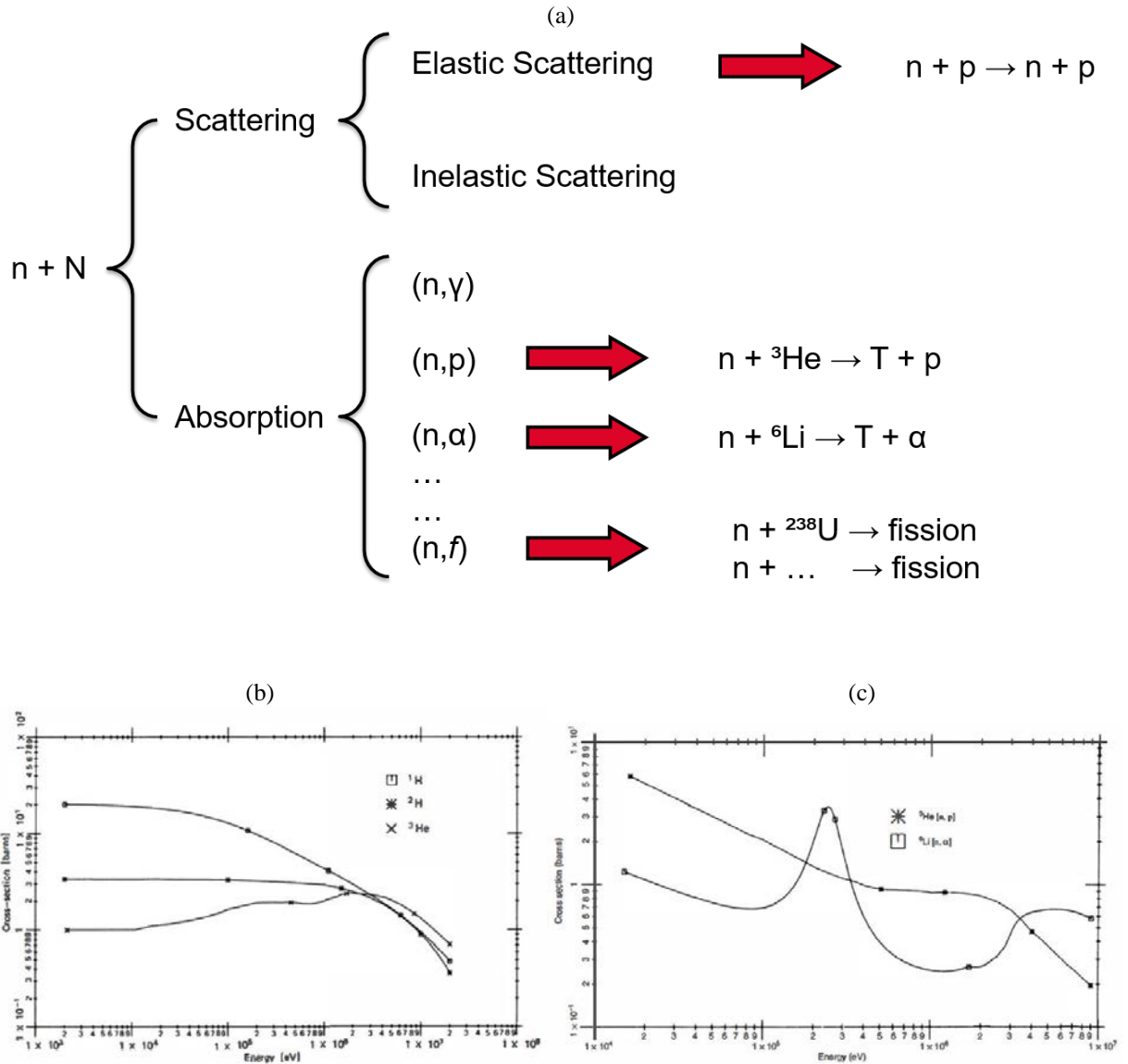


Figure 4.4. (a) Reactions of interest for neutron spectroscopy. (b) Elastic cross sections of ${}^1\text{H}$, ${}^2\text{H}$ and ${}^3\text{He}$; (c) ${}^3\text{He}(n,p)$ and ${}^6\text{Li}(n,\alpha)$ cross sections.

From these techniques, four types of detectors have been found suitable for the purposes of this work:

- Ionization chambers and proportional counters (gas-filled detectors);
- Organic scintillators;
- Solid-state detectors (such as sandwich detectors);
- Proton recoil telescopes.

In the following, a description of the listed detectors is provided.

4.3 Gas-filled Detectors

Gas-filled detectors consist of a volume of gas between two electrodes, with an electrical potential difference applied between the electrodes (Figure 4.5). The ionizing radiation, passing through the gas, excites and ionizes molecules along its path. The ionization of a neutral molecule results in a positive ion, attracted to the negative electrode (cathode) and a free electron, attracted to the positive electrode (anode). The produced ion and free electron are called an *ion pair*. The energy deposited by a particle in the volume, assuming that it is fully stopped in the gas, is proportional to the number of ion pairs formed.

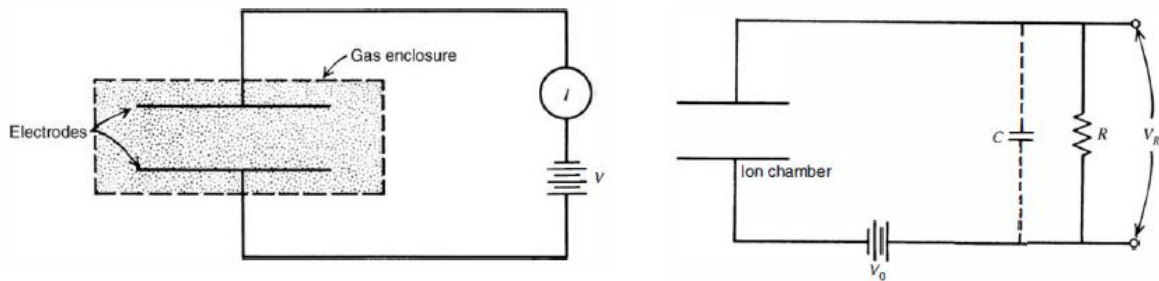


Figure 4.5. Typical gas-filled detector.

Neutrons need to first interact with a ‘converter’ for producing or putting in motion an associated charged particle, which will start the gas ionization process. For gas-filled detectors there are numerous solutions. As we said at the beginning of the chapter for fission chambers, it is possible to create a coating around the gas volume made of fissile materials and use the FPs for ionizing the gas. Other types of coating can be used, such as Boron or Lithium, which are useful for thermal neutron detection. For fast neutron spectroscopy, good candidates are the ^3He -filled detectors, based on the $^3\text{He}(n,p)$ reaction, and the recoil counters, filled with a low-Z gas (like H or methane) and based on elastic scattering.

In the following, only gas-filled detectors operating in the pulse mode are considered, since they are the best suited to neutron spectroscopy. Drifting charges, created in the passage of an ionizing

radiation, give rise to induced charges on the electrodes of the ion chamber that reduce the ion chamber voltage from its equilibrium value. The signal produced is thus a difference in the potential whose amplitude indicates the magnitude of the original charge generated within the ion chamber. This is generally true if the time constant of the external circuit is long compared with the time required to collect the charges within the chamber.

Gas-filled detectors exist in different geometries: parallel plates, cylindrical, spherical, etc. (Figure 4.6).

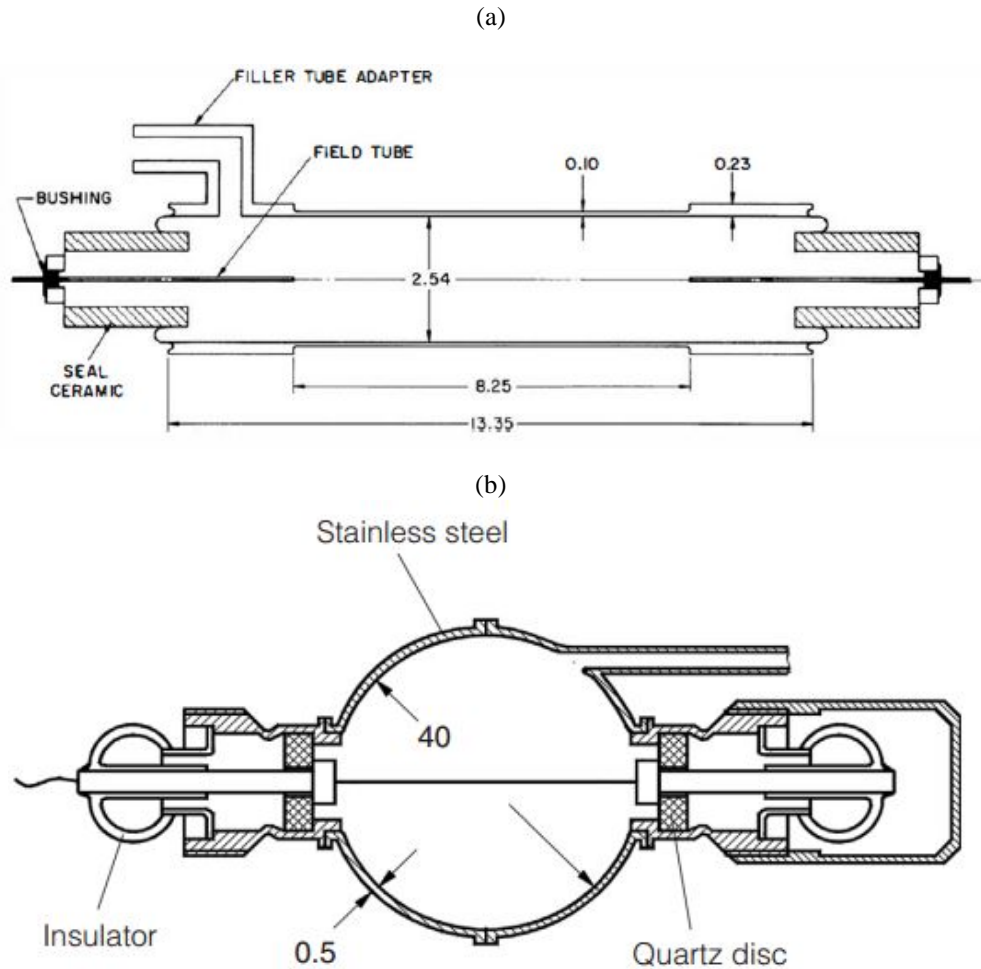


Figure 4.6. (a) Cylindrical and (b) spherical gas-filled detector.

4.3.1 Regions of Operation

There are three types of gas-filled detectors in common use: ionization chambers, proportional counters and Geiger-Mueller counters. The type is primarily determined by the voltage applied between the cathode and the anode.

It is possible to distinguish six regions of operation (Figure 4.7):

- I. Recombination region;
- II. Ion saturation region (ionization chambers);
- III. Proportional region (proportional counters);
- IV. Region of limited proportionality;
- V. Geiger-Mueller region (Geiger-Mueller counters);
- VI. Continuous discharge region.

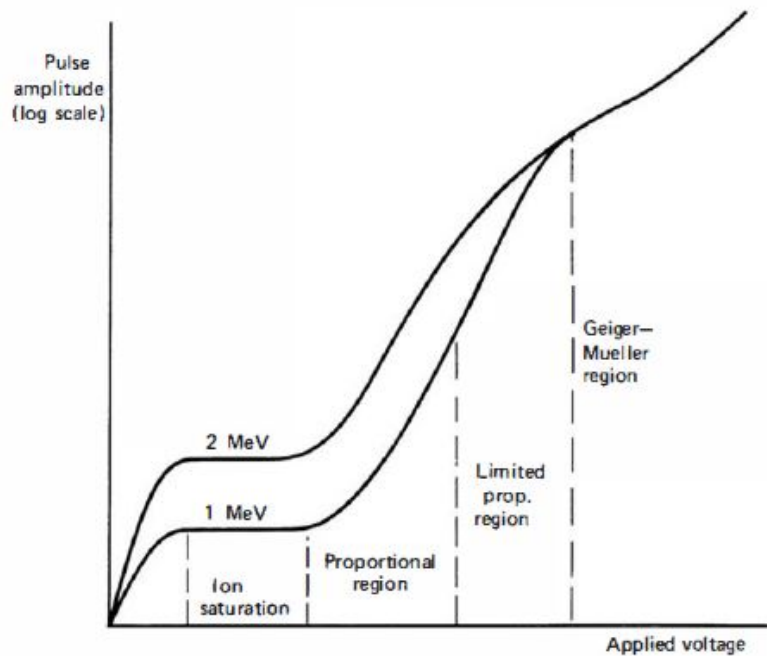


Figure 4.7. Regions of operations of gas-filled detectors.

The applied voltage influences the gas ionization process and, as a consequence, the amplitude of the observed pulse (ordinate, Figure 4.7).

In the recombination region, at very low voltage values, the charges produced quickly recombine to re-form neutral molecules. Operating a detector in this region would be useless.

As the voltage is raised, the region of ion saturation is achieved. This is the region of ionization chambers and all the produced charges are collected.

As the voltage is further increased, the threshold at which gas multiplication begins is reached. At this point, free electrons produced by ionization are sufficiently accelerated by the applied field (have sufficiently kinetic energy) to create additional ion pairs in the collisions with neutral gas molecules during the migration towards the anode. The electrons liberated by the secondary ionization process will also be accelerated by the electric field and can thus create additional ionization. As this process continues, it takes the form of a cascade (Townsend avalanche) in which each free electron created in a collision can potentially create more free electrons. The process is known as gas multiplication process and, under proper conditions, the number of secondary

ionization events can be kept proportional to the number of primary ion pairs formed. Detectors operating in this region are called proportional counters and the charge amplification within the detector itself can result in significantly improved signal-to-noise characteristics compared with pulse-type ionization chambers.

In the region of limited proportionality, the proportionality between the initial charges produced and the total charges collected is no more guaranteed. Detectors do not operate in this region.

The fifth region is characterized by the fact that each particle interacting with the gas causes a breakdown. Each output pulse from the detector is of the same amplitude and no longer reflects any properties of the incident radiation. This is the Geiger-Mueller region of operation and is not intended for spectroscopy.

In the last region, continuous discharges are produced and cannot be controlled unless the voltage is lowered. Electric arcs can appear between the electrodes, damaging the detector.

4.3.2 ^3He -filled Gas Detectors

Detectors based on ^3He are sensitive to several competing reactions. When the total energy of the reaction products is entirely absorbed within the gas volume, it is possible to clearly distinguish three separate features in the Pulse Height Spectrum (Figure 4.8), PHS. At least, that is the case if wall effects are not taken into account.

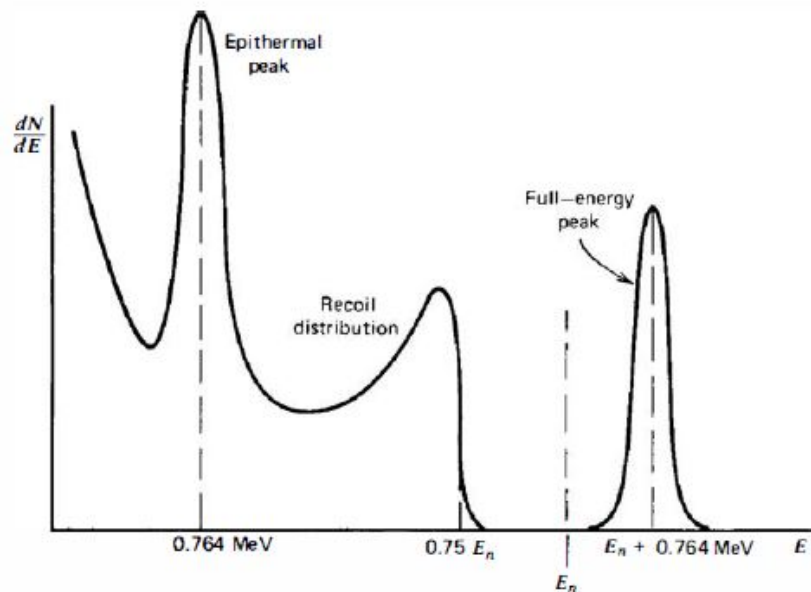


Figure 4.8. Typical pulse height spectrum of a ^3He gas detector.

The ${}^3\text{He}$ (n,p) T reaction provoked by a fast neutron is represented by a full-energy peak at an energy equal to the neutron energy plus the Q-value of the reaction (0.764 MeV).

Elastic scattering of neutrons and partial energy transfer to recoiling helium nuclei creates a continuum in the pulse height spectrum with a maximum energy equal to 75% of the incoming neutron energy.

Thermal neutrons, present in the starting field or moderated by external material, give rise to an epithermal peak at an energy equal to the Q-value.

Wall effects arise whenever the dimensions of the detector are not large enough compared to the range of the secondary particles produced. The effect on the pulse height spectrum is to fill the region between the end of the continuum and the full-energy peak.

${}^3\text{He}$ -filled gas detectors are constructed as proportional counters or as ionization (gridded [Knoll]) chambers. In fast neutron spectroscopy, there are several advantages in using ionization chambers, mainly because they have a superior energy resolution (about 2% at 1 MeV). The better energy resolution is achieved by avoiding the added fluctuations introduced by avalanche formation. The problem of this kind of detector is the slow charge collection time and small pulse amplitude (compared to the corresponding proportional counter).

For both types of detectors, the high sensitivity to thermal neutrons and the current shortage of ${}^3\text{He}$ supply sources are expected to pose practical problems. In order to attenuate the thermal neutron sensitivity, materials - such as cadmium - can be utilized around the detector for lowering the fraction of slow neutrons interacting with the gas volume.

4.3.3 Proton Recoil Proportional Counters

Proton recoil proportional counters are usually filled with hydrogen or a hydrogen-containing gas such as methane. In recoil detectors, protons are usually preferred as recoil particle because the total incoming neutron energy can be transferred to them. From kinetics, it is well known that the maximum possible recoil energy E_r is:

$$E_r^{max} = \frac{4A}{(1+A)^2} E_n \quad . \quad (4.1)$$

E_n being the energy of the incident neutron and A the mass number. For hydrogen, $A = 1$ and the maximum transferable energy is equal to the hitting neutron energy.

The expected PHS should be a simple rectangular distribution extending from zero to the full incident neutron energy (Figure 4.9a) and the response function of the detector should therefore have a correspondingly rectangular shape. In reality, different effects distort the simple rectangular shape. These are mainly due to: (i) edge effects, as protons do not lose all their energy in the gas

volume; (ii) field effects, as gas multiplication is less important at the ends of the (wire) anode; (iii) influence of photons; (iv) scattering by carbon nuclei ; (v) multiple scattering by hydrogen (low for proton recoil gas detector); and (vi) detector resolution. The combination of these effects is results in a PHS of the type presented in Figure 4.9b.

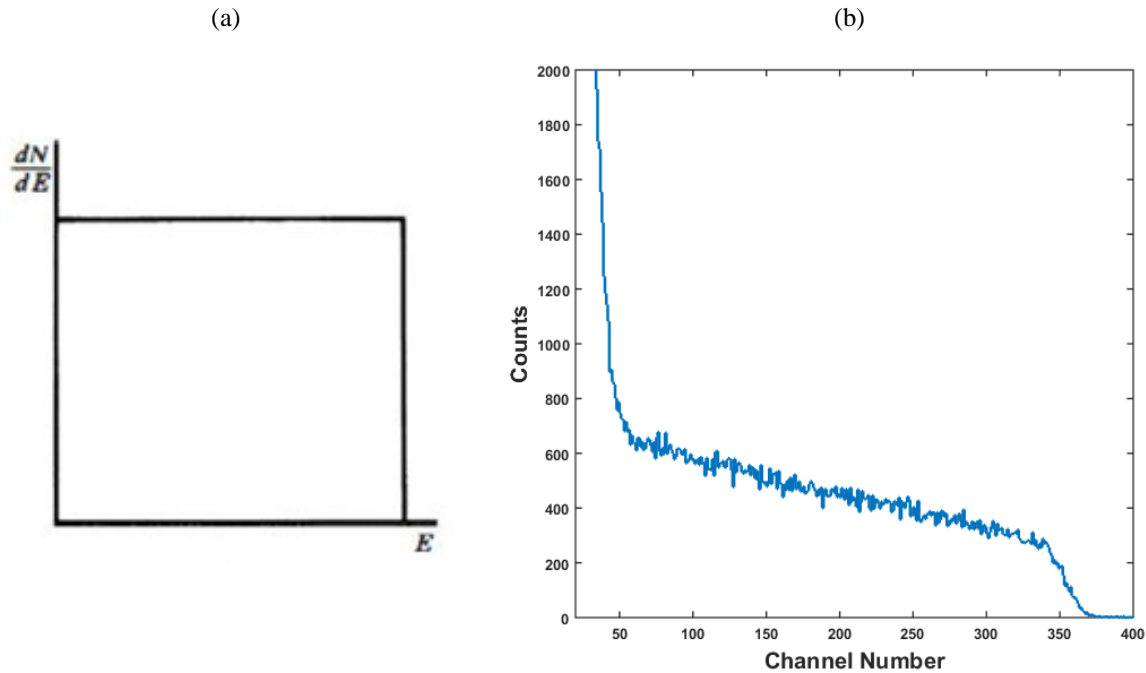


Figure 4.9. (a) Theoretical and (b) actual PHS of a typical proton recoil detector [Dioni 2017 (2)].

The more complicated a response function is, the more complicated the unfolding procedure is.

Spherical counters (Figure 4.6b) have isotropic properties, the detector response is nearly independent of the direction of the incident neutron. Cylindrical (Figure 4.6a), on the other hand, have an anisotropic response, which could cause problems in multidirectional neutron fields. In general, recoil proportional counters are more sensitive to practical problems than other spectrometers, such as organic scintillators. Purity of the fill gas, constancy of the electric field over the wire anode, microscopic air leaks are some of the issues to be faced with such detectors.

The energy range of application is usually extended by simply using a series of proportional counters with different gas pressure and different types of gasses. Reported successful applications use a set of three proportional counters for covering the energy domain between few keV up to 1.5 MeV [Tagziria 2003, Jansky 2014]:

- 1) 100 kPa H₂: few (~ 10 keV) - 250 keV;
- 2) 300-400 kPa H₂: 200 - 650 keV;
- 3) 1000 kPa H₂ or 400 kPa CH₄: 500 - 1500 keV.

For simple hydrogen-filled counters, typical values of detection efficiency and energy resolution are around 1 % and between 2 and 6 %, respectively.

4.4 ${}^6\text{Li}$ Sandwich Detector

The ${}^6\text{Li}(n,\alpha)\text{T}$ reaction can be used for fast neutron applications by depositing a thin layer of lithium fluoride (${}^6\text{LiF}$) between two solid-state detectors (Figure 4.10a), such as semiconductors [Love & Murray 1961] or CVD diamonds [Osipenko 2015 (1), Osipenko 2015 (2), Osipenko 2016]. Each detector has its own pair of electrodes and produces its own output signal. The use of the sandwich set-up is particularly convenient because it allows to suppress noise and competing reactions when the two work in coincidence.

4.4.1 Principle of Operation

Solid-state detectors are somewhat analogous to gas-filled detectors, in the sense that fundamental information carriers are pairs created in the ionization and excitation process. In this case, charged particles (primary or secondary) travelling in the active volume create *electron-hole pairs*. For diamonds, electrons and holes are able to move within the diamond lattice and their motion in an applied electric field generates the basic electrical signal for the detector (Figure 4.10b).

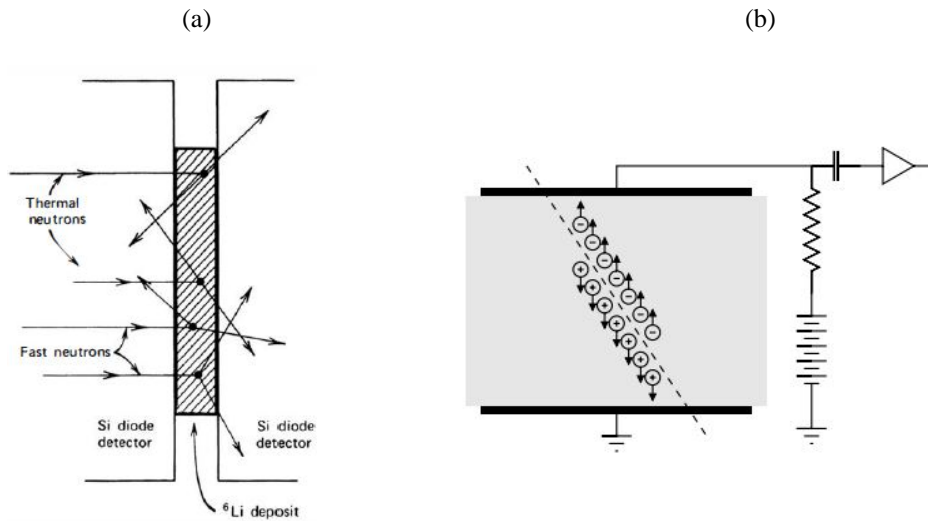


Figure 4.10. (a) Sandwich detector. (b) Principle of operation of a solid-state detector.

In the sandwich configuration, neutron energy is derived from α and T particles, whose total energy comprehend the energy of the incident neutron plus the Q-value of the reaction (4.78 MeV).

Resulting pulse height spectra for Li-based detector are similar to those seen for detectors using the ${}^3\text{He}(n,p)$ reaction, with a peak at the impinging (fast) neutron energy plus Q-value, another peak at the Q-value and a continuum due to recoil particle background (Figure 4.11 [Love & Murray 1961]).

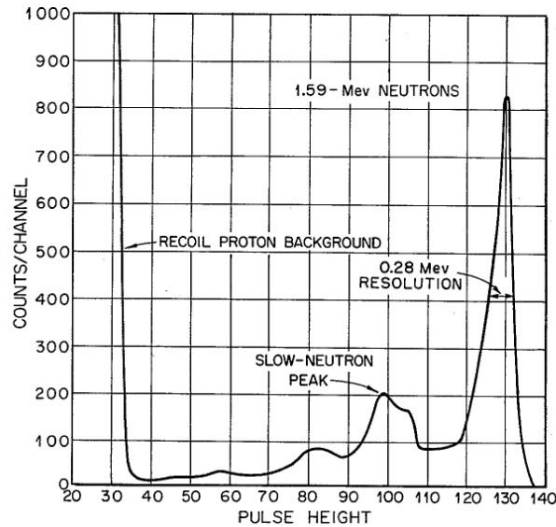


Figure 4.11. Typical pulse height spectrum of a ${}^6\text{Li}$ detector [Love & Murray 1961].

In the case of fast neutrons, apart from the alpha and tritium coming from the lithium, other reactions come into play. The fast neutron field interacts also with the diamond, and other structures can be seen in the output spectrum. The main nuclear reactions on ${}^{12}\text{C}$ and ${}^{13}\text{C}$ (neutron energies below 20 MeV) are: elastic scattering on ${}^{12}\text{C}$, ${}^{13}\text{C}(n,\alpha){}^{10}\text{Be}$, ${}^{12}\text{C}(n,\alpha){}^9\text{B}$. These reactions are shown in Figure 4.12 for a diamond detector and mono-energetic neutrons of 14.3 MeV [Weiss 2016]. Generally, the preferred use of this kind of detector is for neutron energies lower than 6 MeV [Osipenko 2015 (1)]. In fact, in this energy range, the most probable reaction in the diamond is neutron elastic scattering of carbon nuclei, which deposits about 25% of its energy in the detector. Thanks to the highly exothermic reactions on ${}^6\text{Li}$, this carbon scattering background can be removed by a high energy threshold with minimal efficiency loss.

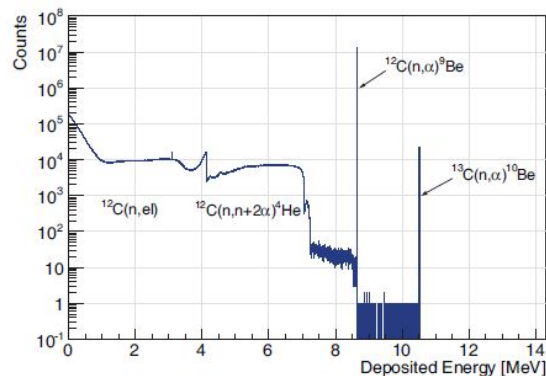


Figure 4.12. Response of a diamond detector to 14.3 MeV mono-energetic neutrons [Weiss 2016].

4.4.2 Main Features

Solid-state detectors achieve the best energy resolution achievable for a radiation spectrometer. This is due to the large number of information carriers (electron-ion pairs, electron-hole pairs, photoelectrons, ...) produced per pulse recorded. Thanks to higher densities (about 1000 times greater), the number of pairs created is larger than the one produced - for example - in a gas detector. Compared to scintillation materials, they are still better, since the production of information carriers in scintillators - photoelectrons - goes through many, less efficient, steps (see next paragraph). With diamond ^6Li sandwich detectors, energy resolutions on the order of 2% (at 3 MeV) [Osipenko 2015 (1)] are achievable.

The compact size of solid-state detectors is a big advantage; they can be positioned in tight places with small perturbations to the environment, while having a good energy resolution. However, this can lead to detectors with low efficiencies. This is the case of ^6Li sandwich detectors, which additionally suffer from the $^6\text{Li}(n,\alpha)$ cross section value for fast neutrons. Typical efficiencies are on the order of 10^{-8} for fast neutrons (3 MeV), versus 10^{-4} for thermal neutrons (25 meV) [Osipenko 2015 (1)].

Because of this low efficiency at high energies, ^6Li -based fast spectroscopy is applicable only when the (fast) neutron fluxes are larger than 10^7 neutrons $\text{cm}^{-2} \text{s}^{-1}$, that is, for measuring neutron spectra inside or near the core of fast research reactors, assuming that any contributions from low-energy neutrons are low enough or can be properly removed.

Other noticeable features are the relatively fast timing characteristics and an effective thickness that can be varied to match the requirements of the application. Possible drawbacks include the limitation to small sizes and the relatively high susceptibility of these devices to performance degradation from radiation-induced damage. Radiation hardness of diamond and silicon sensor is discussed in [De Boer 2007].

4.5 Proton Recoil Telescopes

Different types of proton recoil telescopes exist. In general, they are composed of a thin foil of hydrogenous material (called “radiator”) for n-p conversion and, at a selected angle, a charged particle detector (Figure 4.13). This one can be a solid-state spectrometer, such as a semiconductor [Cambiaghi 1970], a diamond [Caiffi 2015], or a proportional counter filled with a non-hydrogenous gas [Marini 2016, Maire 2013], for example CF_4 .

The great advantage of recoil telescopes is that, for mono-energetic neutrons, they perform a “direct measurement” of the energy, in the sense that it is not necessary to predetermine a response function to infer the neutron energy. By selecting an angle θ with respect to the incoming neutron direction, the recoil proton energy is fixed and the response function to mono-energetic neutrons approaches an ideal narrow peak. The energy of recoil protons observed is given by:

$$E_p = E_n \cos^2 \theta \quad . \quad (4.2)$$

E_n is the energy of the incoming neutrons. θ can also be equal to 0, in that case, all the energy of the impinging neutron is transferred to the recoil proton.

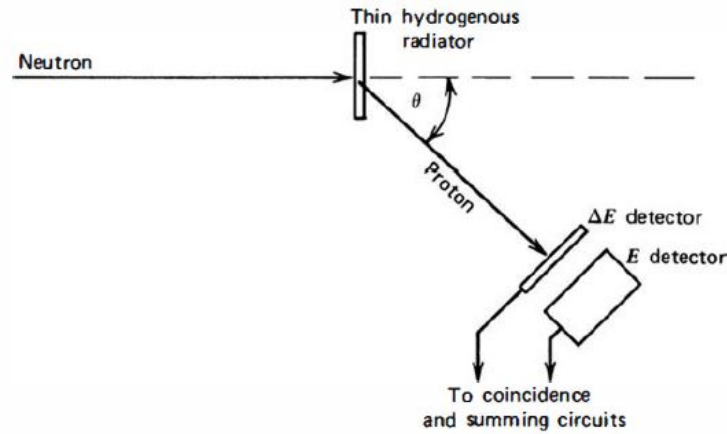


Figure 4.13. Typical proton-recoil telescope [Knoll].

For telescopes, it is necessary that the incoming neutron direction be well defined in order to establish a proper value of θ . This can be done by a collimator or by other means. In several systems, a collimator is also added after the radiator, for selecting a smaller solid angle of the recoil particles. Multiple detectors can be used in coincidence to reduce the background from competing reactions and other unwanted events.

The big drawback of telescopes is their low efficiency, usually on the order of 10^{-5} - 10^{-6} . This is due the fact that the n-p converter is kept very thin for avoiding proton energy loss in the material.

Typical energy resolutions are between 3% and 10%. The accessible energy domain is limited in the lower part of the neutron energy spectrum (keV region) due to gamma-ray background. Reported values are between 8 keV [Maire 2013] up to 200 keV (more typical).

4.5.1 Gas Telescopes

An interesting configuration for measuring fast neutrons is the one proposed by [Marini 2016]. Protons are generated in the converter and detected at $\theta = 0$ in a two-stage parallel plate proportional counter. The operating principle is shown in the Figure 4.14. Ion-electron pairs are mainly created in the ionization region. Electrons drift toward the micromesh by the application of a low electric field that is set below the threshold of gas multiplication. Then, most of the

electrons pass through the mesh in the proportional region (micromegas [Giomataris 1996]), where the a Townsend avalanche occurs thanks to a strong electric field. Typical gains are between 10^3 and 10^4 .

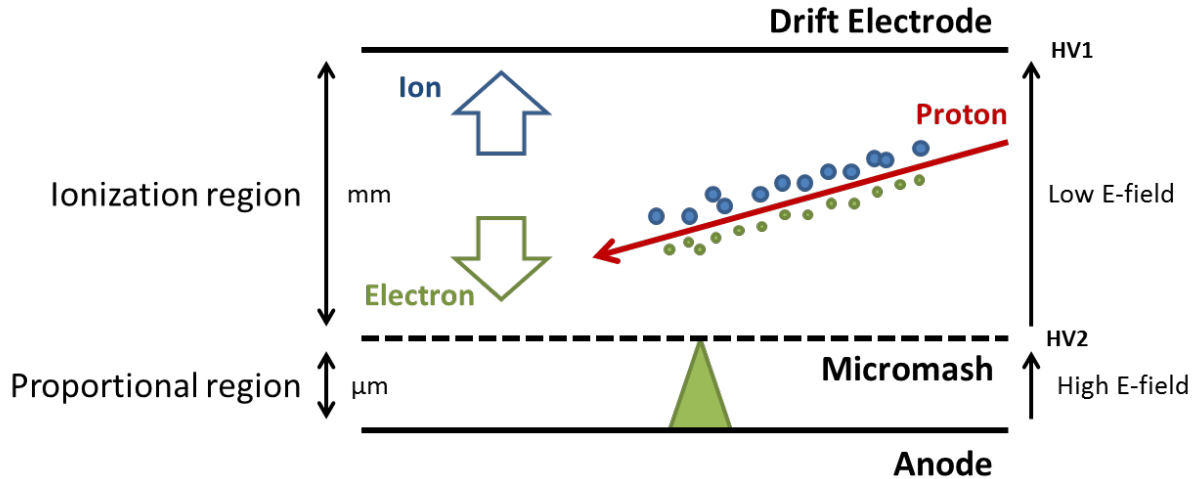


Figure 4.14. Example of gas telescope based on micromegas (proportional region).

The anode of the spectrometer actually consists of a series of smaller independent anodes (pixel configuration), able to spatially record the centroid of the avalanche and reconstruct the particle trajectory. The gas pressure is adjusted to the proton energy range. This kind of configuration is used for performing *Bragg Spectroscopy*. The Bragg's curves represent the energy loss of a particle (protons, alpha, ... with a given energy) in a material as a function of its penetration. The curves are characterized by a peak that corresponds to the point where the particle loses the major part of its energy. Thanks to the reconstruction of the trajectory and the height of the signal recorded, is possible to know where the particle has lost the biggest fraction of its energy (in which pixel). Then, by comparison with the Bragg's curves, it is possible to deduce the energy of the incident particle.

A collimator is used after the radiator for a correct analysis of the proton range and the associated Bragg curve, since it is important to keep only the protons with a straight trajectory.

Another interesting configuration, based on a similar principle, is the one proposed in [Maire 2013], where the energy detection lower limit is 8 keV. The detector, due to its relative bulky dimensions, shows interesting features only for beam-type and out-of-core applications.

4.5.2 Diamond Telescopes

Another possibility is to use diamonds (or SiC) as proton detectors. The scheme of the telescope proposed by [Caiffi 2015] is shown in the Figure 4.15. This telescope is meant for neutrons with energies higher than 1 MeV. This double-diamond configuration has been chosen for removing the background due to elastic scattering of the neutrons on the carbon nuclei (by using fast

coincidence measurements), which would otherwise compromise the measurements of lower energy neutrons. In practice, the lower energy limit is imposed by the thickness of the first diamond. With commercially available diamonds, it is possible to reconstruct neutron spectra down to 4 MeV. The efficiency of this kind of detector is on the order of 10^{-6} .

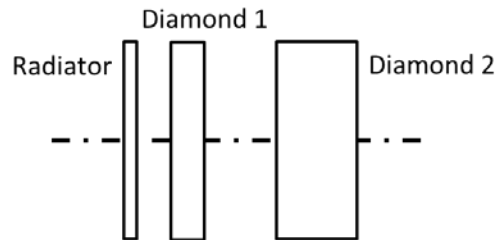


Figure 4.15. Example of diamond (or semiconductor) telescope.

4.6 Organic Scintillators

Organic scintillators are organic materials that exhibit the property of scintillation, which is referred to as the capability of producing optical photons when excited by ionizing radiation.

Organic scintillator spectrometers (Figure 4.16a) are usually composed of a scintillator cell, encapsulated in an aluminum canister with an optical window, coupled with a photomultiplier (PMT) through a partially coated glass or Plexiglas light guide. Typically, the PMT is surrounded by a solid mu-metal (nickel-iron alloy) shield against magnetic fields.

4.6.1 Principle of Operation

In scintillation counting [Birks], an incident ionizing particle of energy E interacts with the scintillation volume where it dissipates its energy in the ionization and excitation of the molecules. A fraction of this energy is converted into N photons, which are radiated in all directions. A part of these photons (N') passes through the optical window and hits the photocathode in the PMT, causing the emission of T photoelectrons. Electrons are then accelerated by the potential applied between the cathode and the first electrode (dynode). PMT are constructed with several stages (dynodes) and at every stage, further electrons are created by secondary emission, generating an electron multiplication process (Figure 4.16b). Typical gains are from 10^5 to 10^9 . This electron avalanche produces a voltage pulse in the output capacitor, which is applied to an external pulse-recording circuit, usually through a linear pulse amplifier. Under normal operating conditions, the PMT has a linear characteristic, *i.e.* the detector response is proportional to N' and the instrument can be used as a spectrometer.

Neutrons and gamma-rays, being uncharged radiations, have to first pass (all or part of) their energy to an associated charged particle for the ionization and excitation of molecules in the

scintillator. For neutrons, this process is the elastic scattering with protons, while for gamma-rays, it is mainly Compton scattering with electrons.

The pulse height spectrum of organic scintillators is similar to the PHS of proton recoil proportional counters, since both detectors are based on the elastic scattering of neutrons with protons. The main differences are the non-linearity of the scintillator response (see 5.2.2) and the magnitude of the multiple scattering on hydrogen effect, which has a bigger impact in the denser (solid or liquid) organic volume. Organic scintillators will be described and discussed in detail in the next chapter (V); in the section below, only general considerations are made, for comparison with the other detectors.

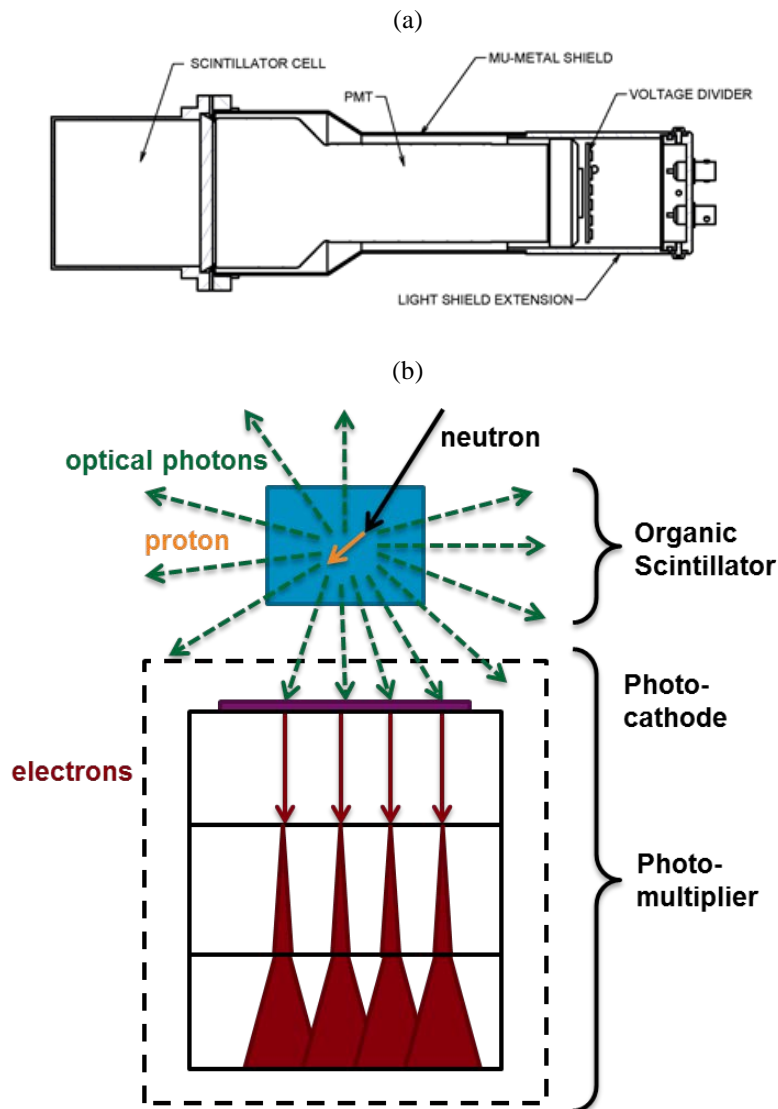


Figure 4.16. (a) Typical organic scintillator detector and (b) principle of operation of an organic scintillator.

4.6.2 Main Features

The main characteristics of organic scintillators (liquid, plastic and crystal) in terms of energy domain of application, radiation discrimination capability between different types of radiations, efficiency and energy resolution are discussed in the following.

Organic scintillators are a suitable choice for neutron energies above about 1 MeV [Klein 2003] and have the great advantage of being relatively cheap and adaptable in size and shapes. Exceptions are large crystal scintillators, which are more expensive because of the difficulty of growing large-size single crystals, although new growing techniques are becoming available to overcome this limitation [Van Loef 2011, Carman 2013, Zaitseva 2015].

As organic scintillators are based on recoil methods (elastic scattering of neutrons by protons), they are insensitive to thermal neutrons. Therefore, they are well suited for fast neutron spectrum measurements in a mixed fast and thermal field, although low-energy neutrons can create background gamma-rays by capture interactions with the surrounding materials, which will lower the neutron-to-gamma ratio.

Liquid and crystal scintillators exhibit good n - γ discrimination properties in the (neutron) energy range of application. Crystals, such as stilbene, exhibit even better discrimination capability than liquids ones [Bourne 2016; Chernov 2002]. Plastic scintillators with n - γ discrimination capability are still in an R&D phase, but they show promising capabilities for the future [Bertrand 2015].

In general spectroscopy applications, liquid scintillators are usually preferred because they combine the qualities of plastic (cheap also for large volumes) and crystal (good n - γ discrimination capability) scintillators. Moreover, they are well known and well characterized, after more than 40 years of experience with them worldwide. Possible drawbacks are (i) the inflammability of the liquid, the container must be carefully prepared; and (ii) the ambient temperature sensitivity, the temperature conditions of the measurement must be kept under control.

Another possibility is to use single crystal scintillators. A promising candidate among those is stilbene, which is characterized by an excellent n - γ discrimination capability and by a wider energy domain compared to liquid scintillators like BC501A, NE-213 and EJ-309. There are reports of stilbene crystals being used for neutron spectrum measurements starting at 400 keV [Chernov 2002], and even as low as 100 keV when used with a lead filter [Jansky 2002]. Another advantage is that they do not suffer from the inflammability problem. Possible disadvantages are the sensitivity to temperature changes, like for the liquid scintillators, and the anisotropy of the response, which will be discussed in the following chapters.

As the size of the scintillator plays a major role, a compromise between energy resolution and detection efficiency has to be found. By making the scintillator thicker, the efficiency is enhanced (for the same incident radiation field, the detection volume is larger and the probability of interaction is higher), but the energy resolution worsens, mainly because it is more difficult to achieve uniform light collection. Another problem when the detector dimensions are increased is the multiple scattering of neutrons, which makes the response function more complicated. The length of the proton mean free path, which depends on the incident neutron energy, may also impose a constraint on the scintillator size. For higher neutron energies, larger scintillators are

needed. In general, for scintillation volumes on the order of tens of cubic centimeters (proper energy domain and good efficiency, 10-30%), typical values of energy resolutions are from 4% to 20% [Klein 2003, Chernov 2002].

For these kinds of detector sizes, maximum count rates are on the order of 10^3 (counts/s) with analog systems. Higher count rates, reaching more than one million counts per second, can be processed with digital electronics [Veskna 2014].

4.7 Comparison and Pre-Selection

Table 4.2 is a summary of the characteristics of the candidate detectors. All of them have good n - γ discrimination capability, but only the systems based on elastic scattering are insensitive to low-energy neutrons. In fact, ^3He and ^6Li cross sections are very high in the thermal region, which means unfavorable conditions whenever low-energy neutrons are present. This would be the case - for example - of out-of-core measurements in the experimental room of MASURCA.

Table 4.2. Comparison of the discussed fast neutron spectrometers.

	Conversion	Energy Resolution	Detection Efficiency	Time Response	Discr. n - γ	Sens. to n_{th}	Energy Domain
^3He Proportional Counter	$^3\text{He}(n,p)$	Good (~2%)	Average	Slow	Very Good	High	10 keV - 1 MeV
Proportional Counter (p-recoil)	$n - p$	Good (~2-6%)	Low (~1-3%)	Slow	Very Good	No	10 keV - 1 MeV
Organic Scintillator Liquid	$n - p$	Average (~3-15%)	Good (~10-20%)	Fast	Good	No	> 1 MeV
Organic Scintillator Crystal	$n - p$	Average (~3-10%)	Good (~10-30%)	Fast	Good	No	> 400 keV
Proton Recoil Telescope	$n - p$	Average (~3-10%)	Very Low (~ $10^{-5}/10^{-6}$)	Depend*	Very Good	No	> 200 keV
^6Li -Sandwich Diamond	$^6\text{Li}(n,\alpha)$	Good (~2%)	Very Low (~ $10^{-7}/10^{-8}$)	Fast	Good	High	200 keV - 6 MeV

* If the detection system is composed by solid-state spectrometers (fast) or gas-filled detectors (slow).

Regarding detection efficiency, organic scintillators (liquid and crystal) are the best among the selected candidates and overall, they are good-compromise spectrometers. The only weakness could be the average energy resolution, around 10%, which is the upper limit of the desired properties listed in 4.2.

The very low detection efficiency of the ^6Li -Sandwich diamond spectrometers makes them appropriate only for in-core applications. Their small size is an advantage, as they will cause only small perturbations of the local neutron flux.

Table 4.2 suggests that no single detector is capable of covering the entire 10 keV - 10 MeV range. A practical solution would therefore have to take the form of a multi-detector system, such as a combination of proportional counters, organic (liquid or crystal) scintillators and, if necessary, proton recoil telescopes.

This is the topic of the next chapter.

V. The Stilbene Scintillator

5.1 The Spectral Project

5.1.1 Down-selection of Organic Scintillators

5.2 Organic Scintillators as Mixed Radiations Fields Spectrometers

5.2.1 PSD - Pulse Shape Discrimination

5.2.2 PHS - Pulse Height Spectrum

5.3 Stilbene

5.3.1 Features of Stilbene

5.3.2 Solution-grown Stilbene

5.4 Methodology for Simulating the Response of Organic Scintillators

Introduction

In this chapter, the reasons behind the selection of a particular crystal organic scintillator, namely solution-grown stilbene, is explained. The organic scintillator has been chosen as the leading component of a multi-purpose intermediate-to-fast spectrometric system, worthy of an in-depth study, including experimental tests. The chapter begins with a presentation of the collaborative SPECTRAL project, which was born out of this PhD project, when it became clear that the development and testing of a prototype spectrometer would benefit from the expertise of other research groups using fast neutron sources and detectors. At the end of this chapter, the description of the calculation procedure adopted for simulating the response of the scintillator is provided.

5.1 The SPECTRAL Project

The SPECTRAL project was proposed in response to the NEEDS Call for Proposals issued in January 2016. The NEEDS challenge is an interdisciplinary research effort on Nuclear Energy, Environment, Waste and Society between French organizations (CNRS, Universities, CEA, IRSN, EDF, AREVA, ANDRA and BRGM). NEEDS supports actions in a wide range of scientific areas, such as nuclear data, integral experiments, instrumentation, innovative reactor concepts and simulation tools, etc. The SPECTRAL project was evaluated positively and approved for funding for two years.

The purpose of the SPECTRAL project is the development of a combined neutron spectroscopy concept based on a combination of detectors (Figure 5.1):

- Proportional Counters, for covering the energy domain from 10 keV up to 1.5 MeV;
- Organic Scintillators, commonly used starting from 1 MeV (BC501A, NE213, ...);
- Proton recoil telescopes, for bridging the gap between the first two (if necessary).

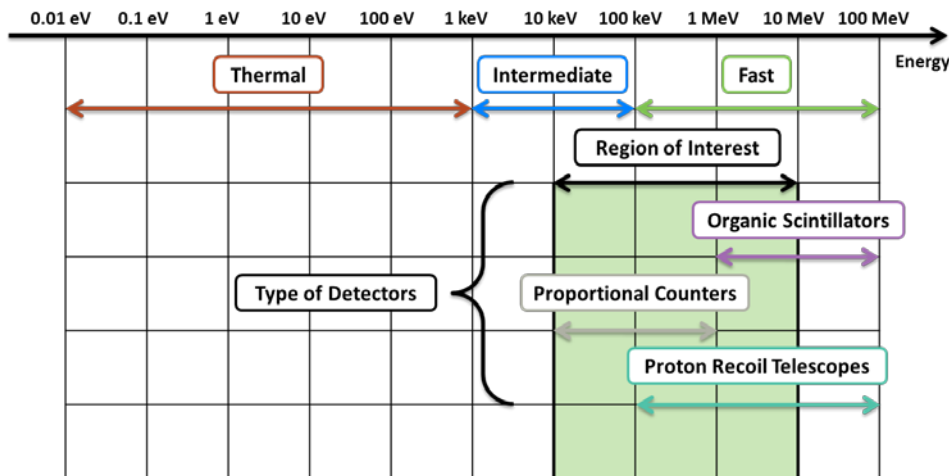


Figure 5.1. Energy domain covered by the different instruments chosen for the SPECTRAL project.

The motivation of the SPECTRAL project stems from this PhD work, but it is not specifically focused on the MASURCA facility. Actually, other research groups expressed interest in the proposed spectrometer development. All the applications listed in Chapters I and II which use intermediate-to-fast energy neutrons are targeted. These include pulsed and continuous neutron beam characterization for guaranteeing the delivery of reference neutron fields [Gressier 2004, Sorieul 2014]; neutrons sources for nuclear physics and nuclear data measurements, *e.g.* photo-, prompt and delayed fission neutron measurements [Clarke 2017, Lee 2013, Haight 2014], transmission and shielding experiments [Oka 1998 (2), Jansky 2002, Leconte 2016]; neutron-induced material activation and irradiation. Other interested applications are detector calibration, nuclear fusion, safeguards, etc.

In SPECTRAL, several groups with complementary competences are involved:

- CEA/DEN/CAD/DER/SPRC: reactor physics, nuclear physics, neutron transport code validation;
- CEA/DEN/CAD/DTN/SMTA/LMN: neutron and gamma detection using organic scintillators;
- IRSN/LMDN: operation of the AMANDE facility, neutron and gamma metrology using organic scintillators and proportional counters;
- CENBG (Bordeaux Gradignan): neutron production at the AIFIRA accelerator, nuclear physics and radiation detection using proton recoil techniques;
- Institut Fresnel (AMU): photon physics.

Thanks to the NEEDS funding of SPECTRAL, it was possible to manufacture and test a real prototype detector, as we will see later.

5.1.1 Down-selection of Organic Scintillators

At the conclusion of Chapter IV, four types of detectors were identified as eligible candidates:

1. Diamond sandwich detectors;
2. Proportional counters;
3. Organic scintillators;
4. Gas and diamond proton recoil telescopes.

Diamond detectors require quite high fluxes, they are of interest only for reactor in-core applications. Proportional counters and organic scintillators can arguably be used for all the applications discussed. Proton-recoil telescopes are an interesting option only for beam-type measurements.

For this PhD, it was decided to focus the efforts on only one type of detector, so as to have enough time to build a prototype, model it, perform some experiments with it, and compare the results with numerical simulations. The chosen detector was a new type of organic crystal scintillator, which appeared to be very promising but for which little was known. The other candidate detectors were assessed with the help of the various research groups within the SPECTRAL collaboration.

Proportional counters had already been extensively tested at IRSN, mainly a spherical counter filled with 3 atm of pure H₂ [Pichenot 2002]. By collaborating with the IRSN metrologists at AMANDE, it was also possible to learn about reference neutron and gamma-ray sources, detector response matrices and calibration procedures.

Liquid organic scintillators (BC501A and NE213) had also been tested at IRSN. As part of this PhD, time was initially spent studying and practicing with analogic systems for neutron spectrometry in mixed radiations fields, as this would be later required for performing measurements with the crystal scintillator.

Thanks to the help of CEA/DTN and IRSN experts, it was possible to compare actual data with the results of simple simulations performed with Monte Carlo codes (MCNP-PoliMi [Pozzi 2012]) and ancillary programs personally written. It was possible, for example, to assess the neutron-

gamma discrimination capability of a liquid scintillator and to evaluate the response of a proportional counter. The procedure for deriving a pulse height spectrum from the corresponding simulated spectrum and the proper detector response matrix was also studied with commercially available codes [Schmidt 2002].

Proton-recoil telescopes were experienced thanks to CENBG Bordeaux. The limits and the strengths of a proton-recoil silicon telescope were tested for neutron flux measurements as part of a program on actinide fission cross section (an accurate flux measurement is mandatory for normalizing experimental cross sections). To overcome the problem of measuring neutrons with energies lower than 700 keV (difficult with the silicon detector), it was possible to participate in the development of a proton-recoil gas telescope (4.6.1) [Marini 2016]. The gas telescope has the big advantage that the gas pressure can be adjusted to fit the proton ranges, and thus make the measurements less sensitive to the gamma-ray and electron background.

Diamond detectors were also tested with financial support provided by the AMIDEX fund, not by the SPECTRAL project. Thanks to INFN Genova, it was possible to take part in the measurements performed with a diamond ^6Li sandwich detector [Osipenko 2015 (1)] at the FNG facility (ENEA Frascati). Further experience on diamond detectors was acquired thanks to CIVIDEC, both for fast and thermal neutron applications.

When considering versatility, overall performance (energy domain and resolution), detection efficiency, n - γ discrimination capability, and ease of use, organic scintillators appear to be the best-compromise choice. They allow a preliminary analysis of a measurement on-line, by means of Pulse Height Spectrum behavior and Pulse Shape Discrimination. They also represent a good compromise in terms of detection efficiency-to-dimensions. Since they rely on elastic scattering of neutrons, low-energy neutron background is not a concern and, in general, they allow a reasonably good discrimination between neutrons and gamma-rays. Regarding the uses in the MASURCA facility, they would be applicable to beam-type experiments in the experimental room, as well as near-core applications. For in-core measurements, the dimensions and types of material (hydrogenated and, for liquid one, inflammable) and the maximum available count rate, could pose problems, although, as a reassuring fact, other groups already used them for such applications (see 5.3.1).

Organic scintillators are actually a large family of detection system. It is therefore not simple to identify the best one and usually is a choice related to the type of application, but a down-selection is needed. Liquid scintillators, such as the tested BC501A, are generally considered reference detectors for multi-purpose neutron spectrometry in mixed radiations fields [Klein 2003], but alternatives exist, in particular solid scintillators based on a plastic matrix (such as EJ-299-33 [Pozzi 2013]) or crystals scintillators like stilbene [Broek & Anderson 1960] or p-terphenyl [Sardet 2015]. As several types of organic scintillators (solution-grown crystals, plastic scintillators with PSD capability, etc.) were being studied by different research groups during this PhD, it was possible to take advantage of recently reported results and advances.

Before deciding which organic scintillator to select, it is necessary to introduce several fundamental concepts and to delve into neutron-gamma discrimination in scintillators.

5.2 Organic Scintillators as Mixed Radiations Fields Spectrometers

As stated before, organic scintillators are organic materials that exhibit the property of scintillation, which is referred to as the capability of emitting light (visible or ultraviolet) when excited by ionizing radiation. Neutrons interact with protons in the scintillation volume by means of elastic scattering, while for gamma-rays, the main interaction type is Compton scattering with electrons. Both mechanisms can transfer to the secondary charged particles all or a part of the primary non-ionizing radiation's energy.

5.2.1 PSD - Pulse Shape Discrimination

For all practical applications of interest to this work, neutrons and gamma-rays are mixed together in a mixed radiation field. Therefore, in order to spectrally characterize the two, it is important to well separate the contribution of both. The Pulse Shape Discrimination (PSD), referred to as the capability - for a given type of scintillator - of being able to distinguish between pulses produced by neutrons and gamma-rays, it is possible thanks to the fact that the ionization mechanism induced by protons and electrons is slightly different. Electrons scattered by gamma-rays in a Compton interaction and protons scattered by neutrons in an n - p elastic interaction, excite the scintillation material with a spatial range that depends on the charged particle energy (Figure 5.2).

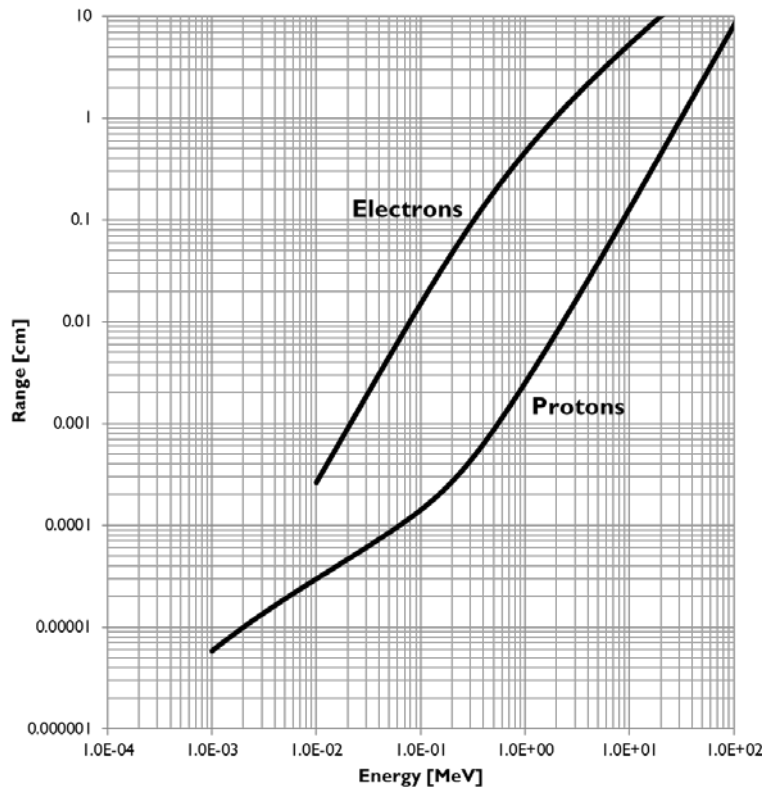


Figure 5.2. Electron and proton range for stilbene [NIST - ESTAR and PSTAR]

This ionization range is shorter for protons, which deposit energy in a smaller scintillation volume compared to electrons. The high linear energy transfer of protons leads to a high concentration of excited molecules, which causes the main difference between neutron and gamma ionization (Figure 5.3).

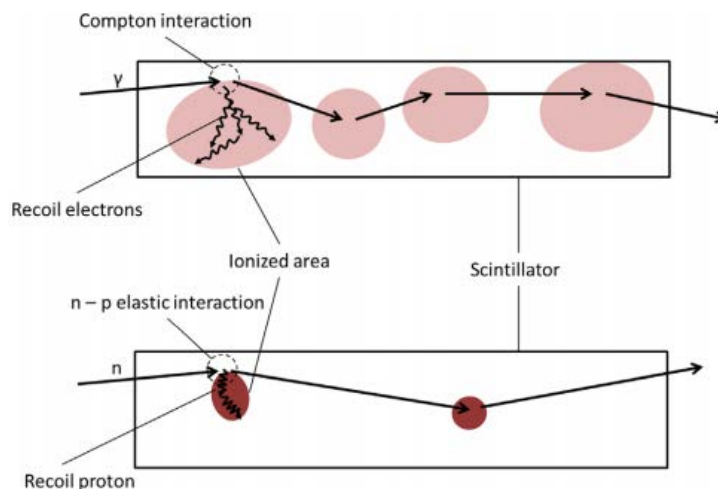


Figure 5.3. Comparison of gamma-ray and neutron induced ionization repartition in organic scintillators [Bertrand 2015].

There are two main excitation processes. The first is the excitation of molecules into singlet states (S_1), resulting in the emission of prompt fluorescence (by de-excitation to S_0). The other is the excitation into triplet states (T_1). The first process has a lower probability than the second one and its time scale is typically on the order of 10^{-9} to 10^{-8} s (from ns to tens of ns). The triplet state de-excitation is non-radiative and has longer characteristic times.

The high density of excited states in the proton ionization mode increases the probability of a special mechanism: the triplet-triplet annihilation. When two triplet excited state molecules are close enough, they are able to annihilate each other. One molecule reaches the ground state S_0 meanwhile the other reaches the singlet excited state (S_1). The latter subsequently emits the so-called delayed fluorescence in the de-excitation process (Figure 5.4a). This phenomenon has a typical time scale on the order of 10^{-7} s (hundreds of ns).

The PSD is possible since the pulse of the optical photons created in a gamma-ray interaction inherits only the time scale of the prompt fluorescence process whereas the pulse of the optical photons created in a neutron interaction has a longer time scale, since it includes the contribution of the delayed fluorescence.

In practice, for a scintillator with n - γ discrimination properties, the time dependence of the scintillation intensity should be similar to the one reported in Figure 5.4b.

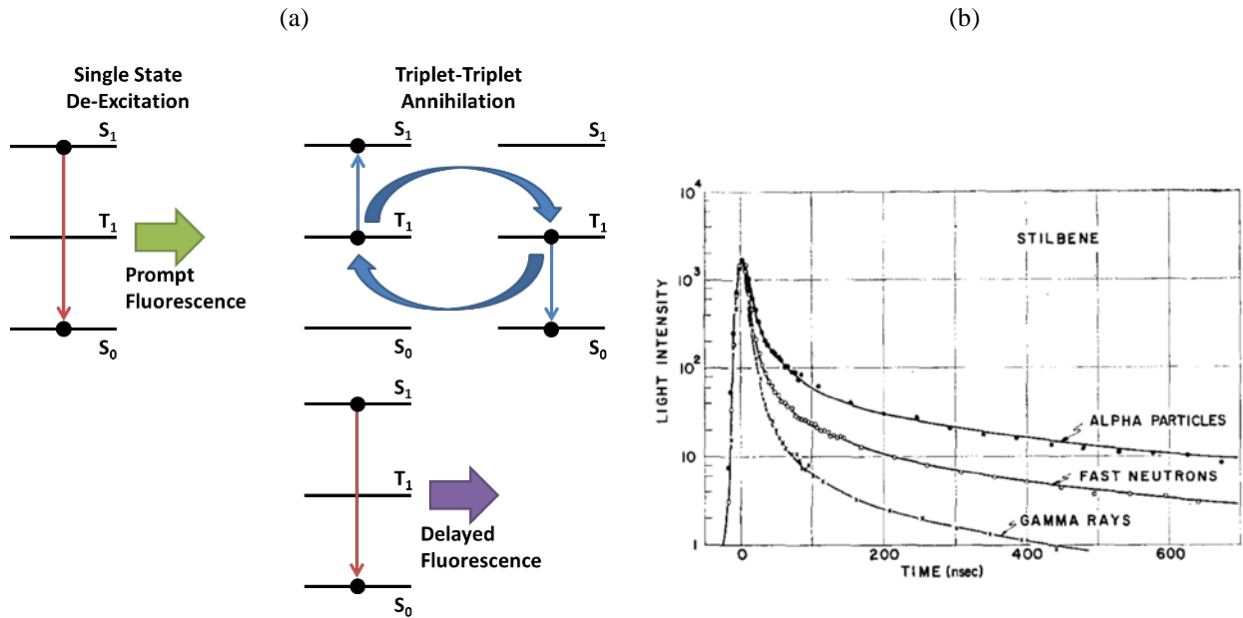


Figure 5.4. (a) Prompt and delayed fluorescence mechanism and (b) time dependence of scintillation intensity for stilbene [Bollinger & Thomas 1961].

PSD PATTERNS AND FIGURES OF MERIT

The pulse shape discrimination capability can be quantified by evaluating the so-called PSD pattern and the associated Figure of Merit (FoM). PSD patterns are obtained thanks to proper electronic systems (with PSD characteristics [Owen 1958]) used together with the organic scintillator. Such systems are able to distinguish neutrons from gamma-rays thanks to the difference in decay time of the produced signals. An example of a typical PSD profile that can be obtained with an analogic system is shown in Figure 5.5a, which is the result of the measurements performed with an organic scintillator (solution-grown stilbene, see 5.3) and an Am-Be source (March 2017).

The associated FoM is defined as:

$$FoM = \frac{Peak_n - Peak_\gamma}{FWHM_n + FWHM_\gamma} \quad , \quad (5.1)$$

where the experimental data for neutrons and gamma-rays are fitted by Gaussian curves (Figure 5.5b).

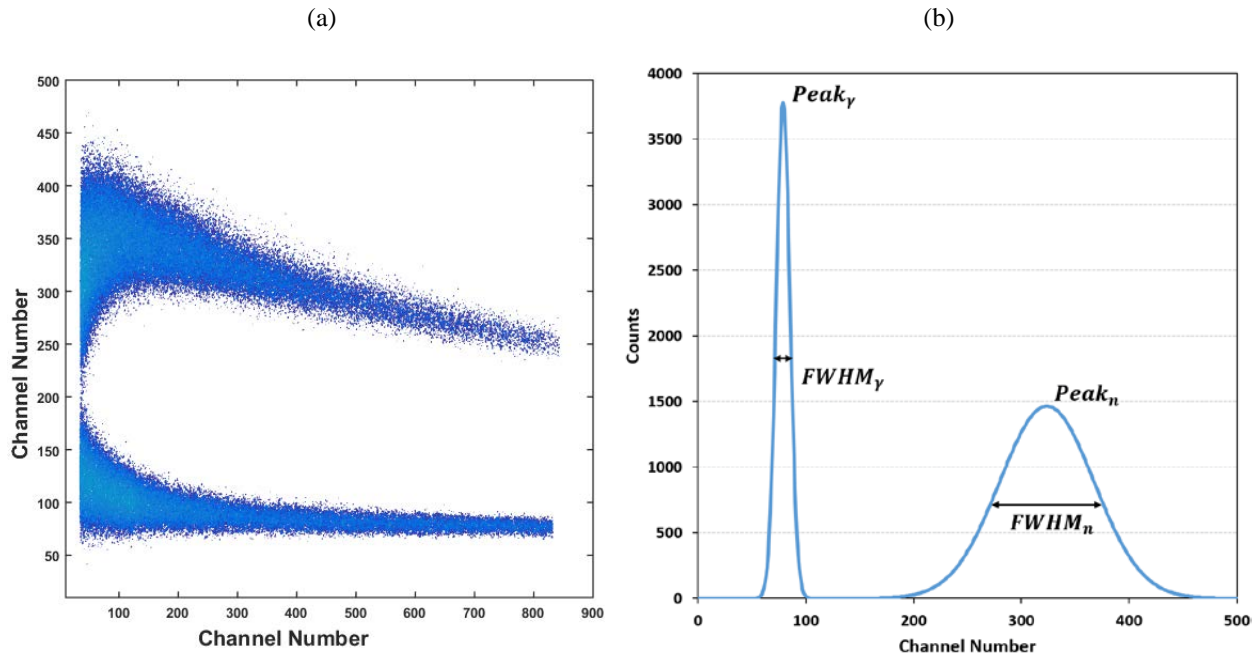


Figure 5.5. (a) Example of a measured PSD pattern for an AmBe source (solution-grown stilbene) and (b) corresponding FoM (Gaussian fit).

5.2.2 PHS - Pulse Height Spectrum

For spectroscopy purposes, it is not sufficient to distinguish between neutrons and gamma-rays, it is also necessary to measure and quantify the energy distribution of the two radiation fields. The light produced in the ionization process is emitted in all directions and is referred to as the *Light Yield (LY)* of the scintillator, usually given in the number of photons produced when the scintillator absorbs 1 MeV of energy. The *LY* is a property of the scintillation material and does not depend on other factors. Since a scintillator detector is mainly composed of an organic scintillation material and a photomultiplier (with possibly a light guide between the two), the quantity that is actually measured is the *Light Output (LO)*, which is the amount of light that reaches the PMT. The relation between the *LY* and the *LO* can be expressed as follows:

$$LO = K_{LC} \times LY \quad . \quad (5.2)$$

K_{lc} is known as the light collection efficiency, which depends on the size, shape, surface treatment and packing of the scintillation material. Typical values of *LO*, *LY* and K_{lc} for several organic scintillators are reported in Table 5.1 ([Galunov 2013]).

Table 5.1. Values of K_{lc} , LO and LY (in Photons per MeV) for several organic scintillators [Galunov 2013].

Sample	Anthracene	<i>Trans</i> -stilbene	<i>p</i> -Terphenyl (pure)	<i>p</i> -Terphenyl (doped)	Polystyrene
LO	17330	9670	9745	15345	6660
K_{lc}	0.596	0.659	0.576	0.615	0.725
LY	29080	14700	16920	24950	9190

The pulse height (PH) produced at the output of a measuring circuit depends on the LO , the maximum average quantum efficiency of the photocathode (K_{av}^{max}), the coefficient of spectral matching of the photomultiplier and the scintillator (K_{pmt}^{sc}) and on another efficiency coefficient (K) that takes into account the amplification of the measuring circuit and the PMT:

$$PH = LO \times K_{av}^{max} \times K_{pmt}^{sc} \times K \quad (5.3)$$

The product of the first three terms on the right side of Equation 5.3 defines the *Photoelectric Yield* (L_{phe}), that is the number of photoelectrons emitted by the photocathode per MeV absorbed in the scintillator. Under normal operating conditions, K has a linear characteristic, thus the *Pulse Height* is linearly proportional to the energy deposited in the scintillator (the instrument can be easily used as a spectrometer). The theoretical *Pulse Height Spectrum* is shown in Figure 5.6a but, as already mentioned in Chapter IV, different effects distort the simple rectangular shape: finite detector resolution (Figure 5.6b); scattering by carbon nuclei (Figure 5.6c); multiple scattering by hydrogen; and non-linearity of the scintillation response (the LO is a non-linear function of the neutron energy).

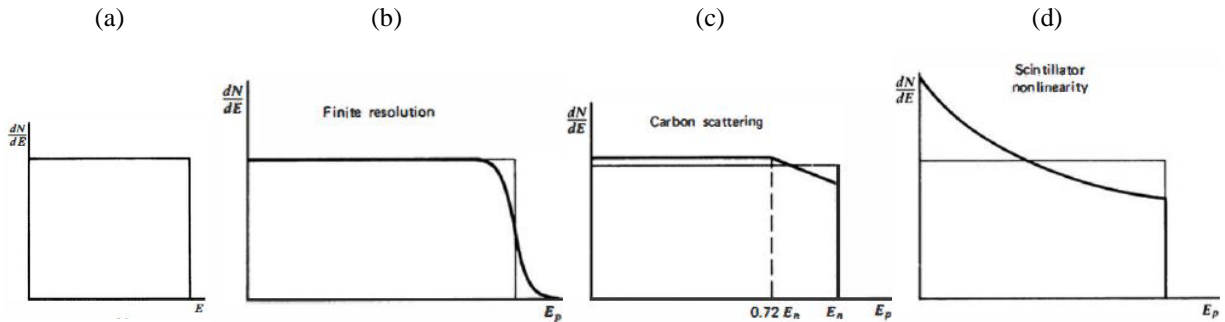


Figure 5.6. (a) Theoretical Pulse Height Spectrum of an organic scintillator. Effect produced on the PHS by (b) finite resolution, (c) carbon scattering and (d) non-linearity of the scintillator response [Knoll].

Actually, the *Pulse Height Spectrum* produced in an organic scintillator is similar to the PHS under the label “d” of Figure 5.7, which considers all the distortion effects mentioned earlier. All PHSs reported in Figure 5.7 take into account the non-linearity of the scintillation response. The PHS

“a” correspond to the case of a perfect resolution; “b” to FWHM of 15 %; “c” is “b” plus the effect of scattering on carbon; and “d” is “c” plus the influence of multiple scattering on hydrogen.

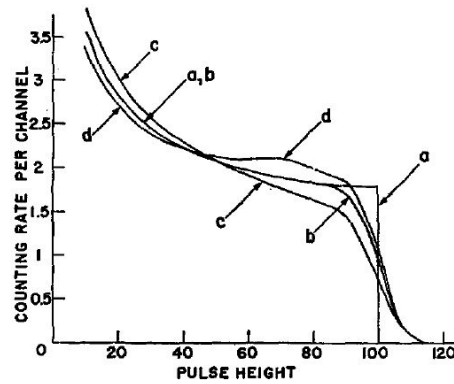


Figure 5.7. Pulse Height Spectra produced in a stilbene crystal by mono-energetic 4 MeV neutrons [Broek & Anderson 1960].

NON-LINEARITY OF THE SCINTILLATION RESPONSE

The non-linearity of the scintillation response has been evinced experimentally in the fifties. For crystal scintillators, of particular interest are the works of [Brooks 1956, Taylor 1951, Fowler & Ross 1955, King & Birks 1952]. An example of what non-linearity means, is reported in Figure 5.8 for Anthracene [Brooks 1956] (similar behaviors were found for other organic scintillators like stilbene, plastic and liquid solution [Birks]). On the ordinate axis, the response L can be read as a LO (or PH). As Figure 5.8 shows, different radiations exhibit different behaviors, and, in the energy domain of interest (10 keV - 10 MeV), only protons - hence neutrons -, exhibit a non-linear trend.

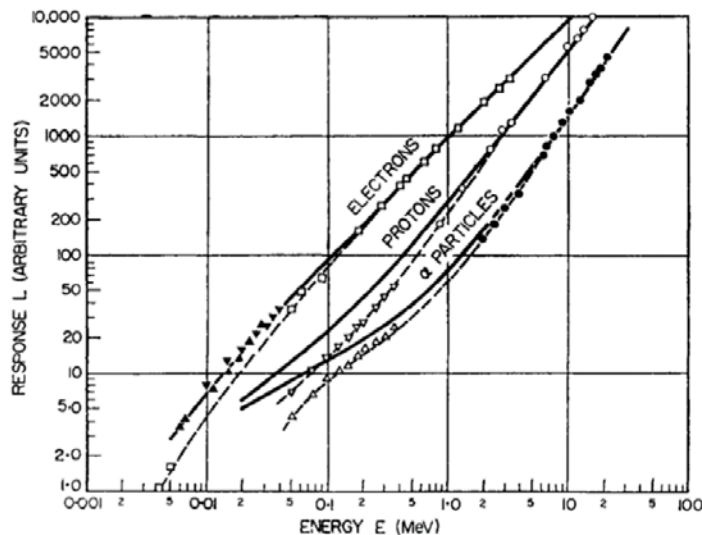


Figure 5.8. Anthracene crystal scintillation response to electrons, protons and alpha particles [Brooks 1956].

The work of [Taylor 1951] shows that the response to electrons above about 25 keV is linear for stilbene and anthracene crystals (Figure 5.9a and 5.9b). On the other hand, as already noted for anthracene, the proton response is non-linear for energies lower than about 2 MeV, and this non-linearity becomes more pronounced at inferior energies [Fowler & Ross 1955] (Figure 5.9c and d). This is the main reason for the behavior of the proton-recoil PHS.

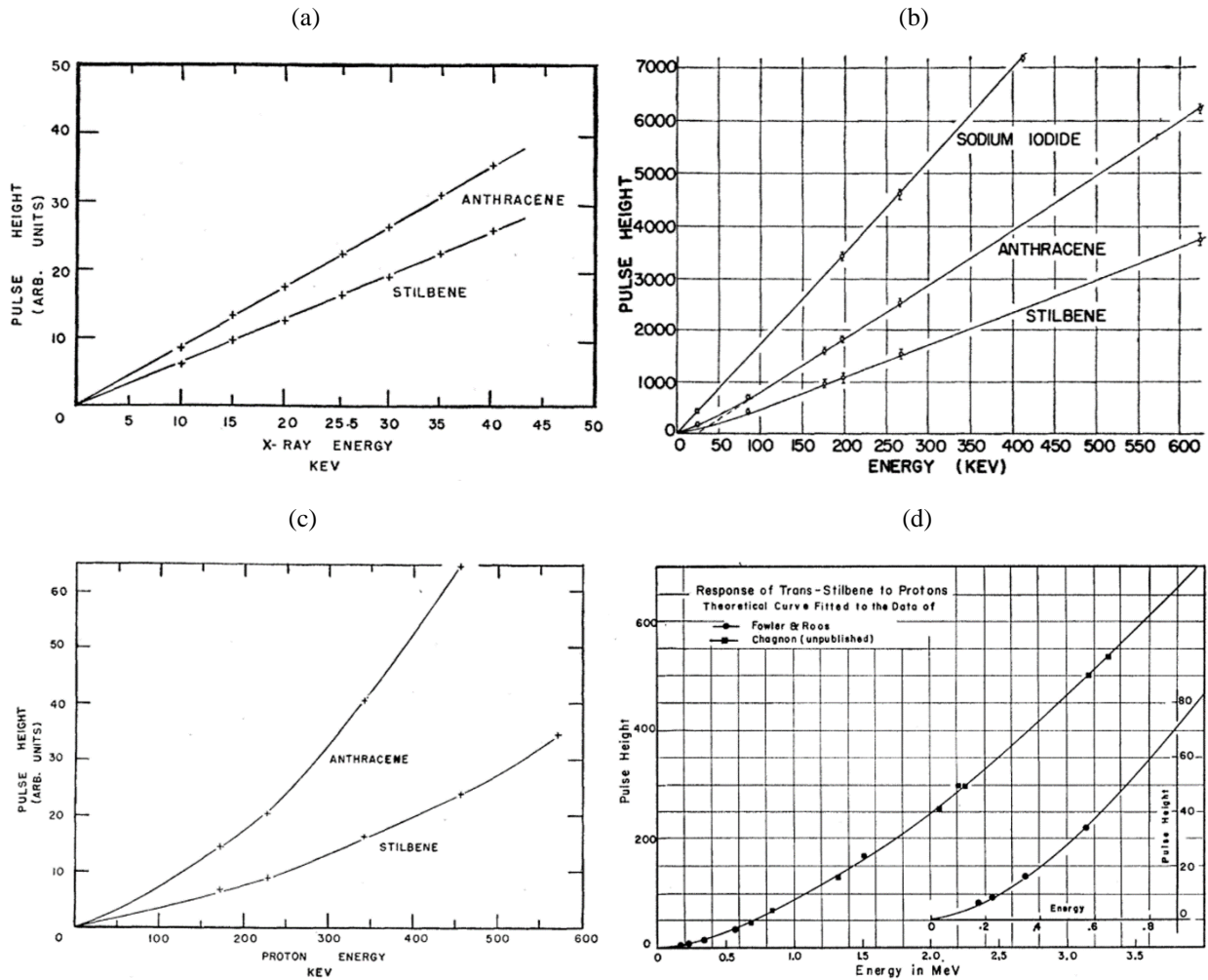


Figure 5.9. (a) PH of anthracene and stilbene as a function of electron energy [Fowler & Ross 1955], (b) PH of sodium iodide, anthracene and stilbene as a function of electron energy [Taylor 1951], (c) and (d) PH of anthracene (only c) and stilbene as a function of proton energy [Fowler & Ross 1955].

GAMMA CALIBRATION OF ORGANIC SCINTILLATORS

In practice, for a given electronic set-up, the PHS coming from a radiation source is in the form of counts per channel number (often called multichannel PHS, Figure 5.10a). In spectroscopy, the abscissa values expressed in number of channels have to be converted into an energy scale. This procedure, called *energy calibration*, consists in determining the position of the Compton edge of

“mono-energetic” gamma-ray sources, such as ^{137}Cs , ^{60}Co , ^{22}Na , ^{207}Bi , etc. The maximum Compton electron energy is derived from the well-known formula:

$$E_C = \frac{2E_\gamma^2}{0.511 + 2E_\gamma} \text{ [MeV]} . \quad (5.4)$$

Where E_γ represents the gamma energy emitted by the source and E_C the value of the maximum energy of the Compton electrons.

Different approaches have been used for determining the position of Compton edges by means of experimental measurements and simulations [Cherubini 1989, Dietze and Klein 1982, Verbinsky 1968, Jie 2010]. In this work, the first derivative (of the measured gamma PHS) is used to find them. With this procedure, it is possible to associate a channel number to a known energy (E_C). By using different gamma energy sources (Table 5.2), it is thus possible to calibrate the detection system in terms of the so-called electron-equivalent energy (or gamma-equivalent). The *LO* of an organic scintillator is usually given in electron-equivalent energy (e.g. keV_{ee} , MeV_{ee} , ...), since the response to gamma-rays is supposed to be linear for the energies of interest. The dependence between the channel number (X) and the electron equivalent energy (Y in MeV_{ee}) is of the form:

$$Y [\text{MeV}_{ee}] = a \cdot X [\#] + b . \quad (5.5)$$

Table 5.2. Typical “mono-energetic” gamma sources used for calibration.

Source	E_γ [MeV]	E_C [MeV]
^{22}Na	0.511	0.341
	1.275	1.062
^{60}Co	1.173	0.963
	1.332	1.117
^{137}Cs	0.662	0.477
^{207}Bi	0.570	0.393
	1.063	0.857
	1.170	1.547

Nevertheless, it is a good practice to check the linearity of a specific set-up because factors like the voltage applied to the photomultiplier could distort this linear relationship (see 7.2.1). This is why several gamma sources with different energies are used, as in the example shown in the Figure 5.10b (March 2017 - ^{137}Cs source measured with a solution-grown stilbene, see 5.3).

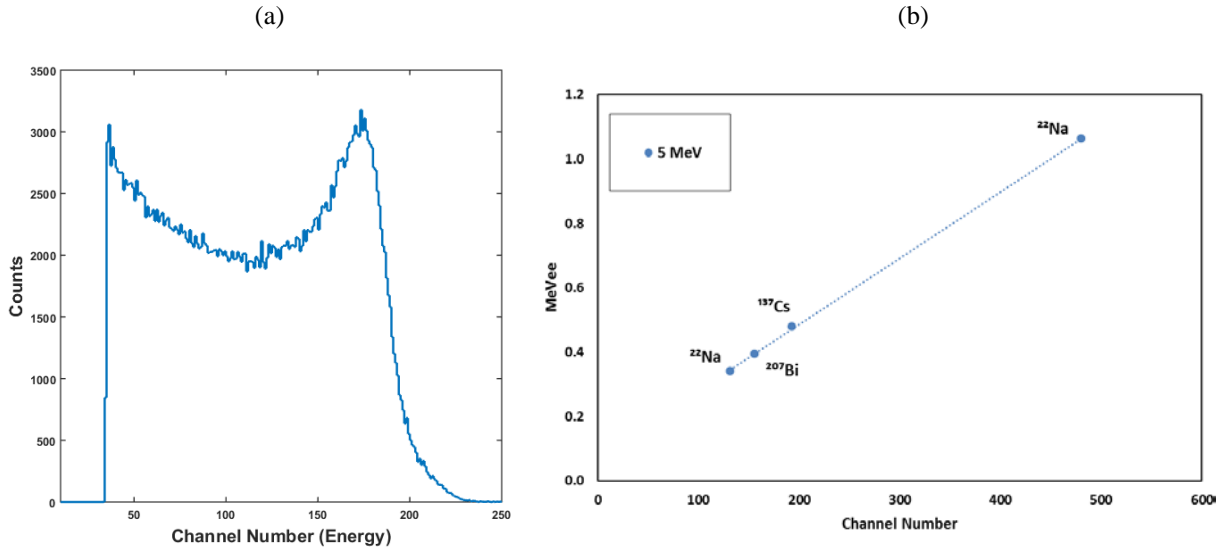


Figure 5.10. (a) Multichannel PHS coming from a ^{137}Cs source, and (b) example of a calibration performed for the measurement of a 5 MeV mono-energetic neutron field [Dioni 2017 (2)].

NEUTRON CALIBRATION OF ORGANIC SCINTILLATORS

As already shown in Figure 5.8, the responses produced by electrons and protons are different. The first one is linear in the energy range of interest (thus picked as a convention for expressing the *LO*). The second one - on the other hand - exhibits a non-linear behavior. For neutron spectroscopy purposes, the gamma calibration is not valid for representing the neutron energy scale. A relationship between the gamma-equivalent energy and the neutron-equivalent energy has to be defined and used (usually, neutron energy-to-*LO* or vice versa). This can be done experimentally by using time-of-flight techniques or in proton recoil mode [Kornilov 2009]. The latter (used in this work, Chapter VI) is based on the detection of reference mono-energetic neutron fields and the subsequent localization of the respective proton recoil edges. The idea is exactly the same as for the gamma calibration, and the proton recoil edge is also found by using the first derivative of the PHS. An example is shown in Figure 5.11a, which is the neutron PHS (after gamma subtraction) obtained at the 5 MeV mono-energetic neutron beam produced by the AIFIRA facility [Sorieu 2014], plus the relative first derivative for finding the proton edge (in this case, where the 5 MeV energy point is located, see 7.1.1). By associating the two calibrations (for several mono-energetic energies) it is possible to construct the *LO*-to-energy curve. Examples for stilbene are presented in Figure 5.11.

In summary, the construction of the neutron and gamma response matrix of an organic scintillator requires calibration data at various reference mono-energetic neutron and gamma fields covering the whole energy domain intended for the detector. These calibration data plus mono-energetic response functions make it possible to get the *LO*-to-energy curve, which is required to convert the scintillator outputs into “measured” neutron and gamma spectra.

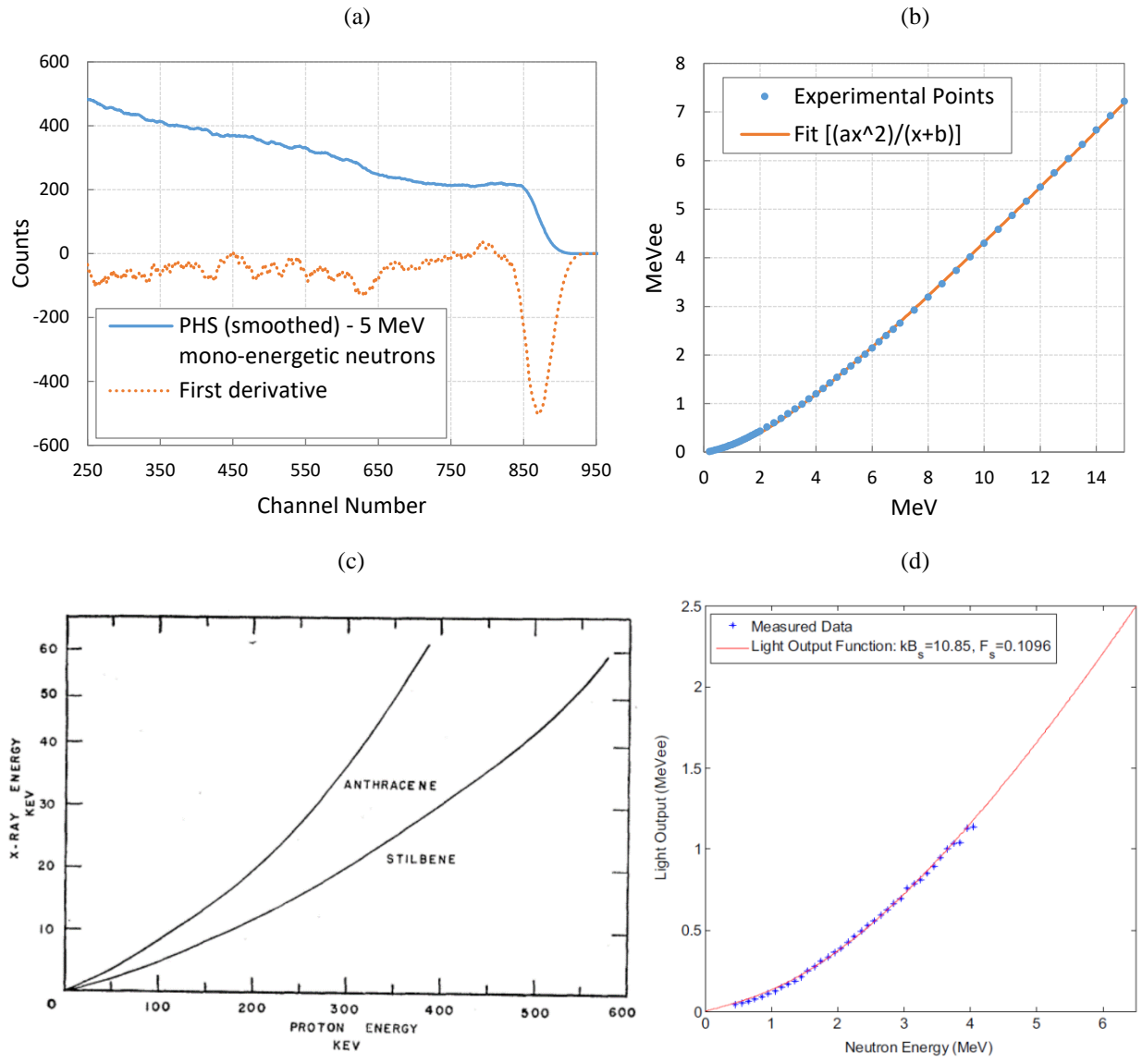


Figure 5.11. (a) 5 MeV smoothed PHS, (b) LO-to-energy for $\varnothing 1 \times 1$ cm² stilbene [Kostal 2017 (private)], (c) electron energy versus proton energy for equal pulse heights [Fowler & Ross 1955], (d) electron energy (LO) versus proton (Neutron) energy for solution-grown stilbene [Bourne 2016].

5.3 Stilbene

For covering the intermediate-to-fast energy domain, a combination of proportional counters and organic scintillators have been pre-selected in the context of the SPECTRAL project and for this work: (i) A set of proportional counters for the energy range between 10 keV and 1.5 MeV, and (ii) organic scintillators for higher energies.

The choice of the organic scintillator mainly depends on its flexibility (temperature range of applications, radiation hardness, ...) and energy domain of application (mainly depending on its n - γ discrimination capability and LO).

The capability, for the organic scintillator, to cover as wide an energy domain as possible in the lower energy part, and thus to overlap with the range covered by the proportional counters, is being sought, as this would help assure consistency of the results (neutron flux normalization purposes). Liquid scintillators, like Saint-Gobain BC501A [BC501A - Saint-Gobain], are a solid choice for neutron spectrometry in mixed radiation but they are usually used as standard for neutron energies over 1 MeV [Klein 2003]. Single crystal scintillators like stilbene, anthracene or p-terphenyl [Broek & Anderson 1960, Birks, Sardet 2015] are strong contenders as their n - γ discrimination properties and LO (see 5.3.2) are better than those of liquid scintillators, and their energy domain of application is wider.

A possible drawback related to the employment of liquid scintillators is the inflammability of the liquid (flash point 24° C), which could be a limitation in ZPRs, although nowadays containers - aluminum capsules wrapped in a polyethylene expansion tube - are well suited for most applications. On the other hand, for crystal scintillators, a possible limitation is the anisotropy of the response (in the following and again in Chapter VII), which could complicate the measurement.

By analyzing the pros and the cons of liquid and crystal scintillators, the latter seem to be the better solution for this work. Moreover, there are two additional favorable and important considerations enhancing the choice of crystal scintillators: (i) There is prior positive experience with the use of crystal scintillators in ZPRs (for neutron and gamma spectrum measurements); and (ii) recent developments in stilbene crystal growing techniques show considerable promise.

The stilbene single-crystal organic scintillator has thus been chosen for further studies in this work.

Several references reporting on the use of stilbene as a radiation (neutrons, gamma-rays, X-rays, protons, electrons, alphas, ...) spectrometer were found, some dating back to the 50s: [Broek & Anderson 1960, Fowler & Ross 1955, Taylor 1951, Birks 1952, King & Birks 1952, Bollinger & Thomas 1961, Owen 1958, Owen 1959].

ANISOTROPY

The anisotropy of the scintillation response is referred to as the dependence of the detector response to the neutron field incidence direction with respect to the crystal axis [Birks, Tsukada & Kikuchi 1962, Brooks & Jones 1974, Cvachovec 2002, Schuster & Brubaker 2017]. The anisotropy is a result of internal effects due to the molecular and crystal structure of the organic crystal scintillator. An example of the effect of anisotropy on a stilbene detector is reported in Figure 5.12 (for 5 MeV mono-energetic neutrons [Dioni 2017 (2)]). No anisotropy is observed with electron excitation (*i.e.* for gamma-rays) [Heckmann 1959]. The observed anisotropy of the crystal response, if considered too severe, suggests that the preferred operating conditions could be those applications where the neutron field is either isotropic (such as inside the core of a research reactor) or monodirectional (such as in a colimated beam).

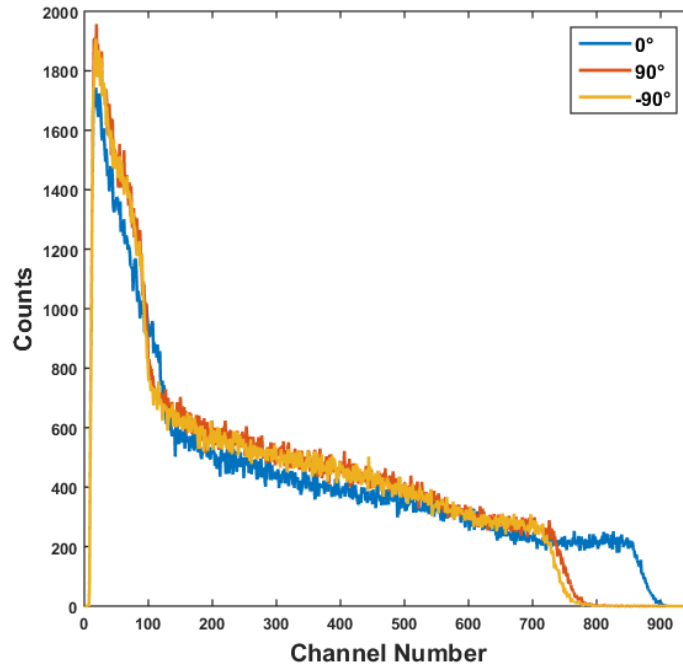


Figure 5.12. 5 MeV mono-energetic neutron PHS of a $\varnothing 2.54 \times 2.54$ cm² stilbene at 0°, 90° and -90° with respect to the beam axis [Dioni 2017 (2)].

5.3.1 Features of Stilbene

In this section, the flexibility of stilbene is evaluated. First, the radiation hardness and temperature sensitivity are discussed. Second, as further evidence of the compatibility of stilbene with reactor conditions, examples of measurements performed by the Rez group in the Czech Republic are provided.

RADIATION HARDNESS AND TEMPERATURE EFFECT

Radiation hardness is discussed in [Klimenkov 2004] for nuclear fusion applications (ITER). Similar stilbene crystals were subject to a different total neutron fluence (neutrons cm⁻²) in the central channel of the BR-1 reactor. The response to a ⁶⁰Co source was measured before and after irradiation. The overall conclusion is that the stilbene crystal can be reliably used at least up to total fast neutron fluence levels on the order of 10¹³ neutrons cm⁻² without any appreciable change in energy resolution (Figure 5.13). Above this value, at 10¹⁴ neutron cm⁻², the stilbene crystal becomes turbid and acquires a yellow-brown tint.

Typical fast neutron fluxes in the BR-1 reactor were on the order of 10⁸-10⁹ neutrons cm⁻² s⁻¹ for reaching these irradiation levels in a reasonable time. This means that, in practice, the upper flux limit for stilbene as a neutron-gamma spectrometer will be set by the electronics. As already discussed, with digital systems, count rates on the order of one million of counts per second can

be reached, allowing the use of stilbene detectors in neutron fields having intensities on the order of 10^6 - 10^7 neutrons $\text{cm}^{-2} \text{s}^{-1}$.

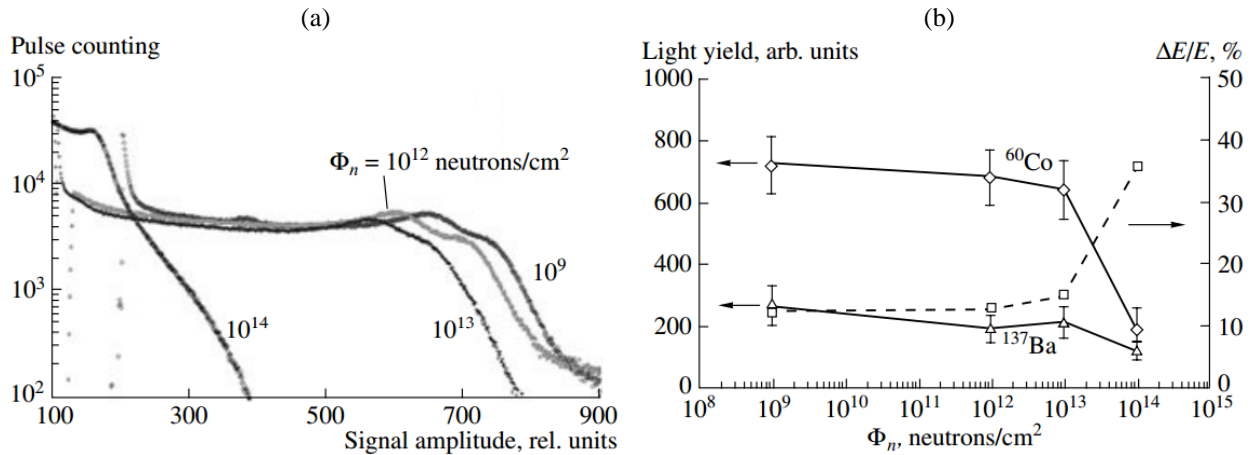


Figure 5.13. (a) PHSs of ^{60}Co after different irradiations and (b) relative LY and energy resolution ($\Delta E/E$) as a function of the fast neutron fluence [Klimenkov 2004].

Instead, the temperature dependence of stilbene single crystal LY was analyzed in [Baker 2008]. The results (Figure 5.14) show a linear behavior of the LY with temperature in the range between 180 K and 350 K. Knowing that the melting point of a stilbene crystal is 397 K [Galunov 1997], for temperatures higher than 350 K, sublimation of the stilbene material takes place and its transparency drops. This leads to a decrease of the scintillation LY above 350 K, as shown in Figure 5.14.

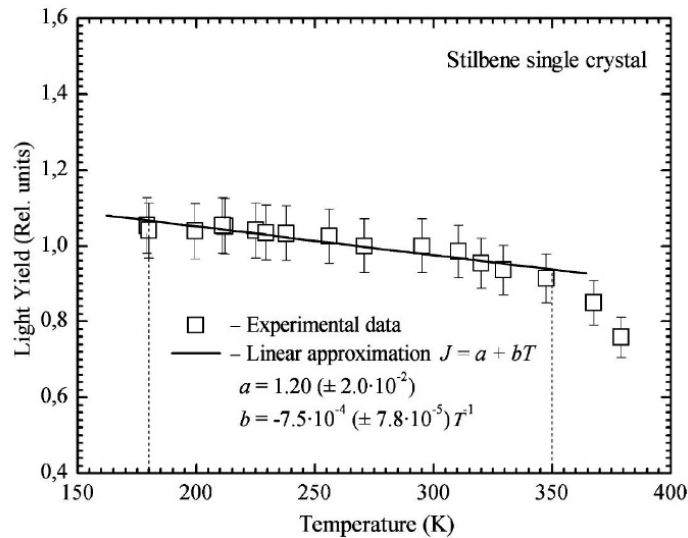


Figure 5.14. Relative light yield versus temperature for a $\varnothing 24 \text{ mm} \times 5 \text{ mm}$ stilbene single crystal irradiated by a ^{137}Cs source [Baker 2008].

The stable temperature domain of application of stilbene crystals below 350 K is compatible with the conditions found in Zero Power Reactors (ZPRs), in some irradiation RRs, in accelerators, and for common nuclear physics measurements.

APPLICATIONS

In-core and near-core neutron (and gamma) spectra have been extensively characterized at the LR-0 facility (Rez, Czech Republic). The full description of the LR-0 research reactor is deferred to the next chapter (6.2.3).

Two stilbene crystals of dimensions $\varnothing 10 \times 10 \text{ mm}^2$ and $\varnothing 45 \times 45 \text{ mm}^2$ were employed for the characterization, respectively, of neutron and gamma spectra (400 keV - 15 MeV) in different positions inside and near the LR-0 light water reactor core (in dry channels) [Kostal 2017; Kostal 2016].

Figure 5.15 reports the results of the measurements performed with the detectors placed inside the central dry channel (label 8 in Figure 5.15a), in a position corresponding to the critical water high level [Kostal 2017].

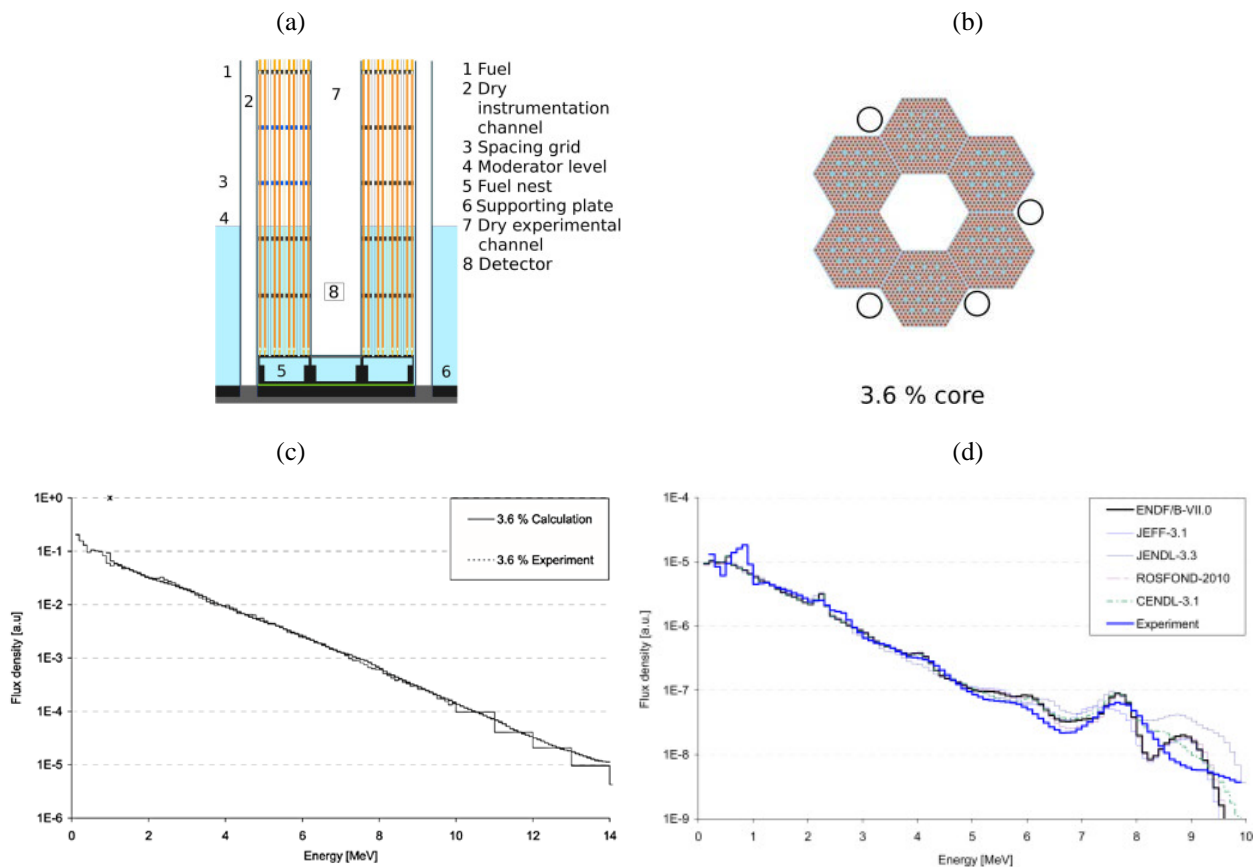


Figure 5.15. (a) Axial plot of LR-0, (b) radial cross-section of the experimental configurations, (c) measured and calculated neutron spectrum, (d) measured and calculated gamma spectrum [Kostal 2017].

Experimental uncertainties are reported in the range of 5 % below 5 MeV, about 5 – 8 % in 5 - 8 MeV and reach 10 % in the energy region above 8 MeV. The main contributions are statistical uncertainties, along with the uncertainties of calibration and of detector resolution.

Figure 5.16 shows the results of near-core measurements performed past the reactor pressure vessel and inside the biological concrete shield [Kostal 2016].

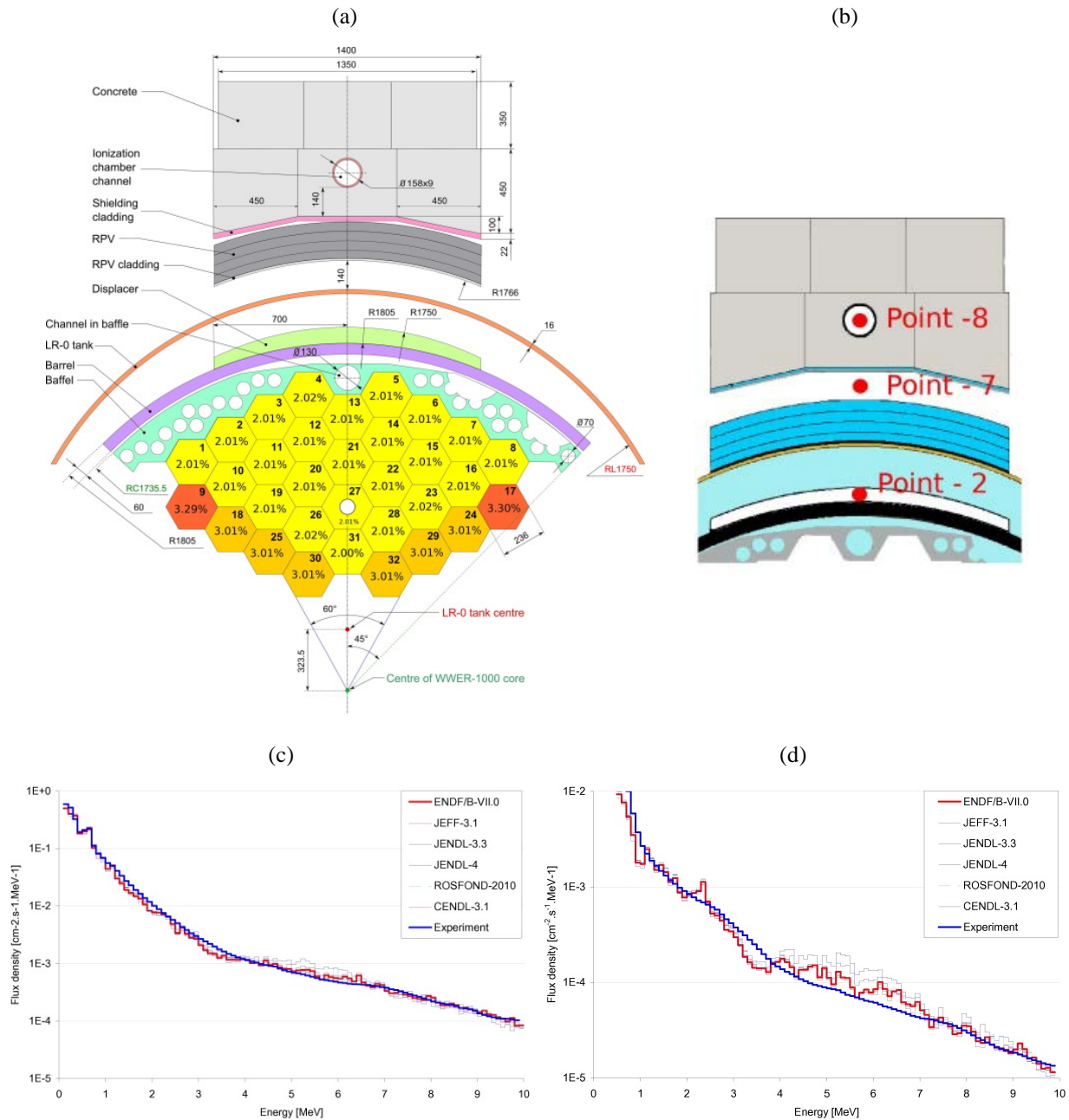


Figure 5.16. (a) LR-0 experimental configuration, (b) measuring points, (c) measured neutron flux density at point 7, (d) measured neutron flux density at point 8 [Kostal 2016].

Out-of-core and beam type applications were studied by the same Czech group at the German research reactor AKR-2 [Kostal 2011]. The AKR-2 is a very small training reactor (2 W rated power) at the Technical University of Dresden. It has a homogenous core made of a mixture of 20 % enriched uranium oxide and polyethylene as a solid moderator. Leakage neutrons can be measured at the end of different radial experimental channels (Figure 5.17a and b). Neutron and gamma leakage spectra were characterized thanks to stilbene detectors positioned at the end of the extraction channel 7. The results are presented in Figure 5.17c and d.

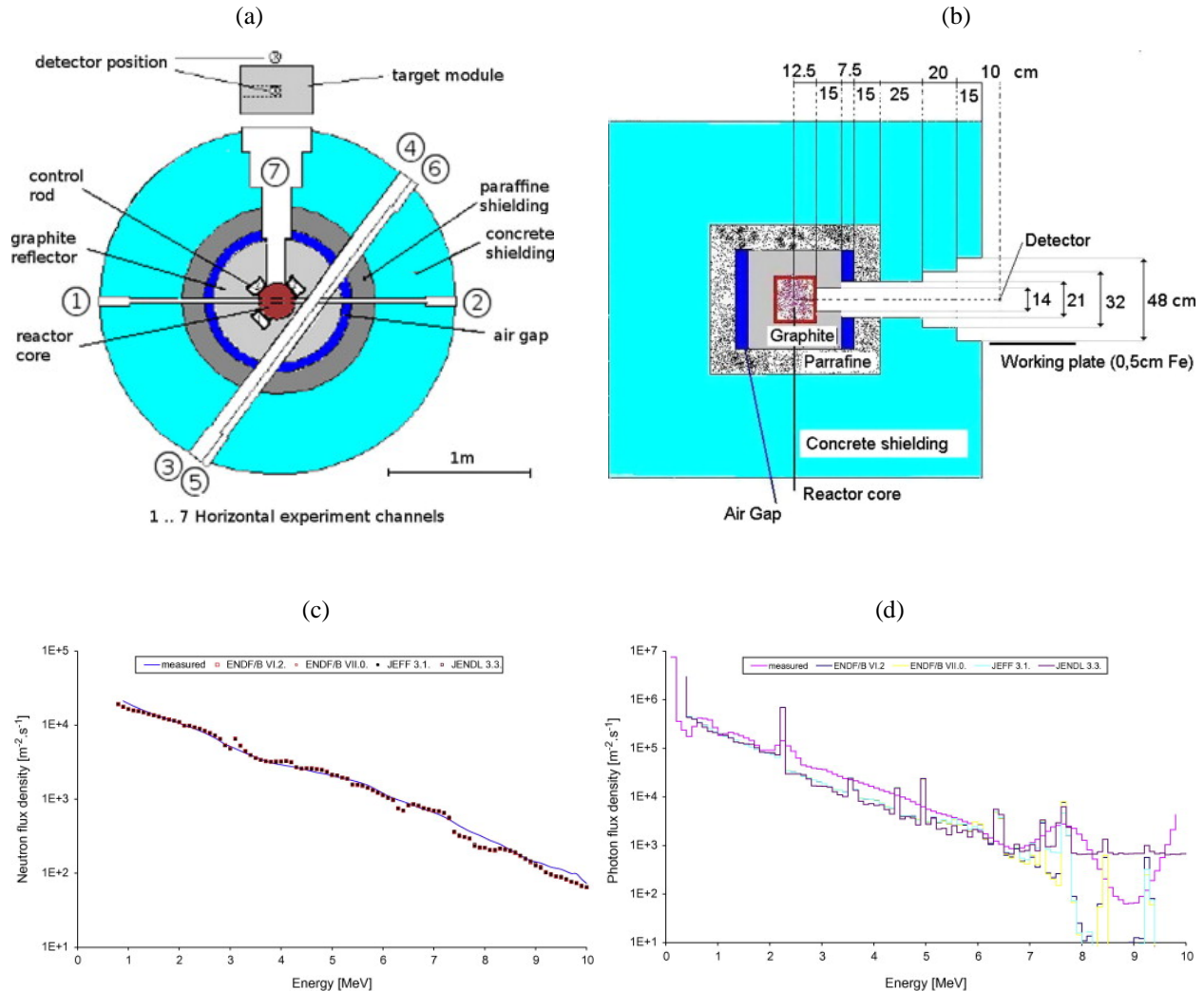


Figure 5.17. (a) Horizontal cross section of AKR-2, (b) vertical cross section of AKR-2, (c) measured neutron flux density, (d) measured gamma flux density [Kostal 2011].

The neutron (and gamma) beam extracted from the AKR-2 reactor was also successfully used for transmission experiments in iron and water, despite the very limited reactor power. The measured neutron and gamma spectrum after 25 cm of iron is shown in Figure 5.18.

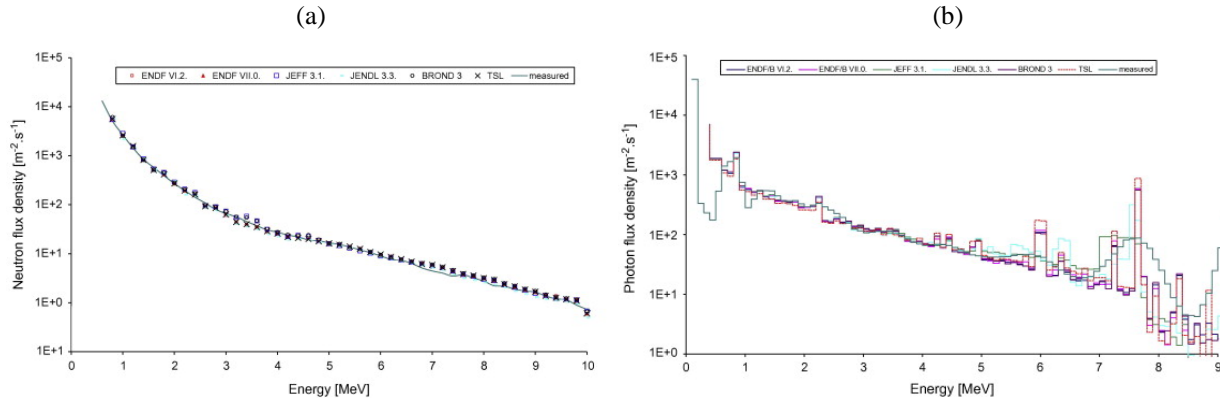


Figure 5.18. (a) Neutron flux density behind 25 cm of Fe, (b) photon flux density behind 25 cm of Fe [Kostal 2011].

Another interesting example is the series of transmission experiments performed in benchmark spherical iron assemblies with a ^{252}Cf source in the center (Figure 5.19) [Jansky 2002]. Here, a set of proportional counters were used for covering the neutron energy range between 10 keV and 1.3 MeV, while a set of stilbene crystals ($\varnothing 31.5 \text{ mm} \times 10 \text{ mm}$, $\varnothing 37.5 \text{ mm} \times 10 \text{ mm}$ and $\varnothing 40 \text{ mm} \times 40 \text{ mm}$) were used for neutron energies between 100 keV and 16 MeV. Lead filters (max 10 cm) were inserted where necessary for lowering the gamma-ray component.

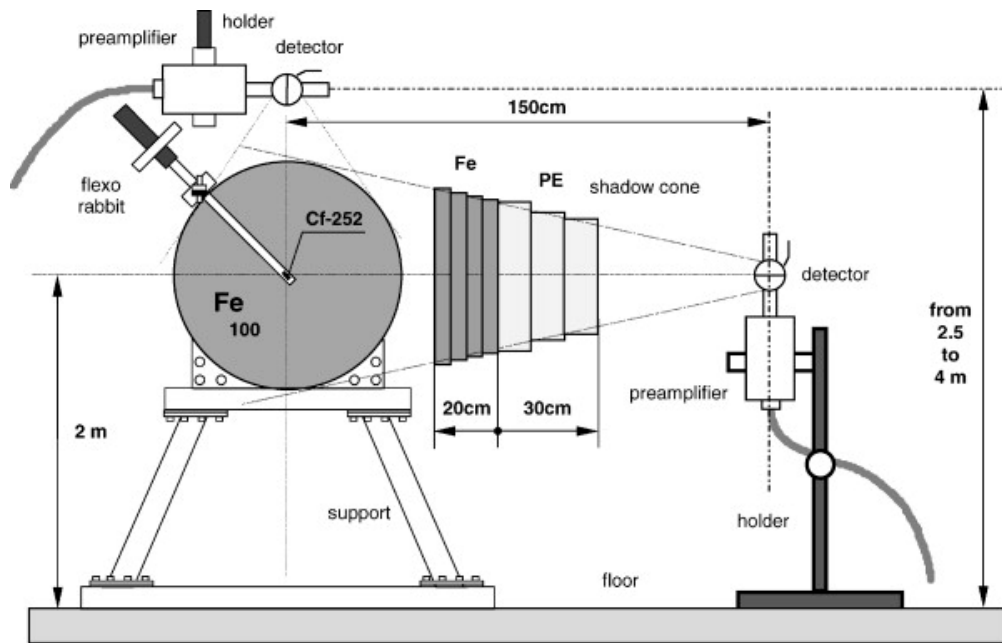


Figure 5.19. Scheme of measurement assembly [Jansky 2002].

This set-up is of particular interest, as it consists of overlapping neutron spectrum measurements performed with different types of detectors. In Figure 5.20a (top curve), it is possible to appreciate

the wide energy range covered by stilbene (“FEI”) and the overlapping measurement with proportional counters (“NRI”). The region in common is particularly extended, permitting a good normalization of the two spectra. This would not be possible with other types of organic scintillators and. Figure 5.20b shows the overall results of the experiment.

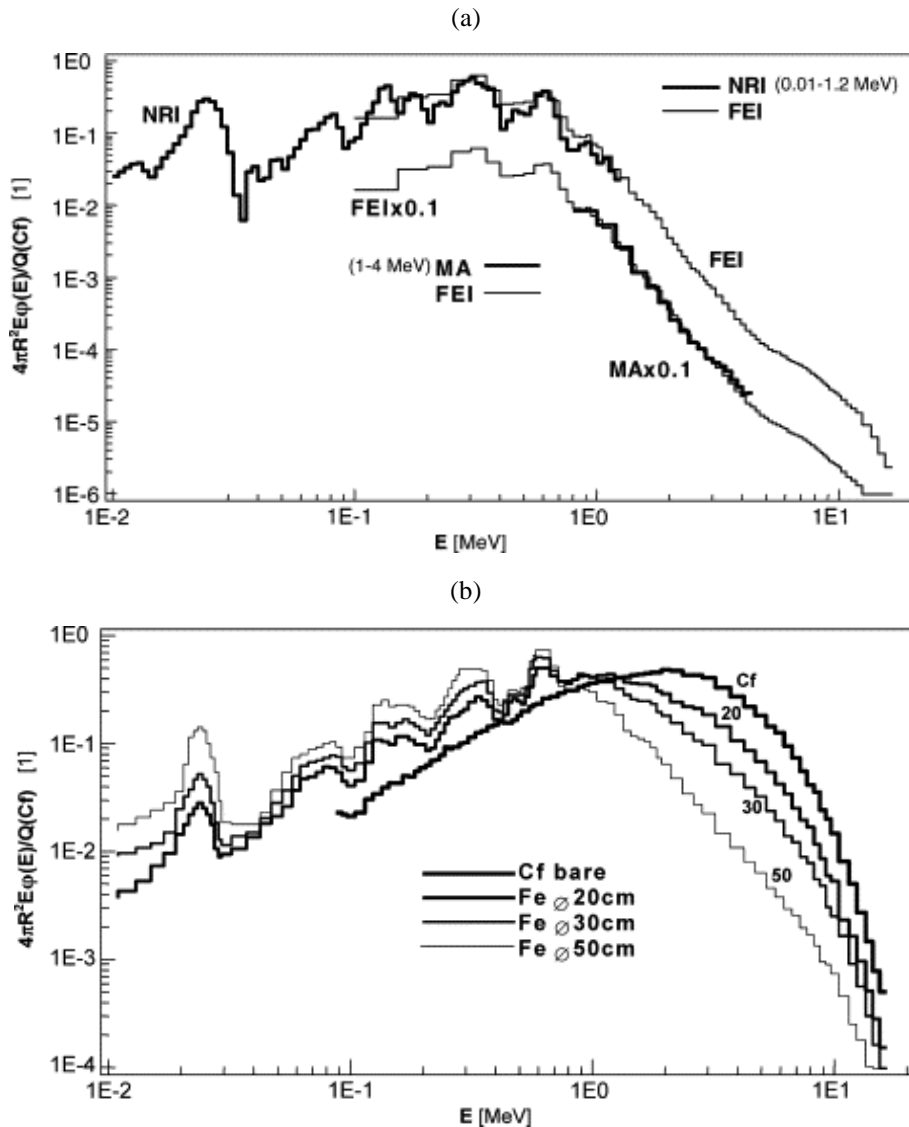


Figure 5.20. (a) Measured neutron spectrum with 100 cm iron sphere, (b) Leakage neutron spectra from iron spheres of different diameters [Jansky 2002].

5.3.2 Solution-grown Stilbene

The choice of stilbene is motivated not only by past successful reactor applications, but also by recent improvements made in stilbene crystal-growing techniques. A new solution-grown (s-g) stilbene has been recently reported [Zaitseva 2015], yielding a much more homogeneous crystal structure than that of traditional melt-grown (m-g) stilbene [Budakovsky 1990] and liquid

scintillators (EJ-309, BC501A, NE213, etc.). These new solution-grown crystals are expected to have significantly better performance.

Solution growth produces single stilbene crystals of the same crystallographic symmetry and basic physical properties than those produced with classical melt-grown techniques (same material $C_{14}H_{12}$ with same photoluminescence spectrum and melt point), but with a more homogenous structure (Figure 5.21). This leads to a better *LO* and pulse shape discrimination. For scintillators of the same sizes, 50 % higher *LO* and 30 - 40 % higher PSD FoM (at all energies) values have been reported. This means almost a doubled *LO* compared to liquid scintillators (EJ-309). The results are summarized in Figure 5.22. Furthermore, single stilbene crystals of fairly large dimensions (10 cm) can be grown with this technique, for high efficiency detectors.

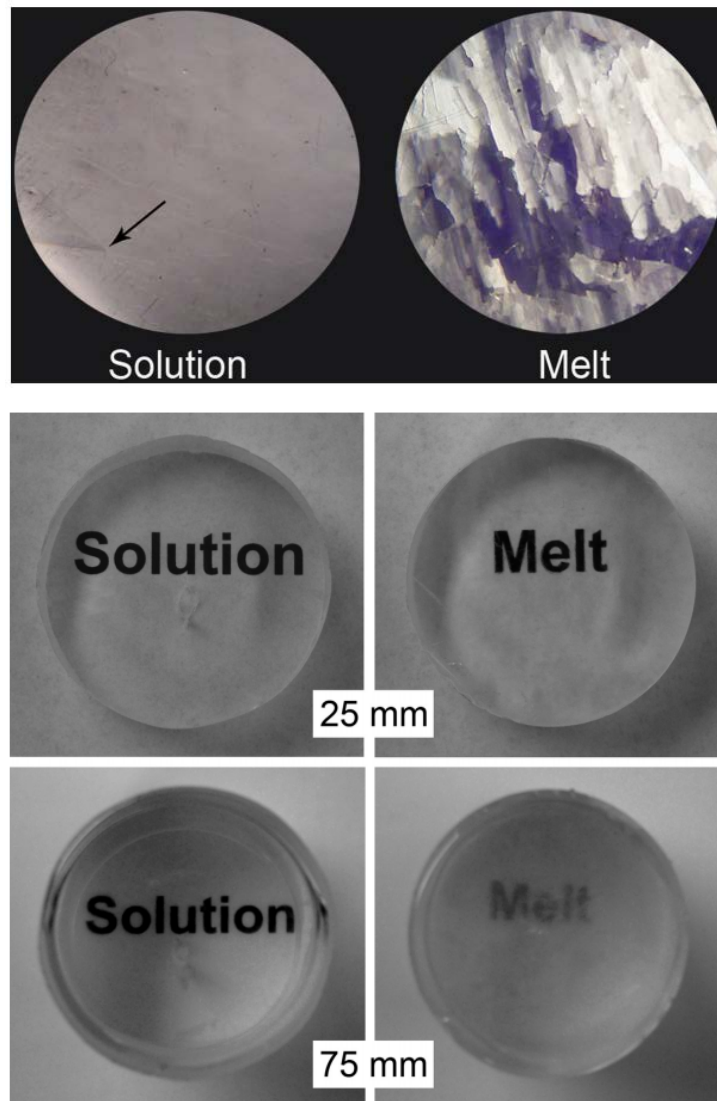


Figure 5.21. The more homogenous structure of solution-grown stilbene crystals [Zaitseva 2015].

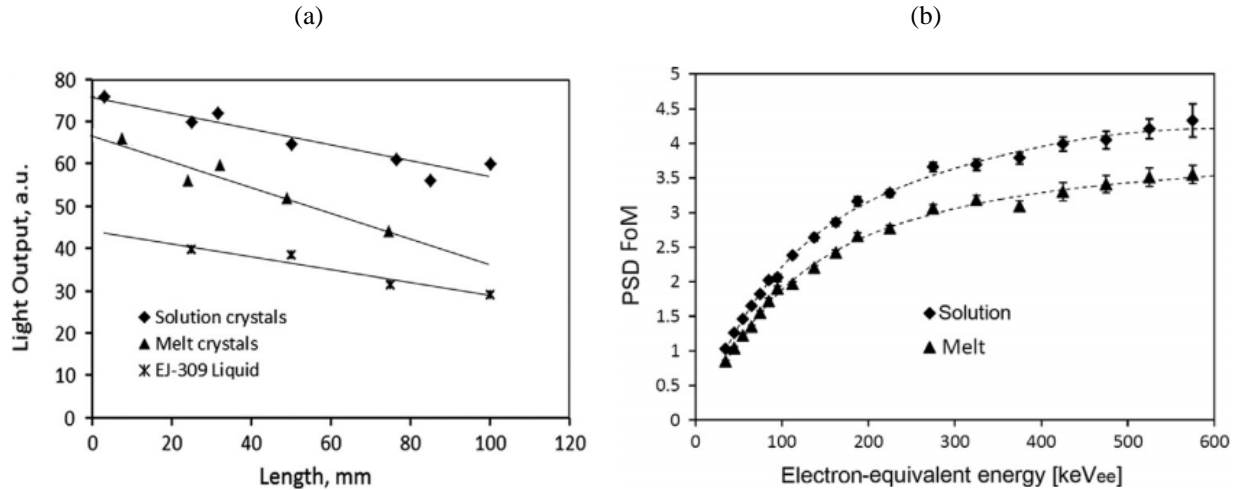


Figure 5.22. (a) Normalized measured scintillation LO and (b) Experimental dependences of PSD FoMs on electron-equivalent energy [Zaitseva 2015].

In light of the arguments developed in the preceding sections and chapters, the solution-grown stilbene was selected as the organic scintillator to be prototyped and tested as part of this PhD work. A 25.4 mm \times 25.4 mm ortho-cylindrical solution-grown stilbene crystal was ordered to Inrad Optics [Stilbene - Inradoptics], thanks to fundings provided by the SPECTRAL project. The crystal was mounted on a 9214B-series photomultiplier tube provided by ET Enterprise. The whole detector was assembled by SCIONIX: the stilbene was encapsulated in an aluminium canister and optically coupled to the photomultiplier, which was itself surrounded by a solid mu-metal shield. A picture and the drawings of the detector are shown in Figure 5.23 and Figure 5.24.



Figure 5.23. 25.4 mm \times 25.4 mm ortho-cylindrical solution-grown stilbene detector (plus PMT).

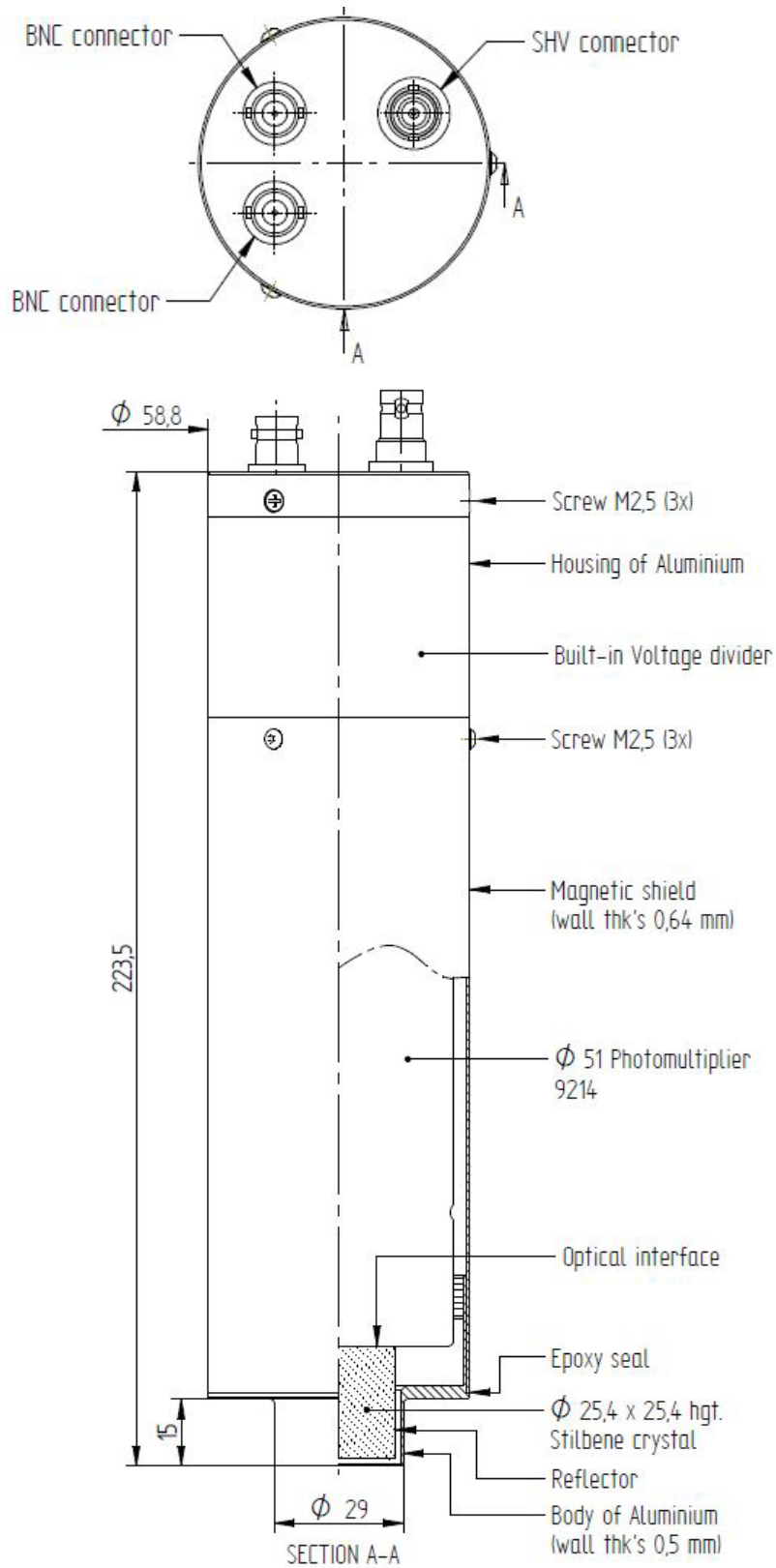


Figure 5.24. Solution-grown stilbene detector (assembled by SCIONIX).

5.4 Methodology for Simulating the Response of Organic Scintillators

Chapter VII will be devoted to the experimental evaluation of the prototype detector capabilities in different mixed neutron-gamma fields. For comparison and validation purpose, it was decided to develop a simulation capability of the scintillator response, as such capability did not exist (in the group). A Monte Carlo approach was adopted. The chosen code was MCNPX-PoliMi [Pozzi 2012], plus the associated post-processing software for detector response simulations, called MPPost [Miller 2012].

The MCNPX-PoliMi code is an extension of the standard MCNPX code and preserves its structure as much as possible. It runs with analog particle tracking, thus all particles have unit weight until they escape or are absorbed, making the interaction and detection processes simpler to model. The code output is a printout of all neutron and photon collisions that occurs inside the detector cells (specified by the user) with relevant information such as reaction type, target nucleus, energy deposited, time and position. An example of an MCNPX-PoliMi output is shown in Figure 5.25.

MPPost is a code that was developed to interpret the results produced by MCNPX-PoliMi and provide a simulated detector response. A flow diagram of the software is shown in Figure 5.26. The only needed inputs are the MCNPX-PoliMi collision file and the MPPost input. The code can simulate the response of organic scintillators, ^3He detectors, and of a few other common detector types. This was the main reason for choosing MCNPX-PoliMi rather than another code. An example of simulated response is shown in Figure 5.27, which compares measured and simulated 5 MeV mono-energetic neutrons using the solution-grown stilbene detector (see 7.1.1).

History number	Particle number	Particle type ^a	Interaction type ^b	Target nucleus ^c	Cell no. of collision event	Energy deposited in collision (MeV)	Time (shakes)	Collision position (x, y, z)			Generation number	Weight	Number scatterings	Code	Energy (MeV)
151	4	1	-99	6000	9	0.33893	0.944	-16.71	-1.73	3.92	0	1.000	0	0	1.61E+00
151	4	1	-99	1001	9	0.71283	1.158	-15.55	-4.66	2.84	0	1.000	1	0	1.27E+00
151	20	1	-99	1001	8	0.10313	1.464	13.4	3.95	-4.48	3	1.000	0	0	2.61E+00
151	20	1	-99	1001	8	1.20735	1.488	13.91	3.96	-4.51	3	1.000	1	0	2.50E+00
151	20	1	-99	1001	8	0.05711	1.493	13.98	3.9	-4.49	3	1.000	2	0	1.30E+00
151	20	1	-99	1001	8	0.6134	1.640	15.9	2.76	-4.28	3	1.000	3	0	1.24E+00
151	20	1	-99	1001	8	0.42279	1.756	16.49	2.15	-3.34	3	1.000	4	0	6.24E-01
151	20	1	-99	1001	8	0.07376	1.974	17.29	2.74	-2.42	3	1.000	5	0	2.01E-01
151	20	1	-99	1001	8	0.08552	2.297	17.55	2.64	-0.89	3	1.000	7	0	1.14E-01
164	23	1	-99	1001	9	0.22836	4.210	-18.07	-4.43	-3.21	1	1.000	3	10	2.84E-01
164	4	2	1	1	8	0.11409	0.193	14.87	4.73	-1.2	0	1.000	1	0	6.49E-01

^a1 = neutron; 2 = photon
^b-99 = elastic scattering; 1 = Compton scattering
^c1001 and 1 = hydrogen; 6000 = carbon

Figure 5.25. Example of the output produced by MCNPX-PoliMi [Pozzi 2003].

VI. Experiments

6.1 Tests of the Solution-grown Stilbene Detector

6.1.1 Electronics

6.2 Description of the Experiments

6.2.1 Measurements at AIFIRA

6.2.2 Measurements at LVR-15

6.2.3 Measurements at LR-0

Introduction

The first part of this chapter is a presentation of the experimental campaign dedicated to the solution-grown stilbene detector shown at the end of Chapter V, with a description of the associated electronic systems. The second part is fully devoted to the experiments themselves, and the installations in which they were performed (AIFIRA, LVR-15 and LR-0).

6.1 Tests of the Solution-grown Stilbene Detector

The scintillation detector built with a new solution-grown crystal stilbene is expected to have better performances compared with those of earlier detectors which used melt-grown stilbene. However, the latter have been extensively tested and used in a host of experiments (as shown in the previous chapter), validating its characteristics in terms of PSD and energy domain of application. For solution-grown stilbene, only limited experimental information is available in the literature. Mainly, the results come from measurements performed with gamma sources and ^{252}Cf [Zaitseva 2015, Bourne 2016]. Other interesting results are reported for different plutonium arrangements [Bourne 2017]. Only two mono-energetic neutron fields, coming from D-D and D-T reactions, have been characterized with this new type of crystal scintillator [Shuster & Brubaker 2017].

In this PhD work, a series of experiments intended to verify the expected properties and performance of the solution-grown stilbene detector is proposed. The detector was tested in three well-characterized neutron-gamma mixed fields with three different objectives:

- In mono-energetic neutron beams produced by an accelerator (AIFIRA), for evaluating the detector energy domain and overall performances compared to a well-known liquid scintillator (BC501A) [Dioni 2017 (2)];
- In a neutron beam at a research reactor (LVR-15), for assessing the detector use in out-of-core conditions;
- Inside a zero-power reactor (LR-0), for testing the detector in-core and near-core performance.

Before describing the experiments, the detector associated electronics will be briefly presented.

6.1.1 Electronics

Both analog and digital systems were tested. The analog system was provided by IRSN. It is the electronics normally employed with their liquid scintillator BC501A. The digital system was provided by the research center Rez. It is normally coupled with their set of melt-grown stilbene crystals.

A simplified diagram of the analog system is presented in Figure 6.1. The electronics is similar to the one described by [Klein 2003] without the use of the LED. The anode signal is used for pulse-shape analysis (in red), while the dynode signal is integrated by a preamplifier and processed in an amplifier with suitable pulse shaping for a proper pulse-height analysis (in green).

The second type of electronics is a digitalized two parametric system for neutron/gamma spectrometry [Veskrna 2014]. A diagram of the system is presented in Figure 6.2. The anode signal is split into two amplifiers with different amplifications for increasing the signal to noise ratio. The signals are then digitalized by separate Analog-to-Digital Converters (ADCs) and sent to a Field-Programmable Gate Array (FPGA) for data processing. The discrimination algorithm is based on the principle of charge comparison (CC). Typical signals from gamma and neutron events are shown in Figure 6.3, together with the CC method.

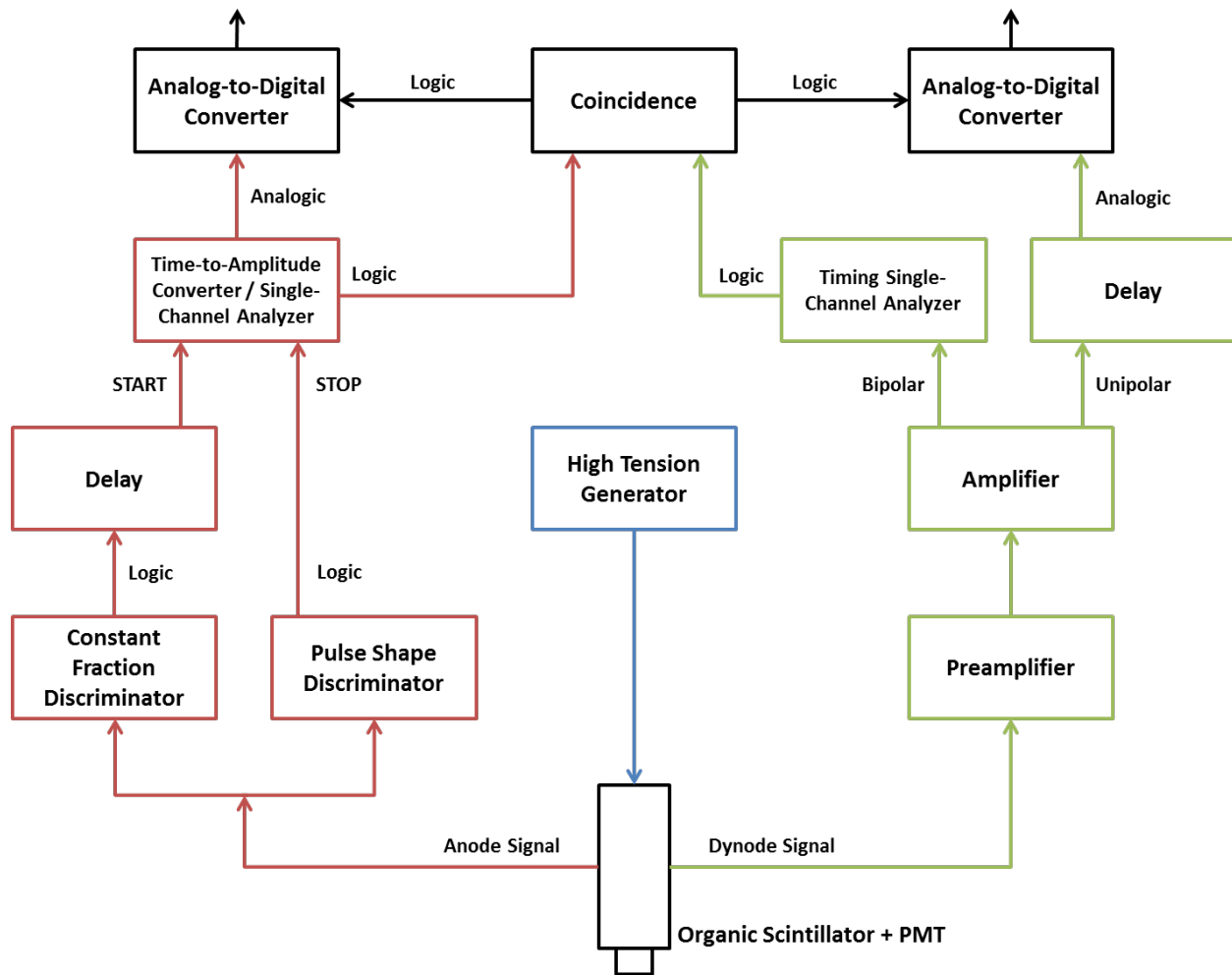


Figure 6.1. Diagram of the analog system.

Some of the advantages of digital systems are:

- Minimum number of components. The system is compact and easy to transport;
- Higher number of processed pulses per second. Digital system can reach count rates on the order of one million of pulses per second (analog systems are limited to some thousands of pulses per second)
- Etc.

Digital electronic systems are particularly useful for in-core and near-core reactor applications, where high neutron fluxes are expected.

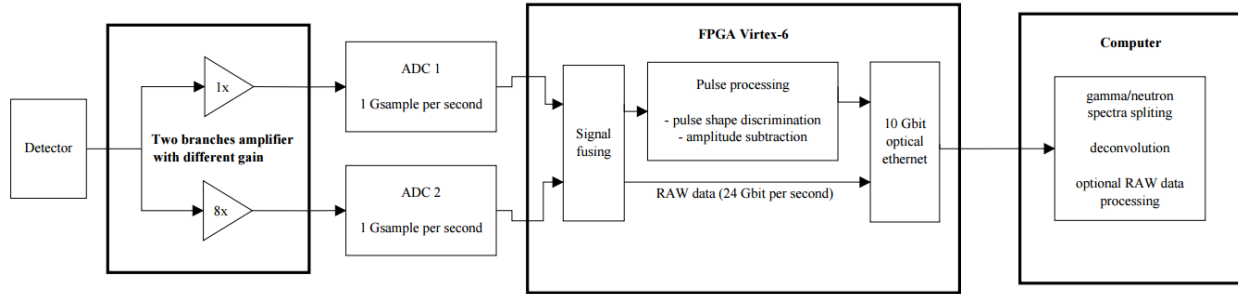


Figure 6.2. Scheme of the two parametric digital spectrometer [Veskrna 2014].

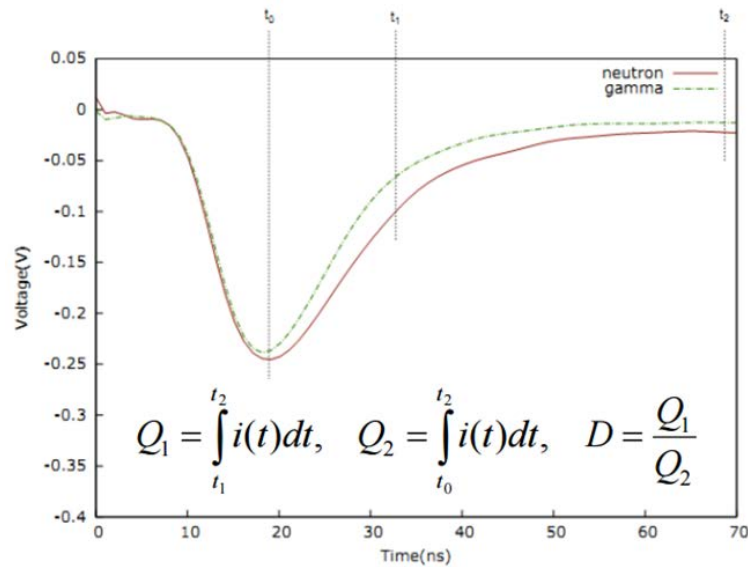


Figure 6.3. Framework layout of parameters of integration method [Veskrna 2014].

6.2 Description of the Experiments

6.2.1 Measurements at AIFIRA

THE FACILITY

The AIFIRA accelerator (Figure 6.4) is a 3.5 MV Singleton from HVEE Company situated at CENBG near Bordeaux [Sorieu 2014]. $^1\text{H}^+$, $^2\text{H}^+$ and $^4\text{He}^+$ ion beams can be produced with intensities ranging from a few hundred nA up to 80 μA . A switching magnet connects the primary beamline to five secondary beamlines. The “physics beamline”, devoted to the external beam, is the one placed at the -45° port of the switching magnet. Different target materials can be placed at

the end of the physics beamline for producing steady-state mono-energetic neutron beams ranging from 2 keV up to 6 MeV.

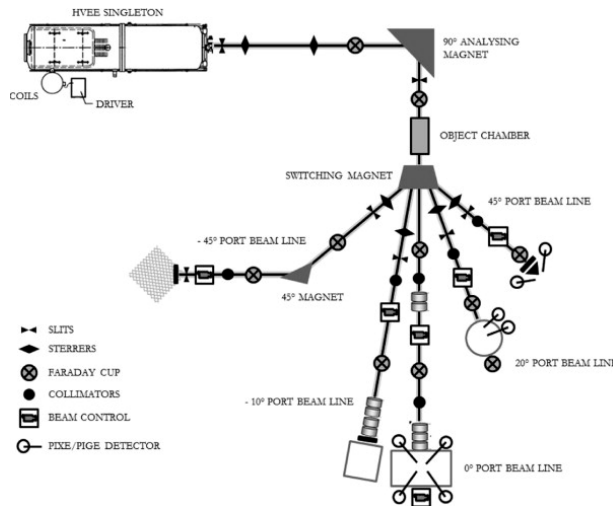


Figure 6.4. The AIFIRA facility [Sorieuil 2014].

DESCRIPTION OF THE EXPERIMENT

The AIFIRA facility was used for delivering two mono-energetic neutron fields of 565 keV and 5 MeV. The two neutron fields were produced with a 2295 keV proton beam and a 1791 keV deuteron beam of about $1 \mu\text{A}$ sent onto a $45 \mu\text{g}/\text{cm}^2$ thick LIF target and a $200 \mu\text{g}/\text{cm}^2$ thick TiD target, respectively.

The goal of the experiment at 5 MeV is the comparison of the performances of the $\varnothing 2.54 \text{ mm} \times 2.54 \text{ cm}$ solution-grown stilbene detector with a well-known $\varnothing 50.8 \text{ cm} \times 5.08 \text{ cm}$ BC501A spectrometer for confirming the published data. The liquid scintillator was provided by IRSN and is a secondary standard instrument for characterizing the neutron fields at the AMANDE facility in Cadarache. The analysis took into account PSD FoM, PHS and anisotropy of the response.

The goal of the measurement at 565 keV is to verify the lower energy capabilities of the s-g stilbene, as no information was found in the literature for this new crystal. As the BC501A was not able to measure this neutron field, a spherical proportional counter (also provided by IRSN) with 3 atm of pure H_2 [Pichenot 2002] was used as a reference.

An ^3He gas filled detector with a polyethylene layer (a kind of long counter) was used as a monitor for all the irradiations.

The experimental set-up is presented in Figure 6.5. The detectors were placed at $21.1 \pm 0.1 \text{ cm}$ from the target. For quantifying the anisotropy of the response, the two organic scintillators were irradiated at different orientations: 0° , 90° and -90° with respect to the accelerator ion beam direction. The photomultiplier high voltage was set to 930 V (manufacturer's value) and 1230 V, for the measurements at 5 MeV and 565 keV, respectively.

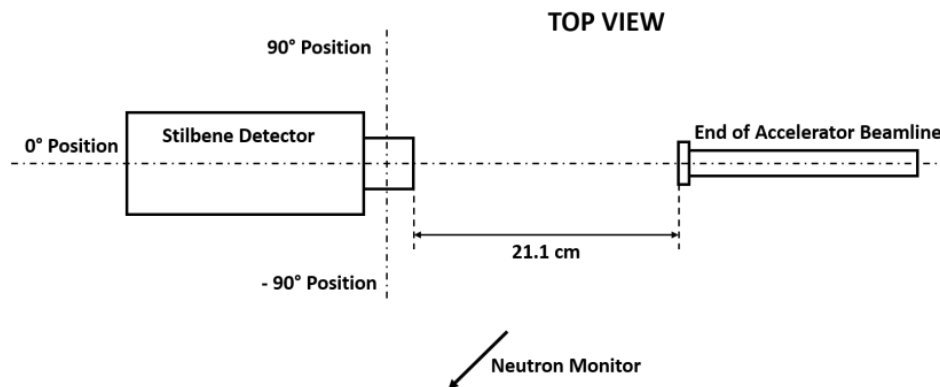


Figure 6.5. Experimental set-up at the AIFIRA facility.

The gamma calibration of the two organic scintillators was performed with ^{137}Cs , ^{22}Na and ^{207}Bi gamma-ray reference sources. The linearity between the channel number and the electron equivalent energy was verified at each variation of the electronics set-up (mainly related to the gain). Time thresholds for PSD were fixed with the help of a ^{252}Cf source.

Some photos of the AIFIRA experience are shown in Figure 6.6.

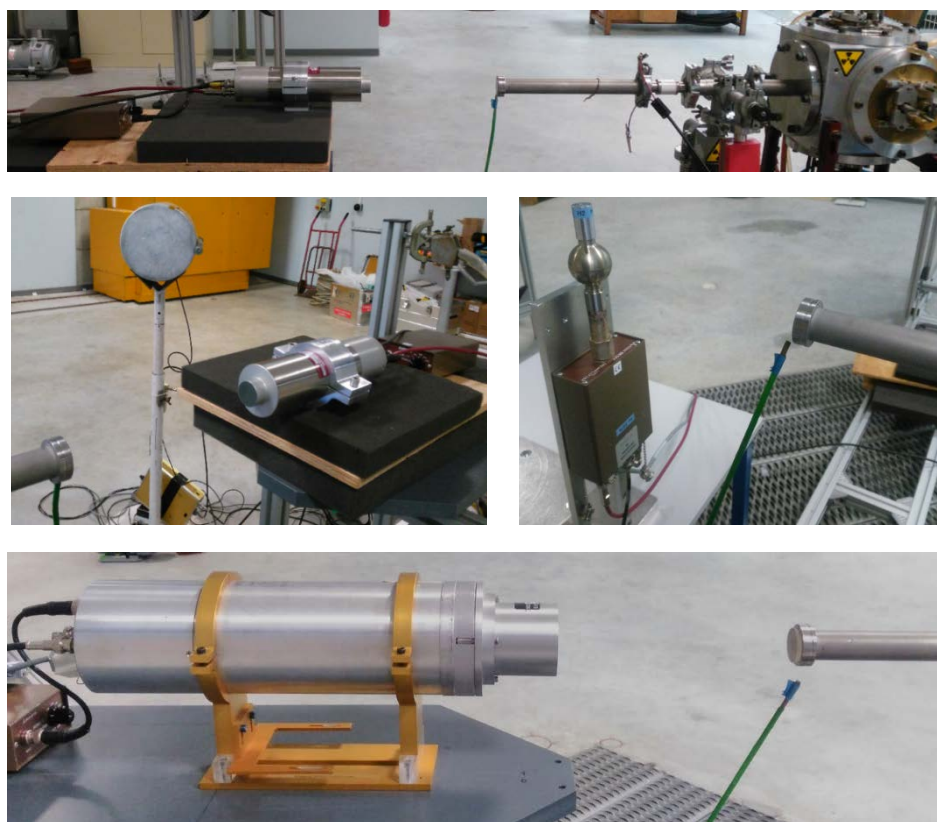


Figure 6.6. Photos of the AIFIRA experiments with stilbene, spherical proportional counter and BC501A.

6.2.2 Measurements at LVR-15

THE FACILITY

LVR-15 is a light water, pool type reactor operated at 10 MW of thermal power (Figure 6.7) located at the nuclear research center Rez. It is a multi-purpose facility, working as a neutron source for several research and commercial activities [Koleska 2015]. The reactor is equipped with nine horizontal channels capable of providing different neutron beams (Figure 6.7) for additional applications.

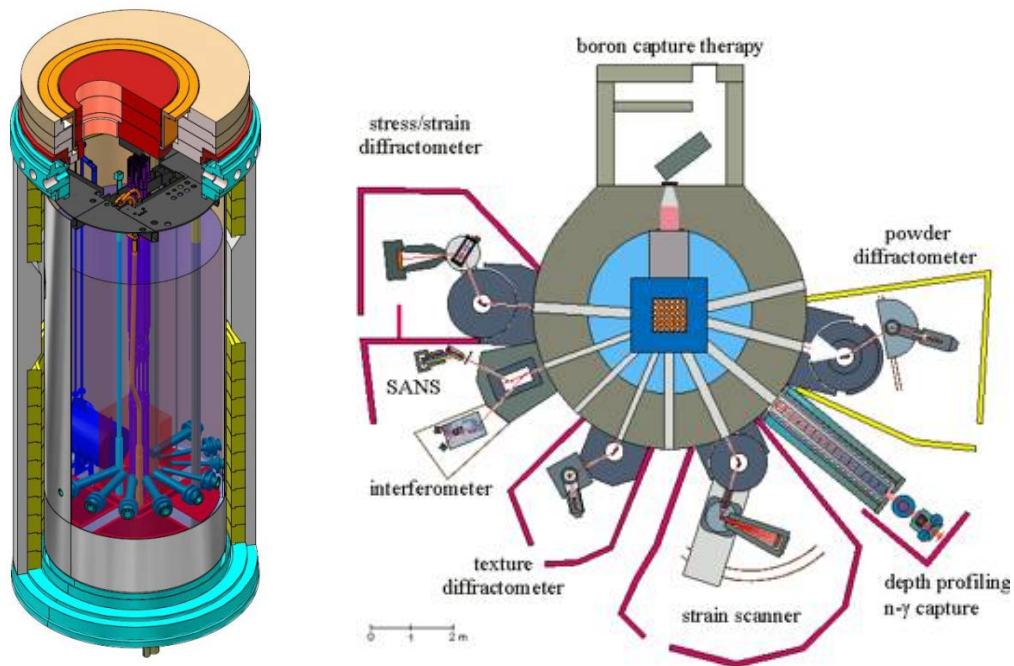


Figure 6.7. The LVR-15 research reactor.

The main characteristics of the reactor are listed in Table 6.1. Researches at LVR-15 are in the following areas:

- Material research (e.g. irradiation of reactor pressure vessel materials);
- Corrosion tests of primary circuit and internal structural materials of nuclear power plants in experimental loops and probes;
- Water chemistry experiments for nuclear power plant primary circuits;
- Neutron activation analysis (used to determine materials composition);
- Development and production of new radiopharmaceuticals (^{153}Sm , ^{161}Tb , ^{165}Dy , ^{166}Ho , ^{169}Er , ^{60}Co , ^{192}Ir , ^{182}Ta , ^{198}Au);
- Production of silicon through neutron doping for the electronic industry;
- Irradiation services (production of radioisotopes: ^{99}Mo - $^{99\text{m}}\text{Tc}$, ^{113}Sn - $^{113\text{m}}\text{In}$, ^{188}W - ^{188}Re);
- Scientific research on material basics properties (neutron physics and solid state physics);
- Neutron capture therapy (irradiation of patients with glioblastoma-type brain tumors).

Table 6.1. Features of the LVR-15 research reactor.

Reactor Vessel	Diameter	2300 mm
	Height	5760 mm
	Wall Thickness	15 mm
	Bottom Thickness	20 mm
	Water Volume in the Vessel	22 m ³
	Weight (without water)	7900 kg
Operation Parameters	Max Thermal Power	10 MW
	Max Neutron Flux (Thermal)	10 ¹⁴ neutrons cm ⁻² s ⁻¹
	Pressure	Atmospheric
	Temperature	Max 56°C
Fuel	Type	IRT-4M – tube sandwich
	Active Length	600 mm
	Cladding	Al
	Fuel Core	UO ₂ + Al
	Enrichment	19.75 % ²³⁵ U
Power Control	12 Control Rods, 3 Groups	Compensation (8) Safety (3) Automatic regulator (1)
	Absorber	B ₄ C

The available neutrons beams are mainly used for:

- Neutron measurement of structures and textures at room and liquid-helium temperatures;
- Deep neutron profiling and study of immediate gamma radiation from neutron radiation capture;
- Neutron optics and neutron topography;
- Measuring textures in semi-crystalline metal materials;

- Study of structural in-homogeneities using the diffraction and the small-angle neutron scattering methods;
- Neutron interferometry;
- Study of local tension in polycrystalline materials.

DESCRIPTION OF THE EXPERIMENT

The silicon filtered neutron beam delivered by one of the experimental channels of LVR-15 is used for testing the solution-grown stilbene in an extended neutron spectrum having special distinctive features.

Indeed, the LRV-15 experimental channel previously devoted to neutron radiography is capable of providing a highly-attenuated silicon filtered neutron beam. The fast neutron fraction after one meter of pure silicon (about 4 meters away from the core) is on the order of 10^4 neutrons $\text{cm}^{-2} \text{s}^{-1}$, with a total flux (fast neutron plus gamma) on the order of 10^5 # $\text{cm}^{-2} \text{s}^{-1}$. The strong thermal flux), which decreases the (fast) neutron-to-gamma ratio in the mixed field (radiative captures), is cut down with more filters (made of ^6Li and $^{\text{nat}}\text{Cd}$). The gamma flux is further attenuated with lead and bismuth filters (12 cm of Bi plus 15 cm of Pb).

These experimental conditions are interesting to test the response of the s-g crystal detector (PMT included). The silicon filtered spectrum is characterized by different peaks in the MeV region, which permit to evaluate the influence of the anisotropy simply by looking at the displacement of the edges in the recoil proton spectra, or directly in the unfolded neutron spectra. Moreover, the digital system used for the measurements was particularly easy to operate. Several tests with applied voltages varied from about 900 V up to 1200 V were done for studying the influence of the electron multiplication in the PMT on the linearity of the response. Higher voltages permit to have higher multiplication which lead to higher intensity signals. This permits to detect the weak signals produced by lower energies neutrons (from 500 keV to 1 MeV). It is thus possible, with the use of a single detector, to perform multiple measurements with different high voltages applied to the PMT, and later reconstruct a broad energy spectrum.

Future developments foresee a comparison, under the same conditions, with melt-grown stilbene crystals.

The set-up of the experiment is shown in Figure 6.8. The responses coming from different orientations with respect to the LVR-15 beam axis have been registered, namely at 0° , 30° , 45° , 60° and 90° . A list of the various tests is given in Table 6.2.

Table 6.2. Measurements performed at LVR-15 neutron beam (silicon filtered).

	0 degrees	30 degrees	45 degrees	60 degrees	90 degrees
900 V	×				×
930 V	×	×	×	×	×
1000 V	×				×
1100 V	×				×

Gamma calibration was performed on-line with ^{137}Cs and ^{60}Co sources at each measurement. The PHS spectra produced by gamma-rays always exhibited the three edges due to the calibration sources (one from ^{137}Cs and two ^{60}Co). It was systematically possible to find the Compton edges by means of the derivative approach.

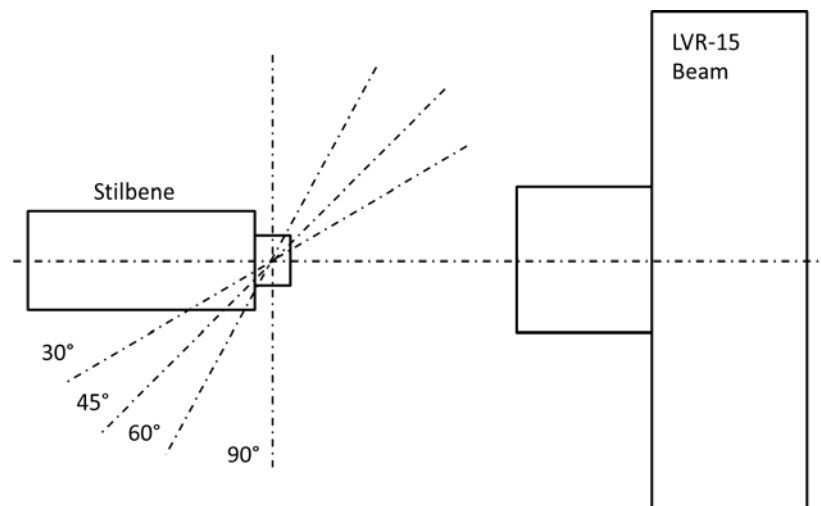


Figure 6.8. Experimental set up at the LVR-15 research reactor.

6.2.3 Measurements at LR-0

THE FACILITY

The LR-0 research reactor (Figure 6.9) is a light-water, zero-power, pool-type reactor located next to the LVR-15 facility. It serves as an experimental reactor for measuring neutron-physical characteristics of VVER (Water-Water Energetic Reactor) type reactors.

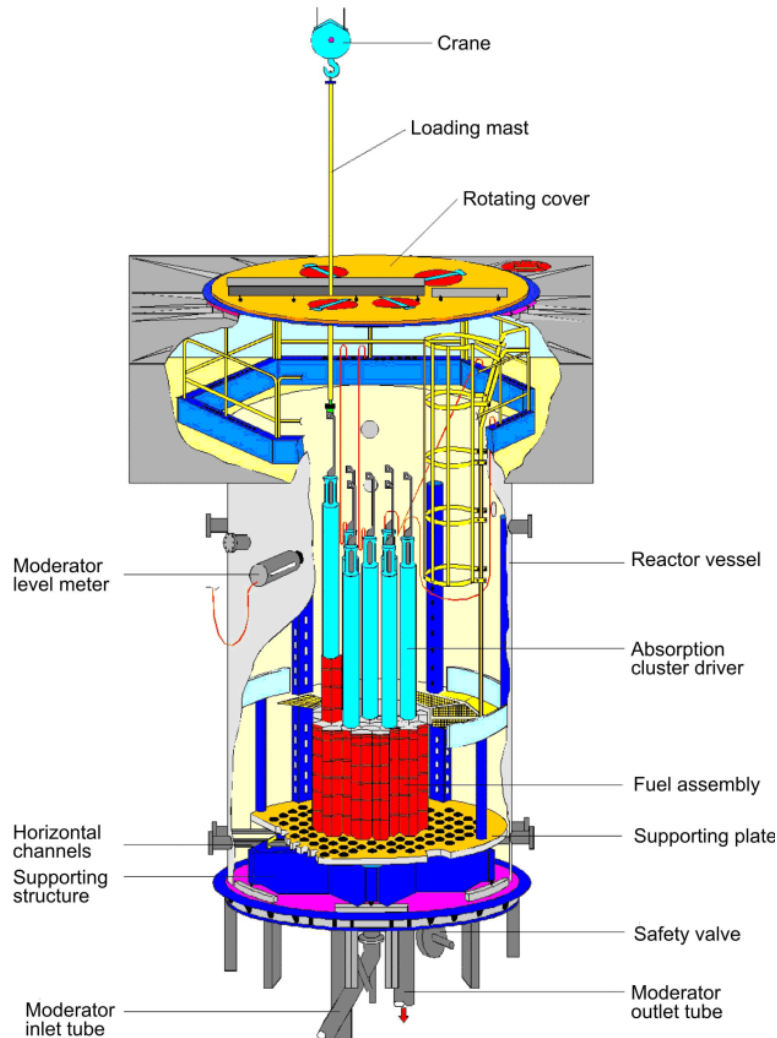


Figure 6.9. LR-0 scheme.

The principle features of the LR-0 reactor are reported in Table 6.3. The main LR-0 activities are in the following areas:

- Measurement of neutron flux distribution in pins and fuel assemblies with and without control clusters - radial and axial fission density distribution;
- Spent fuel storage - experimental verification of nuclear safety in relation to proposed geometry and various absorbing materials;
- Models of VVER-440 and VVER-1000 fuel assemblies - measurement of neutron flux distribution from the perspective of biological shielding and other dosimetry purposes;

- Space-time kinetics for assembly of benchmark data and codes;
- Neutron-physics reactor parameter research and verification - integral and differential efficiency of control and emergency clusters, critical water surface level, surface reactivity coefficient;
- Experiments with new fuel assemblies - influence of new profiled fuel assemblies and grid materials on flux density distribution;
- Influence of control assembly in VVER-400 zones - measurement of the neutron flux distribution in fuel with a partially inserted control assembly;
- Study of burnable Gd and CrB₂ absorbers - measurement of output distribution during operation with these absorbers;
- Measurement of neutron flux distributions in elements with molten salts for the SPHINX program as part of an EURATOM project.

Table 6.3. Characteristics of the LR-0 research reactor.

Reactor Vessel	Diameter	3.5 m
	Height	6.5 m
Operating Conditions	Maximum Output	1 kW
	Maximal Output (1 hour)	5 kW
	Maximum Thermal Flux	10^{13} neutrons $\text{cm}^{-2} \text{s}^{-1}$
	Pressure	Atmospheric
	Temperature	Room or up to 70°C
Fuel	Fuel Assembly Type	VVER-1000 or VVER-440
	FA Active Length	1250 mm
	FA Sheathing	pr. 9.15x tl. 0.72 mm ZrNb
	Tablets (Fuel Cell Contents)	UO ₂
	Enrichment	1.6 - 4.4 % ²³⁵ U
Power Control	Control Method	Moderator level, boric acid
	H ₃ BO ₃ in Moderator	0 -12 g/kg
	Absorption Clusters	B ₄ C Tablets
	Shielding	A concrete bunker, cadmium sheet metal, mobile platforms and a gate

DESCRIPTION OF THE EXPERIMENT

Neutron spectra were measured with the s-g stilbene detector in three positions inside the LR-0 research reactor.

The reactor arrangement is the VVER-1000 transport Mock-Up core [Kostal 2016], which consists of a full scale radial VVER-1000 segment (Figure 6.10), extending from the core to the biological shielding (included) of the reactor. The simulated reactor elements (core, baffle and barrel) are located inside the LR-0 tank, while the pressure vessel and biological shielding mock-ups are

outside the tank (not taken into account in this experiment). The fuel assemblies are shorter than the ones of an actual VVER NPP (about 1/3). They contain different ^{235}U enrichments, as specified in Figure 6.10. The active length is 125 cm. Axial measurement channels are made of stainless steel having a minimum inner diameter of 6.3 cm. The measurements were realized at atmospheric pressure and room temperature. The reactor was operated at a few Watts for the whole experiment and the fast neutron flux was on the order of 10^5 - 10^6 neutrons $\text{cm}^{-2} \text{s}^{-1}$.

The goal of the measurements is to test the detector performance in a ZPR environment, for in-core and near-core neutron/gamma spectrum characterization. The LR-0 was particularly suitable for this purpose, having sufficiently large experimental channels to place the detector (which has an outer radius of about 6 cm) in different radial positions. Three positions were tested (Figure 6.10 and Figure 6.11). The first, called B0, corresponds to the center of the LR-0 core (but not of the experimental configuration) and is representative of the fast neutron flux in the core active zone. The second, B1, is in the core baffle, in conditions representative of the transmitted neutron flux along the whole (radial) core. The third, B2, is past the core barrel, and is representative of a transmission-like experiment behind different core constituents (moderator, baffle and barrel). The axial positions of the detector were kept constant for the three measurements.

As for the measurements performed at LVR-15, different high voltages were applied to the PMT (Table 6.4) and the on-line gamma calibration was performed with ^{137}Cs and ^{60}Co gamma sources. It is worth noticing that, in this case, it was more difficult to individuate the peaks of the calibration sources, but it was still feasible. This was due to the lower neutron-to-gamma ratio inside the research reactor which slightly hides the calibration Compton edges.

Table 6.4. Measurements performed at LR-0.

	B0	B1	B2
930 V	×	×	×
1000 V	×	×	×
1100 V		×	×
1200 V		×	×



Figure 6.10. Photo of the radial section of VVER-1000 transport Mock-Up at LR-0 [Kostal 2016].

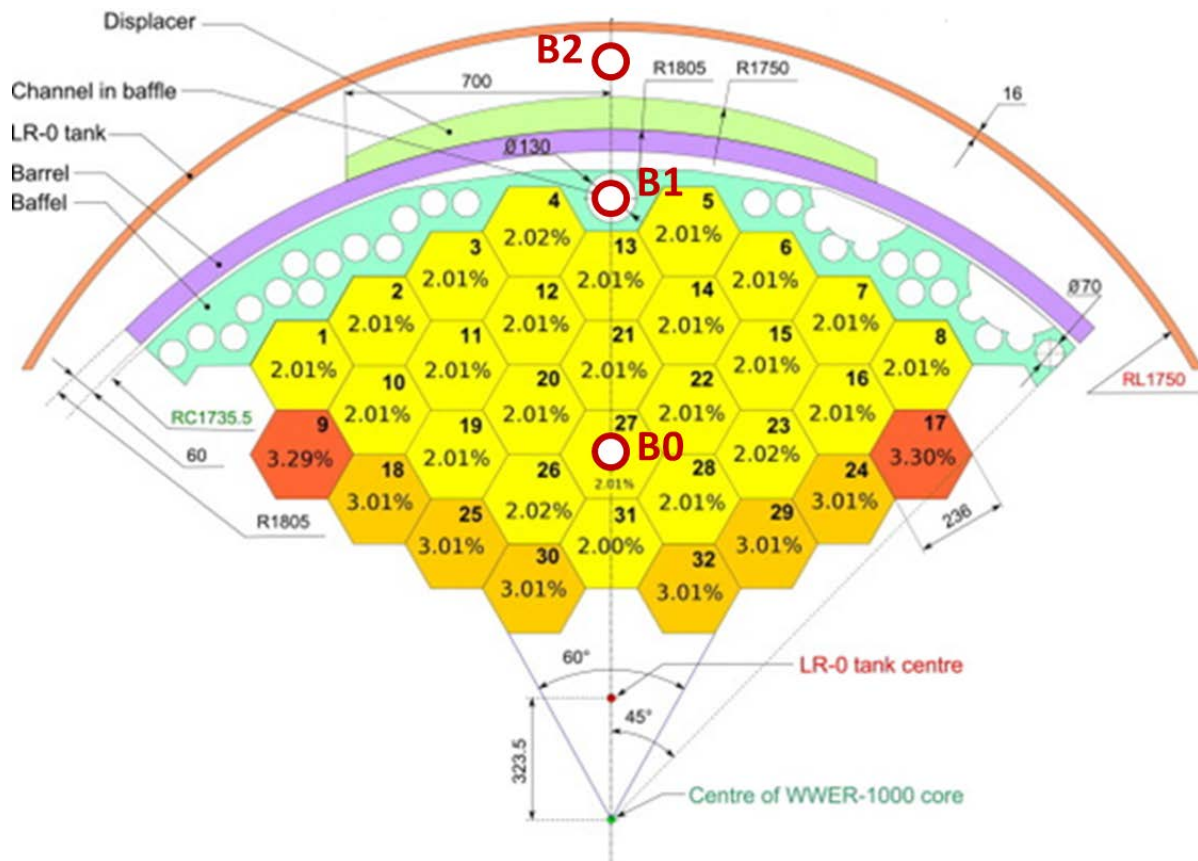


Figure 6.11. Measurements points.

VII. Results & Discussion/Difficulties

- 7.1 The Mono-energetic Neutron Fields of the AIFIRA Facility
 - 7.1.1 Measurements at 5 MeV
 - 7.1.2 Measurements at 565 keV
- 7.2 The Si-filtered Extended Neutron Beam Delivered by LVR-15
 - 7.2.1 Effects of the Applied High Voltage
 - 7.2.2 Measurements at Different Orientations
 - 7.2.3 Simulation of the Detector Response
- 7.3 Neutron Spectra Measurements at the ZPR LR-0
 - 7.3.1 B0
 - 7.3.2 B1 & B2
- 7.4 Discussion/Difficulties
 - 7.4.1 Anisotropy
 - 7.4.2 Simulation

Introduction

The experimental results obtained at the AIFIRA accelerator, at the irradiation reactor LVR-15 and at the ZPR LR-0 are discussed in detail in this chapter. Comparison with simulations are presented. The last part is a discussion of the outcome of the experimental campaign.

7.1 The Mono-energetic Neutron Fields of the AIFIRA Facility

Hereafter are presented the results of the measurements performed at the AIFIRA facility (April 2017).

7.1.1 Measurements at 5 MeV

The measurements at 5 MeV were done with the $\varnothing 25 \text{ mm} \times 25 \text{ mm}$ s-g stilbene detector and with a $\varnothing 50 \text{ mm} \times 50 \text{ mm}$ BC501A (provided by IRSN with a known response matrix). The same electronics (analog), discussed in the previous chapter, were used for both organic scintillators. The comparison between the two detectors takes into account PSD patterns, FoMs, and response anisotropy.

GAMMA CALIBRATION

The gamma calibration has been performed with ^{137}Cs , ^{22}Na and ^{207}Bi . The results of the measurements plus calibration for the ^{137}Cs and ^{22}Na are presented in Figure 7.1a and 7.1b respectively. The dependence between the channel number (X) and the electron equivalent energy (Y in MeV_{ee}) is linear, as shown in Figure 7.1c:

$$Y [\text{MeV}_{ee}] = a \cdot X [\#] + b \quad . \quad (7.1)$$

As already mentioned in Chapter V, no anisotropy was found for gamma-rays and the same calibration is used for the measurements at 0° , 90° and -90° .

PULSE SHAPE DISCRIMINATION

The experimental PSD patterns for stilbene and BC501A at 0° are shown in Figure 7.2. The greater separation between the neutron events (at the top of the PSD chart) and the gamma-ray events (at the bottom of the PSD chart) of Figure 7.2a, suggests a better discrimination capability of stilbene compared to that of BC501A (Figure 7.2b). This is confirmed by the FoMs, which result to be 1.89 for the s-g stilbene and 1.40 for the BC501A. The s-g stilbene has a 35% higher FoM than BC501A.

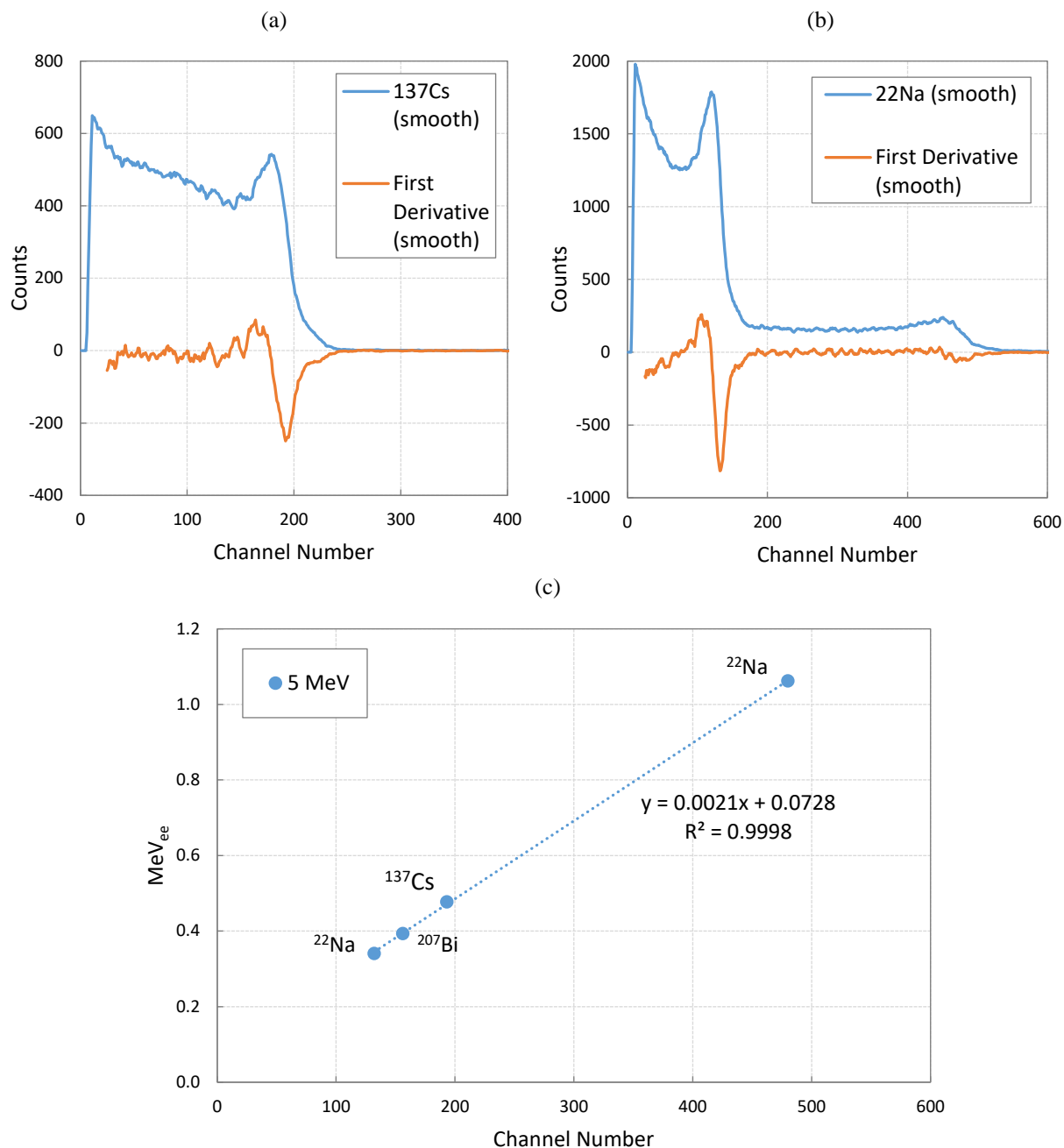


Figure 7.1. Gamma calibration with (a) ^{137}Cs and (b) ^{22}Na . (c) Linearity of the gamma-ray calibration (930 V).

The PSD profile is also used for separating neutron from gamma events. This is necessary in order to obtain a proper proton recoil spectrum. The net separation between the two types of events makes the separation quite simple for stilbene (also for BC501A, but it is more difficult at lower energies). After subtracting the gamma-ray contribution from the total PHS (sum of the two), it is possible to proceed with the analysis of the neutron PHSs.

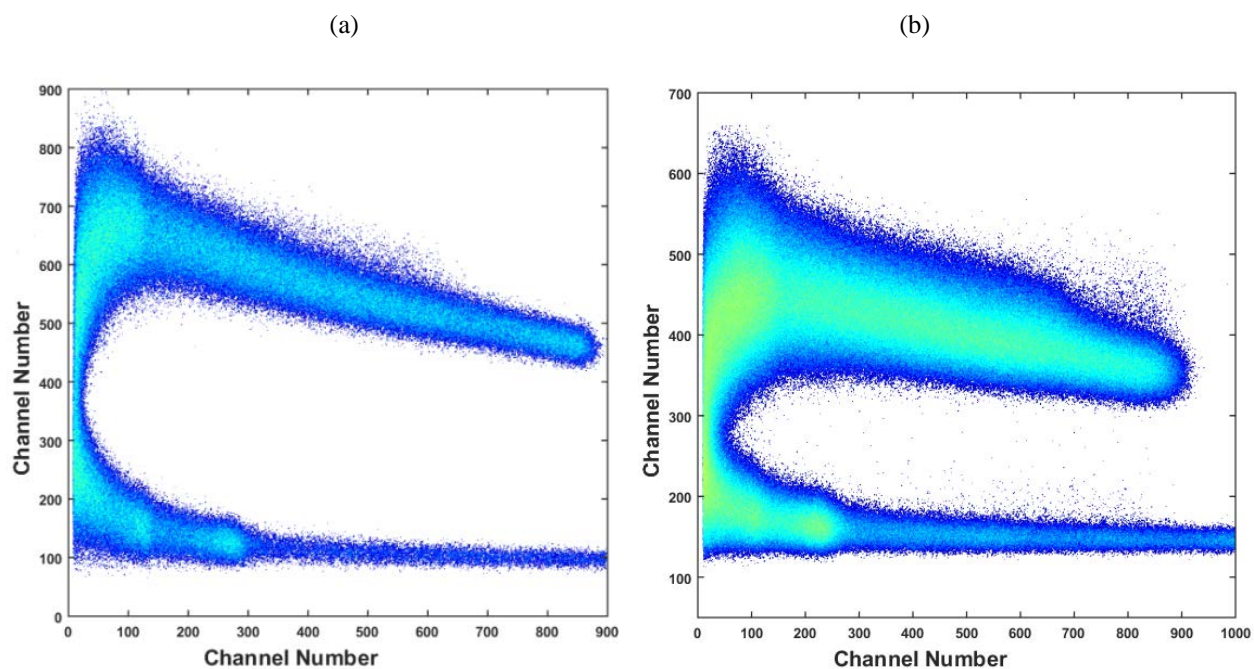


Figure 7.2. Experimental PSD profile of (a) s-g stilbene and (b) BC501A irradiated with 5 MeV neutrons (plus gamma-rays background) at 0° .

PULSE HEIGHT SPECTRUM AND ANISOTROPY

The obtained PHSs of s-g stilbene (with gamma calibration) are presented in Figure 7.3a. These PHSs differ slightly from the expected ones, as they show a bump around the electron-equivalent energy 1.2 MeV_{ee} . This is confirmed by the measurements performed with the BC501A, which presents the same bump (around channel 600, Figure 7.3b). The unfolding of the liquid scintillator PHS clearly shows a secondary peak in the neutron energy near 4 MeV (Figure 7.5b). This secondary peak comes either from neutron scattering (no subtraction using shadow cones has been performed), or - most probably - from deuterium diffusion in an intermediate layer between target backing and reactive layer, as previously observed in a TiT target at the AMANDE facility [Gressier 2013].

The anisotropy of the response of s-g stilbene can be seen in Figure 7.3a. By using the first derivative method for neutron calibration purpose, the 5 MeV proton edge is found for the three PHSs and is reported in Table 7.1. The anisotropy leads to differences on the order of 14 to 15 %, in agreement with results reported by other authors at different energies [Cvachovec 2002, Schuster & Brubaker 2017]. The BC501A shows no anisotropy (Figure 7.3b).

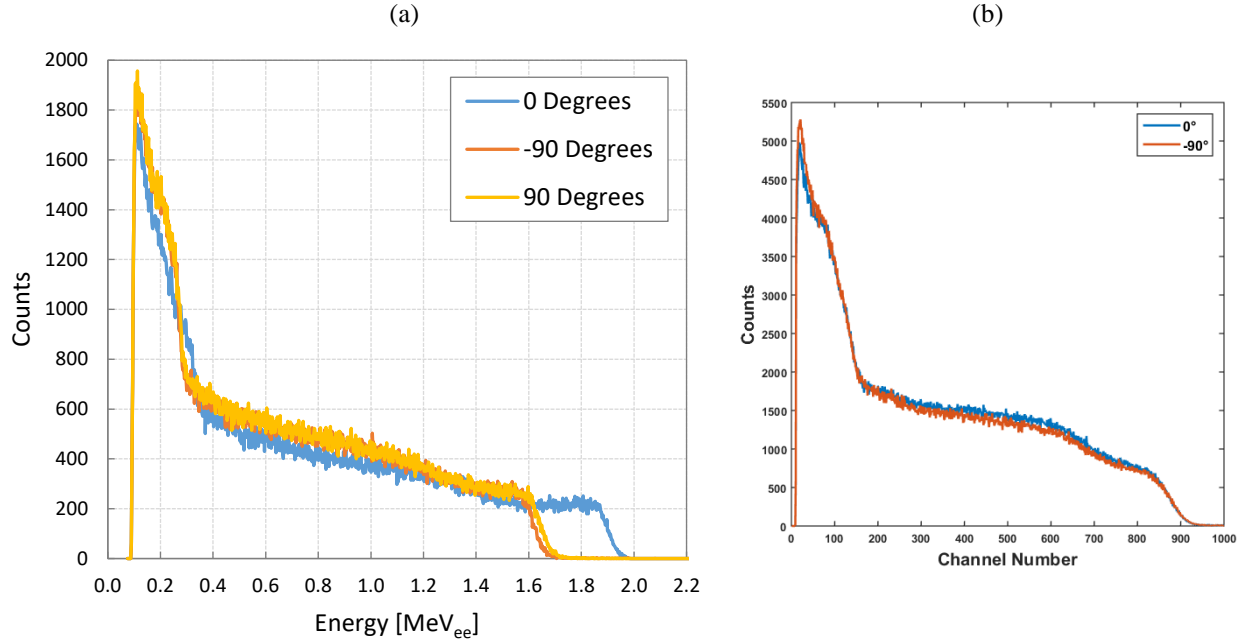


Figure 7.3. (a) Stilbene 5 MeV PHS after gamma calibration at 0°, 90° and -90° and (b) BC501A 5 MeV PHS at 0° and -90°.

Table 7.1. Neutron calibration using the first derivative method.

	0 Degrees	-90 Degrees	90 Degrees
MeV	5	5	5
MeV _{ee}	1.90	1.63	1.65
Channel	870	742	751

As mentioned in chapter V, the conversion from gamma-equivalent energy to neutron-equivalent energy requires the so-called LO-to-energy curve (measured experimentally). In this case, only the 5 MeV point is found, therefore it is not possible to construct the whole neutron energy scale. A possibility is to use the LO-to-energy curve measured by other groups with similar detector, just for comparison purpose. The LO-to-energy curve showed in Figure 5.11b [Kostal 2017 (private)] is the one employed in Rez for a melt-grown stilbene crystal of dimensions $\varnothing 20 \text{ mm} \times 20 \text{ mm}$ and it has been chosen for the conversion. The results are shown in Figure 7.4, where it is possible to appreciate that the measurements performed with the detector orientated perpendicular to the beam axis (90°) are in good agreement with the $\varnothing 20 \text{ mm}$ m-g stilbene LO-to-energy relationship used at Rez. This means that the s-g stilbene detector of this work is orientated in a different manner (shifted by 90 degrees) compared to the m-g one of Rez [Kostal 2017 (private)] (their response matrix was measured parallel to the beam axis).

Since the results are satisfying (for 90 and -90 degrees), the Rez response matrix (associated to the tested LO-to-energy relationship) is used in the following for unfolding the proton recoil spectra.

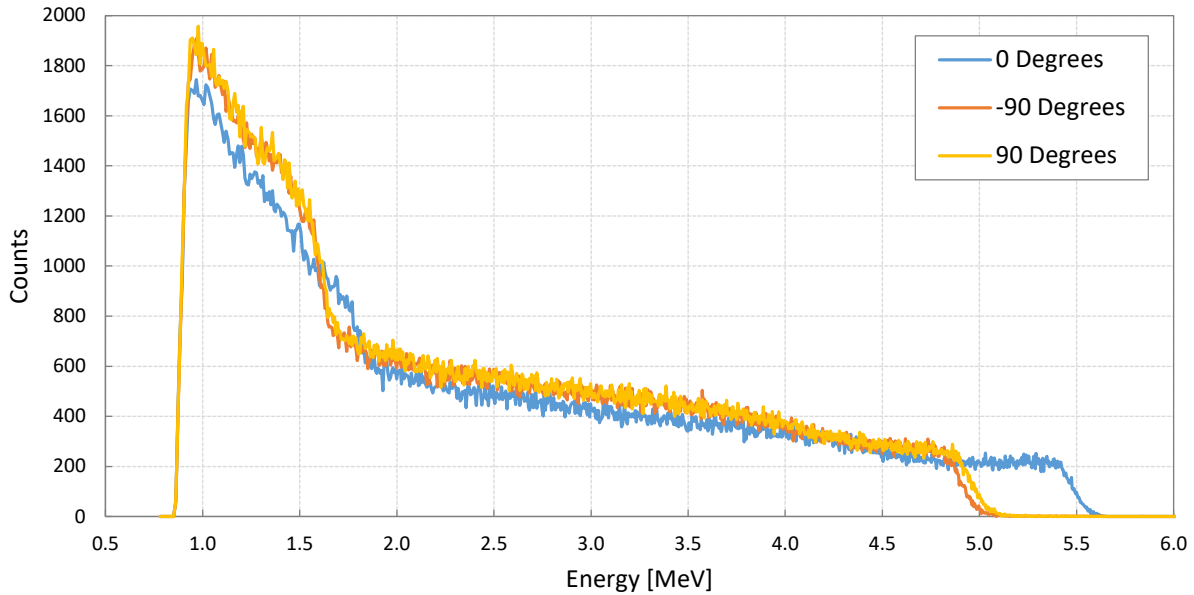


Figure 7.4. S-g stilbene PHSs at 5 MeV using the neutron LO-to-energy curve of Figure 5.12b.

UNFOLDED NEUTRON SPECTRA

The employed deconvolution method for the measurements performed with the stilbene detector is the one proposed in [Cvachovec 2008], based on a maximum likelihood estimation algorithm. On the other hand, for the measurements performed with the BC501A, the procedure used in [Schmidt 2002] has been followed.

The results of the unfolded neutron spectra are presented in Figure 7.5. The neutron spectrum of the BC501A detector was found using its response matrix (available at IRSN). The 5 MeV peak is well centered and the second peak is clearly visible around 4 MeV. Another peak is found around 1.5 MeV. The unfolded stilbene spectra are also a good representation of the measurements, although the Rez response matrix was used. The 5 MeV peak seems to be slightly displaced towards the 4.9 MeV energy and the second and third peaks are less visible. These results show only the potential of the \varnothing 25 mm s-g stilbene, the proper analysis will be performed after the full characterization of the detector and of its response matrix, foreseen after the end of this work.

SIMULATION OF THE RESPONSE

The MCNPX-PoliMi code plus the MPPost software were used for simulating the response function of the s-g stilbene detector. The simulated neutron spectrum used as input is the stilbene unfolded spectrum (with the Rez response matrix). As already mentioned, this phase aims at validating a simulation scheme alongside the experimental measurements. The simulation was kept purposely simple and all information about the inputs are reported in **APPENDIX C**. For

MPPost, the neutron calibration was set using the same LO-to-energy relationship employed above. The results are presented in Figure 7.6, where only the 90 degrees spectra are considered.

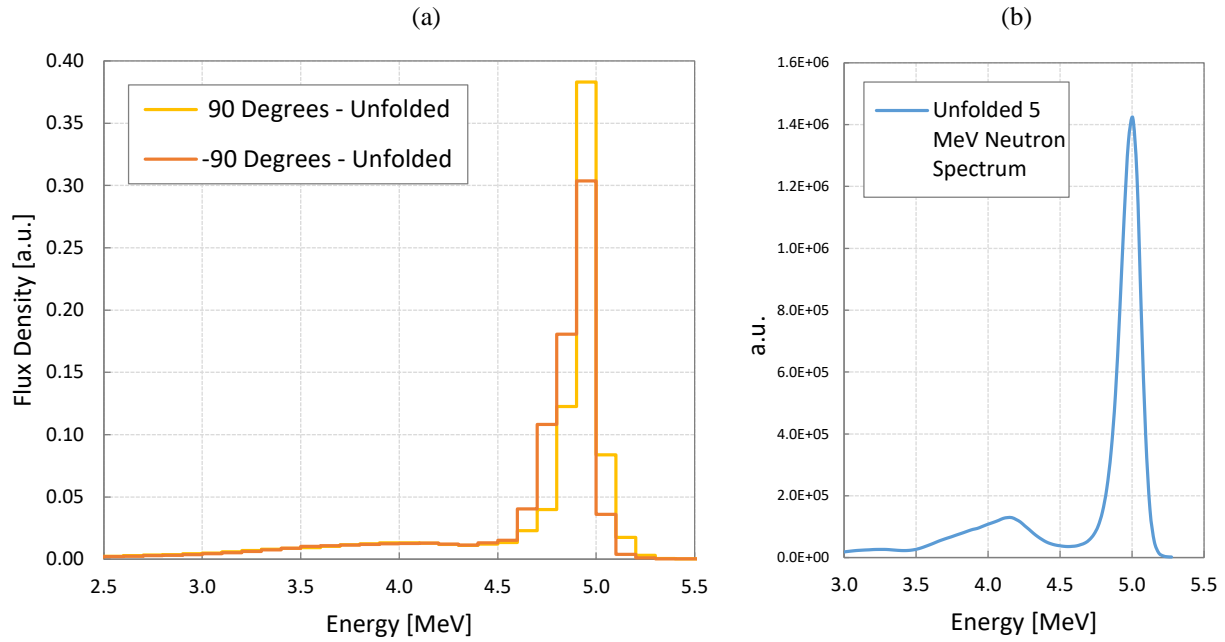


Figure 7.5. Unfolded 5 MeV neutron spectrum measured by (a) s-g stilbene (90 and -90 degrees) and (b) BC501A.

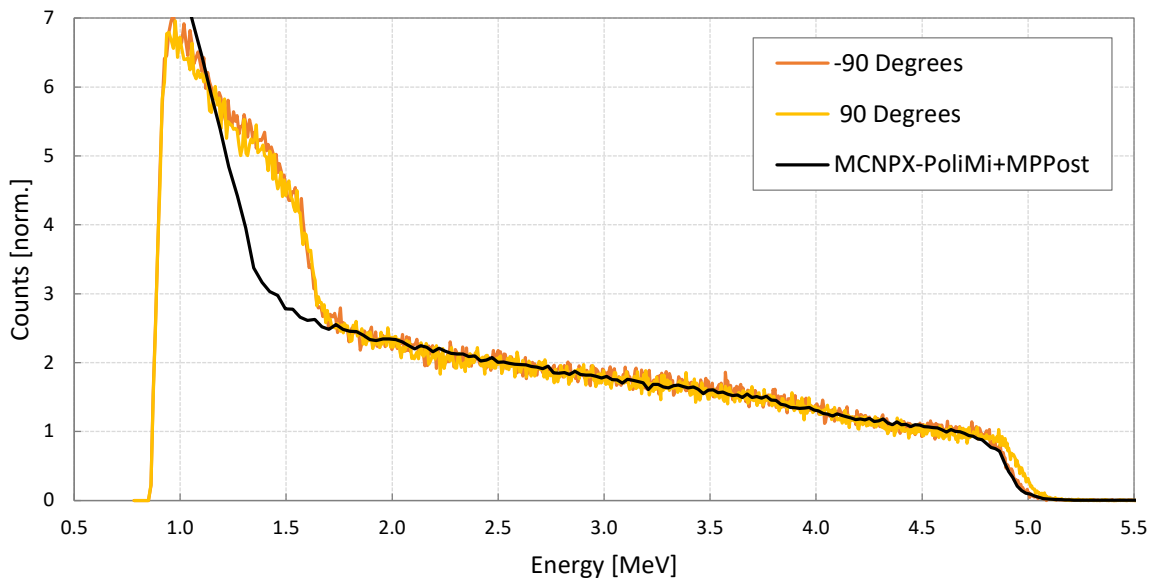


Figure 7.6. Comparison between measured and simulated PHSs.

The simulation is in good agreement with the measured spectra except for the lower energy part, around 1.5 MeV neutron energy. There are two possibilities, the first is a higher neutron peak around this energy point (already taken in consideration in the simulations), the second is that the separation of neutron and gamma events in the lower energy part could lead to an overestimation of the proton recoil PHS. Since the separation was quite easy, the most probable explanation is the first one.

In spite of this difficulty, the simulation procedure has been judged correct and a satisfying result was obtained.

7.1.2 Measurement at 565 keV

The same type of analysis has been performed for the measurement at 565 keV. The BC501A was not able to detect this type of neutron field, and a spherical proportional counter was used instead for comparison purposes. The scope of this measurement was to test the s-g stilbene at an energy lower than 1 MeV, usually considered a lower limit for organic (liquid) scintillators. The results are summarized in the following figures. The separation between neutron and gamma events is clearly visible in the PSD chart (Figure 7.7a), which shows that the scintillator is well suited for neutron spectrometry in this energy range and, possibly, at even lower neutron energies. The FoM is equal to 1.03 and is found starting from Figure 7.7b.

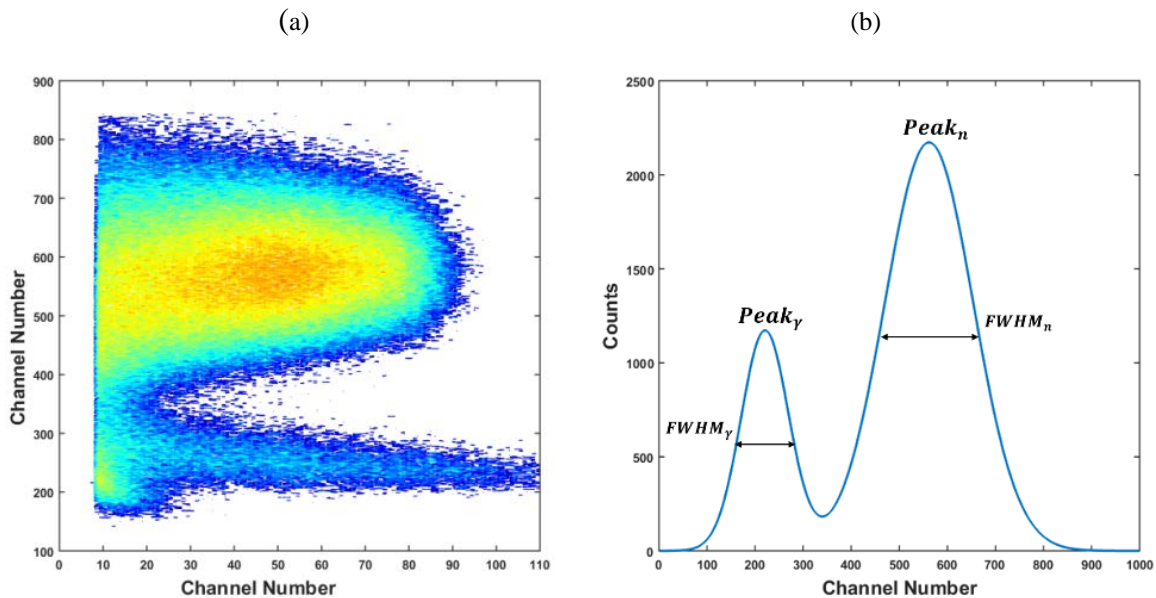


Figure 7.7. (a) Experimental PSD pattern of stilbene scintillator obtained at AIFIRA 565 keV monoenergetic neutron field at 0°, (b) stilbene FoM at 565 keV (Gaussian Fit).

The PHS after gamma discrimination of the s-g stilbene and the PHS of the proportional counter are shown in Figure 7.8.

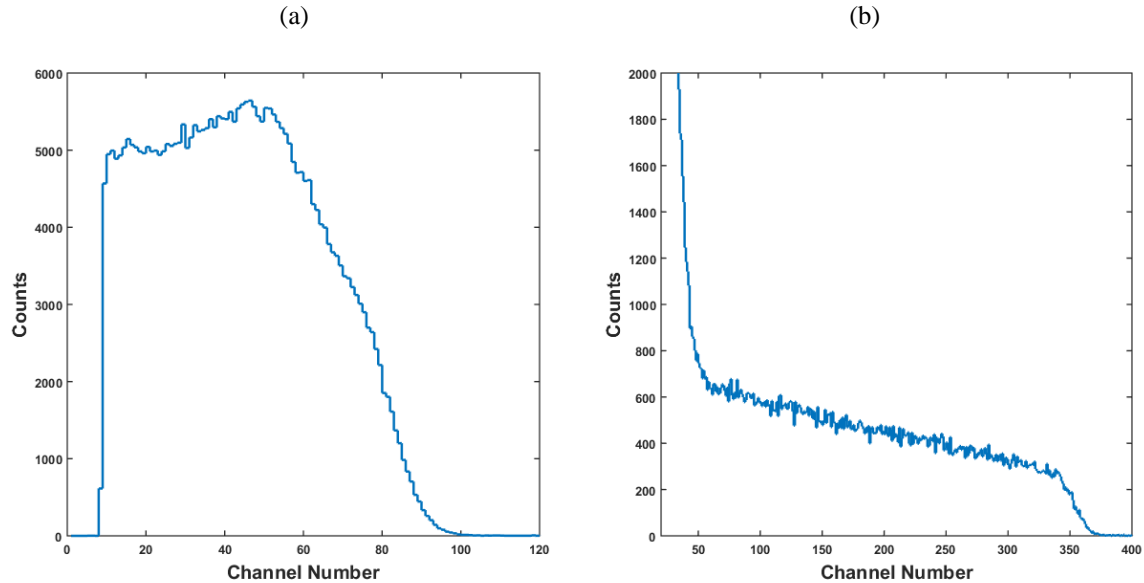


Figure 7.8. (a) Stilbene response at 565 keV monoenergetic field after subtraction of gamma contribution, (b) Proton-recoil spectrum obtained with the proportional counter SP2 at 565 keV.

7.2 The Si-filtered Extended Neutron Beam Delivered by LVR-15

The effects of the applied high-voltages and of the anisotropy were studied with the Si-filtered extended neutron beam delivered by LVR-15 (May 2017). In the previous paragraph, the response matrix of a $\varnothing 20 \text{ mm} \times 20 \text{ mm}$ m-g stilbene available at Rez has been judged sufficiently representative as well for the s-g stilbene (orientated perpendicular to the beam) and will be employed in the unfolding procedure in the following.

7.2.1 Effects of the Applied High Voltage

The s-g stilbene detector was placed in front of the beam exit, orientated in a perpendicular manner with respect to the beam axis (90°). This type of study was performed for evaluating at which high-tension value the linearity of the relation between the gamma-ray response and the channel numbers is lost. The results of the acquisition performed at 930 V (manufacturer's value), 1000 V and 1100 V are shown in Figure 7.9. Starting from 1000 V, after about channel 2000, the gamma response begins to become non-linear. The effect is clearer in the acquisition performed at 1100 V (Figure 7.9c). The non-linearity appears to be a threshold effect for higher energy signals, thus the measurements can be trusted until the threshold. This is of particular interest, since for higher voltage values, it is easier to recognize the signals produced by low-energy gamma-rays (and neutrons), and consequently to enlarge the energy domain of applications of the detector towards the low energies (keV) by performing a multi-measurement with different applied high voltage values.

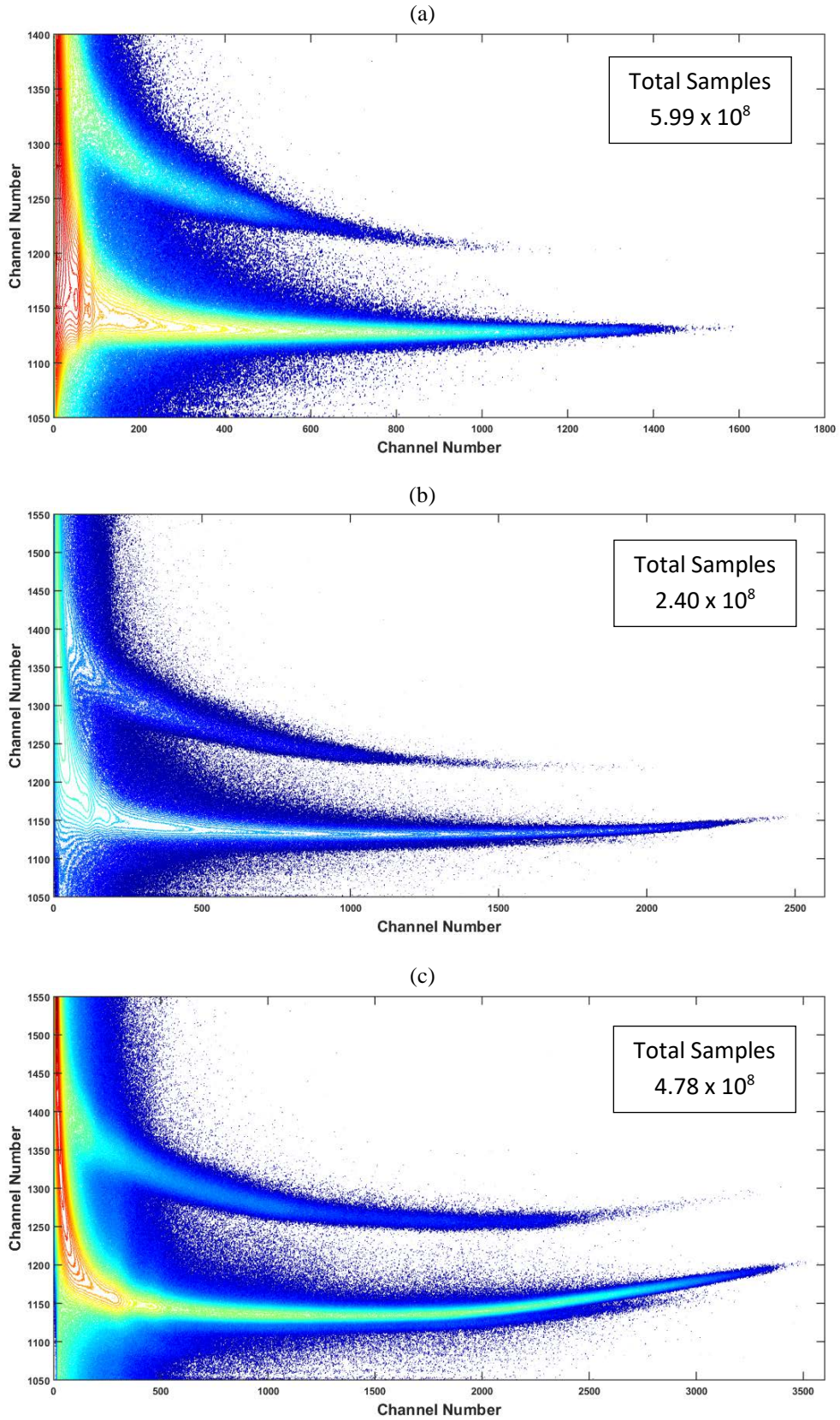


Figure 7.9. Acquisition at (a) 930 V, (b) 1000 V and (c) 1100V.

GAMMA CALIBRATION

On-line gamma calibration was performed at every measurement with the help of a ^{137}Cs source and ^{60}Co one. The two calibration sources were collated to the detector and left in their positions during the acquisitions. This is particularly useful because the “signatures” of the two sources will always be present in the resulting PSD patterns and gamma PHSs.

Before performing the measurements with neutrons, the responses coming only from the two calibration sources were registered. Several values of high-voltage values were tested again, from 800 V to 1200V. The results of these acquisitions are summarized in Figure 7.10.

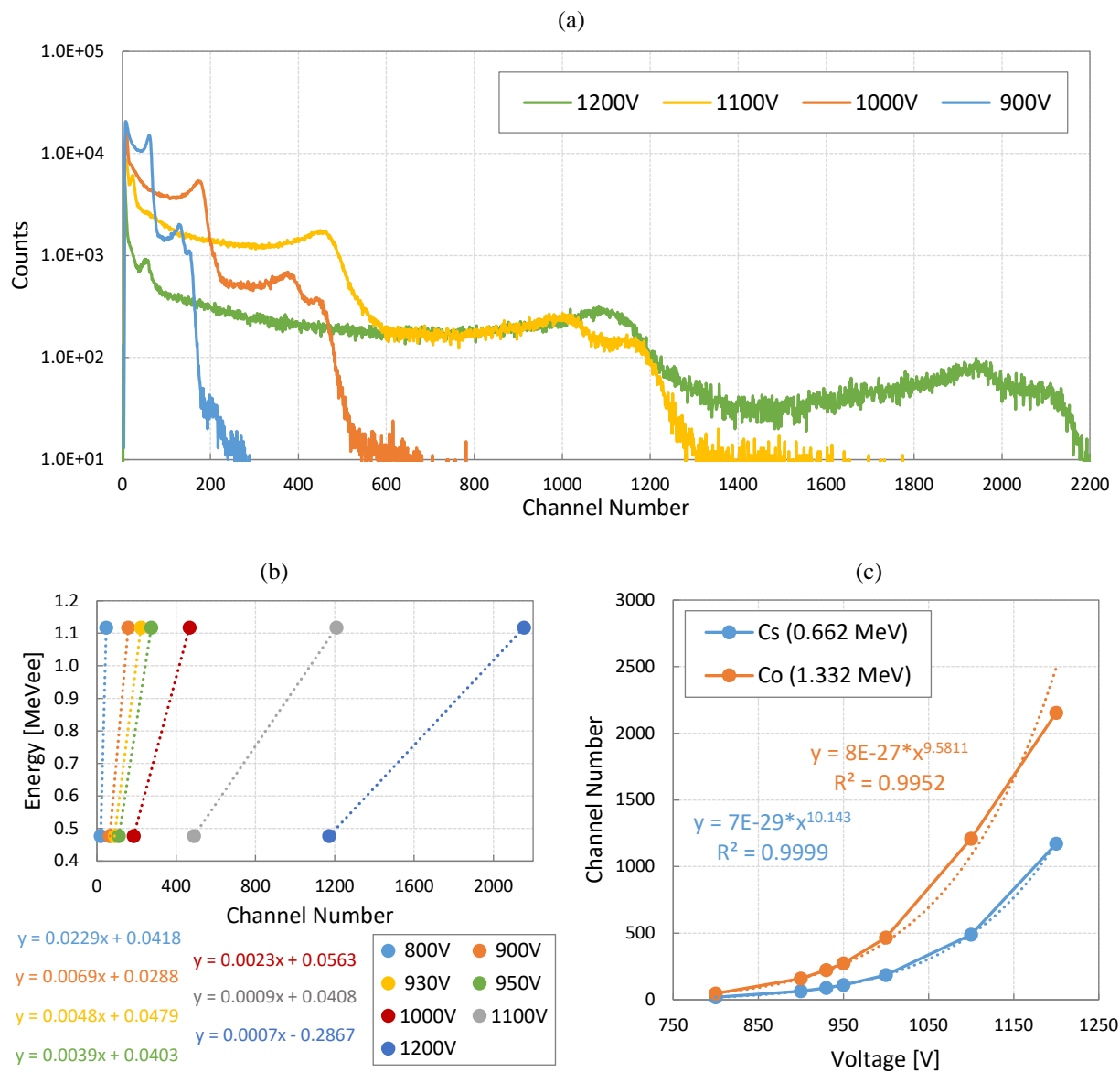


Figure 7.10. (a) Gamma PHSs produced by ^{137}Cs plus ^{60}Co and (b) gamma calibration at various high-voltage values. (c) Evolution of the ^{137}Cs and ^{60}Co calibration points with the high-voltage.

The gamma PHSs at 900, 1000, 1100 and 1200 V are compared in Figure 7.10a. The Compton edge of ^{137}Cs and the two of ^{60}Co are well visible in all measurements. The gamma calibration is presented in Figure 7.10b, where all tested high-voltage values are taken into account. Figure 7.10c is a representation of the evolution of the ^{137}Cs and ^{60}Co calibration points with the applied high-voltage. The observed behavior is the one of a power law (shown in the figure), which is particularly correct in the case of ^{137}Cs .

The gamma responses of the measurements performed with the neutron beam, after neutron-gamma separation, are the ones displayed in Figure 7.11. For the sake of clarity, only three cases are taken into consideration (the same as in Figure 7.9).

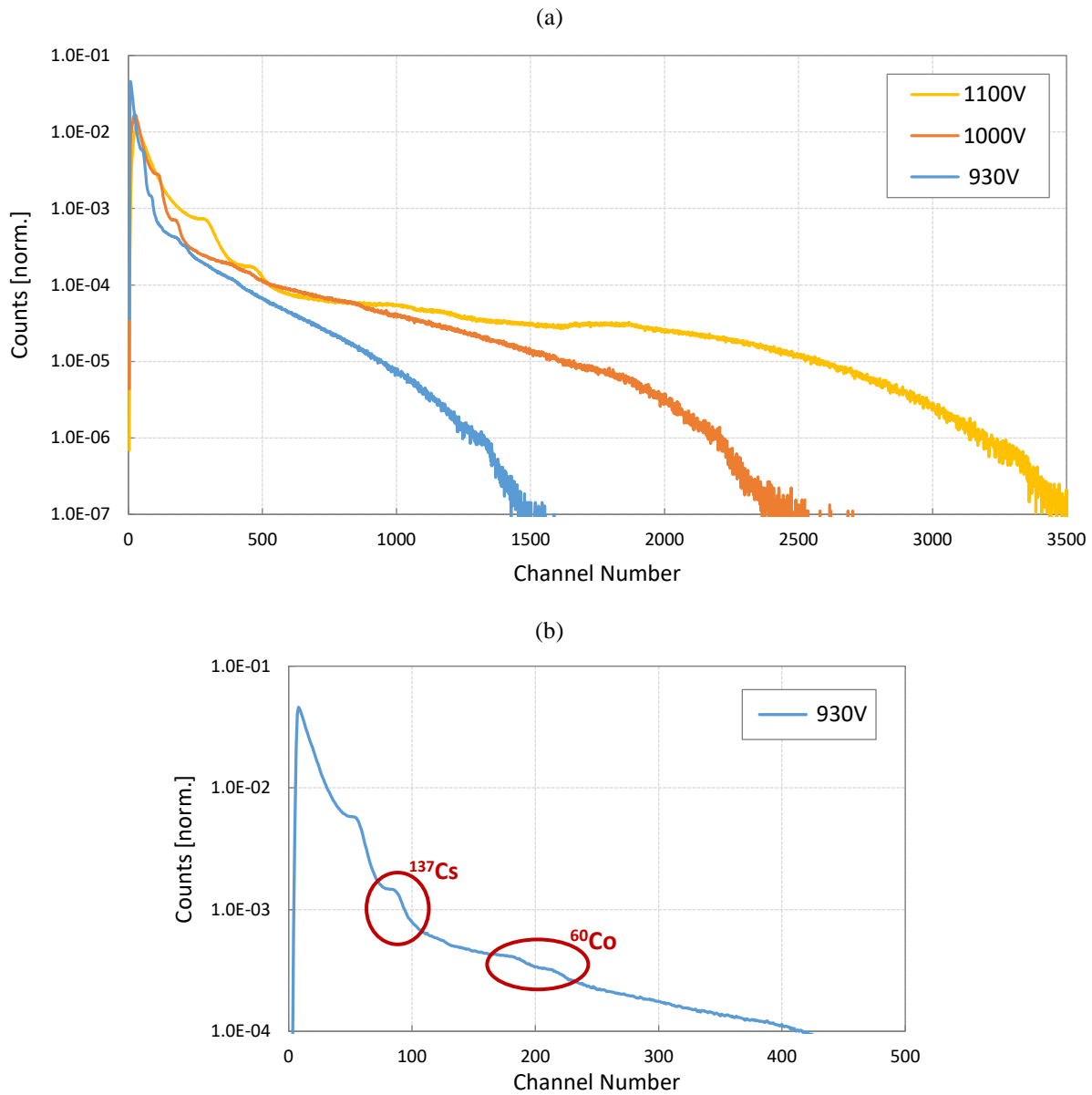


Figure 7.11. (a) Gamma PHS after discrimination at 930 V, 1000 V and 1100 V; (b) ^{137}Cs and ^{60}Co Compton edges.

The three gamma PHSs differ from those showed in Figure 7.10a. In this case, all gammas coming from the beam port are present in the PHSs. Nevertheless, it is still possible to individuate the Compton edges for “on-line” gamma calibration, as reported - for example - in Figure 7.11b, which is a zoom of the response at 930 V, for better showing the Compton edges produced by the ^{137}Cs and ^{60}Co sources.

NEUTRON PHSs AND UNFOLDED SPECTRA

The neutron spectrum produced by the LVR-15 reactor and filtered by one meter of pure Si has several peaks in the MeV region. These peaks are visible in the form of proton edges in the PHS (after gamma separation), as it is possible to appreciate in Figure 7.12 for the high-voltage values considered here (930 V, 1000 V and 1100 V).

The unfolded neutron spectra are shown in Figure 7.13. The three measurements are compared to the results obtained by simulation (black dashed line). A good agreement between the calculated and measured spectrum is found. The multi-measurement performed at different high-voltages permits to extend the energy domain of the spectrometer. The 1100 V measurement is able to distinguish the first peak, although it is necessary to cut the results at about 5 MeV, since the non-linearity of gamma response is present after that point (Figure 7.9c). The 930 V measurement is able to cover the energy domain up to 10 MeV (and beyond). Thanks to the peaks in the delivered neutron spectrum, it is also possible to verify if the three measurements are mutually consistent. This is the case, since several peaks belonging to the different acquisitions are located at the same positions and have the same behaviors.

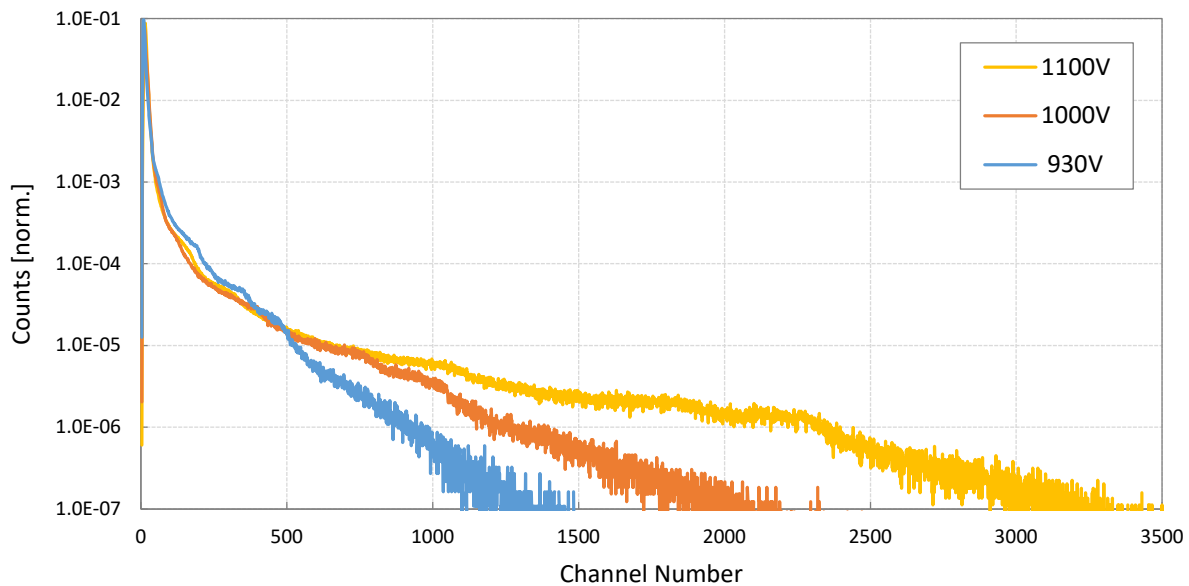


Figure 7.12. Proton recoil spectrum at 930 V, 1000 V and 1100 V.

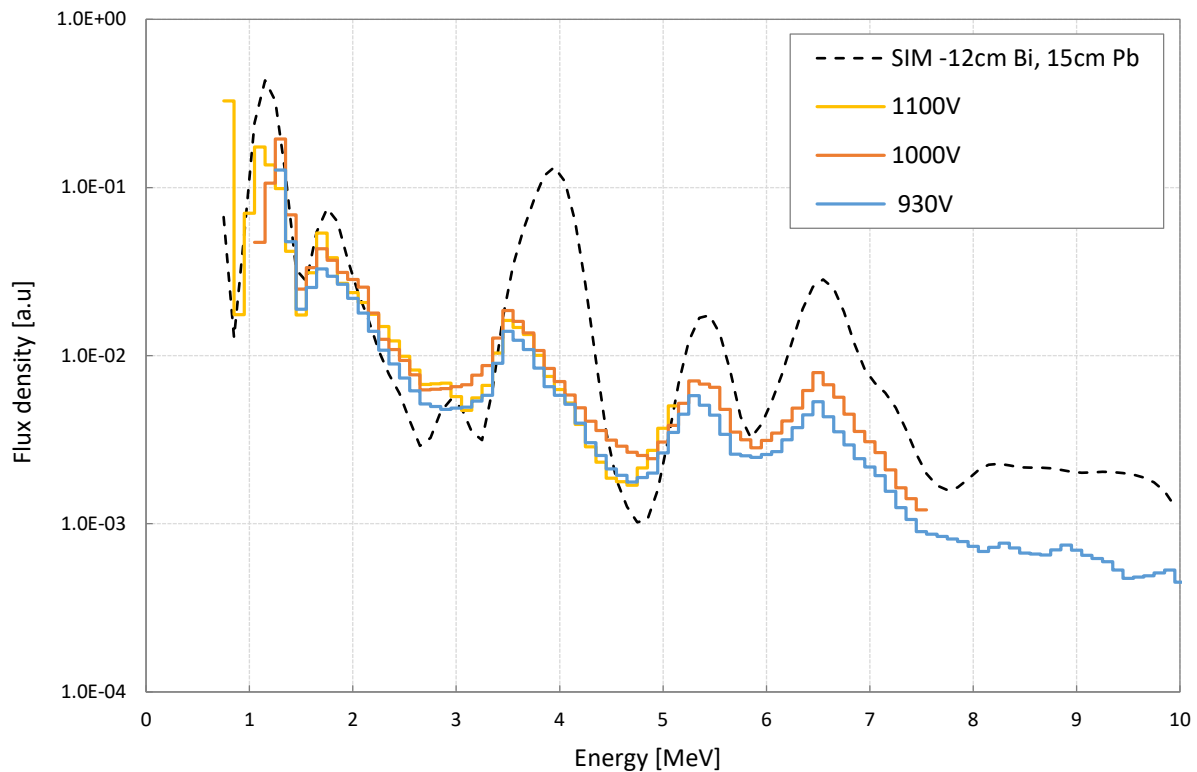


Figure 7.13. Comparison between the unfolded neutron spectrum at 930 V, 1000 V and 1100 V (\varnothing 20 mm \times 20 mm m-g stilbene response matrix) and simulation.

7.2.2 Measurements at Different Orientations

Measurements were also performed at different detector orientations with respect to the beam axis. The value of the high-voltage was set to 930 V and the tested positions were 0, 30, 45, 60 and 90 degrees. This type of experiment was done for evaluating the anisotropy of the s-g stilbene scintillation response.

The proton recoil spectra are shown in Figure 7.14a, while the unfolded neutron spectra are in Figure 7.14b. The positions of the proton edges are visible in all measurements (Figure 7.14a), although they are not the same for different orientations. The shift of the proton recoil edges is translated into the shift of the peaks in the unfolded neutron spectra, clearly observable in Figure 7.14b. The maximum neutron peak shift is estimated to be around 11 %.

The unfolded spectra at 60 and 90 degrees appear to be the most correct compared to the simulation (black dashed line). It seems that the relative orientation of the s-g crystal with respect to the PMT is turned by 60-to-90 degrees compared to that of the m-g crystal (with respect to its PMT and measured response matrix), as already noticed in the AIFIRA measurements.

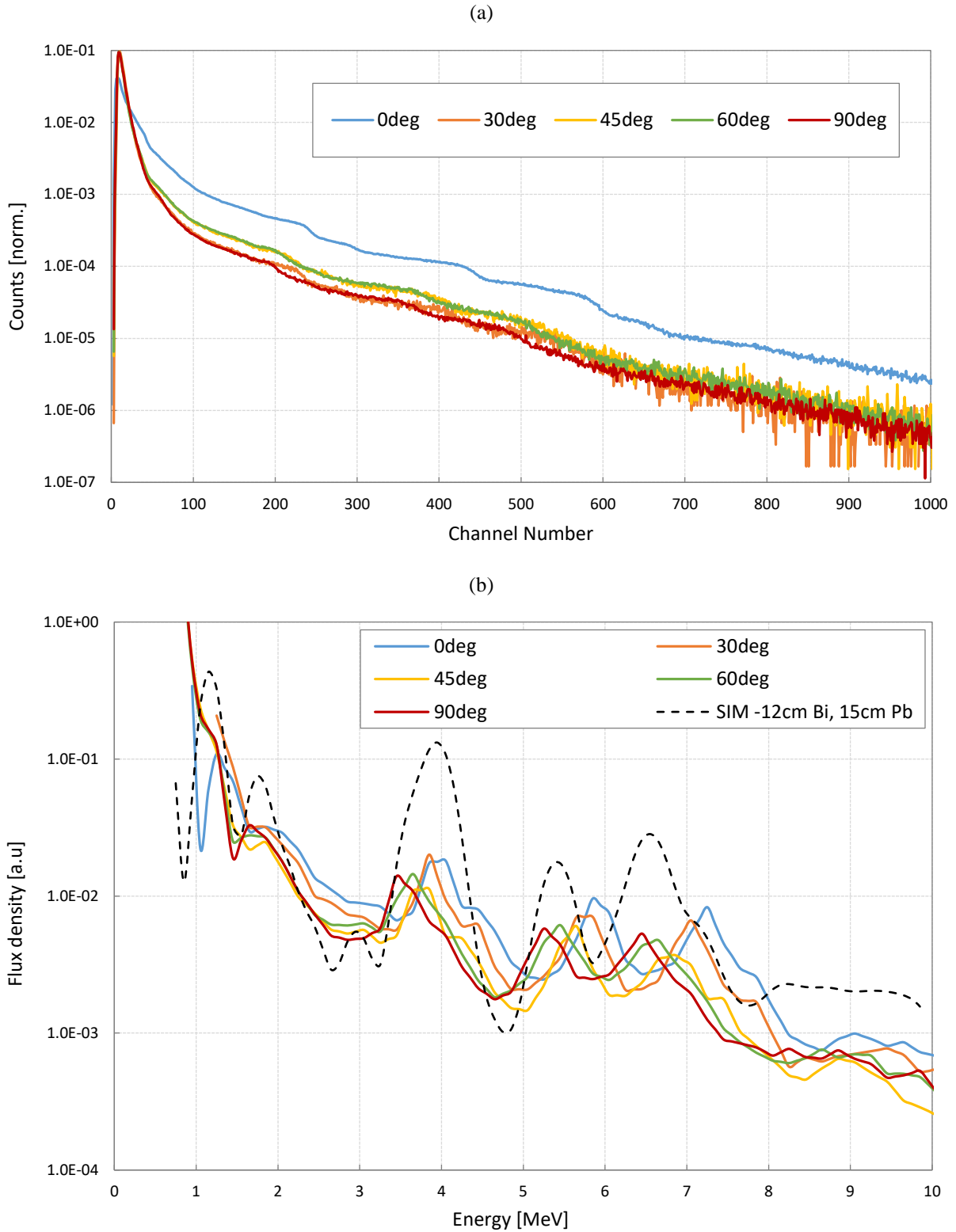


Figure 7.14. (a) Comparison of the proton recoil spectra measured at different orientations. (b) Comparison between the unfolded neutron spectra (\varnothing 20 mm \times 20 mm m-g stilbene response matrix) and simulation.

7.2.3 Simulation of the Detector Response

For comparison and validation purposes, the simulation scheme is also tested in the case of the neutron beam delivered by LVR-15. The $\varnothing 25 \text{ mm} \times 25 \text{ mm}$ s-g stilbene (plus the Rez LO-to-energy) is used. The simulated neutron response is reported in Figure 7.15a and the resulted unfolded spectrum in Figure 7.15b. The higher peaks are well described and are located in the right positions, although the results are less representative of the experimental measurement than those obtained at AIFIRA.

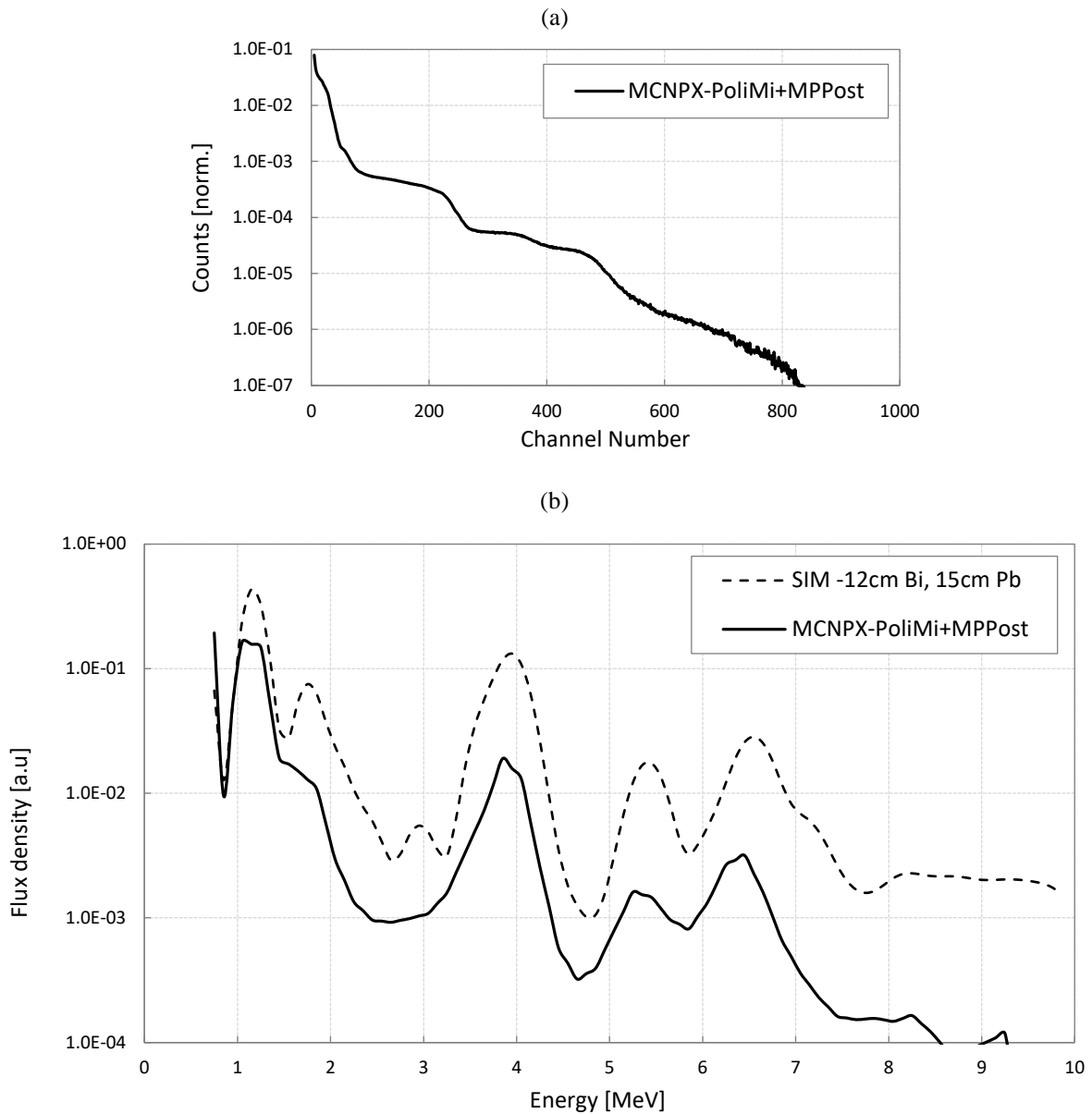


Figure 7.15. (a) Simulated proton recoil spectrum of the LVR-15 neutron beam. (b) Comparison between the unfolded spectra (calculated and measured) [Kostal 2017 (private)].

7.3 Neutron Spectra Measurements at the ZPR LR-0

The s-g stilbene detector was employed in the LR-0 research reactor for testing its capabilities as an in/near-core fast neutron spectrometer. Three positions were tested: B0, which corresponds to the center of the LR-0 core (but not of the experimental configuration); B1, in the baffle of the core; and B2, after the barrel. The axial position of the detector was kept constant for the three measurements. In the following, only the results at 930 V are presented, although other high-voltage values were tested. As for LVR-15, for the unfolding part, the response matrix of a $\varnothing 20$ mm \times 20 mm m-g stilbene is used.

7.3.1 B0

The separation between neutron and gamma events was feasible also in such a kind of environment (Figure 7.16) and the proton recoil spectrum, after gamma discrimination, is presented in Figure 7.17a. The reactor was operated at a few Watts (~ 1 W) and the count rate was kept around 100000 counts per second. The unfolded neutron spectrum, compared to the simulated one at the same position, is shown in Figure 7.17b. The two spectra are not in good agreement, due to the fact that the employed LO-to-energy relationship (for neutron calibration) and the associated response matrix (for the unfolding part) are not describing exactly the response of the s-g stilbene (correct only in the 90 degree case, see above). Nevertheless, these results are shown because the objective of this study is not to provide an exact characterization of the neutron spectrum inside the LR-0 reactor but rather to provide experimental data on s-g stilbene and to prove the practical feasibility of this kind of measurements with a new type of organic scintillator. By looking at the results from this point of view, the obtained spectrum is considered a good representation of the capabilities of the detector (which will be calibrated and unfolded with the correct LO-to-energy relationship and response matrix in the future).

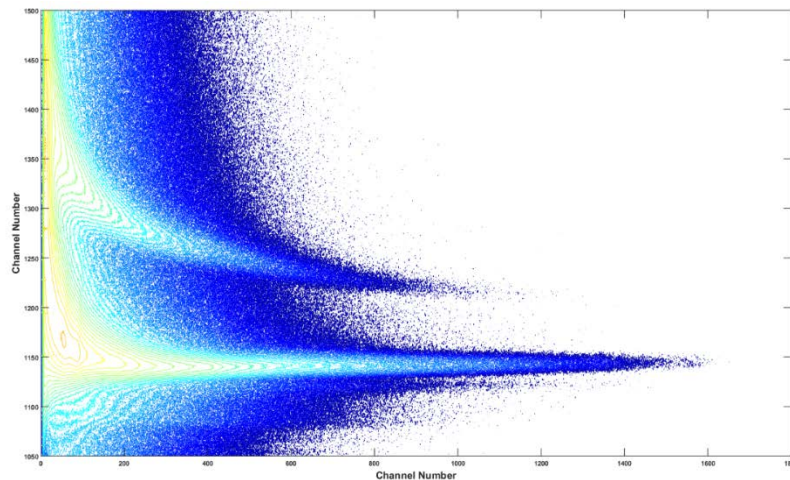


Figure 7.16. Acquisition at B0 in the LR-0 reactor (930 V).

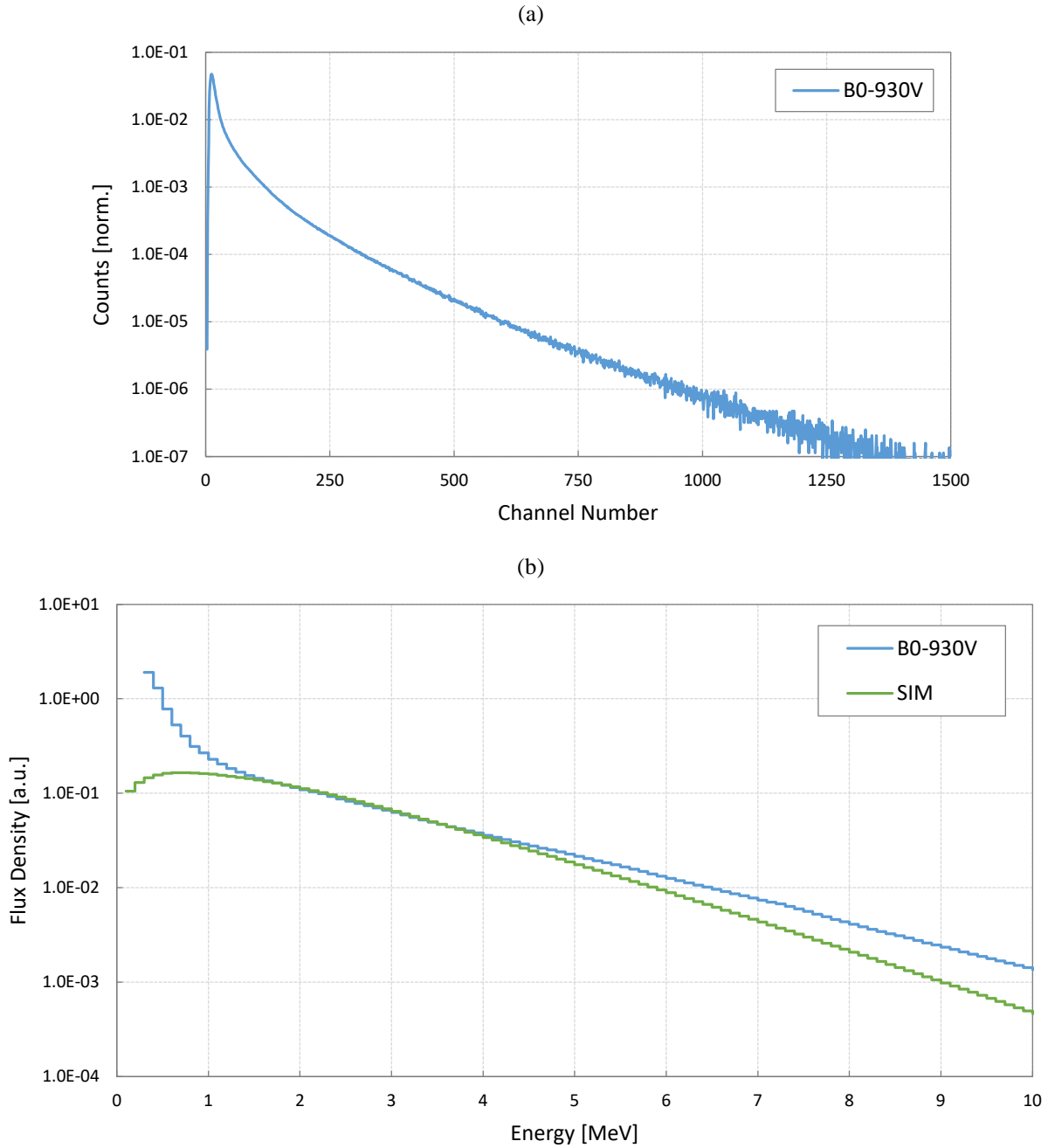


Figure 7.17. (a) Proton recoil spectrum and (b) comparison between the unfolded neutron spectrum (\varnothing 20 mm \times 20 mm m-g stilbene response matrix) and the simulated spectrum at the B0 position in LR-0.

SIMULATION

A simulation using MCNPX-PoliMi plus MPPost was done also for the B0 position in LR-0. The calculation took into account the simulated neutron spectrum at B0 and a \varnothing 10 mm \times 10 mm m-g

stilbene, because of the availability of proven correct measurements with such a crystal. The comparison of the calculated and measured detector response is shown in Figure 7.18.

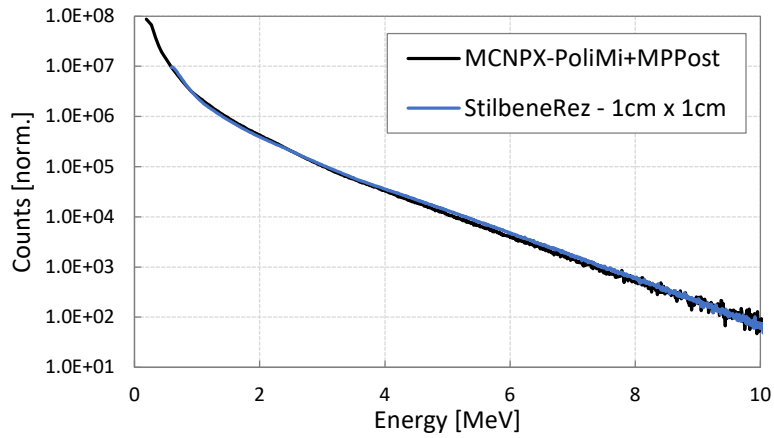


Figure 7.18. Comparison between simulated and measured detector response.

The result of the comparison is satisfying and it was possible to reproduce well the experimental response.

The unfolded neutron spectrum of the simulated proton recoil response is presented in Figure 7.19. The behavior of the two curves is in good agreement.

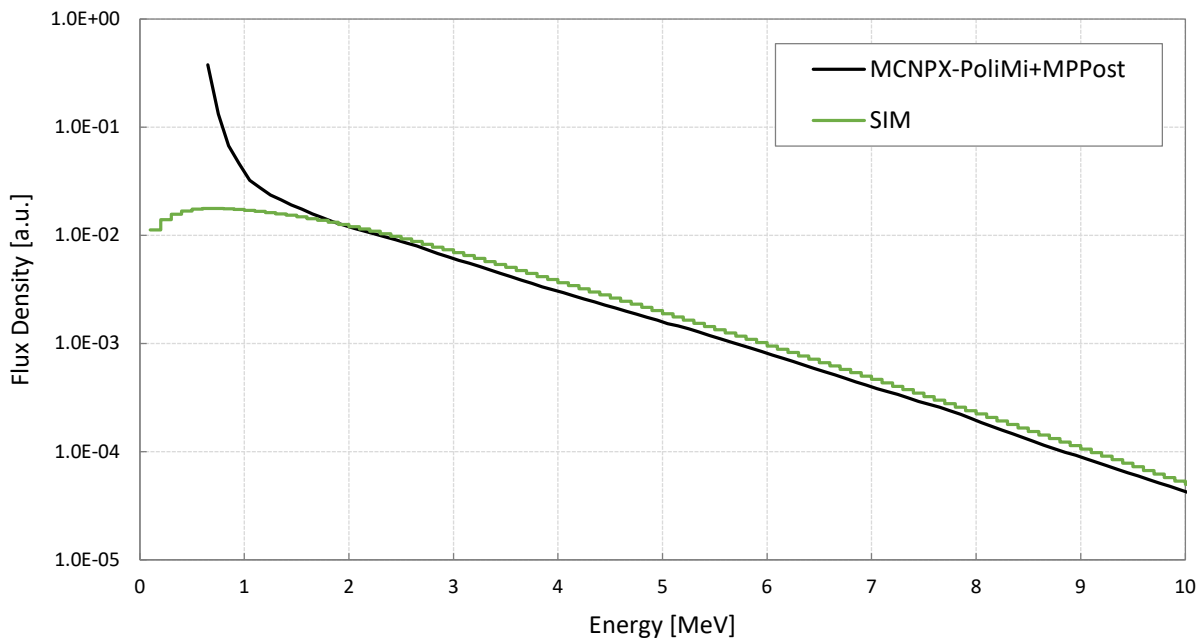


Figure 7.19. Comparison between simulated and measured detector response.

7.3.2 B1 & B2

The same considerations done for the measurement at B0 can be extended also for those performed at B1 and B2. The results are summarized in Figure 7.20 for B1 and in Figure 7.21 for B2.

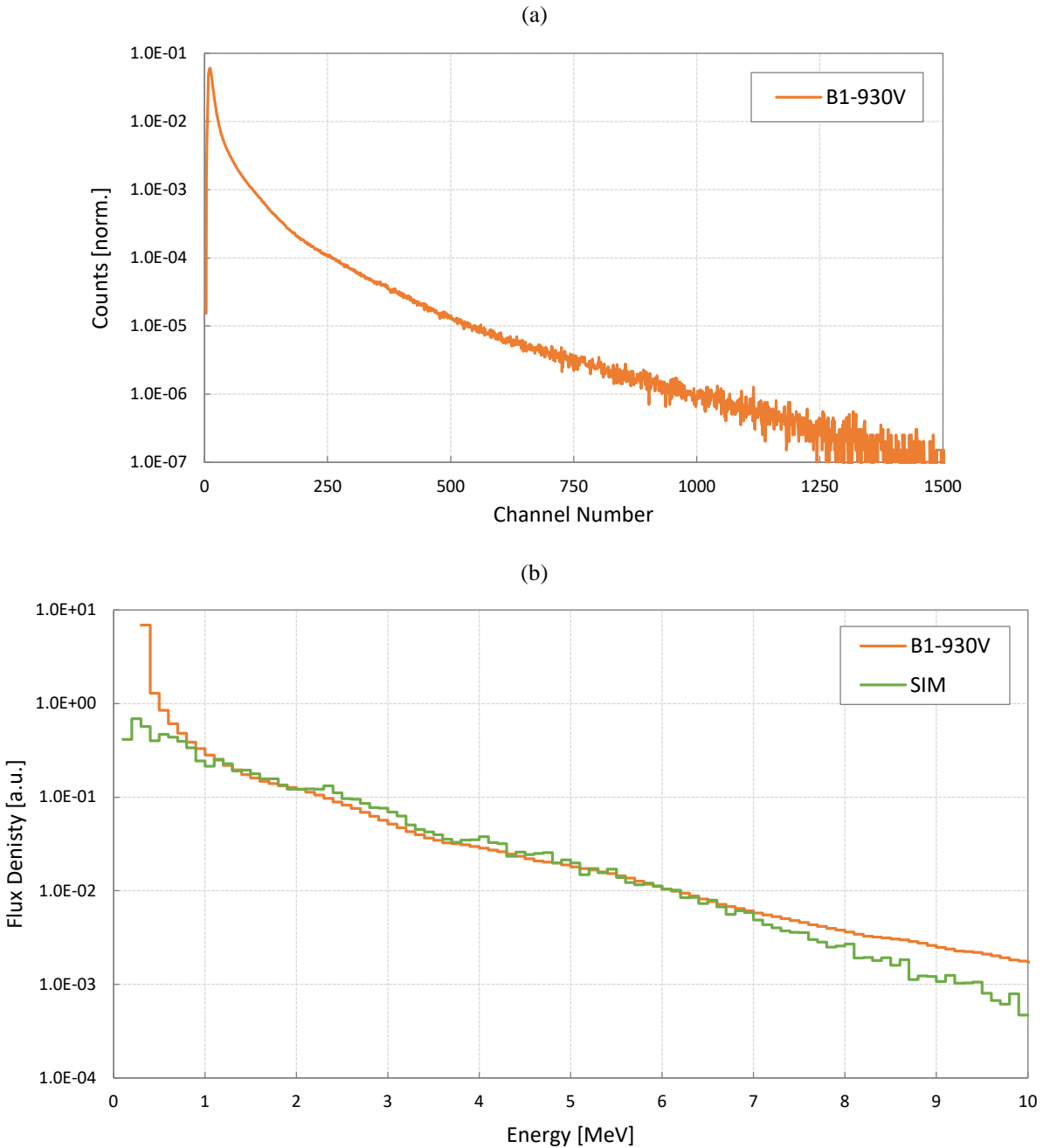


Figure 7.20. (a) Proton recoil spectrum (930 V) and (b) comparison between the unfolded neutron spectrum (\varnothing 20 mm \times 20 mm m-g stilbene response matrix) and the simulated spectrum at the B1 position in LR-0.

The comparison with the simulated spectra (Figure 7.20b and Figure 7.21b) shows the same issue as for the B0 one, but it clearly confirms the potential of this technique.

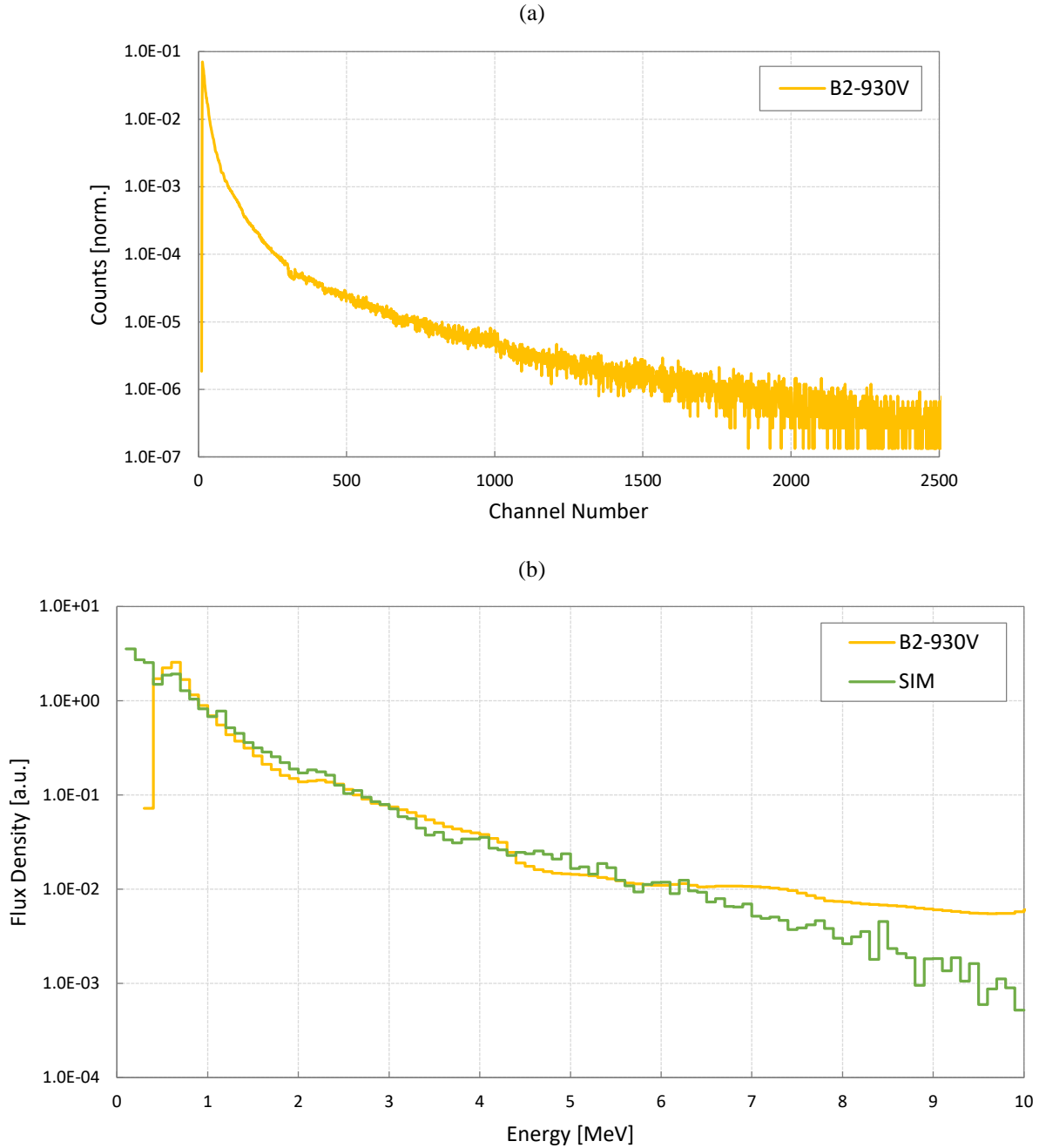


Figure 7.21. (a) Proton recoil spectrum (930 V) and (b) comparison between the unfolded neutron spectrum (\varnothing 20 mm \times 20 mm m-g stilbene response matrix) and the simulated spectrum at the B2 position in LR-0.

7.4 Discussion/Difficulties

The first experimental campaign carried out on the \varnothing 25.4 mm \times 25.4 mm s-g stilbene started in March 2017 and ended in May 2017. The scope was to learn about the capabilities of this new type of organic scintillation material and to test its range of applications. Different mixed radiation fields were measured and comparisons with classical proton recoil detectors were made. Preliminary unfolded spectra, using a \varnothing 20 mm \times 20 mm m-g stilbene response matrix (thanks to Michal Kostal), have been shown and discussed.

The measurements performed at AIFIRA demonstrated that the s-g stilbene detector has truly attractive properties, which outperform those of the BC501A (\varnothing 5 cm \times 5 cm). The comparison clearly showed better discrimination capabilities (35 % higher FoM) and a wider energy domain of application (measurements also possible at 565 keV). The latter was one of the major concerns for well overlapping the measurement (in the lower energy part) with proportional counters. This confirms the pertinent choice of the s-g stilbene as a part of the multi-detector system that will be developed within the SPECTRAL project. Only a few orientations were tested for evaluating the anisotropy, which will be discussed in the following, taking into account also the measurements performed at LVR-15.

The difficulties were mainly related to the fact that this experiment was the first one for the new scintillation detector. During the preparation, which took place at the AMANDE facility in Cadarache (thanks to Vincent Gressier), much time was spent in testing the electronic system with calibration sources, trying to adapt that of the BC501A. It was really a valuable training experience, but several weeks were dedicated to this task. During the actual measurements at AIFIRA, no particular difficulties were encountered. It was a learning process, with its pros and cons.

The experience at Rez was amazing. Mainly because it was possible to measure several extended neutron fields in different types of environments, and also because of the great knowledge and expertise of the Rez scientists in neutron (and gamma) spectroscopy techniques using crystal organic scintillators and proportional counters. It was possible to discuss, to exchange ideas and to perform various tests. It was also possible, thanks to the availability of both LVR-15 and LR-0, to evaluate all the envisaged uses proposed for the MASURCA facility as a multi-purpose physics installation (Figure 7.22).

The most interesting test, was the experiments performed at LVR-15, for assessing the feasibility of out-of-core measurements. With total neutron plus gamma fluxes on the order of 10^5 # cm⁻² s⁻¹, the feasibility was rapidly confirmed. Thanks to the simplicity of the electronics system (digital), remotely controllable, it was easy to perform parametric studies on the role of the applied high-voltage and on anisotropy. The first ones bring valuable informations for the full characterization of the s-g stilbene detector, which has to take into consideration also the important role of the photomultiplier. Around 1000 V, the distortion caused by the PMT starts to be evident. As already mentioned, the non-linearity appears to be a threshold effect for higher energy signals, and therefore only the part of the acquisition up to the threshold can be trusted. This permits to extend the energy domain of application of the detector towards lower energies, and it also provides a wider overlapping window with proportional counters.

No particular difficulties were met in this case, apart from classical experimental physics problems such as the breaking of an electronics component, replaced in one day.

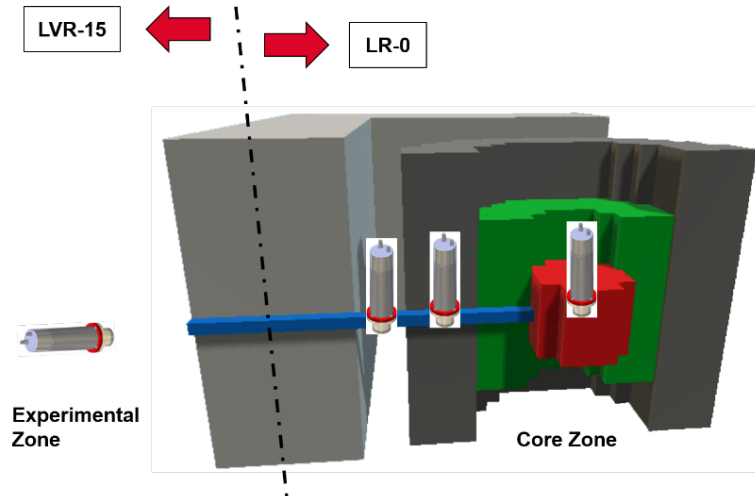


Figure 7.22. MASURCA as a multi-purpose experimental facility.

The tests in LR-0 permitted to confirm the feasibility and to provide experimental evidence of in-core and near-core neutron spectra characterization with the s-g stilbene. The power of the reactor was kept low (around 1 W) for matching typical neutron plus gamma fluxes on the order of 10^5 - 10^6 # $\text{cm}^{-2} \text{s}^{-1}$ (by looking at the count rates). Three positions were tested and three different neutron spectra were found. The comparison with simulation clearly showed discrepancies due to the used LO-to-energy relationship and associated response matrix (mainly in the highest part of the energy domain).

Again in this case, no particular difficulties were experienced. The reactor staff and the scientists were familiar to these types of measurements and changing the position of the detector was relatively fast.

Overall, the mission to Rez was extremely valuable as it permitted to better understand the operation of crystal scintillators in general and for research reactor applications.

7.4.1 Anisotropy

The role of the anisotropy of the response was tested at AIFIRA and at LVR-15. The effect of anisotropy was clear both in the 5 MeV mono-energetic neutron field produced by AIFIRA and in the silicon-filtered extended neutron beam delivered by LVR-15.

Maximum differences in the position of the proton recoil edges of ~15 % were found in both measurements before gamma calibration (Table 7.1 and Figure 7.14a). After gamma calibration,

i.e. after setting the electron-equivalent (MeV_{ee}) energy scale on the abscissa, differences on the order of 14 to 15 % were observed (Table 7.1 and Figure 7.3a).

For neutron calibration, there is an issue with the use of only one LO-to-energy curve for all orientations. As previously discussed and showed, the same LO-to-energy relationship (that of a $\varnothing 20 \text{ mm} \times 20 \text{ mm}$ m-g stilbene) was employed for all orientations, but it was found to be correct only in the case of the detector orientated at 90° (60° -to- 90°) with respect to the beam axis. By using a single LO-to-energy curve, differences in the position of the proton recoil edges of $\sim 10\%$ were found (Figure 7.4). The possibility to unfold the proton recoil spectra permitted to first evaluate also the maximum shift of the neutron peaks, which is roughly the same as the one of the proton recoil edges: about 10 %. For example, the shift in the unfolded 5 MeV mono-energetic neutron peak of AIFIRA corresponds to about 9.7 % and the one of the picks of the unfolded Si-filtered neutron spectrum to about 10.6 % (Figure 7.14b).

For taking into account this aspect, thus for associating to different gamma-equivalent responses (because of the anisotropy) a unique neutron-equivalent response (representative of the neutron field), the use of different LO-to-energy curves is now analyzed.

In an attempt to explain the shift observed in the responses, a numerical shift of the same order of magnitude is applied to the experimental points used for constructing the LO-to-energy curve. This was done by modifying so that they follow a law of the following type (Figure 7.23, “Fit (Experimental Point)” [Kostal 2017 (private)]):

$$y [\text{MeV}_{ee}] = \frac{ax^2}{b+x} [\text{MeV}] \quad . \quad (7.2)$$

As already said, this curve describes well the behavior of the responses when the detector is orientated at 90 degrees with respect to the beam axis. Evidence of this is the 5 MeV point, which was found to be 1.64 MeV_{ee} (on average) at AIFIRA, and which is equal to 1.66 MeV_{ee} on the LO-to-energy curve.

The earlier considerations on the magnitude of the shift found by using the gamma-equivalent or the neutron-equivalent energy scale suggest that it is possible to proceed in two ways: the first option is to apply a +15 % shift to the gamma-equivalent values, the second possibility is to apply a -10 % shift to the neutron-equivalent values. With either method, the new associated value to the 5 MeV point become $\sim 1.90 \text{ MeV}_{ee}$, that is the same as the one found in the AIFIRA measurement with the detector orientated at 0 degrees (Table 7.1). The new points are then fitted with a curve of the same type as that used for the experimental points (7.2). The results are shown in Figure 7.23a and 7.23b and the comparison between the two custom LO-to-energy curves in Figure 7.23c. The two curves are very similar, so that one can be used instead of the other.

A test with MPPost is done for three LO-to-energy relationships. The MCNPX-Polimi output (input for MPPost) is the same for the three simulations and is the neutron field delivered by the 5 MeV beam of AIFIRA interacting with the s-g stilbene (**APPENDIX C, C.1**). The “neutron

calibration” is changed according to the three fitted curves. The results in gamma-equivalent energy and neutron-equivalent energy are presented in Figure 7.24a and 7.24b respectively.

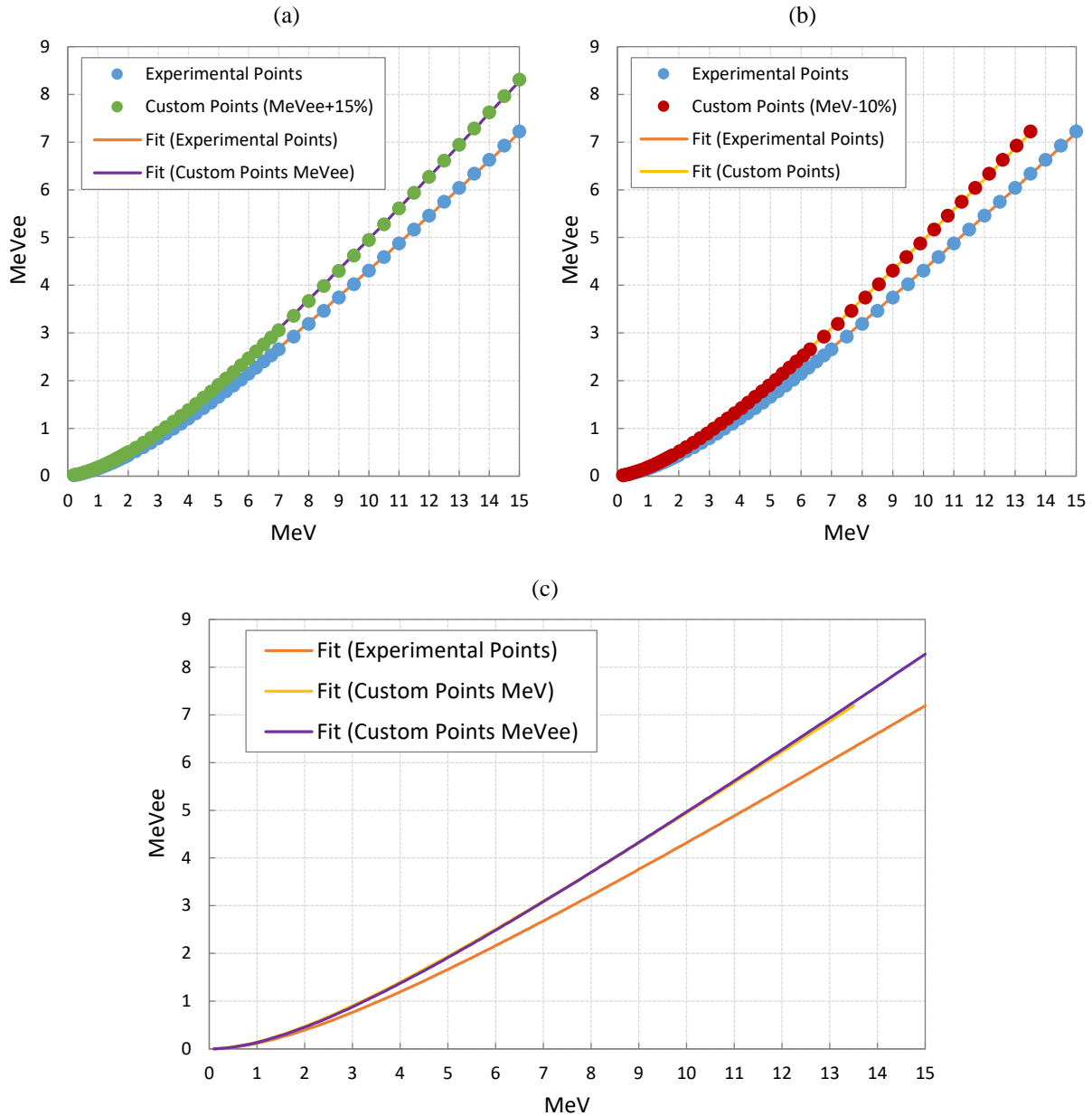


Figure 7.23. Experimental [Kostal 2017 (private)] and custom LO-to-energy.

By comparing the two figures (7.24a and 7.24b), one can see that the differences between the gamma-equivalent responses are accounted for in the neutron calibration when using the modified LO-to-energy curves, yielding as a result the same response in neutron-equivalent energy.

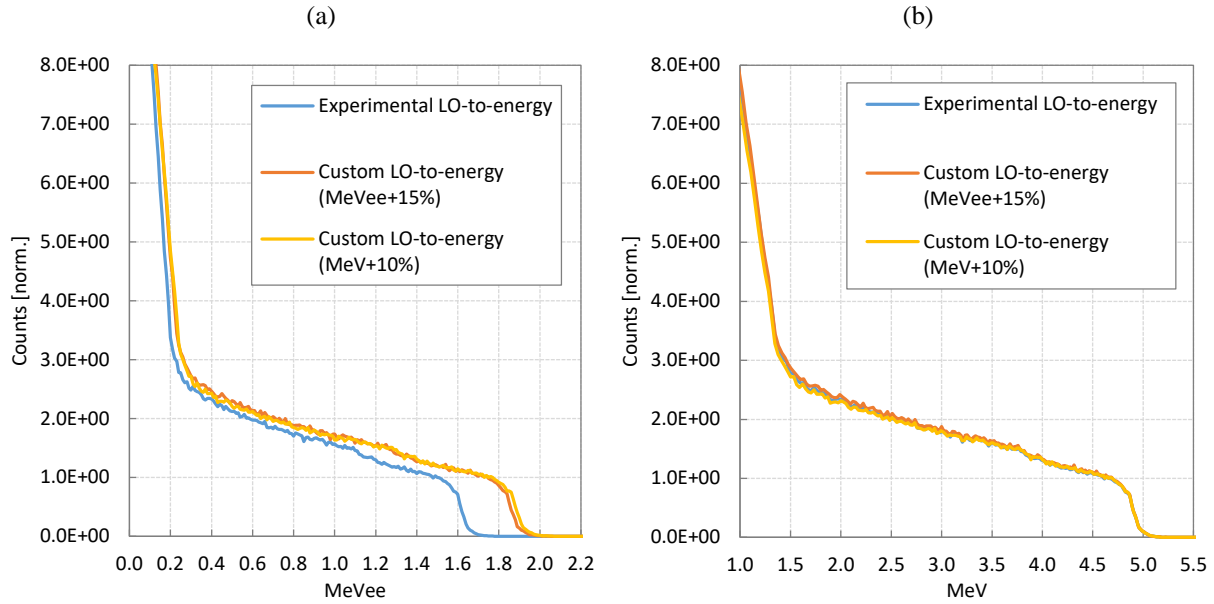


Figure 7.24. Simulated PHSs with three different neutron calibrations in (a) gamma-equivalent and (b) neutron-equivalent energy.

The same approach is applied to the experimental results obtained at AIFIRA (5 MeV case) and at LVR-15, considering only the 90° and the 0° measurements, and one of the custom LO-to-energy curves (MeV+10%). The results are compared in Figure 7.25.

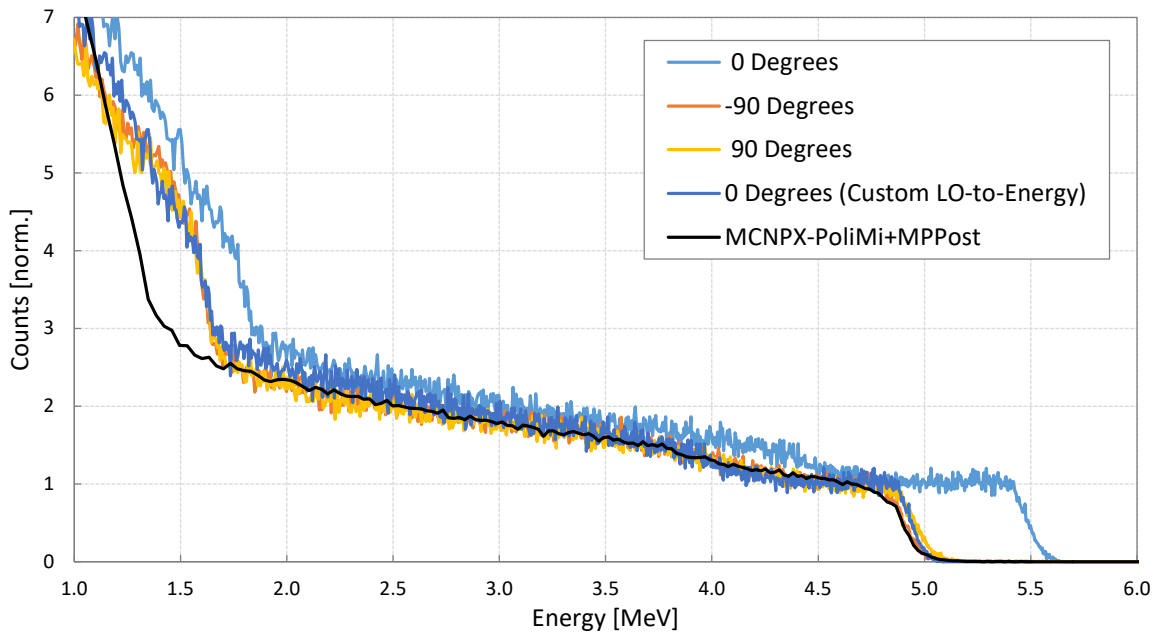


Figure 7.25. Comparison between the measurements performed at 90° and 0° with the experimental and custom LO-to-energy at AIFIRA.

The 0° proton recoil spectrum with custom LO-to-energy is in good agreement with those at 90° with the experimental LO-to-energy. The anisotropy is fully taken into account (at all energies) simply by modifying the neutron calibration.

This is also true in the LVR-15 case (Figure 7.26), starting from about 2 MeV. The Si-filtered spectrum delivered by LVR-15 is particularly interesting for studying the organic scintillator response, giving the possibility to distinguish different proton edges in the energy domain of application. Taking as a reference the 90° measurement with the experimental LO-to-energy, all edges are well represented also by using the proposed method for the 0° one, making it possible to compensate for the anisotropy effect.

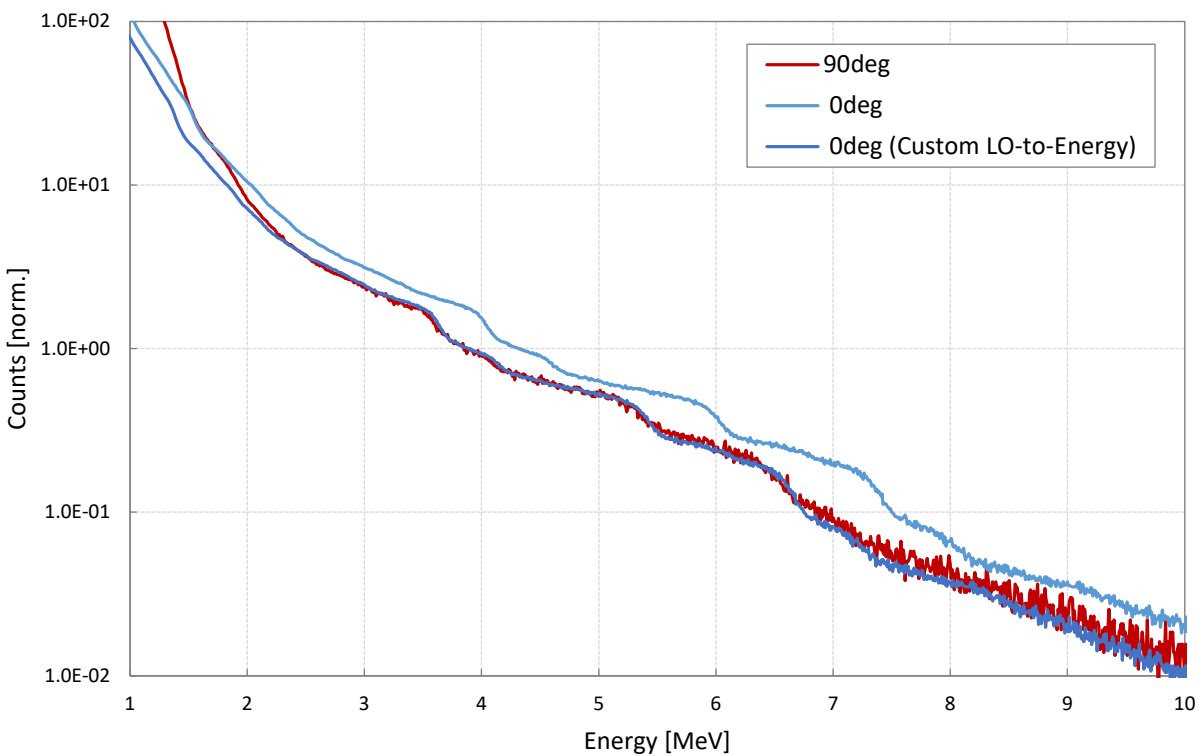


Figure 7.26. Comparison between the measurements performed at 90° and 0° with the experimental and custom LO-to-energy at LVR-15.

This approach suggests that the measurement of a crystal scintillator response matrix at different orientations may not be necessary. The measurement of the response matrix at one orientation, together with the associated gamma calibration, permits to construct an experimental LO-to-energy curve for neutron calibration. The proposed method acts only on the neutron calibration, modifying the LO-to-energy relationship in such a way as to compensate for the anisotropy effect.

Future studies will further investigate this aspect. The work will take into consideration also the measurements performed at LR-0, in which neutrons come from all directions. Recall that the

experimental results demonstrated the feasibility of in-core applications, but the agreement with the simulations was only partial. By looking at the proton recoil spectra and at the unfolded neutron spectra (B0, B1 and B2), the common denominator is the presence of quite high discrepancies between calculated and measured spectra in the higher energy part. This is the same problem encountered in AIFIRA and LVR-15 when using the experimental LO-to-energy relationship for the measurements at 0° (anisotropy). It would therefore seem that the PHS of the s-g stilbene in LR-0 mostly kept the characteristics of the 0° response. The approach used for correcting the shift of the 0° measurement is thus applied also to this case. The results are in Figure 7.27.

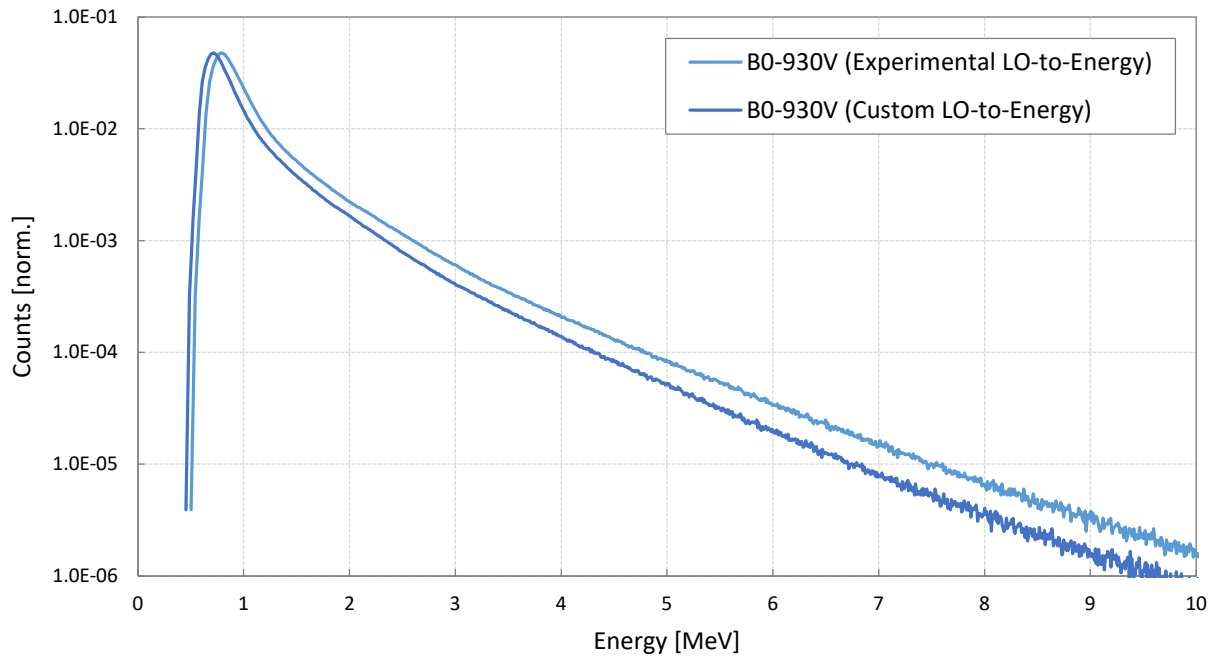


Figure 7.27. Comparison between the measurement performed at LR-0 (B0) with the experimental and the custom LO-to-energy.

With the custom LO-to-energy relationship, the proton recoil spectrum seems to be in a better position for describing the neutron spectrum of LR-0 with the s-g grown stilbene detector.

In general, if the response produced by a crystal scintillator irradiated with a neutron field coming from all directions keeps only the characteristics of the response of a particular orientation, it is sufficient to recognize which is the correct LO-to-energy curve (experimental or custom) and to modify the neutron calibration so as to compensate for the anisotropy effect.

7.4.2 Simulation

The simulation scheme based on MCNPX-PoliMi and MPPost proved to work properly, in particular with simple mono-energetic neutron fields and with extended neutron spectra that present a smooth behavior, like the ones in the experimental channel B0 of LR-0. Also in the special Si-filtered neutron field delivered by LVR-15 sufficiently good results were achieved, capable of reproducing all the edges in the proton recoil spectrum.

Recall that the two parts of the second objective of this work are the evaluation of the feasibility of different neutron spectra measurements in MASURCA as a multi-purpose facility and the development of a detection system capable of characterizing them. An interesting exercise is to use a 100 % simulation approach for evaluating if the selected solution for the higher part of the energy domain (organic scintillators) is able to describe the MASURCA spectrum in a specific position. First, a simulation of the MASURCA core with the s-g stilbene detector located in the radial channel is done for evaluating to what extent the hydrogenated material (the scintillator) modifies the local neutron spectrum. Second, an MCNPX-Polimi plus MPPost simulation is performed for predicting the response of the detector.

The chosen MASURCA model is REF (Chapter III, **APPENDIX A**) and the position of the detector is the beginning of the radial channel, shown in Figure 7.28. The simulated scintillator is made of stilbene ($C_{14}H_{12}$) having the dimension of $\varnothing 25.4 \text{ mm} \times 25.4 \text{ mm}$. The PMT is simply represented by a volume of pure aluminum with the density of air [Bourne 2010]. The container of the scintillator and of the PMT is made of aluminum. Only neutrons were considered for the calculation.

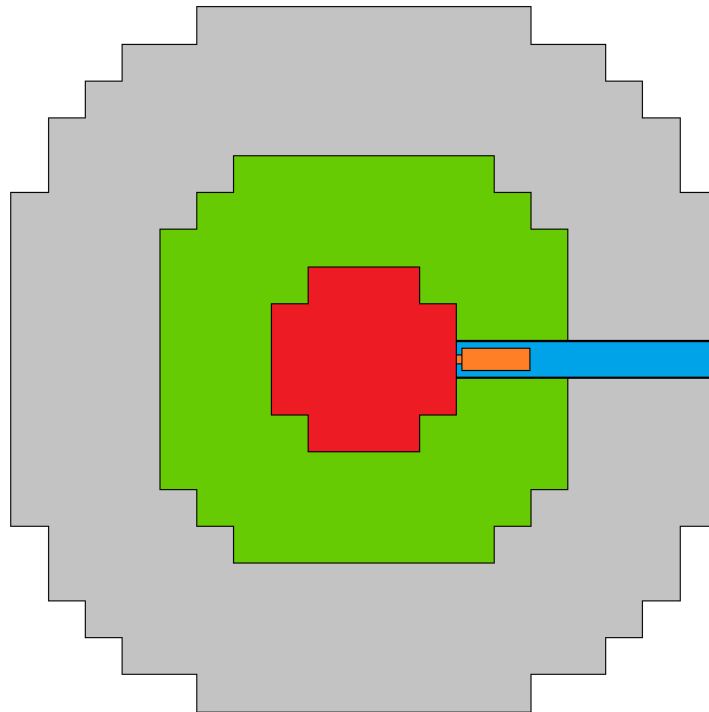


Figure 7.28. MASURCA REF model with the stilbene detector in the radial channel.

The computed k_{eff} values of the system with and without the stilbene detector are reported in table 7.2. The presence of the detector, a small volume of hydrogenated material plus some aluminum, leads only to a difference of 10 pcm between the two values.

Table X.1. Computed k_{eff} values for the two models.

	k_{eff}	1σ stat. unc.
REF	1.0141	5E-05
REF + Stilbene	1.0142	6E-05

A comparison between the neutron fluxes in the core with and without the detector (in a lin-log and a log-log scale) is done in Figure 7.29. The difference between the two can be seen only in the log-log representation, for the low-energy neutrons. No appreciable modification of the fast flux is noted, clarifying that the moderation in the stilbene detector is negligible.

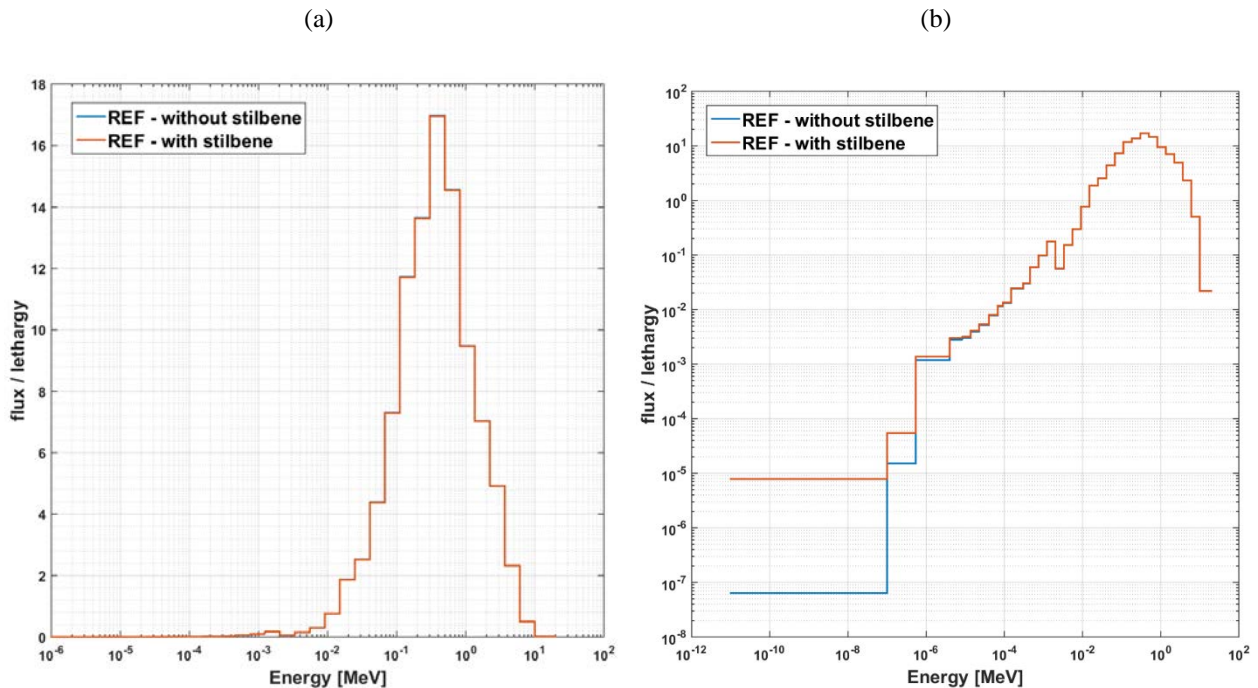


Figure 7.29. Comparison of the neutron fluxes in the fuel region in a (a) lin-log and a (b) log-log scale.

The behaviour of the neutron flux along the abscissa coordinate (at $y = 0$ and $z = 0$) is shown in Figure 7.30. The detector starts and ends at about $x = 20$ cm and $x = 40$ cm, respectively. A

difference in the radial neutron flux can be seen in this range, which corresponds to a percentage variation of 1.4 % (integrated flux between 20 cm and 40 cm). The total difference (integration over the whole x domain) is equal to 0.03 %. This confirms that the modification of the radial neutron flux introduced by the organic scintillator of dimension $\varnothing 25.4 \text{ mm} \times 25.4 \text{ mm}$ (plus PMT) is negligible and that such kind of detector is suitable also for in-core neutron (and gamma) spectrum measurements.

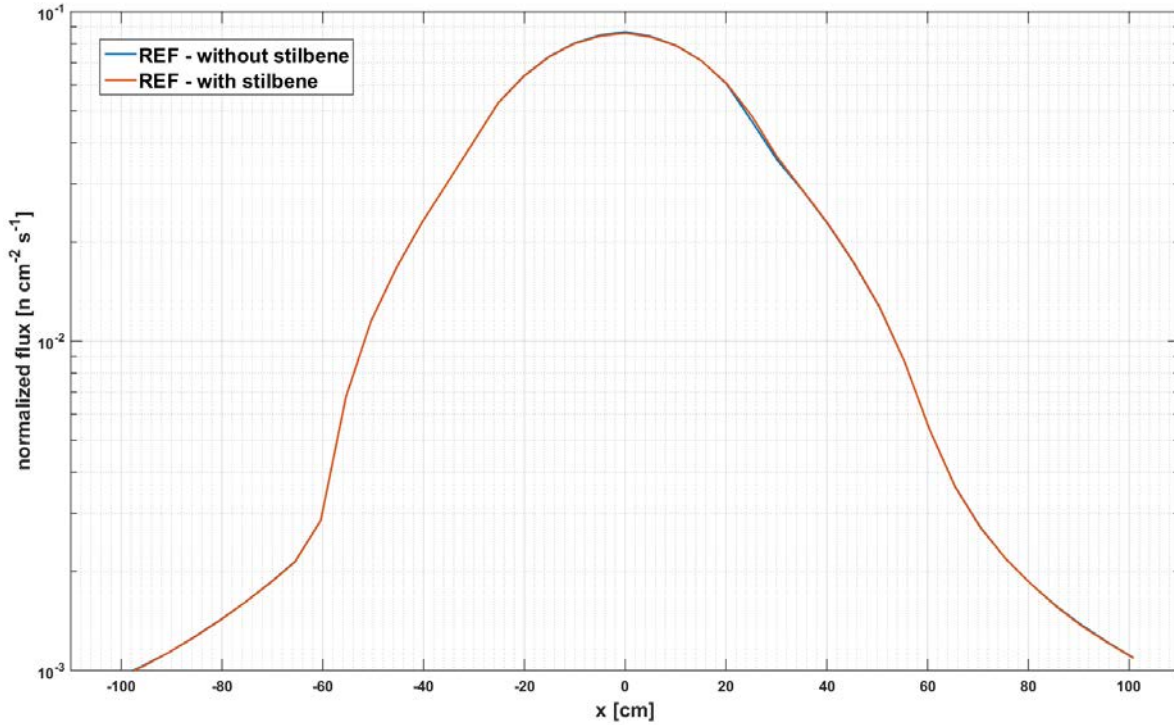


Figure 7.30. Flux traverse in the core at $z = 0$ and $y = 0$ as a function of relative x position (normalized).

The neutron spectrum used in the MCNPX-PoliMi simulation is the one plotted in Figure 7.29 (REF - without stilbene). The MCNPX-PoliMi plus MPPost simulation is similar to the one performed for LR-0 (7.3). Details can be found in **APPENDIX C**.

The proton recoil spectrum calculated by MPPost is presented in Figure 7.31a, while the comparison between the simulated MASURCA neutron spectrum at the beginning of the channel (Tripoli 4®) and the unfolded simulated PHS is in Figure 7.31b. A satisfying first evaluation of the fast neutron spectrum of MASURCA is achieved, although there are margins for improvement.

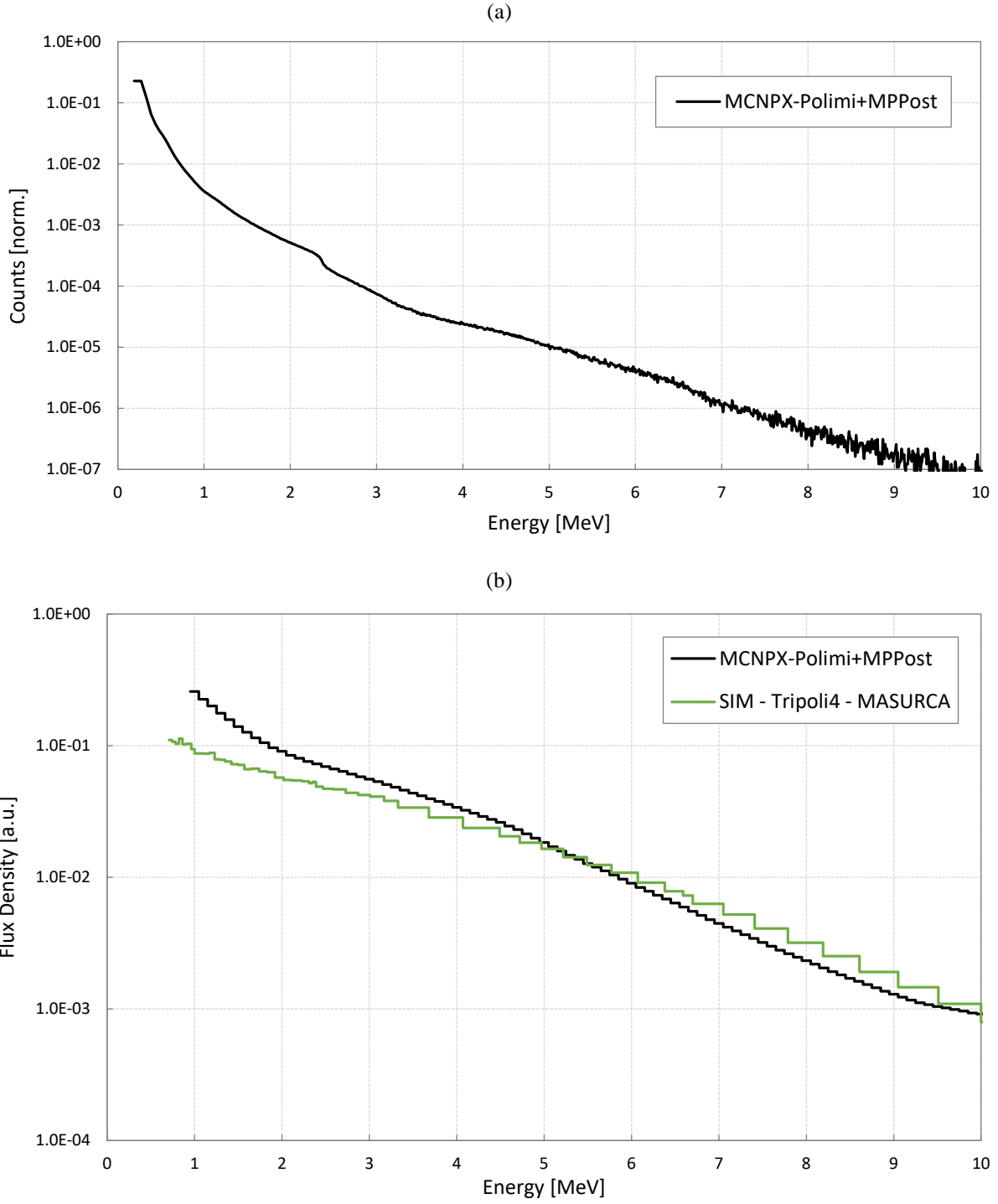


Figure 7.31. (a) Simulated MASURCA proton recoil spectrum and (b) comparison between the unfolded simulated spectrum and the simulated neutron spectrum.

VIII. Conclusion & Perspectives

8.1 Conclusion

8.2 Perspectives

8.1 Conclusion

MASURCA

In the first part of this work, the possibility of enlarging the capabilities of MASURCA was investigated by studying a new experimental configuration: MASURCA as a beam facility. This option is of particular interest as there are few fast neutron source reactors and ZPRs still in operation worldwide, although there are needs for several related research topics and applications remain of great interest.

Using MASURCA as a neutron source is practically feasible thanks to numerous favorable features of the reactor building and core characteristics (Chapter II). The properties of the potential neutron beam were studied by simulation (Monte Carlo) and the results compared to those of actual neutron beams delivered by the fast neutron source reactors YAYOI, TAPIRO and AFNS (Chapter III).

The general conclusion is that the MASURCA source configuration compares favorably with them. MASURCA could deliver a neutron beam having a maximum continuous intensity of $\sim 1 \times 10^8$ neutrons $\text{cm}^{-2} \text{s}^{-1}$ in the adjacent accelerator room (at $P = 5$ kW), with about 89% (resp. 75%) of the neutrons having energies above 10 keV (resp. 100 keV).

By adding this capability and by exploiting the potential of the installation, MASURCA could operate as a multi-purpose physics platform for:

- In-core and near-core studies, mainly (but not only) for validating neutron transport calculations in high-leakage SFR cores;
- Out-of-core researches, for beam-type applications.

A comparison with the past R&D programs of YAYOI, TAPIRO, etc. indicates that MASURCA could be used for:

- Fast neutron shielding and transport experiments;
- Delivery of standard (reference) fast neutron fields;
- Researches on advanced fast neutron detection systems;
- Studies of irradiation effects and neutron damage on organic materials, semi-conductors and metals;
- Fast neutron radiography.

FAST NEUTRON SPECTROSCOPY FOR RESEARCH REACTOR APPLICATIONS

The subject of the second part of this work was the development of an intermediate-to-fast (10 keV - 10 MeV) neutron spectrometric capability, flexible enough to accomplish the characterization of the neutron energy distribution in the foreseen experimental configurations. The instrumentation is intended to be a complementary system to the well-known fission chambers and activation foil detectors, already in use at MASURCA.

In-core neutron spectra measurements are characterized by a fairly high-intensity continuous fast flux (max 10^{11} neutrons $\text{cm}^{-2} \text{s}^{-1}$ at 5 kW, but adjustable at will to lower levels) and by experimental channels with a typical cross sectional area of $12.7 \text{ mm} \times 12.7 \text{ mm}$. Detectors for this type of

environment should be small enough to enter the experimental channels without perturbing too much the local neutron flux. Nevertheless, thanks to the possibility of installing larger channels (like the radial tube employed in the MUSE-4 campaign), bigger detectors were taken into consideration.

Near-core measurements are less restrictive in terms of space and therefore in terms of detector dimensions. However, due to the proximity of the concrete biological shield (and of the stainless steel shielding tubes), the neutron spectrum contains also lower-energy neutrons so that a spectrometer that is too sensitive to this fraction of neutrons would not be adequate.

Beam-type applications in the large, shielded, experimental room next to the core of MASURCA have similar constraints to those near the core. No problem related to the detector dimension exists, although the fraction of thermal neutrons is higher, due to ~ 1 meter of heavy concrete separating the two zones.

Gamma-ray background is always present in all the envisaged measurements, so that spectroscopy techniques insensitive or capable of discriminating between different radiations should be used. In this sense, the measurements are considered in mixed radiation field conditions.

Four candidates, flexible enough and with proper characteristics, were found and analyzed (Chapter IV) for the aforementioned task:

- Gas-filled detectors (ionization chambers and proportional counters);
- Organic scintillators;
- Solid-state detectors (semi-conductors and diamonds);
- Proton recoil telescopes.

Among them, a system based on the combination of proportional counters and organic scintillators was chosen as a solution for this project (and for the NEEDS-funded SPECTRAL project). Such a system is capable of providing the means for a fine-enough spectral characterization of neutron fields in the energy domain between 10 keV and 10 MeV (also higher, until 15 - 20 MeV). A set of proportional counters is typically used for covering the energy region between 10 keV and 1.15 MeV, while classical - liquid - organic scintillators, are employable from around 1 MeV.

Overlapping the two neutron spectra coming from the different detectors over a large interval is fundamental for normalization purposes. As the common energy region between proportional counters and liquid organic scintillators (BC501A, EJ-309, NE-213) is relatively low, the study of new organic scintillators was initiated.

A new type of single organic crystal, namely solution-grown stilbene, was selected and prototyped for this purpose (Chapter V). This new type of organic scintillator is expected to deliver higher performances than those of both liquid and traditional melt-grown stilbene crystal scintillators. However, no experimental data was available in the literature about the use of this novel crystal scintillator for research reactor applications, especially in- and near-core measurements in a ZPR and out-of-core conditions in an irradiation reactor.

For this reason, an experimental campaign for validating the use of s-g stilbene in such environments started in 2017 (Chapter VI). The main tests took place at AIFIRA (Bordeaux), LVR-15 and LR-0 (Rez).

The outcome of the experimental campaign was really satisfactory and positive. The use of s-g stilbene for research reactor applications was proven and validated (Chapter VII). It was possible to confirm the wider energy domain coverage compared with liquid scintillators. Also, thanks to the use of a digital system, the detector was able to characterize mixed radiations fields (fast neutrons and gamma-rays) having typical magnitudes of $10^5 - 10^6 \# \text{ cm}^{-2} \text{ s}^{-1}$. Furthermore, various parametric studies on FoMs, high-voltage linearity and on response anisotropy were performed to fully understand the capabilities and the limitations of the $\varnothing 25.4 \text{ mm} \times 25.4 \text{ mm}$ s-g stilbene. These researches will continue in the future.

Thanks to these experimental results, it is possible to conclude that the use of s-g stilbene and - in general - of organic scintillators, will provide the fast neutron spectrometric capability envisaged at the beginning of this work for the MASURCA facility. Furthermore, the combination with proportional counters will also provide the capability to characterize intermediate neutrons, and therefore to cover the continuous neutron energy domain between 10 keV and 10 MeV.

Limitations of this solution are mainly related to the acquisition rate and to the crystal dimensions. The first one is resolved by using digital systems, which allow relative high count rates, $\sim 10^6$ counts per second. The second one could be an issue only in the case of in-core measurements, if the use of a larger experimental channel (in MASURCA) is not possible. Potential solutions to this problem are proposed in the next Paragraph (8.2).

SIMULATION

Alongside the experimental campaign, a calculation procedure for simulating the scintillator response was tested and compared with the measured data. The scheme is based on MCNPX-PoliMi plus MPPost. It was found appropriate and satisfactory. The calculation results are particularly in good agreement with the experimental ones concerning mono-energetic neutron beams (AIFIRA) and smoothed neutron spectra (LR-0).

THE SPECTRAL PROJECT

The SPECTRAL project is aimed at developing a flexible, innovative detection system for mixed neutron-gamma radiation field spectrometry, the neutron energy region of interest being between 10 keV and 10 MeV. This is of interest not only for research reactor applications but, in general, for measurements of mixed radiations fields, *e.g.* continuous and pulsed neutron beams from accelerators, prompt and delayed fission neutrons in nuclear physics, transmission and shielding benchmarks, safeguards, fusion, medical applications, etc.

This PhD work contributed significantly to the SPECTRAL project.

8.2 Perspectives

SOLUTION-GROWN STILBENE

Further studies of the $\varnothing 25.4 \text{ mm} \times 25.4 \text{ mm}$ s-g stilbene detector are planned for the near future. The first will be the construction of its response matrix at reference installations dedicated to metrology and calibration, such as the AMANDE facility.

The re-evaluation of the measurements performed at LVR-15 and LR-0 will be done with the proper response matrix, together with the evaluation of new measurements performed in ZPRs.

The detector is going to be tested also in other mixed radiation fields for other applications such as neutron transmission and shielding experiments, and various nuclear physics measurements.

ORGANIC SCINTILLATORS FOR RESEARCH REACTOR APPLICATIONS

The limitation imposed by the dimension of the photomultiplier will also be addressed for in-core neutron flux measurements in ZPRs. Possible solutions are the use of silicon photomultipliers [Allier 1999, Herbert 2006] or the employment of optical fibers [Mori 1994, Yagi 2011] as optical guides connecting the organic scintillator inside the experimental channel to the photomultiplier located outside the core.

Other types of organic scintillators with isotropic response are going to be tested (mainly plastic but also liquid). This will be done for better understanding the role of anisotropy in in-core-type measurements with crystal scintillators.

CONTINUATION OF THE SPECTRAL PROJECT

The development of the combined spectroscopy system will continue in the future. The focus will be placed on the electronics for the organic scintillator part and on the detectors for the proportional counter part.

Furthermore, the project will try to enlarge its scope, by considering other types of instrumentation for intermediate-to-fast neutron spectroscopy. For example, diamond or semiconductor detectors for in-core measurements and proton recoil telescopes for beam-type applications.

References

- [Assal 2012] W. Assal, J.C. Bosq, F. Mellier. "Experimental Measurements at the MASURCA Facility." *IEEE Transactions on Nuclear Science* 59, n. 6 (2012) 3180-3188. doi:10.1109/TNS.2012.2215341.
- [Akijama 1998] Masatsugu Akiyama, Yoshiaki Oka, and Shigehiro An. "Measurement of Decay Heat of Fast Neutron Fission Products." *Progress in Nuclear Energy, Fast Neutron Reactor YAYOI and Related Nuclear Engineering Researches of the University of Tokyo*, 3-A Comprehensive Review, 32, no. 1 (January 1, 1998): 53-60. doi:10.1016/S0149-1970(97)00007-3.
- [Allen] W.D. Allen. Neutron Detection. WILLIAM CLOWES AND SONS, 1960.
- [Allier 1999] C.P. Allier, R.W. Hollander, P.M. Sarro, C.W.E. van Eijk. "Thin Photodiodes for a Scintillator-Silicon Well Detector." *IEEE Transactions on Nuclear Science* 46 (1999) 1948-1951.
- [Amudson 1969] P. I. Amudson, W. G. Davey, R. N. Curran, G. S. Brunson, and R. J. Huber. "Reactor Physics Measurements in the Argonne Fast Source Reactor." Argonne National Lab., Idaho Falls, Idaho (United States), October 31, 1969. <http://www.osti.gov/scitech/biblio/4764378/>.
- [Angelone 1998] M. Angelone et al. "APD Irradiation in Support to CMS Experiences." CMS NOTE 1998/060 (1998).
- [Angelone 2010] M. Angelone et al. "Self Powered Neutron Detectors." Final Report on Task 3.1.1 - F4E-2010-GRT-056-02 (ES-AC) on Nuclear Data Studies/Experiments in Support of TBM Activities (2010).
- [Astrid] Fourth-generation Sodium-cooled Fast Reactors – The ASTRID Technological Demonstrator, Online CEA Report: <http://www.cea.fr/english/Documents/corporate-publications/4th-generation-sodium-cooled-fast-reactors.pdf>.
- [Baker 2008] J. H. Baker, N. Z. Galunov, and O. A. Tarasenko. "Variation of Scintillation Light Yield of Organic Crystalline Solids for Different Temperatures." *IEEE Transactions on Nuclear Science* 55, no. 5 (October 2008): 2736-38. doi:10.1109/TNS.2008.2002146.
- [Bartlett 2003] D.T. Bartlett, J.-L. Chartier, M. Matzke, A. Rimpler, D.J. Thomas. "Concepts and Quantities in Spectrometry and Radiation Protection."

Radiation Protection Dosimetry 107, no. 1–3 (November 1, 2003): 23-35.

- [BC501A - Saint Gobain] http://www.crystals.saint-gobain.com/sites/imdf.crystals.com/files/documents/sgc-bc501-501a-519-data-sheet_69711.pdf.
- [Bechurts&Wirtz] K.H. Beckurts and K. Wirtz. *Neutron Physic*. Springer-Verlag (1964).
- [Beckurts 1962] K.H. Beckurts, P.A. Egelstaff and H. Goldstein. "SPECIAL BEAMS FROM REACTORS AND ACCELERATORS." *Journal of Nuclear Energy Parts A/B* 17, n. 4/5 (1962).
- [Bertrand 2015] Guillaume H. V. Bertrand, Matthieu Hamel, Stéphane Normand, and Fabien Sguerra. "Pulse Shape Discrimination between (Fast or Thermal) Neutrons and Gamma Rays with Plastic Scintillators: State of the Art." *Nuclear Instruments and Methods in Physics Research Section A: Accelerators, Spectrometers, Detectors and Associated Equipment* 776 (March 11, 2015): 114-28. doi:10.1016/j.nima.2014.12.024.
- [Bignan 2008] G. Bignan, A. Zaetta, P. Fougeras, R. Jacqmin, J. C. Bosq, J. C. Klein, A. Lyoussi, F. Mellier, P. Blaise, A. Chabre, P. Sacristan. "Experimental Reactor Physics Perspectives in France." *International Conference on the Physics of Reactors "Nuclear Power: A Sustainable Resource"*, Interlaken (Switzerland) September 14-19 (2008).
- [Bignan 2010] G. Bignan, P. Fougeras, P. Blaise, J.-P. Hudelot, F. Mellier. *Handbook of Nuclear Engineering, Chapter 18: "Reactor Physic Experiments on Zero Power Reactors."* Springer (2010).
- [Bignan 2011] G. Bignan; J.-F. Villard, C. Destouches, P. Baeten, L. Vermeeren, S. Michiels. "The Key-role of Instrumentation for the New Generation of Research Reators." *IEEE Transactions on Nuclear Science* (2011).
- [Birks] J. B. Birks. *The Theory and Practice of Scintillation Counting*. Pergamon (1964)
- [Blaise 2016] P. Blaise, F. Boussard, P. Ros, P. Leconte, M. Margulis, G. Martin, K. Blandin. "Experimental R&D innovation for Gen-II,III & IV neutronics studies in ZPRs: a path to the future ZEPHYR facility in Cadarache." *IGORR 2016* (2016)
- [Bollinger & Thomas 1961] L.M. Bollinger and G.E. Thomas. "Measurement of the Time Dependence of Scintillation Intensity by a Delay-Coincidence Method." *The Review of Scientific Instruments* 32, n. 9 (1961).

- [Bourne 2010] M.M. Bourne, S.D. Clarke, E.C. Miller, M. Flaska, S.A. Pozzi. "Measurement of Detector Resolution for Neutral Particle Detection with Liquid Scintillators." *IEEE* (2010) 981-985.
- [Bourne 2016] M. M. Bourne, S. D. Clarke, N. Adamowicz, S. A. Pozzi, N. Zaitseva, and L. Carman. "Neutron Detection in a High-Gamma Field Using Solution-Grown Stilbene." *Nuclear Instruments and Methods in Physics Research Section A: Accelerators, Spectrometers, Detectors and Associated Equipment* 806 (January 11, 2016): 348–55. doi:10.1016/j.nima.2015.10.025.
- [Bourne 2017] M. M. Bourne, S. D. Clarke, M. Paff, A. DiFulvio, M. Norsworthy, and S. A. Pozzi. "Digital Pile-up Rejection for Plutonium Experiments with Solution-Grown Stilbene." *Nuclear Instruments and Methods in Physics Research Section A: Accelerators, Spectrometers, Detectors and Associated Equipment* 842 (January 11, 2017): 1–6. doi:10.1016/j.nima.2016.10.023.
- [Broek & Anderson 1960] H.W Broek and C.E. Anderson. "The Stilbene Scintillation Crystal as a Spectrometer for Continuous Fast-Neutron Spectra." *Review of Scientific Instruments* 31 (1960).
- [Brooks & Jones 1974] F. D. Brooks, and D. T. L. Jones. "Directional Anisotropy in Organic Scintillation Crystals." *Nuclear Instruments and Methods* 121, no. 1 (October 1, 1974): 69–76. doi:10.1016/0029-554X(74)90141-4.
- [Brooks & Klein 2002] F. D Brooks, and H Klein. "Neutron Spectrometry - Historical Review and Present Status." *Nuclear Instruments and Methods in Physics Research Section A: Accelerators, Spectrometers, Detectors and Associated Equipment, Int. Workshop on Neutron Field Spectrometry in Science, Technology and Radiation Protection*, 476, no. 1–2 (January 1, 2002): 1–11. doi:10.1016/S0168-9002(01)01378-X.
- [Brooks 1956] F.D. Brooks. "Liquid Scintillation Counting." *Progress in Nuclear Physics* 5 (1956)
- [Budakovsky 1990] Sergei Budakovsky, Nikolai Galunov, and Igor Krainov. "The Growth of Stilbene Single Crystals with High Structural Perfection." *Molecular Crystals and Liquid Crystals Incorporating Nonlinear Optics* 186, no. 1 (August 1, 1990): 159–66. doi:10.1080/00268949008037206.
- [Caiffi 2015] B. Caiffi, M. Osipenko, M. Ripani, M. Pillon, and M. Taiuti. "Proton Recoil Telescope Based on Diamond Detectors for Measurement of Fusion Neutrons." arXiv:1505.06316 [Nucl-Ex, Physics:physics], May 23, 2015. <http://arxiv.org/abs/1505.06316>.
- [Cambiaghi 1970] M. Cambiaghi, F. Fossati, and T. Pinelli. "Fast Neutron Spectrometry with Identification of Recoil Protons." *Nuclear Instruments and*

Methods 82 (May 30, 1970): 106–8. doi:10.1016/0029-554X(70)90332-0.

- [Carman 2013] Leslie Carman, Natalia Zaitseva, H. Paul Martinez, Benjamin Rupert, Iwona Pawelczak, Andrew Glenn, Heather Mulcahy, Roald Leif, Keith Lewis, and Stephen Payne. “The Effect of Material Purity on the Optical and Scintillation Properties of Solution-Grown Trans-Stilbene Crystals.” *Journal of Crystal Growth* 368 (April 1, 2013): 56–61. doi:10.1016/j.jcrysgro.2013.01.019.
- [Carta 1982] M. Carta et al. "Spectrum Characterization in a Simulated FR Blanket Region via Activation of Threshold and Continuous Detectors." *Proc. of the Fourth ASTM-EURATOM Symposium on Reactor Dosimetry*, NUREG/CP 0029, Vol. I, 211, Gaithersburg, Maryland (1982)
- [Chabre&Bonin] A. Chabre and B. Bonin. *Reacteurs Nucleaires Experimentaux* (2012).
- [Chernov 2002 (1)] V. A. Chernov, V. P. Semenov, and L. A. Trykov. “Spectrometer Equipment for Neutron Spectra Measurements in Mixed Neutron/Photon Fields.” *Nuclear Instruments and Methods in Physics Research Section A: Accelerators, Spectrometers, Detectors and Associated Equipment, Int. Workshop on Neutron Field Spectrometry in Science, Technology and Radiation Protection*, 476, no. 1–2 (January 1, 2002): 374–77. doi:10.1016/S0168-9002(01)01473-5.
- [Chernov 2002 (2)] V. A Chernov, V. P Semenov, and L. A Trykov. “Spectrometer Equipment for Photon Spectra Measurements in Mixed Neutron/Photon Fields.” *Nuclear Instruments and Methods in Physics Research Section A: Accelerators, Spectrometers, Detectors and Associated Equipment, Int. Workshop on Neutron Field Spectrometry in Science, Technology and Radiation Protection*, 476, no. 1–2 (January 1, 2002): 218–21. doi:10.1016/S0168-9002(01)01435-8.
- [Cherubini 1989] R. Cherubini, G. Moschini, R. Nino, R. Policroniades, and A. Varela. “Gamma Calibration of Organic Scintillators.” *Nuclear Instruments and Methods in Physics Research Section A: Accelerators, Spectrometers, Detectors and Associated Equipment* 281, no. 2 (September 1, 1989): 349–52. doi:10.1016/0168-9002(89)91332-6.
- [Clarke 2017] S. D. Clarke, B. M. Wieger, A. Enqvist, R. Vogt, J. Randrup, R. C. Haight, H. Y. Lee, et al. “Measurement of the Energy and Multiplicity Distributions of Neutrons from the Photofission of ^{235}U .” *Physical Review C* 95, no. 6 (June 20, 2017): 064612. doi:10.1103/PhysRevC.95.064612.
- [Cvachovec 2002] F Cvachovec, J Cvachovec, and P Tajovsky. “Anisotropy of Light Output in Response of Stilbene Detectors.” *Nuclear Instruments and Methods in Physics Research Section A: Accelerators, Spectrometers,*

Detectors and Associated Equipment, Int. Workshop on Neutron Field Spectrometry in Science, Technology and Radiation Protection, 476, no. 1 (January 1, 2002): 200–202. doi:10.1016/S0168-9002(01)01431-0.

- [Cvachovec 2007] J. Cvachovec, F. Cvachovec. "Maximum Likelihood Estimation of Neutron Spectrum and Associated Uncertainties." *Advances in Military Technology*, Vol. 3, No. 2 (2008).
- [D'Angelo 1973] A. D'Angelo et al. "The TAPIRO Fast Source Reactor as a Benchmark for Nuclear Data Testing." *Energia Nucleare* 20, n. 11 (1973): 614-621.
- [De Boer 2007] Wim de Boer, Johannes Bol, Alex Furgeri, Steffen Müller, Christian Sander, Eleni Berdermann, Michal Pomorski, and Mika Huhtinen. "Radiation Hardness of Diamond and Silicon Sensors Compared." *Physica Status Solidi (a)* 204, no. 9 (September 1, 2007): 3004–10. doi:10.1002/pssa.200776327.
- [De Caroli 1980] A. De Caroli et al. "Propagation Experiments in Steel-sodium Mixtures at TAPIRO." *Nuclear Energy Agency Committee on Reactor Physics*, Paris (France) 27-29 (1980)
- [Dietze & Klein 1982] G. Dietze, and H. Klein. "Gamma-Calibration of NE 213 Scintillation Counters." *Nuclear Instruments and Methods in Physics Research* 193, no. 3 (March 1, 1982): 549–56. doi:10.1016/0029-554X(82)90249-X.
- [Dioni 2016 (1)] L. Dioni, R. Jacqmin, B. Stout, M. Sumini. "Developing a Fast Neutron Beam Capability in the MASURCA Facility: Spectrum and Intensity Evaluation." *PHYSOR 2016: Unifying Theory and Experiments in the 21st Century* (2016).
- [Dioni 2016 (2)] L. Dioni, R. Jacqmin, B. Stout, M. Sumini. "A Multipurpose Fast Neutron Beam Capability at the MASURCA Facility." *ANIMMA 2015: International Conference on Advancements in Nuclear Instrumentation Measurement Methods and their Applications* (2016).
- [Dioni 2017 (1)] L. Dioni, R. Jacqmin, B. Stout, M. Sumini. "On the Possible Use of the MASURCA Reactor as a Flexible, High-intensity, Fast Neutron Beam Facility." *ND 2016: International Conference on Nuclear Data for Science and Technology* (2017).
- [Dioni 2017 (2)] L. Dioni, V. Gressier, G. Nardin, R. Jacqmin, B. Stout, M. Sumini. "Test of a Solution-grown Stilbene Scintillator in Mono-energetic Neutron Beams of 565 keV and 5 MeV." *Nuclear Instrumentation and Methods in Physics Research A* (2017): accepted.
- [Eranos] G. Rimpault, D. Plisson, J. Tommasi, R. Jacqmin, J.-M. Rieunier, D. Verrier, D. Biron et al. "The ERANOS code and data system for fast reactor neutronic analyses." *PHYSOR 2002, Seoul, KOREA* (2002).

- [Fowler & Ross 1955] J.M. Fowler and C.E. Ross. "Response of Anthracene and Stilbene to Low-Energy Protons and X-Rays." *Physical Review* 98, n. 4 (1955).
- [Fowler&Marion (1)] J. L. Fowler J. B. Marion. *Fast Neutron Physics - Part I*. Vol. 4. Interscience Publisher (1960).
- [Fowler&Marion (2)] J. L. Fowler J. B. Marion. *Fast Neutron Physics - Part II*. Vol. 4. Interscience Publisher (1963).
- [Galunov 1997] N.Z. Galunov and V.P. Seminozhenko. *The Theory and Application of the Radioluminescence of Organic Condensed Media* (in Russian). Kiev, Ukraine (1997).
- [Galunov 2013] N.Z. Galunov, O.A. Tarasenko, V.A. Tarasov. "Determination of the light yield of organic scintillators." *Functional Materials* 20, n. 3 (2013).
- [Giomataris 1996] Y. Giomataris, Ph. Rebourgeard, J. P. Robert, and G. Charpak. "MICROMEGAS: A High-Granularity Position-Sensitive Gaseous Detector for High Particle-Flux Environments." *Nuclear Instruments and Methods in Physics Research Section A: Accelerators, Spectrometers, Detectors and Associated Equipment* 376, no. 1 (June 21, 1996): 29–35. doi:10.1016/0168-9002(96)00175-1.
- [Gressier 2004] V. Gressier, J. F. Guerre-Chaley, V. Lacoste, L. Lebreton, G. Pelcot, J. L. Pochat, T. Bolognese-Milstajn, and D. Champion. "AMANDE: A New Facility for Monoenergetic Neutron Fields Production between 2 keV and 20 MeV." *Radiation Protection Dosimetry* 110, no. 1–4 (August 1, 2004): 49–52. doi:10.1093/rpd/nch185.
- [Gressier 2013] V. Gressier, IRSN report PRP-HOM/SDE/2013-27
- [Haight 2014] R. C. Haight, H. Y. Lee, T. N. Taddeucci, J. M. O'Donnell, B. A. Perdue, N. Fotiades, M. Devlin, et al. "The Prompt Fission Neutron Spectrum (PFNS) Measurement Program at LANSCE." *Nuclear Data Sheets* 119 (May 1, 2014): 205–8. doi:10.1016/j.nds.2014.08.057.
- [Harada 2009] H. Harada, S. Nakamura, Y. Hatsukawa, Y. Toh, A. Kimura, Y. Ishiwatari, A. Yasumi, et al.; "Measurements of Neutron Capture Cross Section of ²³⁷Np for Fast Neutrons"; *Journal of Nuclear Science and Technology* 46; n. 5 (2009) 460-468. doi:10.1080/18811248.2007.9711553.
- [Harrer] Joseph M. Harrer, and James G. Beckerley. *Nuclear Power Reactor Instrumentation Systems Handbook*. Office of Information Services, U.S. Atomic Energy Commission (1974).

- [Herbert 2006] D.J. Herbert, V. Saveliev, N. Belcari, N. D'Ascenzio, A. Del Guerra, A. Golovin. "First Results of Scintillator Readout With Silicon Photomultiplier." *IEEE Transaction on Nuclear Science* 53 (2006) 389-394.
- [ICRU 2011] "FUNDAMENTAL QUANTITIES AND UNITS FOR IONIZING RADIATION (Revised)." ICRU REPORT No. 85 (2011).
- [Jansky 2002] B Janský, E Novák, Z Turzík, J Kyncl, F Cvachovec, L. A Trykov, and V. S Volkov. "Neutron and Gamma Spectra Measurements and Calculations in Benchmark Spherical Iron Assemblies with ²⁵²Cf Neutron Source in the Centre." *Nuclear Instruments and Methods in Physics Research Section A: Accelerators, Spectrometers, Detectors and Associated Equipment, Int. Workshop on Neutron Field Spectrometry in Science, Technology and Radiation Protection*, 476, no. 1–2 (January 1, 2002): 358–64. doi:10.1016/S0168-9002(01)01470-X.
- [Jansky 2014] Bohumil Jansky, and Evzen Novak. "Neutron Spectrometry with Spherical Hydrogen Proportional Detectors." *Nuclear Instruments and Methods in Physics Research Section A: Accelerators, Spectrometers, Detectors and Associated Equipment* 735 (January 21, 2014): 390–98. doi:10.1016/j.nima.2013.08.034.
- [Jeff 3.1] https://www.oecd-nea.org/dbforms/data/eva/evatapes/jeff_31/.
- [Jie 2010] Yan Jie, Liu Rong, Li Cheng, Jiang Li, Lu Xin-Xin, and Zhu Tong-Hua. "Energy Calibration of a BC501A Liquid Scintillator Using a γ - γ Coincidence Technique." *Chinese Physics C* 34, no. 7 (2010): 993. doi:10.1088/1674-1137/34/7/012.
- [King & Birks 1952] J.W. King and J.B. Birks. *Physical Review* 86 (1952)
- [Klein 2003] H. Klein. "Neutron Spectrometry in Mixed Fields: NE213/BC501A Liquid Scintillation Spectrometers." *Radiation Protection Dosimetry* 107, no. 1–3 (November 1, 2003): 95–109.
- [Klimenkov 2004] E. E. Klimenkov, Yu A. Kashchuk, A. V. Krasil'nikov, A. A. Oleinikov, V. D. Sevast'yanov, L. A. Trykov, and N. N. Semenova. "Radiation Hardness of a Fast Neutron Scintillation Spectrometer with a Stilbene Crystal." *Instruments and Experimental Techniques* 47, no. 2 (March 1, 2004): 166–67. doi:10.1023/B:INET.0000025195.61810.11.
- [Knoll] G. F. Knoll. *Radiation Detection and Measurement*. IV Edition, Wiley (2010).
- [Koleska 2015] Michal Kolečka, Zdena Lahodová, Jaroslav Šoltés, Ladislav Viererbl, Jaroslav Ernest, Miroslav Vinš, and Josef Stehno. "Capabilities of the LVR-15 Research Reactor for Production of Medical and Industrial

Radioisotopes.” *Journal of Radio-analytical and Nuclear Chemistry* 305, no. 1 (July 1, 2015): 51–59. doi:10.1007/s10967-015-4025-5.

[Kornilov 2009]

Kornilov, N. V., I. Fabry, S. Oberstedt, and F. -J. Hamsch. “Total Characterization of Neutron Detectors with a ²⁵²Cf Source and a New Light Output Determination.” *Nuclear Instruments and Methods in Physics Research Section A: Accelerators, Spectrometers, Detectors and Associated Equipment* 599, no. 2–3 (February 11, 2009): 226–33. doi:10.1016/j.nima.2008.10.032.

[Koshizuka 1998]

S. Koshizuka, K. Okamoto, and K. Furuta. “Development of Computational Techniques for Nuclear Engineering.” *Progress in Nuclear Energy, Fast Neutron Reactor YAYOI and Related Nuclear Engineering Researches of the University of Tokyo* 3-A Comprehensive Review, 32, no. 1 (January 1, 1998): 209–22. doi:10.1016/S0149-1970(97)00017-6.

[Kostal 2011]

Košťál, Michal, František Cvachovec, Jiří Cvachovec, Bohumil Ošmera, and Wolfgang Hansen. “Determination of AKR-2 Leakage Beam and Verification at Iron and Water Arrangements.” *Annals of Nuclear Energy* 38, no. 1 (January 2011): 157–65. doi:10.1016/j.anucene.2010.07.005.

[Kostal 2016]

Košťál, Michal, František Cvachovec, Bohumil Jánský, Vojtěch Rypar, Vlastimil Juříček, Davit Harutyunyan, Martin Schulc, Ján Milčák, Evžen Novák, and Sergey Zaritsky. “Neutron Deep Penetration through Reactor Pressure Vessel and Biological Concrete Shield of VVER-1000 Mock-Up in LR-0 Reactor.” *Annals of Nuclear Energy* 94 (August 2016): 672–83. doi:10.1016/j.anucene.2016.04.014.

[Kostal 2017 (private)]

Private talk, May 2017.

[Kostal 2017]

Košťál, Michal, Zdeněk Matěj, František Cvachovec, Vojtěch Rypar, Evžen Losa, Jiří Rejchrt, Filip Mravec, and Martin Veškna. “Measurement and Calculation of Fast Neutron and Gamma Spectra in Well Defined Cores in LR-0 Reactor.” *Applied Radiation and Isotopes* 120 (February 2017): 45–50. doi:10.1016/j.apradiso.2016.11.004.

[Leconte 2016]

Internal Report.

[Lee 2013]

H. Y. Lee, T. N. Taddeucci, R. C. Haight, T. A. Bredeweg, A. Chyzh, M. Devlin, N. Fotiadis, et al. “Li-Glass Detector Response Study with a ²⁵²Cf Source for Low-Energy Prompt Fission Neutrons.” *Nuclear Instruments and Methods in Physics Research Section A: Accelerators, Spectrometers, Detectors and Associated Equipment* 703 (March 1, 2013): 213–19. doi:10.1016/j.nima.2012.10.137.

- [Love & Murray 1961] T. A. Love, and R. B. Murray. "The Use of Surface-Barrier Diodes for Fast-Neutron Spectroscopy." *IRE Transactions on Nuclear Science* 8, no. 1 (January 1961): 91–97. doi:10.1109/TNS2.1961.4315805.
- [Lyoussi] Abdallah Lyoussi. *Détection de rayonnements et instrumentation nucléaire*. EDP Sciences (2010).
- [Maire 2013] D. Maire et al. "μ-TPC: a Future Standard Instrument for Low Energy Neutron Field Characterization", *IEEE Transactions on Nuclear Science* (2013).
- [Marini 2016] P. Marini, L. Mathieu, M. Aïche, S. Czajkowski, B. Jurado, and I. Tsekhanovich. "Development of a Gaseous Proton-Recoil Detector for Fission Cross Section Measurements below 1 MeV Neutron Energy." *EPJ Web of Conferences* 111 (2016): 11001. doi:10.1051/epjconf/20161111001.
- [Mellier 2005] F. Mellier (Co-ordinator). "The MUSE experiments for sub critical neutronics validation." Final report of the EU-supported project MUSE; Contract No: FIKW-CT-2000-00063 (2005).
- [Miller 2012] E.C. Miller, S.D. Clark, M. Flaska, S. Prasad, S.A. Pozzi, E. Padovani, *Journal of Nuclear Materials Management* (2012), vol. XL, n. 2
- [Mori 1994] C. Mori et al. "Simple and Quick Measurement of Neutron Flux Distribution by Using an Optical Fiber with Scintillator." *Journal of Nuclear Science and Technology* 31 (1994) 248-249.
- [Nagasaki 1998] S. Nagasaki, S. Tanaka, and A. Suzuki. "Geochemical Behavior of Actinides in High-Level Radioactive Waste Disposal." *Progress in Nuclear Energy, Fast Neutron Reactor YAYOI and Related Nuclear Engineering Researches of the University of Tokyo\3-A Comprehensive Review*, 32, no. 1 (January 1, 1998): 141–61. doi:10.1016/S0149-1970(97)00013-9.
- [Nakazawa 1998] M. Nakazawa, T. Iguchi, H. Takahashi, E. Takada. "Standard Neutron Fields and Researches on Advanced Nuclear Measurement Technique." *Progress in Nuclear Energy, Fast Neutron Reactor YAYOI and Related Nuclear Engineering Researches of the University of Tokyo\3-A Comprehensive Review* 32, n. 1 (1998) 25-41. doi:10.1016/S0149-1970(97)00005-X.
- [NIST - ESTAR and PSTAR] <http://physics.nist.gov/PhysRefData/Star/Text/ESTAR.html> & <http://physics.nist.gov/PhysRefData/Star/Text/PSTAR.html>.
- [Oka 1980] Y. Oka. "Neutron and Gamma-Ray Penetrations in Thick Iron." *Nuclear Science and Engineering* 73 (1980) 259-273.

- [Oka 1981] Y. Oka. "Neutron Penetrations Through Thick Sodium." *Technical Note* (1981).
- [Oka 1998 (1)] Y. Oka, S. Koshizuka, I. Saito, K. Okamura, N. Aizawa, N. Sasuga, T. Sukegawa, et al. "Fast Neutron Source Reactor, YAYOI." *Progress in Nuclear Energy, Fast Neutron Reactor YAYOI and Related Nuclear Engineering Researches of the University of Tokyo\3-A Comprehensive Review*, 32, no. 1 (January 1, 1998): 3–10. doi:10.1016/S0149-1970(97)00003-6.
- [Oka 1998 (2)] Y. Oka, K. Furuta, and S. An. "Fast Neutron Shielding and Neutron Transport Studies at YAYOI." *Progress in Nuclear Energy, Fast Neutron Reactor YAYOI and Related Nuclear Engineering Researches of the University of Tokyo\3-A Comprehensive Review*, 32, no. 1 (January 1, 1998): 11–23. doi:10.1016/S0149-1970(97)00004-8.
- [Oka 1998 (3)] Y. Oka, and S. Koshizuka. "Conceptual Design Study of Advanced Power Reactors." *Progress in Nuclear Energy, Fast Neutron Reactor YAYOI and Related Nuclear Engineering Researches of the University of Tokyo\3-A Comprehensive Review*, 32, no. 1 (January 1, 1998): 163–77. doi:10.1016/S0149-1970(97)00014-0.
- [Osipenko 2015 (1)] M. Osipenko, F. Pompili, M. Ripani, M. Pillon, G. Ricco, B. Caiffi, R. Cardarelli, G. Verona-Rinati, and S. Argiro. "Test of a Prototype Neutron Spectrometer Based on Diamond Detectors in a Fast Reactor." May 23, 2015.
- [Osipenko 2015 (2)] M. Osipenko, M. Ripani, G. Ricco, B. Caiffi, F. Pompili, M. Pillon, M. Angelone, et al. "Neutron Spectrometer for Fast Nuclear Reactors." *Nuclear Instruments and Methods in Physics Research Section A: Accelerators, Spectrometers, Detectors and Associated Equipment* 799 (November 2015): 207–13. doi:10.1016/j.nima.2015.07.050.
- [Osipenko 2016] M. Osipenko, M. Ripani, G. Ricco, B. Caiffi, F. Pompili, M. Pillon, G. Verona-Rinati, and R. Cardarelli. "Response of Diamond Detector Sandwich to 14 MeV Neutrons." *Nuclear Instruments and Methods in Physics Research Section A: Accelerators, Spectrometers, Detectors and Associated Equipment* 817 (May 2016): 19–25. doi:10.1016/j.nima.2016.02.008.
- [Owen 1958] R.B. Owen. "Pulse Shape Discrimination - a Survey of Current Techniques." *I.R.E. Trans. Nucl. Sci.* (1958).
- [Pichenot 2002] G Pichenot, S Guldbakke, B Asselineau, V Gressier, C Itié, H Klein, K Knauf, et al. "Characterisation of Spherical Recoil Proton Proportional Counters Used for Neutron Spectrometry." *Nuclear Instruments and Methods in Physics Research Section A: Accelerators, Spectrometers, Detectors and Associated Equipment, Int. Workshop on Neutron Field*

Spectrometry in Science, Technology and Radiation Protection, 476, no. 1 (January 1, 2002): 165–69. doi:10.1016/S0168-9002(01)01424-3.

- [Pozzi 2003] Sara A Pozzi, Enrico Padovani, and Marzio Marseguerra. “MCNP-PoliMi: A Monte-Carlo Code for Correlation Measurements.” *Nuclear Instruments and Methods in Physics Research Section A: Accelerators, Spectrometers, Detectors and Associated Equipment* 513, no. 3 (November 11, 2003): 550–58. doi:10.1016/j.nima.2003.06.012.
- [Pozzi 2013] S. A. Pozzi, M. M. Bourne, and S. D. Clarke. “Pulse Shape Discrimination in the Plastic Scintillator EJ-299-33.” *Nuclear Instruments and Methods in Physics Research Section A: Accelerators, Spectrometers, Detectors and Associated Equipment* 723 (September 21, 2013): 19–23. doi:10.1016/j.nima.2013.04.085.
- [Rosi 2004] G. Rosi, G. Gambarini, V. Colli, S. Gay, L. Scolari, O. Fiorani, A. Perrone, et al. “Characterisation of the TAPIRO BNCT Thermal Facility.” *Radiation Protection Dosimetry* 110, n. 1-4 (2004) 651–154. doi:10.1093/rpd/nch172.
- [Salvatore 2007] D. Salvatore, P. Branchini, S. Di Luise, E. Graziani, C. Mazzotta, E. Meoni, G. Morello, et al. “Neutron Intensive Irradiation Test on ATLAS MDT Chambers at TAPIRO Nuclear Reactor.” *Nuclear Physics. B, Proceedings Supplements* 172 (2007) 183–186. doi:10.1016/j.nuclphysbps.2007.08.005.
- [Sardet 2015] A. Sardet, C. Varignon, B. Laurent, T. Granier, and A. Oberstedt. “P-Terphenyl: An Alternative to Liquid Scintillators for Neutron Detection.” *Nuclear Instruments and Methods in Physics Research Section A: Accelerators, Spectrometers, Detectors and Associated Equipment* 792 (August 21, 2015): 74–80. doi:10.1016/j.nima.2015.04.038.
- [Schmidt 2002] D. Schmidt, B. Asselineau, R. Bottinger, H. Klein, L. Lebreton, S. Neumann, R. Nolte, G. Pichenot. “Characterization of a liquid scintillation detector.” *Nuclear Instruments and Methods in Physics Research Section A: Accelerators, Spectrometers, Detectors and Associated Equipment* 476(2002)186-189.
- [Schuster & Brubaker 2017] Schuster, P., and E. Brubaker. “Characterization of the Scintillation Anisotropy in Crystalline Stilbene Scintillator Detectors.” *Nuclear Instruments and Methods in Physics Research Section A: Accelerators, Spectrometers, Detectors and Associated Equipment* (2017). doi:10.1016/j.nima.2016.11.016.
- [Shin 1980] K. Shin, T. Nishibe, R. Murakami, H. Fujita, T. Hyodo, Y. Oka, S. An. “Fast Neutron Spectra Transmitted through Iron and Sodium Slabs.”

Journal of Nuclear Science and Technology 17, n. 1 (1980) 37–43.
doi:10.3327/jnst.17.37.

[Sorieul 2014]

S. Sorieul, Ph. Alfaut, L. Daudin, L. Serani, and Ph. Moretto. “Aifira: An Ion Beam Facility for Multidisciplinary Research.” *Nuclear Instruments and Methods in Physics Research Section B: Beam Interactions with Materials and Atoms, 21st International Conference on Ion Beam Analysis*, 332 (August 1, 2014): 68–73.
doi:10.1016/j.nimb.2014.02.032.

[Stilbene - InradOptics]

http://www.inradoptics.com/pdfs/datasheets/InradOptics_Datasheet_Stilbene_Final.pdf.

[Tagziria 2003]

H. Tagziria, and W. Hansen. “Neutron Spectrometry in Mixed Fields: Proportional Counter Spectrometers.” *Radiation Protection Dosimetry* 107, no. 1–3 (November 1, 2003): 73–93.

[Tanaka 1998]

Satoru Tanaka, Takayuki Terai, and Michio Yamawaki. “Study on Tritium Release from Solid Breeding Materials Using the Research Reactor ‘YAYOI.’” *Progress in Nuclear Energy, Fast Neutron Reactor YAYOI and Related Nuclear Engineering Researches of the University of Tokyo\3-A Comprehensive Review*, 32, no. 1 (January 1, 1998): 71–95. doi:10.1016/S0149-1970(97)00009-7.

[Taylor 1951]

C.J. Taylor et al. *Physical Review* 84 (1951)

[Terai 1998]

Takayuki Terai, and Satoru Tanaka. “Tritium Release Behavior from Liquid Tritium Breeding Materials for Fusion Reactor Blanket under Neutron Irradiation.” *Progress in Nuclear Energy, Fast Neutron Reactor YAYOI and Related Nuclear Engineering Researches of the University of Tokyo\3-A Comprehensive Review*, 32, no. 1 (January 1, 1998): 97–112. doi:10.1016/S0149-1970(97)00010-3.

[Thomas & Klein 2003]

D. J. Thomas, and H. Klein. “Introduction.” *Radiation Protection Dosimetry* 107, no. 1–3 (November 1, 2003): 13–21.

[Tripoli]

E. Brun, F. Damian, C.M. Diop, E. Dumonteil, F.X. Hugot, C. Jouanne, Y.K. Lee, F. Malvagi, A. Mazzolo, O. Petit, J.C. Trama, T. Visonneau, A. Zoia. “TRIPOLI-4, CEA, EDF and AREVA reference Monte Carlo code.” *Annals of Nuclear Energy* 82 (2015) 151-160.

[Tsukada & Kikuchi 1962]

Kineo Tsukada, and Shiroh Kikuchi. “Directional Anisotropy in the Characteristics of the Organic-Crystal Scintillators.” *Nuclear Instruments and Methods* 17, no. 3 (December 1, 1962): 286–88.
doi:10.1016/0029-554X(62)90007-1.

- [Van Loef 2011] Edgar V. van Loef, Jarek Glodo, Urmila Shirwadkar, Natalia Zaitseva, and Kanai S. Shah. "Solution Growth and Scintillation Properties of Novel Organic Neutron Detectors." *Nuclear Instruments and Methods in Physics Research Section A: Accelerators, Spectrometers, Detectors and Associated Equipment, Symposium on Radiation Measurements and Applications (SORMA) XII 2010*, 652, no. 1 (October 1, 2011): 424–26. doi:10.1016/j.nima.2010.07.072.
- [Verbinski 1968] V. V. Verbinski, W. R. Burrus, T. A. Love, W. Zobel, N. W. Hill, and R. Textor. "Calibration of an Organic Scintillator for Neutron Spectrometry." *Nuclear Instruments and Methods* 65, no. 1 (October 15, 1968): 8–25. doi:10.1016/0029-554X(68)90003-7.
- [Veskrna 2014] M. Veskrna, Z. Matej, F. Mravec, V. Prenosil, F. Cvachovec, M. Kostal "Digitalized two parametric system for gamma/neutron spectrometry", *ANS RPSD 2014 - 18th Topical Meeting of the Radiation Protection & Shielding Division of ANS*, Knoxville (2014).
- [Wakabayashi 1998] H. Wakabayashi, I. Saito, T. Tamura, S. An. "Operational Experiences of Fast Neutron Source Reactor 'YAYOI' as a Pulsed Fast Reactor." *Progress in Nuclear Energy, Fast Neutron Reactor YAYOI and Related Nuclear Engineering Researches of the University of Tokyo\3-A Comprehensive Review* 32, n. 1 (1998) 195–207. doi:10.1016/S0149-1970(97)00016-4.
- [Weiss 2016] C. Weiss, H. Fraiss-Kölbl, E. Griesmayer, and P. Kavargin. "Ionization Signals from Diamond Detectors in Fast-Neutron Fields." *The European Physical Journal A* 52, no. 9 (September 9, 2016): 269. doi:10.1140/epja/i2016-16269-8.
- [Yagi 2011] T. Yagi, H. Unesaki, T. Misawa, C.H. Pyeon, S. Shiroya, T. Matsumoto, H. Harano. "Development of a small scintillation detector with optical fiber." *Applied Radiation and Isotopes* 69 (2011) 539-544.
- [Yoshii 1998] K. Yoshii and K. Miya. "Fast Neutron Radiography at Reactor YAYOI." *Progress in Nuclear Energy, Fast Neutron Reactor YAYOI and Related Nuclear Engineering Researches of the University of Tokyo\3-A Comprehensive Review* 32, n. 1 (1998) 123–139. doi:10.1016/S0149-1970(97)00012-7.
- [Zaitseva 2015] Zaitseva, Natalia, Andrew Glenn, Leslie Carman, H. Paul Martinez, Robert Hatarik, Helmut Klapper, and Stephen Payne. "Scintillation Properties of Solution-Grown Trans-Stilbene Single Crystals." *Nuclear Instruments and Methods in Physics Research Section A: Accelerators, Spectrometers, Detectors and Associated Equipment* 789 (July 21, 2015): 8–15. doi:10.1016/j.nima.2015.03.090.

APPENDIX A

Simulations of the MASURCA Beam Configuration

A. Simulations of the MASURCA Beam Configuration

A.1. Approaches

A.2. Approach 2 vs Approach 3: the OffCIC-LB model

A.3. Approach 2 vs Approach 4: Comparison of Two OffC Models

A.4. Input Files

In this APPENDIX, the majority of the models and calculations performed concerning MASURCA as a beam facility will be presented and discussed.

As already stated in Chapter III, there are three significant requirements for evaluating the capability of an extracted beam of fast neutrons: intensity of the exiting neutron current, energy spectrum and the ratio between (fast) neutrons and background (low-energy neutrons and gamma-rays).

The problem of this kind of evaluation is to transport particles and radiations created in the MASURCA core all the way down into the experimental zone, that is some two-to-three meters away.

The use of the well-established CEA-developed Monte Carlo code Tripoli-4® was judged appropriate for this application. However, in order to avoid spending excessive computing time for this feasibility study, different approaches were tested.

Complementary information can be found in references [Dioni 2016 (1), Dioni 2016 (2), Dioni 2017 (1)].

A.1. Approaches

Different approaches have been tested with the aim of saving calculation time using stepwise simulations, storage of the particles, variance reduction methods, etc.

The models should consider the MASURCA core, for evaluating the criticality (and the source term if necessary), as well as a simplified structure of the concrete walls around, one with a hole for simulating the extraction channel (Figure A.1). All cores have a radial channel passing through the reflector and the shield, the shape of the channel depending on the case studied. All material zones considered are homogenous: the fuel zone is made of metallic uranium fuel (~ 30 % ^{235}U enriched) and sodium, the reflector zone of stainless steel and sodium, and the shield zone of stainless steel and absorbers. More information about the reactor materials modelled can be found in Section A.4.1, under the tag “*COMPOSITION*”. Concrete walls are all around the core. In the following, “*whole system*” refers to the ensemble of the MASURCA core plus the concrete walls.

Four models are considered:

- a. A reference, first of a kind for MASURCA, beam model: called ‘REF’, reference (schematically presented in Figure A.1a);
- b. A 100 cm off-centred model, for increasing the neutron beam intensity: ‘OffC’, Off-Centred (Figure A.1b);
- c. A model that was built for increasing the fraction of uncollided neutrons and to further augment the neutron intensity at the channel exit: ‘OffCIC’, Off-Centred Inverted Cone (Figure A.1c);
- d. Same as c but with filters for diminishing the impact of low energy neutrons: ‘OffCIC-LB’, Off-Centred Inverted Cone - Low Background (Figure A.1d).

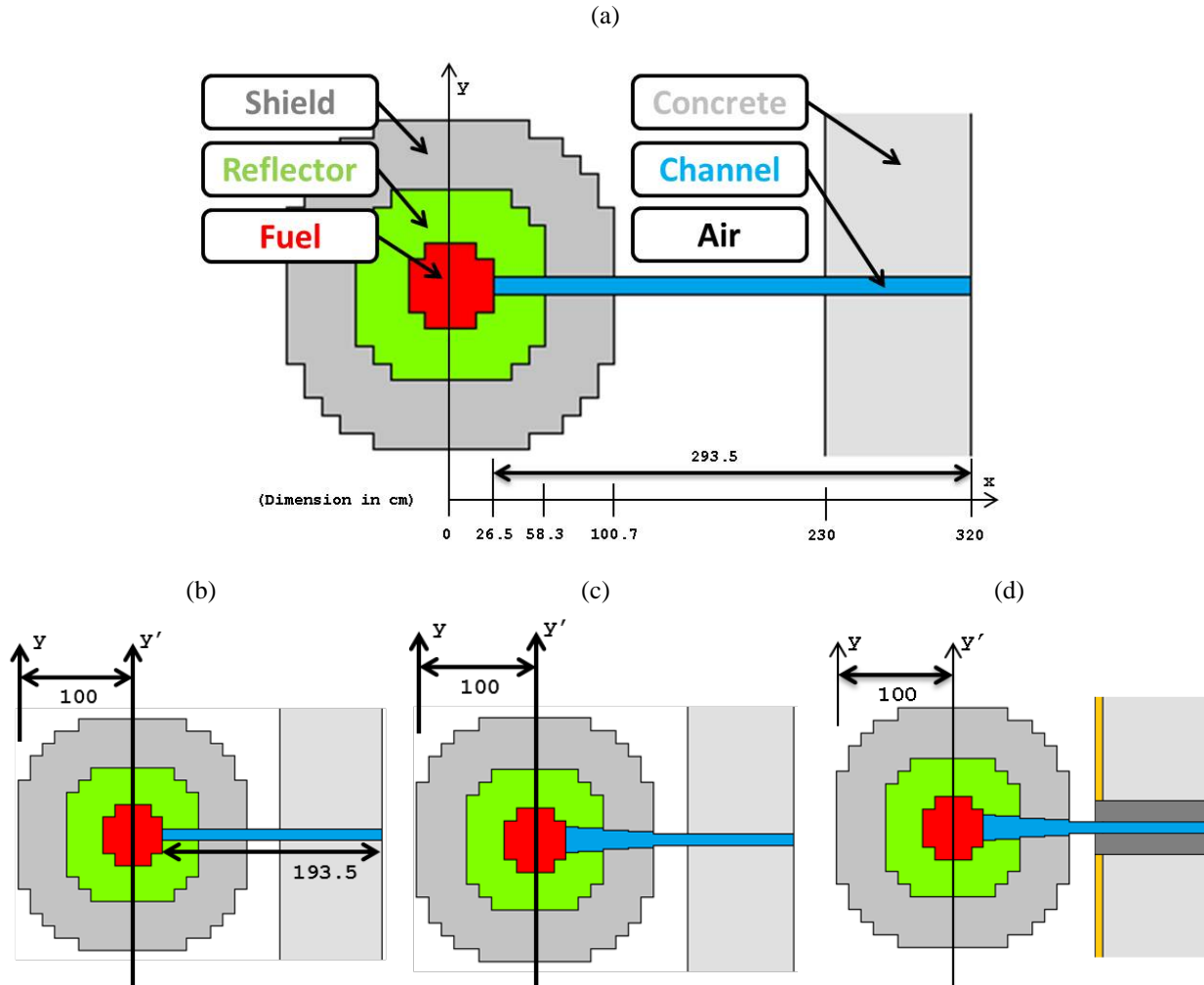


Figure A.1. MASURCA beam configuration models.

Four approaches have been used (Figure A.2):

1. A single criticality calculation of the whole system;
2. A two step calculation: first, a criticality one (whole system) for finding the k_{eff} of the system and the neutron source term; second, a shielding one (whole system) for evaluating the neutron (and photon) intensities and spectra at different positions along the beam channel (as the results presented in Chapter III);
3. Like 2, but the shielding calculation is carried out with variance reduction methods;
4. A two step calculation with storage of particles. The first step is a criticality one, simulating only the core of MASURCA with a surface, just outside the core, for storing particles (Figure A.7). The second is a shielding calculation of the concrete wall with the opening, using the stored particles as source for a separate fixed-source calculation.

Examples of inputs for 2, 3 and 4 are shown in section A.4.

Approach 1 has been used in [Dioni 2016 (1)] for the very first study of this experimental configuration. Already with homogenized and spherical regions, the simulation has been found slow for the purpose of this work, justifying moving to the second approach.

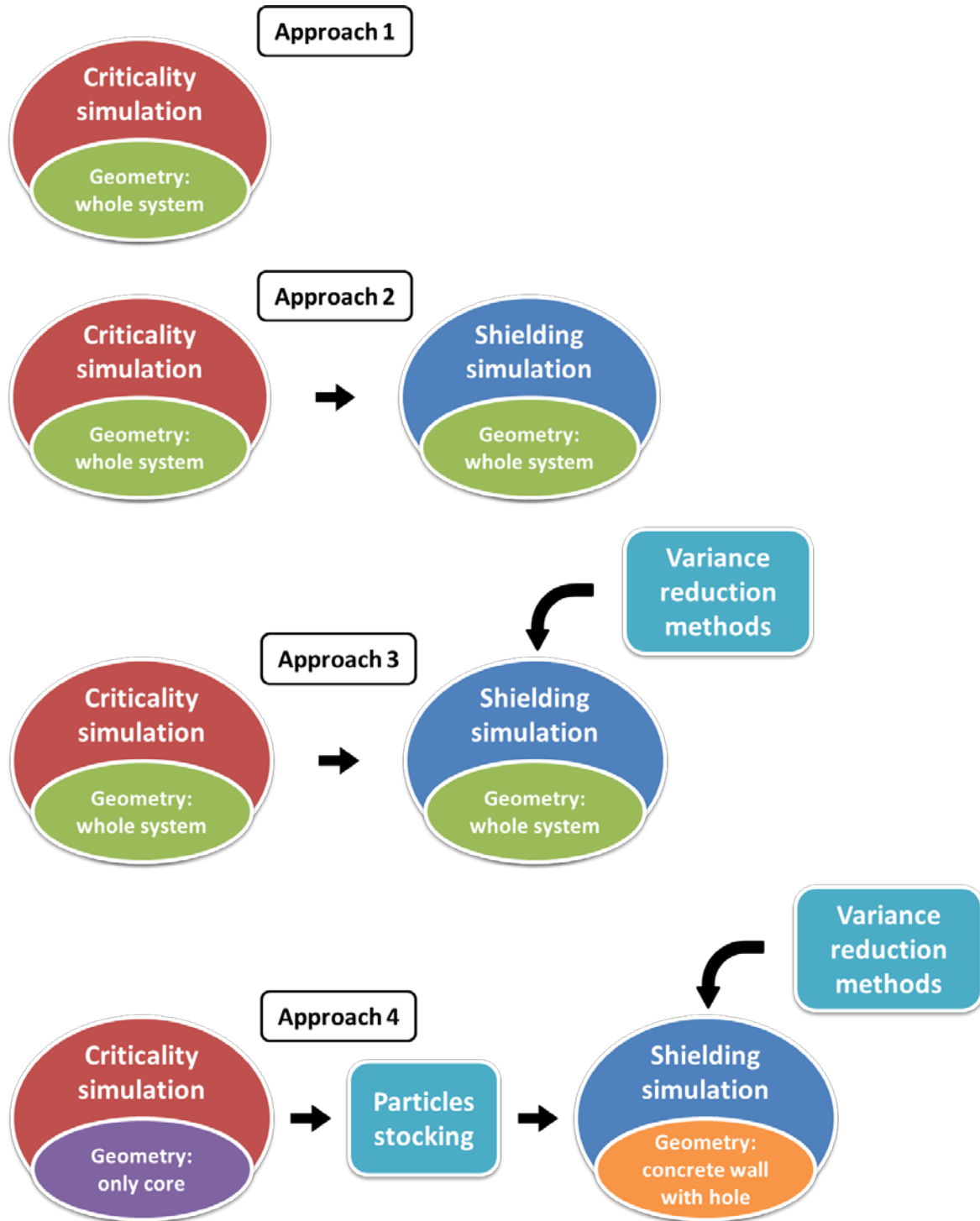


Figure A.2. The four modelling approaches used to simulate MASURCA beam configurations.

Method 2 can be considered as a reference, 3 and 4 have been tested and compared to it. The approach has been found satisfactory for the purpose of this work, although methods 3 and 4 are faster. The first step is a neutron and photon simulation intended for evaluating the k_{eff} of the system (A.4.1: “SIMULATION”, “CRITICALITY”), the neutron flux in the core (A.4.1: “RESPONSE”, “FLUX”) and the energy deposited (A.4.1: “RESPONSE”, “DEPOSITED_ENERGY”). A MATLAB® post processing file has been written for analyzing the results and for creating the source term for the second step. The shielding simulation has the objective of assessing the characteristics of the extracted neutron and photon beams. The tallied quantities are partial neutron (and photon) currents that cross successive surfaces along the radial channel (A.4.2: “RESPONSE”, “CURRENT”).

Approach 3 was devised for studying a special case of the OffCIC model, in order to decrease the low-energy neutron background at the channel exit. The OffCIC-LB model (Figure A.1d) is characterized by (i) a 5 cm layer of borated polyethylene (BPE) containing 30 % of natural boron, covering the inner face of the concrete walls, and (ii) a 10 cm stainless steel filter around the last section of the beam channel, inside the concrete wall.

Approach 4 has been used for testing the capability of Tripoli-4® in storing particles. This is not a study of a new model, like OffCIC-LB for Approach 3, but just a comparison between two approaches with the same OffC model. More simplifications are taken into consideration: for the first step, only the core is considered, without the concrete walls, for keeping the simulation faster and for not storing low-energy neutrons moderated by the biological shield (keeping storing files small). The second step is a quick shielding calculation with variance reduction methods of an air and concrete layer (Figure A.7).

In the next paragraph, A.2, the OffCIC-LB is analysed and compared with the three models considered in Chapter III. In A.3, the approach 4 is discussed in relation to the OffC model.

A.2. Approach 2 vs Approach 3: the OffCIC-LB Model

The first step of Approach 3 is the same as Approach 2. The results are summarized in Table A.1, which is a comparison of the k_{eff} of the systems. Figures A.3a and A.3b are a representation of the normalized neutron flux (33 groups) in a lin-log and a log-log scale of the fuel region. In Figure A.4a, a core flux traversal is plotted at $z = 0$ and $y = 0$, where the coordinate x is not the absolute abscissa but refers to the relative position with respect to the centre of each core.

The small difference in the k_{eff} values between OffCIC and OffCIC-LB can be explained by the fact that less thermal neutrons (moderated by the concrete walls) are present in the low-background model. This is mainly due to the borated polyethylene layer that covers the inner face of the concrete walls.

The second step in Approach 3 permits to save about 70 % of the simulation time needed for the same step in Approach 2. The behavior of the results of the two methods is in good agreement and the variance reduction techniques do not introduce significant biases, as is possible to see in the higher energy part of Figure A.6. The represented quantities are partial outgoing neutron currents that cross successive surfaces at different positions along the radial channel. Figure A.6a is the

neutron current entering the beam channel, while Figure A.6e is the one exiting the channel. Figure A.6b, c and d are at different positions along the channel. By comparing the OffCIC and OffCIC-LB models (Approach 2 versus 3), it is clear that the fast part of the neutron spectra has not changed, suggesting that the results obtained with Approach 3 are reasonable and that, as wanted and expected, the low energy part of the neutron spectrum has been removed.

Figure A.4b compares the total neutron current intensity as it attenuates along the radial channel. Here, the x coordinate is the absolute position. Apart for REF, in which the radial channel starts at $x = 26.5$ cm, all other models have an extraction channel which starts at $x = 126.5$ cm. Since the beam is mainly composed of intermediate-to-fast neutrons, there are no significant differences between the total intensities of OffCIC and OffCIC-LB.

The discrepancies between the OffCIC and OffCIC-LB beam intensities and spectra are evidenced by comparing Figures A.5c and A.5d. These plots show the neutron current intensity attenuation along the radial channel for different energy groups, including the low-energy ones. The OffCIC-LB filters are quite efficient at suppressing the lower energy neutrons from the beam (orange and yellow lines).

All these results are summarized in Table A.2. With the OffC and OffCIC models it was possible to increase the neutron beam intensity and the fraction of uncollided neutrons at the extraction channel exit. The OffCIC-LB model allows to suppress the low-energy neutron background, obtaining a beam with 96 % (81 %) of neutrons with energy over 10 keV (over 100 keV).

Table A.1. Computed k_{eff} values for the four models.

	k_{eff}	1σ stat. unc.
REF	1.0141	5E-05
OffC	1.0139	5E-05
OffCIC	1.0055	5E-05
OffCIC-LB	1.0050	5E-05

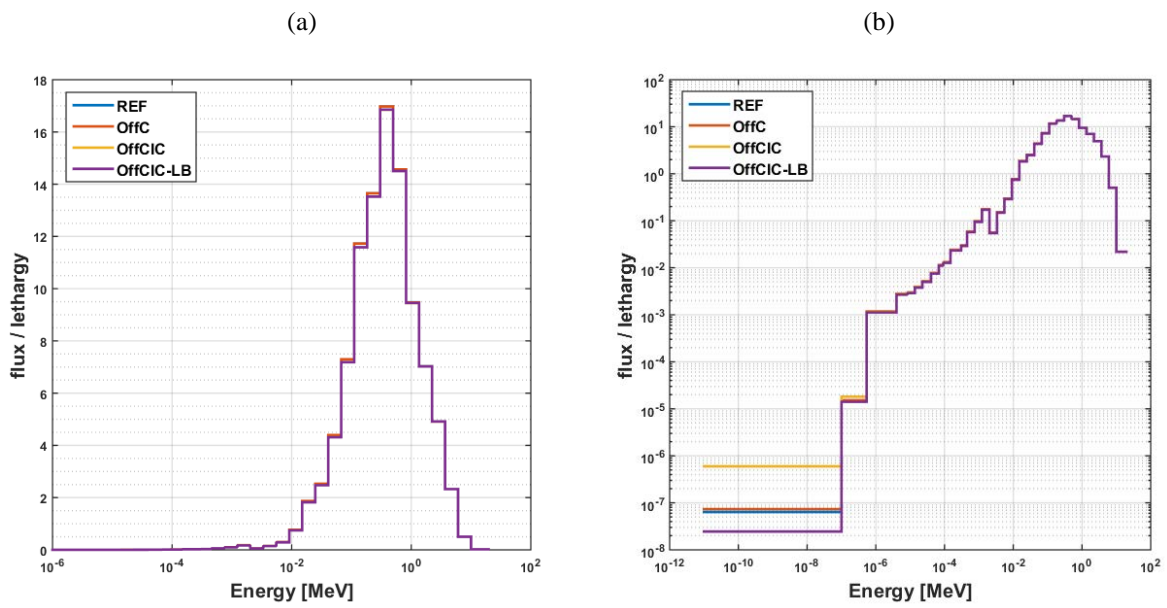


Figure A.3. Comparison of the neutron fluxes in the fuel region in a (a) lin-log and a (b) log-log scale.

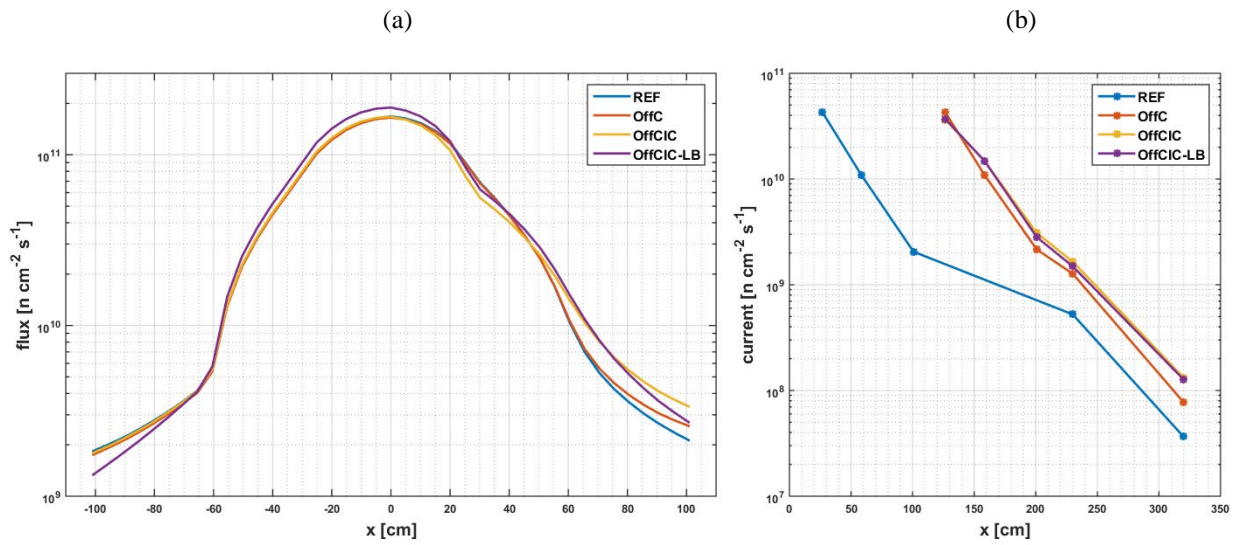


Figure A.4. (a) Flux traverse in the core at $z = 0$ and $y = 0$, as a function of relative x position (5 kW) and (b) total neutron intensity loss along the radial channel as a function of absolute x position.

Table A.2. Neutron Current Intensity and Energy Distribution at the Channel Exit (at 5 kW).

	Total ($\text{n cm}^{-2} \text{s}^{-1}$)	<0.5 eV	0.5 eV-10 keV	>10 keV	<100 keV	>100 keV
REF	3.65E+07	0.07	0.07	0.86	0.31	0.69
OffC	7.74E+07	0.07	0.08	0.85	0.31	0.69
OffCIC	1.32E+08	0.06	0.06	0.89	0.25	0.75
OffCIC-LB	1.27E+08	0.00	0.04	0.96	0.19	0.81

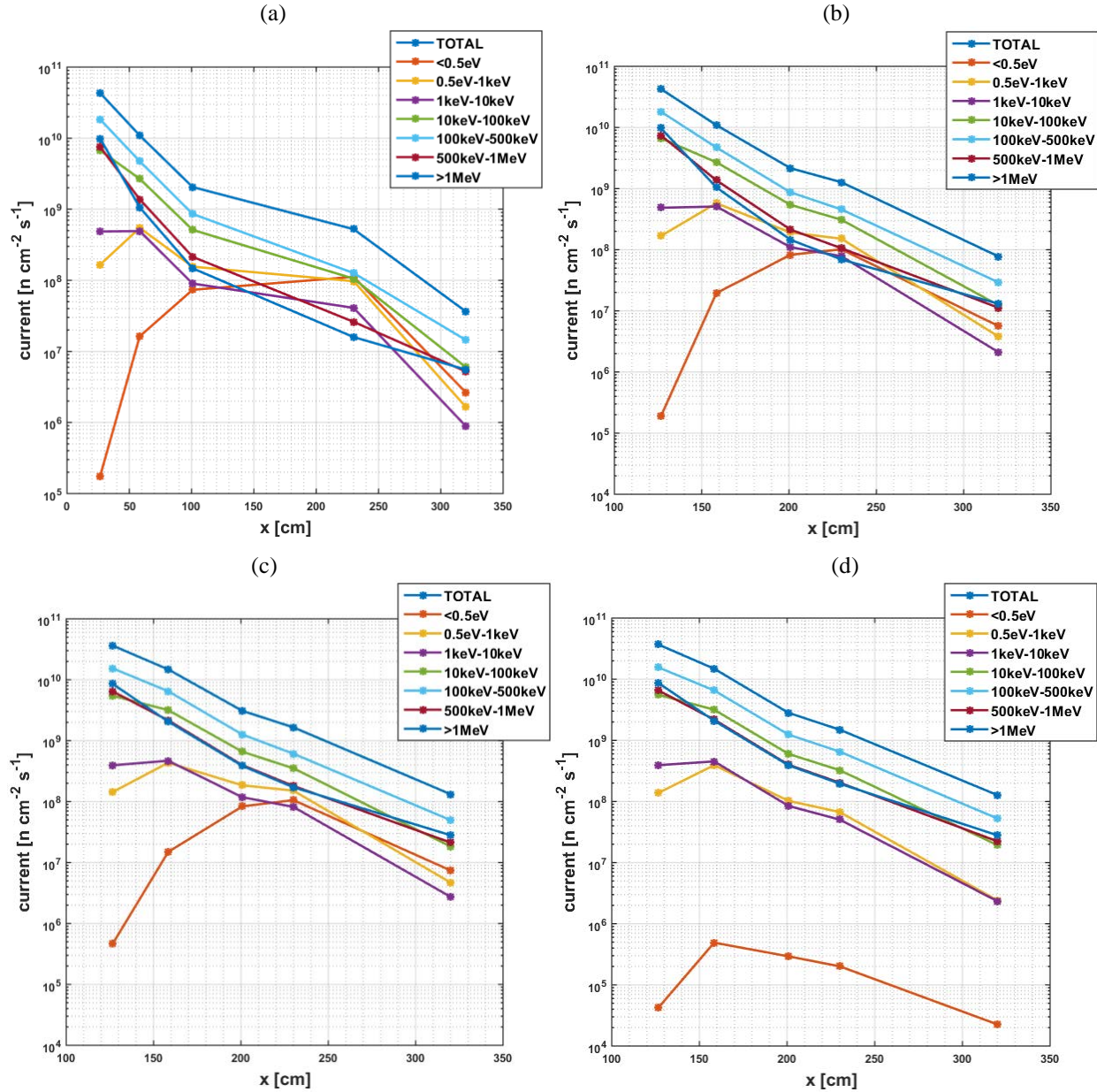


Figure A.5. Neutron current attenuation along the radial channel for the (a) REF, (b) OffC, (c) OffCIC and (d) OffCIC-LB models.

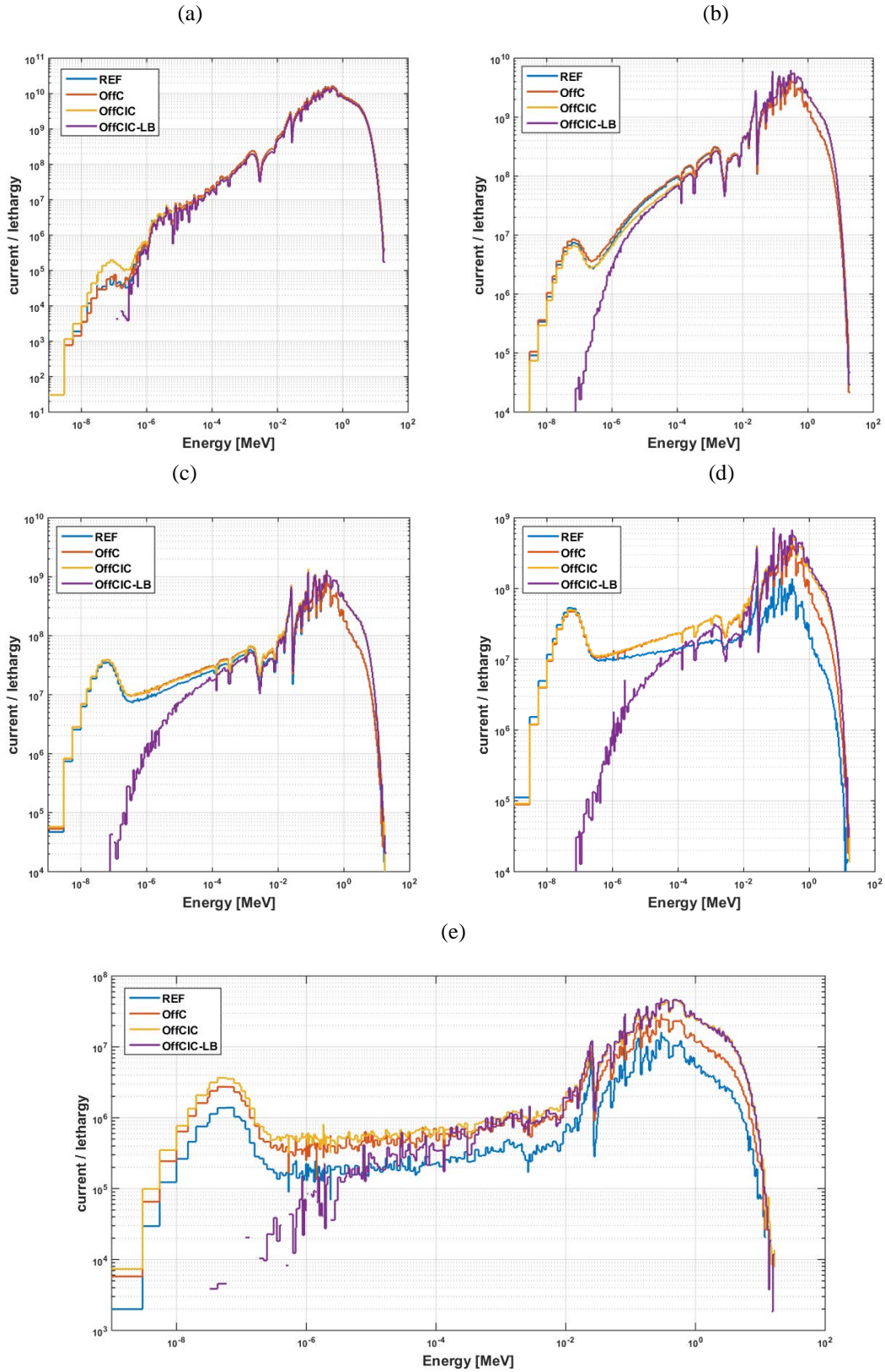


Figure A.6. (a), (b), (c), (d) Neutron currents crossing successive surfaces in the positive x direction within the channel and (e) neutron current spectrum at the beam channel exit.

A.3. Approach 2 vs Approach 4: Comparison of Two OffC Models

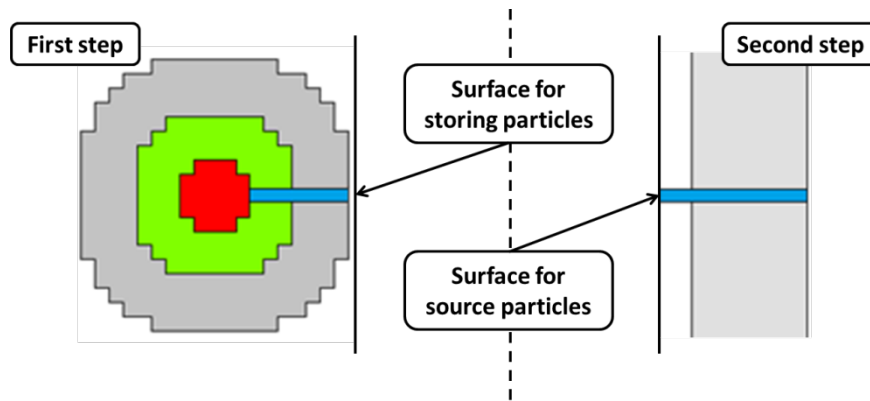


Figure A.7. Approach 4.

The first step of Approach 4 is a criticality simulation of only the MASURCA core (OffC model), without the concrete walls. The purpose is to save calculation time also in this phase and to store only intermediate-to-fast energy neutrons, as to avoid generating huge storage files and data management problems. It is possible to save about 50 % of the time, compared to Approach 2.

In Table A.3 is reported the k_{eff} value obtained by each method. A difference of 70 pcm is found, due to the fact that there are essentially no neutrons that come back to the core after being slowed down in the concrete walls. Figure A.8a and Figure A.8b show the neutron flux in the fuel zone.

Figure A.8c is a comparison between the stored neutron spectrum of the first step and the source spectrum used in the second step. The spectra are in good agreement (this was only a test).

The second step is simply a shielding calculation of an air and concrete (with an opening) layer, using the previously-computed and stored particles as sources (with variance reduction techniques). This is really quick, about 95 % of the simulation time spent in Approach 2 is saved. The outgoing neutron current spectrum at the channel exit is plotted in Figure A.8d. Although a longer simulation could lead to results having smaller uncertainties, already at this level, the behavior of the obtained neutron spectrum is in good agreement with the one obtained in Approach 2.

In summary, this 4th approach is attractive for having fast answers about a model. On the other hand, it is necessary to try to limit the size of the storage files, which can be important.

Table A.3. Computed k_{eff} values for the two models.

	k_{eff}	1σ stat. unc.
OffC (app. 2)	1.0139	5E-05
OffC (app. 4)	1.0132	5E-05

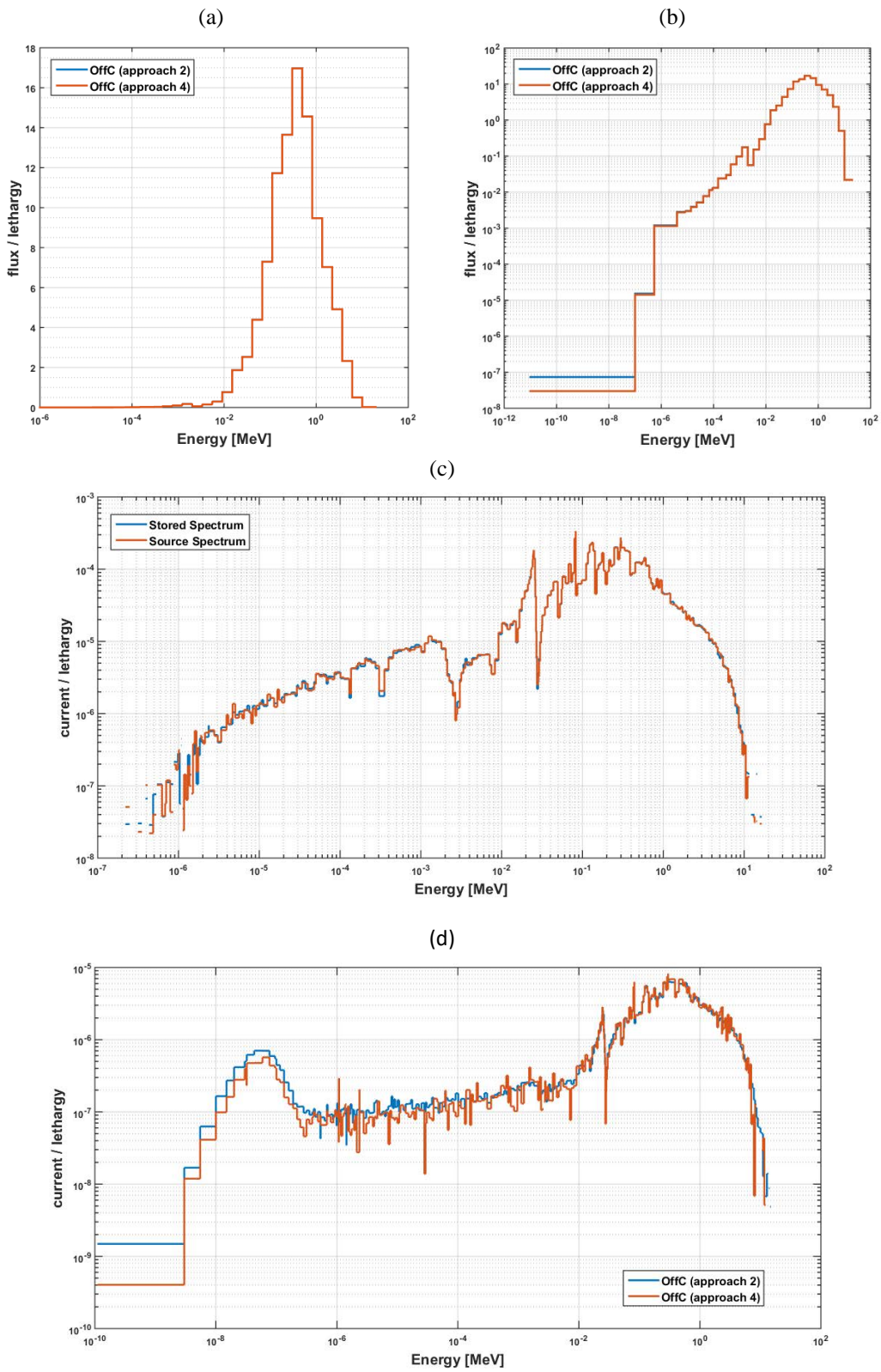


Figure A.8. (a), (b) Neutron flux in the fuel region; (c) comparison between the stored neutron spectrum of step one and the source spectrum of step two. (d) Neutron current spectrum at the beam channel exit.

A.4 Input Files

In the following are reported several TRIPOLI-4® input files used for simulating the MASURCA beam experimental configuration.

A.4.1 Approach no. 2: first step, criticality simulation. Geometry: OffC whole system

```
//
// MASURCA OffC
// Core Map
// Fuel U30
// Channel AIR
//

//
// GEOMETRY
//

GEOMETRY
TITLE geo MASURCA OffC

// R_FUEL
TYPE 100 BOX 31.80 31.80 45.00
TYPE 110 BOX 10.60 31.80 45.00
TYPE 120 BOX 31.80 10.60 45.00

VOLU 110 COMBI 110 121.2 0.0 0.0 FICTIVE ENDV
VOLU 120 COMBI 110 78.8 0.0 0.0 FICTIVE ENDV
VOLU 130 COMBI 120 100.0 21.2 0.0 FICTIVE ENDV
VOLU 140 COMBI 120 100.0 -21.2 0.0 FICTIVE ENDV
VOLU 100 COMBI 100 100.0 0.0 0.0
UNION 4 110 120 130 140
ENDV

// R_REFL
TYPE 200 BOX 95.40 95.40 105.0
TYPE 210 BOX 10.60 74.20 105.0
TYPE 220 BOX 74.20 10.60 105.0

VOLU 210 COMBI 210 153.0 0.0 0.0 FICTIVE ENDV
VOLU 220 COMBI 210 47.0 0.0 0.0 FICTIVE ENDV
VOLU 230 COMBI 220 100.0 53.0 0.0 FICTIVE ENDV
VOLU 240 COMBI 220 100.0 -53.0 0.0 FICTIVE ENDV
VOLU 200 COMBI 200 100.0 0.0 0.0
UNION 4 210 220 230 240
VMINUS 1 100
ENDV

// R_SCREEN
TYPE 300 BOX 159.0 159.0 185.0
TYPE 310 BOX 10.60 137.8 185.0
TYPE 320 BOX 10.60 95.40 185.0
TYPE 330 BOX 137.8 10.60 185.0
TYPE 340 BOX 95.40 10.60 185.0

VOLU 310 COMBI 310 184.8 0.0 0.0 FICTIVE ENDV

VOLU 320 COMBI 310 15.2 0.0 0.0 FICTIVE ENDV
VOLU 330 COMBI 320 195.4 0.0 0.0 FICTIVE ENDV
VOLU 340 COMBI 320 4.6 0.0 0.0 FICTIVE ENDV
VOLU 350 COMBI 330 100.0 84.8 0.0 FICTIVE ENDV
VOLU 360 COMBI 330 100.0 -84.8 0.0 FICTIVE ENDV
VOLU 370 COMBI 340 100.0 95.4 0.0 FICTIVE ENDV
VOLU 380 COMBI 340 100.0 -95.4 0.0 FICTIVE ENDV
VOLU 300 COMBI 300 100.0 0 0
UNION 8 310 320 330 340 350 360 370 380
VMINUS 1 200
ENDV

// R_AIR_INN
TYPE 400 BOX 460.0 460.0 460.0
VOLU 400 COMBI 400 0 0 0 VMINUS 1 300 ENDV

// R_CONCRETE
TYPE 500 BOX 640.0 640.0 640.0
VOLU 500 COMBI 500 0 0 0 VMINUS 1 400 ENDV

// R_AIR_EXT
TYPE 600 BOX 700.0 700.0 700.0
VOLU 600 COMBI 600 0 0 0 VMINUS 1 500 ENDV

// CHANNEL
TYPE 700 BOX 193.5 10.60 10.60
TYPE 701 BOX 31.8 10.16 10.16
TYPE 702 BOX 42.4 10.16 10.16
TYPE 703 BOX 29.3 10.16 10.16
TYPE 704 BOX 90.0 10.16 10.16

VOLU 700 COMBI 700 223.25 0 0 SMASH 4 200 300 400 500 ENDV
VOLU 701 COMBI 701 142.40 0 0 SMASH 1 700 ENDV
VOLU 702 COMBI 702 179.50 0 0 SMASH 1 700 ENDV
VOLU 703 COMBI 703 215.35 0 0 SMASH 1 700 ENDV
VOLU 704 COMBI 704 275.00 0 0 SMASH 1 700 ENDV

// FILTER
TYPE 800 BOX 0.1 10.16 10.16
VOLU 800 COMBI 800 126.55 0 0 SMASH 1 701 ENDV

//

ENDGEOM

//
// COMPOSITION
//
```

COMPOSITION
7
POINT_WISE 300 FUEL
77
U235 5.14212E-03
U238 1.18467E-02
NA23 9.32466E-03
FE54 3.19037E-04
FE56 4.95975E-03
FE57 1.15075E-04
FE58 1.51411E-05
...
POINT_WISE 300 TUBE
38
C 2.020270E-04
SI28 3.377390E-04
SI29 1.714960E-05
SI30 1.130470E-05
CR50 4.834300E-04
CR52 9.322570E-03
CR53 1.056980E-03
CR54 2.631330E-04
MN55 4.446130E-04
FE54 2.422230E-03
FE56 3.765540E-02
FE57 8.621500E-04
FE58 1.149530E-04
NI58 3.243190E-03
NI60 1.249270E-03
...
POINT_WISE 300 REFL
73
C 1.90409E-05
NA23 4.66233E-03
SI28 1.21399E-03
V 1.23596E-04
CR50 5.31389E-04
CR52 1.02474E-02
CR53 1.16184E-03
CR54 2.89237E-04
MN55 7.48998E-04
FE54 2.70787E-03
FE56 4.20960E-02
FE57 9.63822E-04
FE58 1.28510E-04
NI58 3.44669E-03
NI60 1.32765E-03
NI61 5.77173E-05
NI62 1.83987E-04
NI64 4.68827E-05
...
POINT_WISE 300 SCREEN
40
B10 3.22720390E-09
B11 1.29898368E-08
C 1.47487804E-05
FE54 4.71410968E-05
FE56 7.32844604E-04
FE57 1.67790598E-05
FE58 2.23720155E-06
...
POINT_WISE 300 AIR

5
H1 5.79933E-07
H2 6.67000E-11
N14 3.98528E-05
N15 1.47200E-07
O16 1.00000E-05

POINT_WISE 300 CONCRETE
24
H1 5.51937E-03
O16 7.65000E-02
MG24 2.74095E-04
AL27 2.72000E-03
SI28 1.04220E-02
SI29 5.29202E-04
SI30 3.48842E-04
CA40 3.02459E-03
MN55 7.27000E-05
P31 6.89000E-04
S32 1.48091E-04
K39 5.56751E-04
...
POINT_WISE 300 CHANNEL
5
H1 5.79933E-07
H2 6.67000E-11
N14 3.98528E-05
N15 1.47200E-07
O16 1.00000E-05

END_COMPOSITION

//
// GEOMETRY-COMPOSITION
//
GEOMCOMP
FUEL 1 100
REFL 1 200
SCREEN 1 300
AIR 2 400 600
CONCRETE 1 500
TUBE 1 700
CHANNEL 5 701 702 703 704 800
END_GEOMCOMP

//
// SOURCES
//

SOURCES_LIST
1
SOURCE
INTENSITY 1
NEUTRON
PONCTUAL 100.0 0.0 0.0
ENERGETIC_DISTRIBUTION SPECTRUM WATT_SPECTRUM
ANGULAR_DISTRIBUTION ISOTROPIC
TIME_DISTRIBUTION DIRAC 0.0
END_SOURCE
END_SOURCES_LIST

//
// RESPONSE AND SCORE
//

```

RESPONSES
5
FLUX NEUTRON
MACROSCOPIC_REACTION_RATE NEUTRON PROMPT_NUSIGF
MACROSCOPIC_REACTION_RATE NEUTRON DELAYED_NUSIGF
REACTION NEUTRON NUCLEI 2
U235 COMPO FUEL INTERACTION 1 34
U238 COMPO FUEL INTERACTION 1 34
DEPOSITED_ENERGY PHOTON
END_RESPONSES

GRID_LIST
2
3_GRS
GRID_33 35
1.0000E-11 1.0000E-07 5.4000E-07 4.0000E-06 8.3200E-06
1.3700E-05 2.2600E-05 4.0200E-05 6.7900E-05 9.1700E-05
1.4900E-04 3.0400E-04 4.5400E-04 7.4900E-04 1.2300E-03
2.0300E-03 3.3500E-03 5.5300E-03 9.1200E-03 1.5000E-02
2.4800E-02 4.0900E-02 6.7400E-02 1.1100E-01 1.8300E-01
3.0200E-01 4.9800E-01 8.2100E-01 1.3500E+00 2.2300E+00
3.6800E+00 6.0700E+00 1.0000E+01 1.9600E+01 2.0000E+01
END_GRID_LIST

SCORE
6
1 TRACK
GRID GRID_33
VOLUME LIST 3 100 200 300
1 TRACK
GRID 3_GRS
EXTENDED_MESH
WINDOW
-100.7 -100.7 -92.5
100.7 100.7 92.5

41 41 37
FRAME
CARTESIAN
100 0 0
1 0 0
0 1 0
0 0 1
2 MACROSCOPIC_REACTION_RATE
GRID GRID_33
VOLUME LIST 1 100
3 MACROSCOPIC_REACTION_RATE
GRID GRID_33
VOLUME LIST 1 100
4 TRACK
GRID GRID_33
VOLUME LIST 1 100
5 LOCAL_ENERGY_DEPOSITION
GRID GRID_33
VOLUME LIST 3 100 200 300
END_SCORE

//
// SIMULATION
//

SIMULATION
BATCH 20000
SIZE 100000
EDITION 2000
PARTICLE 2
NEUTRON
PHOTON
GLOBAL_SCORES
CRITICALITY
DISCARD 1
END_SIMULATION

```

A.4.2 Approach no. 2: second step, shielding simulation. Geometry: OffC whole system

```

//
// MASURCA OffC
// Beam
// Fuel U30
// Channel AIR
//
//
// GEOMETRY
//
//
// COMPOSITION
//
//
// GEOMETRY-COMPOSITION
//
//
// SOURCES
//
SOURCES_LIST

1
SOURCE
INTENSITY 7.682600E+13 // 1 kW
NEUTRON
FACTORIZED
FRAME
CARTESIAN
100 0 0
1 0 0
0 1 0
0 0 1
VOLUME 1 100
GEOMETRIC_DISTRIBUTION
TABULATED
TYPE F_UVV
VAR_U X 42
-100.7 -95.7 -90.7 -85.8 -80.9 -76 -71.1 -66.2 -61.3 -56.4
-51.5 -46.6 -41.7 -36.8 -31.9 -27 -22.1 -17.2 -12.3 -7.4 -2.5
2.5 7.4 12.3 17.2 22.1 27 31.9 36.8 41.7 46.6
51.5 56.4 61.3 66.2 71.1 76 80.9 85.8 90.7 95.7 100.7
VAR_V Y 42
-100.7 -95.7 -90.7 -85.8 -80.9 -76 -71.1 -66.2 -61.3 -56.4
-51.5 -46.6 -41.7 -36.8 -31.9 -27 -22.1 -17.2 -12.3 -7.4 -2.5
2.5 7.4 12.3 17.2 22.1 27 31.9 36.8 41.7 46.6

```

```

51.5 56.4 61.3 66.2 71.1 76 80.9 85.8 90.7 95.7 100.7
VAR_W Z 38
-92.5 -87.5 -82.5 -77.5 -72.5 -67.5 -62.5 -57.5 -52.5
-47.5 -42.5 -37.5 -32.5 -27.5 -22.5 -17.5 -12.5 -7.5 -2.5
2.5 7.5 12.5 17.5 22.5 27.5 32.5 37.5 42.5
47.5 52.5 57.5 62.5 67.5 72.5 77.5 82.5 87.5 92.5
F_UVW
... ..
... ..
... ..
ENERGETIC_DISTRIBUTION SPECTRUM WATT_SPECTRUM
ANGULAR_DISTRIBUTION ISOTROPIC
TIME_DISTRIBUTION DIRAC 0.0
END_SOURCE
END_SOURCES_LIST

//
// RESPONSE AND SCORE
//

RESPONSES
3
FLUX NEUTRON
CURRENT NEUTRON
CURRENT PHOTON
END_RESPONSES

GRID_LIST
2
GRID_33 35
1.0000E-11 1.0000E-07 5.4000E-07 4.0000E-06 8.3200E-06
1.3700E-05 2.2600E-05 4.0200E-05 6.7900E-05 9.1700E-05
1.4900E-04 3.0400E-04 4.5400E-04 7.4900E-04 1.2300E-03
2.0300E-03 3.3500E-03 5.5300E-03 9.1200E-03 1.5000E-02
2.4800E-02 4.0900E-02 6.7400E-02 1.1100E-01 1.8300E-01
3.0200E-01 4.9800E-01 8.2100E-01 1.3500E+00 2.2300E+00
3.6800E+00 6.0700E+00 1.0000E+01 1.9600E+01 2.0000E+01
TRIPOLI_315
END_GRID_LIST

SCORE
5
1 TRACK
GRID GRID_33
VOLUME LIST 3 100 200 300
2 SURF
GRID TRIPOLI_315
FRONTIER LIST 5

```

```

800 701
701 702
702 703
703 704
704 600
2 SURF
FILTER VOLUME
LIST 1 800
GRID TRIPOLI_315
FRONTIER LIST 4
701 702
702 703
703 704
704 600
3 SURF
GRID TRIPOLI_315
FRONTIER LIST 5
800 701
701 702
702 703
703 704
704 600
3 SURF
FILTER VOLUME
LIST 1 800
GRID TRIPOLI_315
FRONTIER LIST 4
701 702
702 703
703 704
704 600
END_SCORE

//
// SIMULATION
//

SIMULATION
BATCH 20000
SIZE 1000000
EDITION 2000
PARTICLE 2
NEUTRON
PHOTON
GLOBAL_SCORES
SHIELDING
END_SIMULATION

```

A.4.3 Approach no. 3: second step, shielding simulation with variance reduction methods. Geometry: OffCIC-LB whole system

```

//
// MASURCA OffCIC-LB
// Beam
// Fuel U30
// Channel AIR
//

//
// GEOMETRY

//
// COMPOSITION

//
// GEOMETRY-COMPOSITION
//

```

```

//
// SOURCES
//
//
// RESPONSE AND SCORE
//
//
// BIASING
//
VARIANCE_REDUCTION
NEUTRON
GRID
5
  20.0 4.0 0.1 1.0E-3 1.0E-11
DETECT
1
  320.0 0.0 0.0
0.5
MESH
70 70 70
10 10 10
3

FRAME
CARTESIAN
-350.0 -350.0 -350.0
1 0 0
0 1 0
0 0 1
END_MESH
INIPOND
AUTO
END_INIPOND
END_VARIANCE_REDUCTION

//
// SIMULATION
//
SIMULATION
BATCH 40000
SIZE 10000
EDITION 2000
PARTICLE 1
NEUTRON
GLOBAL_SCORES
SHIELDING
END_SIMULATION

```

A.4.4 Approach no. 4: first step, criticality simulation with storage of particles. Geometry: MASURCA only core

```

//
// MASURCA only core
// Fuel U30
// Channel AIR
// storage
//
//
// GEOMETRY
//
GEOMETRY
TITLE geo MASURCA only core + channel

// R_FUEL
TYPE 100 BOX 31.80 31.80 45.00
TYPE 110 BOX 10.60 31.80 45.00
TYPE 120 BOX 31.80 10.60 45.00

VOLU 110 COMBI 110 21.2 0.0 0.0 FICTIVE ENDV
VOLU 120 COMBI 110 -21.2 0.0 0.0 FICTIVE ENDV
VOLU 130 COMBI 120 0.0 21.2 0.0 FICTIVE ENDV
VOLU 140 COMBI 120 0.0 -21.2 0.0 FICTIVE ENDV
VOLU 100 COMBI 100 0.0 0.0 0.0
UNION 4 110 120 130 140
ENDV

// R_REFL
TYPE 200 BOX 95.40 95.40 105.0
TYPE 210 BOX 10.60 74.20 105.0
TYPE 220 BOX 74.20 10.60 105.0

VOLU 210 COMBI 210 53.0 0.0 0.0 FICTIVE ENDV

VOLU 220 COMBI 210 -53.0 0.0 0.0 FICTIVE ENDV
VOLU 230 COMBI 220 0.0 53.0 0.0 FICTIVE ENDV
VOLU 240 COMBI 220 0.0 -53.0 0.0 FICTIVE ENDV
VOLU 200 COMBI 200 0.0 0.0 0.0
UNION 4 210 220 230 240
VMINUS 1 100
ENDV

// R_SCREEN
TYPE 300 BOX 159.0 159.0 185.0
TYPE 310 BOX 10.60 137.8 185.0
TYPE 320 BOX 10.60 95.40 185.0
TYPE 330 BOX 137.8 10.60 185.0
TYPE 340 BOX 95.40 10.60 185.0

VOLU 310 COMBI 310 84.8 0.0 0.0 FICTIVE ENDV
VOLU 320 COMBI 310 -84.8 0.0 0.0 FICTIVE ENDV
VOLU 330 COMBI 320 95.4 0.0 0.0 FICTIVE ENDV
VOLU 340 COMBI 320 -95.4 0.0 0.0 FICTIVE ENDV
VOLU 350 COMBI 330 0.0 84.8 0.0 FICTIVE ENDV
VOLU 360 COMBI 330 0.0 -84.8 0.0 FICTIVE ENDV
VOLU 370 COMBI 340 0.0 95.4 0.0 FICTIVE ENDV
VOLU 380 COMBI 340 0.0 -95.4 0.0 FICTIVE ENDV
VOLU 300 COMBI 300 0.0 0.0 0.0
UNION 8 310 320 330 340 350 360 370 380
VMINUS 1 200
ENDV

// R_AIR_INN
TYPE 400 BOX 460.0 460.0 460.0
VOLU 400 COMBI 400 0 0 0 VMINUS 1 300 ENDV

// CHANNEL

```

```

TYPE 700 BOX 74.2 10.60 10.60
TYPE 710 BOX 31.8 10.16 10.16
TYPE 720 BOX 42.4 10.16 10.16

VOLU 700 COMBI 700 63.60 0 0 SMASH 2 200 300 ENDV
VOLU 710 COMBI 710 42.40 0 0 SMASH 1 700 ENDV
VOLU 720 COMBI 720 79.50 0 0 SMASH 1 700 ENDV

// FILTER
TYPE 800 BOX 0.1 10.16 10.16
VOLU 800 COMBI 800 26.55 0 0 SMASH 1 710 ENDV

//STORAGE
TYPE 1000 BOX 0.1 460.0 460.0

VOLU 1000 COMBI 1000 100.75 0 0 SMASH 1 400 ENDV
VOLU 1100 COMBI 1000 100.85 0 0 SMASH 1 400 ENDV

//
ENDGEOM

//
// COMPOSITION
//
//
// COMPOSITION
//
//
// GEOMETRY-COMPOSITION
//
//
// SOURCES
//
//
// RESPONSE AND SCORE
//
//
// STORAGE
//
STORAGE
2
store_n_0
LIMIT_SIZE 100
NEUTRON
20 1.0E-11
FRONTIER LIST 1
1000 1100
store_ph_0
LIMIT_SIZE 100
PHOTON
20 1.0E-11
FRONTIER LIST 1
1000 1100
END_STORAGE

//
// SIMULATION
//
SIMULATION
BATCH 100000
SIZE 10000
EDITION 5000
PARTICLE 2
NEUTRON
PHOTON
GLOBAL_SCORES
CRITICALITY
DISCARD 1
END_SIMULATION

```

A.4.5 Approach no. 4: second step, shielding simulation with stored particles as source. Geometry: concrete wall with hole

```

//
// MASURCA core zone
// source storage
// Channel AIR
//
//
// GEOMETRY
//
GEOMETRY
TITLE geo MASURCA square

// STORAGE
TYPE 1000 BOX 0.1 460.0 460.0
VOLU 1100 COMBI 1000 100.85 0 0 ENDV

// R_AIR_INN
TYPE 400 BOX 29.1 460.0 460.0

VOLU 400 COMBI 400 115.45 0 0 ENDV

// R_CONCRETE
TYPE 500 BOX 90.0 460.0 460.0
VOLU 500 COMBI 500 175.0 0 0 ENDV

// R_AIR_EXT
TYPE 600 BOX 30.8 460.0 460.0
VOLU 600 COMBI 600 235.4 0 0 ENDV

// CHANNEL
TYPE 700 BOX 119.1 10.60 10.60
TYPE 730 BOX 29.10 10.16 10.16
TYPE 740 BOX 90.00 10.16 10.16

VOLU 700 COMBI 700 160.45 0 0 SMASH 2 400 500 ENDV
VOLU 730 COMBI 730 115.45 0.0 0.0 SMASH 1 700 ENDV
VOLU 740 COMBI 740 175.00 0.0 0.0 SMASH 1 700 ENDV

```

```

//
ENDGEOM

//
// COMPOSITION
//

//
// GEOMETRY-COMPOSITION
//

//
// SOURCES
//

SOURCES_LIST
1
SOURCE
INTENSITY 1
NEUTRON
SOURCE_STORAGE LIST 58
store_n_0.simul1_1_.stock
store_n_0.simul1_2_.stock
store_n_0.simul2_1_.stock
store_n_0.simul2_2_.stock
store_n_0.simul2_3_.stock
....
store_n_0.simul20_1_.stock
store_n_0.simul20_2_.stock
store_n_0.simul20_3_.stock
RANDOM
TIME_DISTRIBUTION DIRAC 0.0
END_SOURCES
END_SOURCES_LIST

//
// RESPONSE AND SCORE
//

RESPONSES
1
CURRENT NEUTRON
END_RESPONSES

GRID_LIST
1
TRIPOLI_315
END_GRID_LIST

SCORE
1
1 SURF
GRID TRIPOLI_315
FRONTIER LIST 3
1100 730
730 740
740 600
END_SCORE

//
// BIASING
//

VARIANCE_REDUCTION
NEUTRON

```

```

GRID
5
20.0 4.0 0.1 1.0E-3 1.0E-11
DETECT
1
220.0 0.0 0.0
0.5
MESH
30 46 46
5 10 10
3
FRAME
CARTESIAN
100.8 -230.0 -230.0
1 0 0
0 1 0
0 0 1
END_MESH
INIPOND
AUTO
END_INIPOND
END_VARIANCE_REDUCTION

//
// SIMULATION
//

SIMULATION
BATCH 100000
SIZE 10000
EDITION 10000
PARTICLE 1
NEUTRON
GLOBAL_SCORES
SHIELDING
END_SIMULATION

```

APPENDIX B

Concepts and Quantities in Radiation Measurements

B. Concepts and Quantities in Radiation Measurements

B.1. Fluence

B.2. Detector Readings and Response Functions

B.3. Modes of Detector Operation

B.4. Pulse Height Spectra

B.5. Gain

B.6. Energy Resolution

B.7. Detection Efficiency

The purpose of this APPENDIX is to recall some basic concepts of radiation measurements, without trying to be exhaustive, since several good textbooks and articles are dedicated to this topic, such as [Knoll, Beckurts&Wirtz, Marion&Fowler, Allen, Lyoussi, ICRU 2011, Bartlett 2003]. In the first version of this manuscript, this APPENDIX was included in Chapter IV. It is thus intended to be read - if necessary - alongside Chapter IV, before the descriptions of the different types of detectors discussed.

We consider now a simple detector system (Figure B.1), the properties described hereafter are generally valid for this kind of set-up.

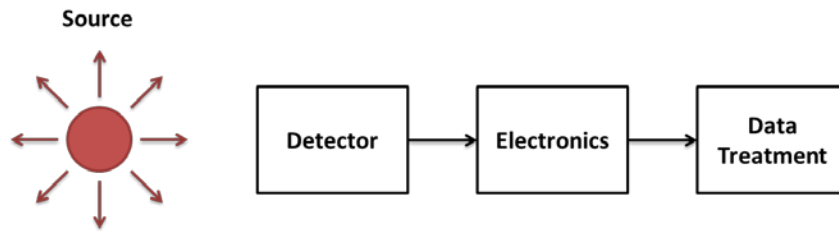


Figure B.1. General detector set-up.

B.1 Fluence

The basic quantity in spectroscopy is the particle, neutron or photon, fluence and its differential distribution in energy and direction. The particle fluence, Φ , can be defined as:

$$\Phi = \frac{dN}{da} , \quad (B.1)$$

with dN as the number of particles incident on a sphere of cross-sectional area da . The most frequently used unit is the reciprocal square centimeter (cm^{-2}). The energy and directional distribution of the particle fluence can be written as:

$$\Phi_E = \frac{d\Phi}{dE} , \quad (B.2)$$

$$\Phi_{\Omega} = \frac{d\Phi}{d\Omega} . \quad (B.3)$$

Where $d\Phi$ is the increment of particle fluence in the energy (direction) interval between E and $E + dE$ (Ω and $\Omega + d\Omega$). Φ_E is the *particle spectrum*. Written with arguments:

$$\Phi_{E,\Omega}(E, \Omega) \text{ (particle fluence) ,} \quad (B.4)$$

$$\Phi_E(E) = \int \Phi_{E,\Omega}(E, \Omega) d\Omega \text{ (particle spectrum) ,} \quad (B.5)$$

$$\Phi_{\Omega}(\Omega) = \int \Phi_{E,\Omega}(E, \Omega) dE \text{ (directional fluence) .} \quad (B.6)$$

The incremental fluence in the time interval dt is called the particle fluence rate and is denoted by φ , φ_E , φ_{Ω} (particles $\text{cm}^{-2} \text{s}^{-1}$).

B.2 Detector Readings and Response Functions

READING

The reading, M , is the value of the output signal obtained by a measuring instrument. The reading is expressed in units of the output signal, regardless of the units marked on the scale of the instrument or read-out equipment. What appears on the scale has to be multiplied by the instrument or read-out equipment constant to provide the reading. It is necessary to make clear whether the reading is raw (uncorrected) or corrected for influential quantities and intrinsic background.

RESPONSE

The response, R , is defined as the ratio of the reading (M) to the value of the quantity to be measured by the instrument for a specific distribution type, energy or direction, of radiation. It is

necessary - in order to avoid confusion - to state the quantity to be measured, for example the 'particle spectrum'. In other terms:

$$R_{\phi} = M/\Phi \quad . \quad (B.7)$$

In general, the determination of the response is made for radiation fields approximating plane parallel beams and for homogeneous irradiation of the detector.

Calibration is a set of operations that establish, under specified conditions, the relationship between values indicated by a detector, and the corresponding, known (i.e. conventionally true), values of the quantity to be measured. This relationship can be established by determining the response of a device for the full range of radiation energies and angles of incidence for its intended use. The Calibrations determine the *calibration factor* for each individual instrument under standard test conditions. In general, the calibration factor N , is the factor by which the reading M of the device is multiplied to obtain the value of the quantity to be measured. Thus, the calibration factor is given by:

$$N = \Phi/M \quad , \quad (B.8)$$

where M is the reading in a standard calibration field with a conventionally true value of Φ .

RESPONSE FUNCTIONS

In the general case of determining a neutron (or photon) spectrum, the measuring device should be capable of giving as a result the particle spectrum at the detector's position in the detector's absence. This means that all disturbances of the radiation field produced by the detector must be taken into account in finding the response functions.

The reading M_i of a spectroscopy system is an integral over the energies E of the incident particles:

$$M_i = \int_{E_{min}}^{E_{max}} R_{\phi,i}(E) \Phi(E) dE \quad . \quad (B.9)$$

For the so-called multichannel detectors, the M_i are the contents of a multichannel spectrum with k channels ($i=1, \dots, k$). For non-isotropic detectors the response function depends also on the direction of the incoming particles.

If we consider a mono-energetic fluence Φ_0 at an energy $E=E_0$:

$$M_i = R_i(E_0) \Phi_0 \quad . \quad (B.10)$$

The M_i values are the elements of a pulse height spectrum (see B.4) and represent the response function of the instrument to particles of energy E_0 . For every (different) mono-energetic incident fluence, exists a corresponding response function for which the instrument responds.

For numerical work, equation B.10 has to be transformed approximately into a discretized linear matrix equation:

$$\mathbf{M} = \mathbf{R} \boldsymbol{\Phi} \quad . \quad (B.11)$$

With \mathbf{R} the *response matrix* and $\boldsymbol{\Phi}$ the fluence column vector ($\boldsymbol{\Phi}^T = (\Phi_1, \dots, \Phi_v, \dots, \Phi_N)$). The N fluence components are considered as (integral) values in the N energy intervals.

REPRESENTATIONS OF THE PARTICLE SPECTRUM

In practice, particle spectra (the energy distribution of particle fluence) are listed as integrals over small energy intervals. For instance, the fluence in an energy interval ΔE between E_i and E_{i+1} , is given by:

$$\Phi_i = \int_{E_i}^{E_{i+1}} \Phi_E(E) dE \quad . \quad (B.12)$$

The Φ_i are often calculated and presented in tabular form together with the upper or lower energy value of the interval.

In graphical representations the Φ_i are usually related to the median value $\bar{E} = 0.5(E_i + E_{i+1})$ of the linear interval, or the median $\bar{E} = \sqrt{E_i E_{i+1}}$ of the logarithmic energy interval.

If spectra are given as a continuous (analytical) function, the most common graphical representations are the particle spectrum $\Phi(E) = d\Phi/dE$ versus energy E , if the E axis is linearly scaled, or $d\Phi/d(\ln(E/E_0))$, if the E axis is logarithmic. The latter have been known historically as *lethargy plots* and the ordinate is often annotated as *fluence per lethargy units*. The arbitrary parameter E_0 is needed to make the argument of the logarithm dimensionless. The lethargy representation is often the most appropriate, since spectra, when plotted on a linear energy scale, may lead to a misleading interpretation of the contribution of low-energy neutrons.

When a continuous function is not available, the values Φ_i are often plotted in a histogram form versus a linear or logarithmic energy scale.

B.3 Modes of Detector Operation

There are three general modes of operation of radiation detectors: i) *pulse mode*, ii) *current mode* and iii) *Campbell mode* (or *mean square voltage mode*).

In *pulse mode* operation, the signal from each interaction is processed individually. The measurement instrumentation is designed to record each individual particle that interacts in the detector. In most common application, the total charge Q (time integral of each burst of current or, simply, the amplitude of each pulse) is recorded, since the energy deposited in the detector is proportional to Q .

At very high event rates, pulse mode operation becomes impractical or even impossible, the time between adjacent events may become too short to carry out an adequate analysis. In such case, it is possible to use *current mode* and *Campbell mode*, which respond to the time average taken over many individual events. All information regarding individual interactions is lost.

In this work the focus is on systems working in *pulse mode*, since it is the proper one for radiation spectroscopy.

B.4 Pulse Height Spectra

When operating in pulse mode, each individual pulse amplitude carries important information regarding the charge generated by a particular radiation interacting with the detector. The pulse amplitude distribution is used to deduce information about the incident radiation or the operation of the detector itself.

Pulse amplitude information is represented in two ways: *differential pulse height distribution* and *integral pulse height distribution* (Figure B.2).

The most common one is the *differential pulse height distribution*. The abscissa is a linear pulse amplitude scale from zero to a value larger than the amplitude of any pulse observed from the source. The ordinate is the differential number dN of pulses observed with an amplitude within the differential amplitude increment dH , divided by that increment, or dN/dH . The horizontal scale has the units of pulse amplitude (directly proportional to energy deposited in the detector), whereas the vertical scale has units of inverse amplitude.

The physical interpretation of differential pulse height spectra always involves areas under the spectrum between two given limits of pulse height: the number of pulses whose amplitude lies between two specific values can be obtained by integrating the area under the distribution between those two limits (Figure B.2). The total number of pulses N_0 is the integral of the area under the entire spectrum.

In the *integral pulse height distribution* representation, the abscissa is the same as before, while the ordinate represents the number of pulses whose amplitude exceeds that of a given value of abscissa H .

The differential and integral distributions communicate exactly the same information and one can be derived from the other.

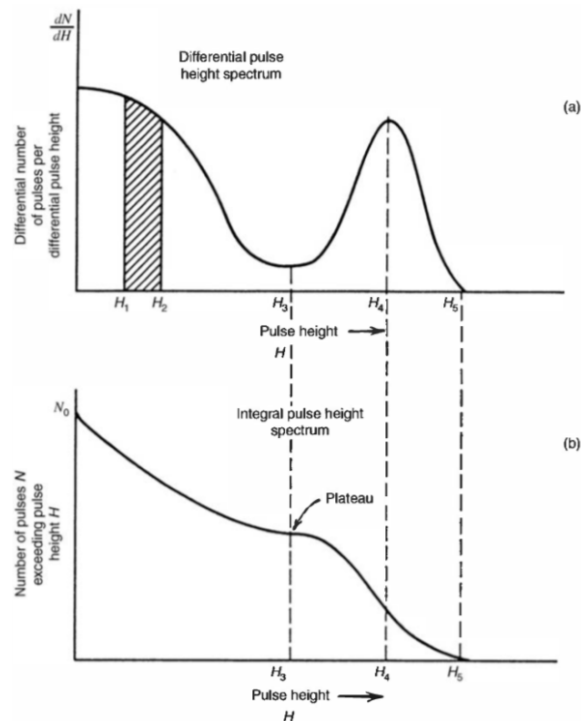


Figure B.2. Pulse height spectrum representations [Knoll].

B.5 Gain

When radiation detectors are operated in pulse mode, signal pulses must usually exceed a given level H_d in order to be registered by the counting circuit. In setting up a pulse counting measurement, it is often desirable to establish an operating point H_d that will provide maximum stability over long periods of time.

In general, it is possible to vary the *gain* of a detector, the amplification (the width) provided for the charge produced in the radiations interactions, to meet the detection system needs. In Figure B.3 it is possible to appreciate the role of the gain, that is used for changing the width of the pulse high distribution to meet the constraint imposed by the operating point. The areas under the curves with different gain are the same.

The variation of the gain could be accomplished by varying the amplification factor of a linear amplifier between the detector and counting circuit, or in many cases more directly by changing the applied voltage to the detector itself.

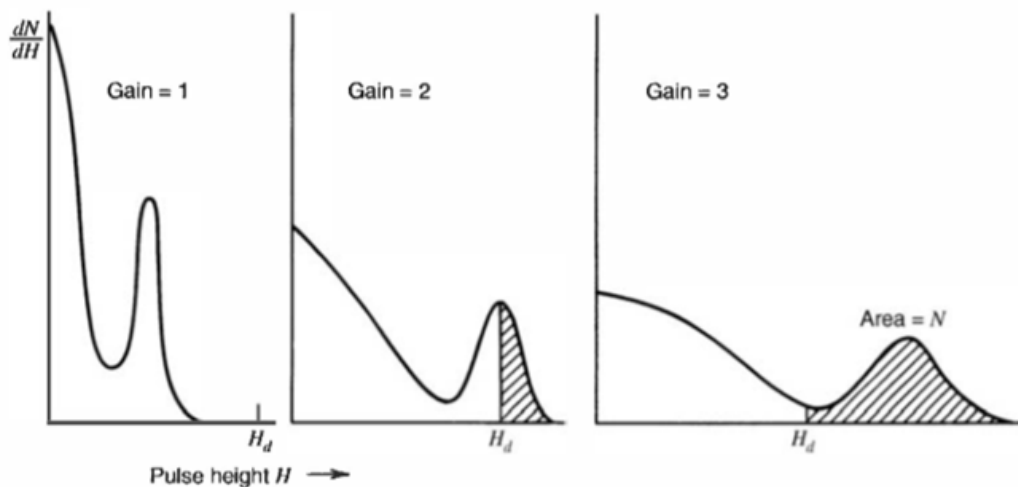


Figure B.3. Gain [Knoll].

B.6 Energy Resolution

The detector *resolution* R defines the ability of an instrument to resolve fine details characteristic of an incident radiation energy spectrum. The resolution is a dimensionless fraction conventionally expressed in percentage and is improved as the width of the response function became smaller and

smaller (Figure X.4). The smaller the resolution, the better the detector will be able to distinguish between two radiations with energies lying near each other. A formal definition requires the introduction of the *FWHM* concept, *full width at half maximum* (Figure B.4), defined as the width of the distribution (the peak) at the half of the maximum ordinate value. The *energy resolution* is conventionally referred to as the FWHM divided by the location of the distribution peak center (H_0):

$$R = FWHM/H_0 \quad . \quad (B.13)$$

If the response function has a Gaussian shape (it is often the case, since N is typically a large number), we can write:

$$G(H) = \frac{A}{\sigma\sqrt{2\pi}} \exp\left(-\frac{(H - H_0)^2}{2\sigma^2}\right) \quad . \quad (B.14)$$

With A representing the area of the distribution and H_0 the center of the distribution peak. The width parameter σ determines the *FWHM* of any Gaussian through the relation $FWHM = 2.35\sigma$.

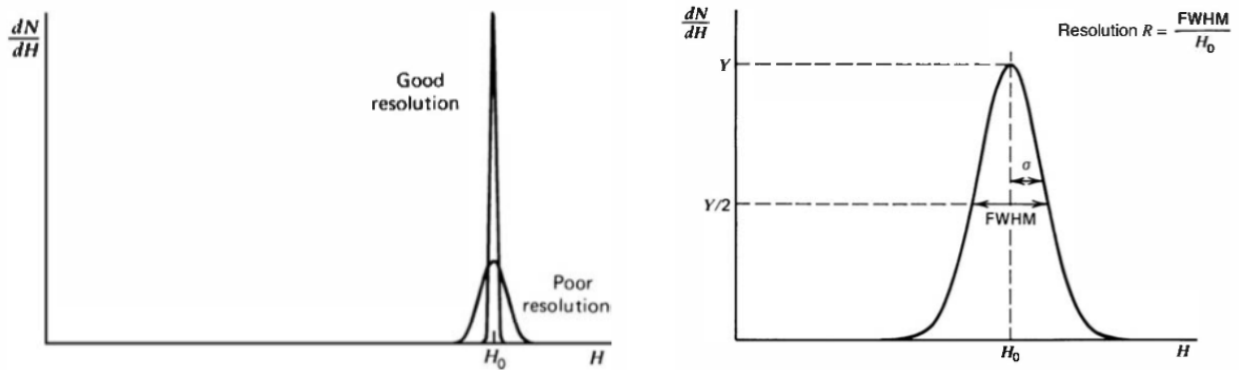


Figure B.4. Resolution [Knoll].

The definition is generally valid if we assume that any background or continuum on which the peak may be superimposed is negligible or has been subtracted.

B.7 Detection Efficiency

In general, for any detector apparatus, *efficiency* is a dimensionless ratio between the output quantity from the system and the input quantity in the system. *Detector efficiency* is usually divided into *absolute* and *intrinsic*, defined as follow:

$$\varepsilon_{abs} = \frac{\text{number of signals recorded}}{\text{number of particles emitted by the source}} , \quad (B.15)$$

$$\varepsilon_{int} = \frac{\text{number of signals recorded}}{\text{number of particles incident on detector}} . \quad (B.16)$$

The two efficiencies are related, for isotropic source, by $\varepsilon_{int} = \varepsilon_{abs}(4\pi/\Omega)$, where Ω is the solid angle of the detector seen from the actual source position.

B.8 Dead Time

In almost every spectrometer operating in pulse mode, there will be a minimum amount of time that must separate two events in order to be recorded as two separate signals. This minimum time separation is usually called *dead time* of the counting system. The ‘dead time losses’ can become rather severe when high counting rates are encountered, and any accurate counting measurements made under these conditions must include some correction for these losses.

APPENDIX C

Simulation of the Organic Scintillator Response with MCNPX-PoliMi and MPPost

C. Simulation of the Organic Scintillator Response with MCNPX-PoliMi and MPPost

C.1. AIFIRA

C.2. LVR-15

C.3. LR-0

C.4. MASURCA

This APPENDIX is entirely devoted to modelling and calculation procedure adopted for simulating the organic scintillator responses. The calculation route is based on MCNPX-PoliMi and MPPost, already discussed in Chapter V.

All the results of the simulations presented here have been shown in Chapter VII.

C.1 AIFIRA

The simulated neutron spectrum used in the MCNPX input is the one of the stilbene unfolded spectrum (with the Rez response matrix), shown in Figure C.1. Only neutrons were taken into account.

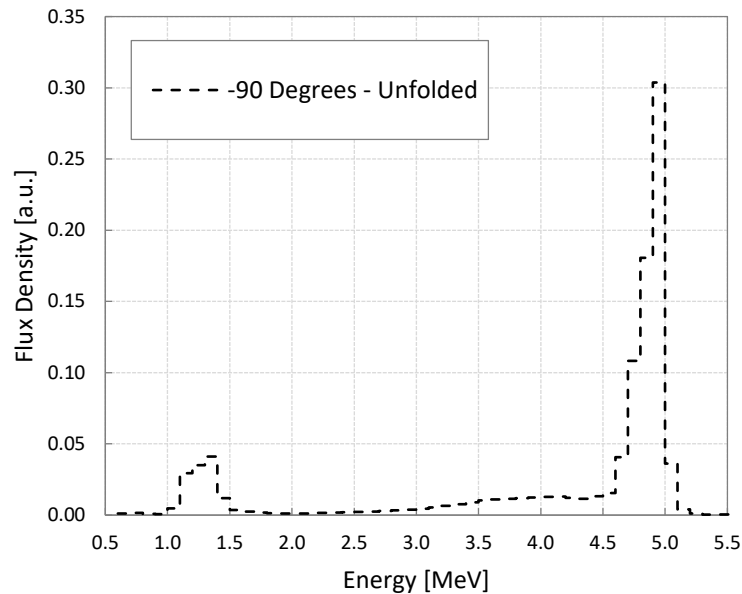


Figure C.1. Unfolded 5 MeV neutron spectrum measured by s-g stilbene (-90 degrees).

As already mentioned, the simulation was kept, purposely, simple. The aim was to test the capabilities of the calculation route and not to provide fully detailed results.

The stilbene detector is represented by a \varnothing 25.4 mm \times 25.4 mm cylinder with a density value provided by Inradoptics (other simulations - not presented here - taking in consideration also the photomultiplier and the other detector components have been performed). The source is a pointwise one, located at the centre of the detector volume. Where not specified, the default options of MCNPX-PoliMi have been used. The input files is presented hereafter:

c -----	3.15E+00
c s-g stilbene 25x25 + AIFIRA 5 MeV neutron spectrum	3.25E+00
c -----	3.35E+00
c -----	3.45E+00
c CELL DESCRIPTION	3.55E+00
c -----	3.65E+00
1 1 -1.15 -1 IMP:n,p=1 \$ Stilbene Inrad Optics	3.75E+00
2 0 1 -2 IMP:n,p=1 \$ Void	3.85E+00
3 0 2 IMP:n,p=0 \$ Outside Univ	3.95E+00
	4.05E+00
c -----	4.15E+00
c SURF DESCRIPTION	4.25E+00
c -----	4.35E+00
c Stilbene	4.45E+00
1 RCC 0 0 0 0 0 2.54 1.27	4.55E+00
c Void	4.65E+00
2 SO 50	4.75E+00
	4.85E+00
c -----	4.95E+00
c MAT DESCRIPTION	5.05E+00
c -----	5.15E+00
c Stilbene	5.25E+00
M1 1001 12	5.35E+00
6012 14	5.45E+00
c -----	5.55E+00
c SOURCE DESCRIPTION	5.65E+00
c -----	5.75E+00
SDEF par=1 pos=0 0 1.27 erg=d1	SP1 d 0
SI1 h 6.50E-01	2.07E+08
7.50E-01	1.19E+08
8.50E-01	7.81E+07
9.50E-01	5.01E+08
1.05E+00	2.42E+09
1.15E+00	3.48E+09
1.25E+00	4.87E+09
1.35E+00	1.25E+09
1.45E+00	3.29E+08
1.55E+00	2.71E+08
1.65E+00	2.23E+08
1.75E+00	1.64E+08
1.85E+00	1.20E+08
1.95E+00	1.13E+08
2.05E+00	1.07E+08
2.15E+00	1.43E+08
2.25E+00	1.92E+08
2.35E+00	2.26E+08
2.45E+00	2.67E+08
2.55E+00	3.08E+08
2.65E+00	3.56E+08
2.75E+00	4.07E+08
2.85E+00	4.66E+08
2.95E+00	5.42E+08
3.05E+00	6.32E+08

7.40E+08	5.49E+07	
8.69E+08	4.87E+07	
9.35E+08	4.20E+07	
1.01E+09	4.14E+07	
1.12E+09	4.00E+07	
1.24E+09	c -----	
1.32E+09	c SIM DESCRIPTION	
1.41E+09	c -----	
1.39E+09	MODE n	
1.37E+09	NPS 10e6	
1.27E+09	PHYS:n J 20	\$ implicit capture
1.18E+09	off	
1.30E+09	c -----	
1.43E+09	c POLIIMI OPTIONS	
2.46E+09	c -----	
4.25E+09	IPOL 0 0 0 0 2J 1 1	\$ standard
1.31E+10	MCNPX + collision info cell 1	
4.08E+10	RPOL 0.001 0.001	\$ n,g energy
8.95E+09	deposition > 1 keV	
1.87E+09	FILES 21 aifira_5mev_thesis.txt	
3.30E+08	c -----	

The MCNPX-PoliMi output is used as input to MPPost. The chosen detector type is “*Liquid Organic Scintillator*” as no option for crystal scintillators pre-existed at the start of this work. For the neutron calibration, as already mentioned, the LO-to-energy relationship provided by Rez has been used (Figure X.2), in the form number “2”:

$$y [MeV_{ee}] = \frac{Ax^2}{(x + B)} [MeV] . \quad (C.1)$$

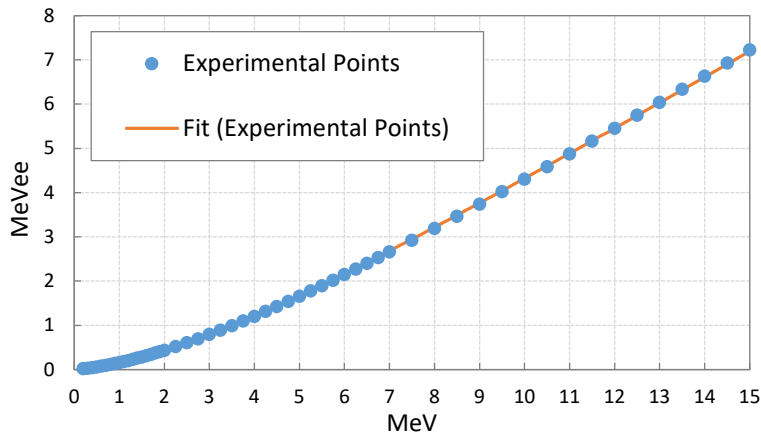


Figure C.2. Experimental LO-to-energy relationship (fitted).

Also in this case, where not specified, the default options of MPPost were used. The MPPost input is shown in the following:

```

# ~~~~~
# ~~~~~
#
# Input file for MPPost
#
# version: 2.1.0
# ~~~~~
# ~~~~~

# ~~~~~
# GENERAL INFORMATION
# ~~~~~
title          stilbene 25x25 @ AIFIRA 5 MeV
username       LD

# ~~~~~

# I/O FILE INFORMATION
# ~~~~~
polimi_det_in      aifira_5mev_thesis.txt    # MCNP-PoliMi detector filename
output_file        out_aifira5mev_thesis  # Desired output name
label_output       yes                # (yes/no) Place labels at the top of the output files
seperate_det_response no            # (yes/no) Print individual distributions for each detector
list_of_pulses     no                # (yes/no) Print a list mode file of all collected pulses
event_inventory_on no                # (yes/no) Print out a table summarizing all events in the file
collision_history  no                # (yes/no) Print summary of how collisions make pulses in the detector
overwrite_files    yes                # (yes/no) Allow the code to overwrite old files
comma_delimited    no                # (yes/no) Output files delimited by a comma

# ~~~~~

# MEMORY
# ~~~~~
division_size      1000    # MB, size of segments to divide the file
cushion            200     # number of lines added to the arrays to prevent overstepping arrays

# ~~~~~

# DETECTOR INFORMATION
# ~~~~~
time_dependent     no                # (yes/no) Perform analysis by time instead of by history
NPS                10e6           # NPS used in the MCNP run
detector_type      1                # Type of Detector - list for each cell number
                                     # 0 = Non Active Volume (i.e. PMT)
                                     # 1 = Liquid Organic Scintillator

```

```

# 2 = He3 (Cannot be run with other types)
# 3 = Plastic Organic Scintillator
# 4 = NaI
# 5 = CaF2
# 6 = LaBr3
threshold          0.001      # MeVee, Threshold for event detection - list for each cell number
upper_threshold    3          # MeVee, the max acceptable light for event detection - list for each cell number
detector_cell_numbers 1      # Cell numbers of the detectors
# NOTE: To group cells add ( ) around the group.
# There must be a space before and after each (

# ~~~~~
# DETECTOR INFORMATION - Pulse Height
# ~~~~~
pulse_height_on    yes        # (yes/no) Print pulse height distributions
sum_then_light     no         # (yes/no) Convert the sum of all contributing particles energy to light
cross_talk_sub_on  no         # (yes/no) Eliminate particles with cross talk

# Pulse Generation Time - ns, Light collection time for a pulse
organic_liq_pgt    10         # Pulse generation time for an organic liquid scintillator
organic_pl_pgt     10         # Pulse generation time for an organic plastic scintillator
nai_pgt            10         # Pulse generation time for a NaI detector
caf2_pgt           10         # Pulse generation time for a CaF2 detector
labr3_pgt          10         # Pulse generation time for a LaBr3 detector

# Deadtime - ns, dead time of the detector between pulses
organic_liq_dt     0          # Dead time for an organic liquid scintillator
organic_pl_dt      0          # Dead time for an organic plastic detector
nai_dt             0          # Dead time for a NaI detector
caf2_dt            0          # Dead time for a CaF2 detector
labr3_dt           0          # Dead time for a LaBr3 detector

histogram_start    0          # MeVee, Min value for the pulse height distribution
histogram_stop     3          # MeVee, Max value for the pulse height distribution
bin_step           0.01      # MeVee, Bin step - top side of the bin

# ~~~~~
# ORGANIC SCINTILLATOR
# ~~~~~
calibration_regions 1        # Number of independently fit neutron light regions
region_type         2        # Specify which form for the coefficients, if multiple regions list selections
# Type  Form    How to enter values on the neutron calibration line
# 1 = Ax^2+Bx+C -> E1 E2 A B C
# 2 = Ax^2/(x+B) -> E1 E2 B A
# 3 = A(Bx-C(1-exp(Dx^E))) -> E1 E2 A B C D E
# Where E1 and E2 are the lower and upper energy bounds respectively in
MeVee
neutron_calibration 0 50 0.6151 4.238 # Neutron Calibration - see above for entry instructions

```

```

photon_calibration      1.000 0.000          # A,B: Parameters for photon light conversion - Ax+B
carbon_light_constant   0.02          # Constant value for carbon light conversion
deuterium_calibration   0 0 0.0131 0.2009 -0.0331      # A,B,C,D,E: Parameters for deuterium light
conversion - Ax^4+Bx^3+Cx^2+Dx+E

# ~~~~~
# Light Output Resolution
# ~~~~~
light_resolution_on    no      # (yes/no) Turns on/off the a Gaussian Light Broadening

# ~~~~~
# Time Resolution
# ~~~~~
tme_resolution_on      no      # (yes/no) Turns on/off time broadening

# ~~~~~
# TIME-OF-FLIGHT, CORRELATION, and AUTOCORRELATION INFORMATION
# ~~~~~
tof_on                 no      # (yes/no) Turn on/off TOF distributions (cannot have a start detector)
cross_correlation_on   no      # (yes/no) Turn on/off cross correlation function
auto_correlation_on    no      # (yes/no) Turn on/off auto correlation function
start_detector         # Cell number of the start detector (leave blank for TOF)
time_start             0      # ns, time for the correlation plot to start
time_stop              100     # ns, time for the correlation plot to stop
time_increment         1      # ns, time increment between the bins - top side of the bin
cc_window_incr        1000    # ns, time window for correlation events for time dependent analysis
# ~~~~~
# Pulse Height Correlation
# ~~~~~
pulse_correlation_on   no      # (yes/no) Turn on/off pulse height correlation analysis

```

C.2 LVR-15

The neutron spectrum of LVR-15 used for the simulation of the detector response is shown in Figure C.3.

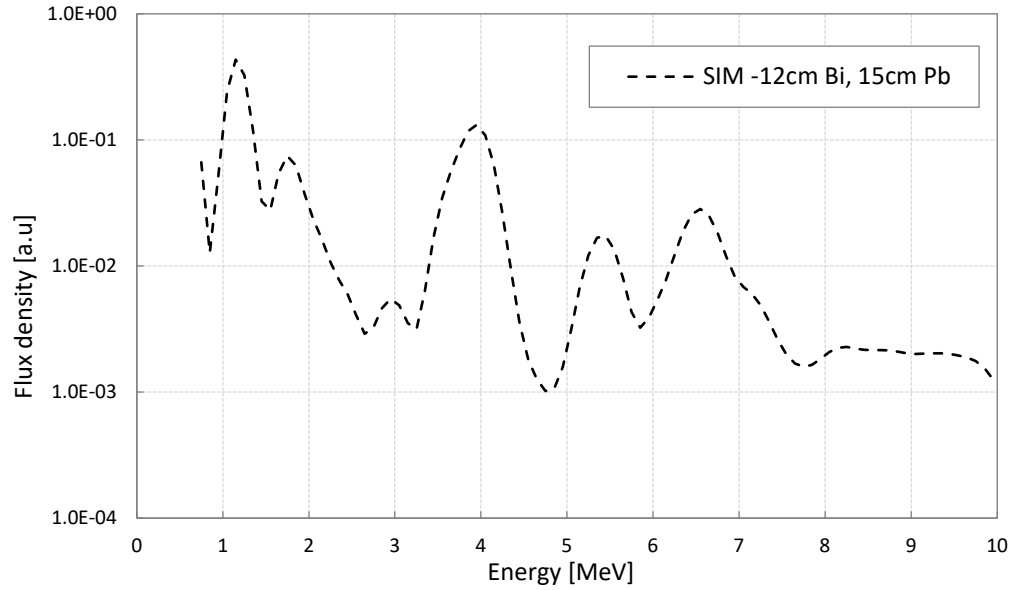


Figure C.3. LVR-15 neutron spectrum used for the simulation.

Hereafter is shown only the MCNPX-PoliMi input, since the MPPost one is the same as the one presented in the AIFIRA case.

```

c -----
c      stilbene 25x25 + LVR-15
c -----
c -----
c CELL DESCRIPTION
c -----
1 1 -1.15 -1    IMP:n,p=1 $ Stilbene InradOptics
2 0   1 -2    IMP:n,p=1 $ Void
3 0   2      IMP:n,p=0 $ Outside Univ

c -----
c SURF DESCRIPTION
c -----
c Stilbene
1 RCC 0 0 0 0 2.54 1.27
c Void
2 SO 50

c -----
c MAT DESCRIPTION
c -----
c Stilbene
M1 1001 12
6012 14
c -----
c SOURCE DESCRIPTION
c -----
SDEF par=1 pos=0 0 1.27 erg=d1
SI1 h 7.59E-01
7.79E-01
7.89E-01
8.09E-01
8.19E-01
8.28E-01
8.48E-01
8.78E-01
8.97E-01
9.17E-01
9.27E-01
9.37E-01
9.66E-01
9.76E-01
1.01E+00
1.02E+00

```

1.04E+00	3.28E+00
1.06E+00	3.32E+00
1.08E+00	3.35E+00
1.11E+00	3.38E+00
1.16E+00	3.41E+00
1.20E+00	3.45E+00
1.25E+00	3.49E+00
1.28E+00	3.55E+00
1.31E+00	3.63E+00
1.34E+00	3.76E+00
1.35E+00	3.82E+00
1.38E+00	3.89E+00
1.40E+00	3.95E+00
1.41E+00	4.00E+00
1.43E+00	4.08E+00
1.45E+00	4.13E+00
1.50E+00	4.18E+00
1.55E+00	4.22E+00
1.59E+00	4.27E+00
1.60E+00	4.32E+00
1.64E+00	4.38E+00
1.67E+00	4.44E+00
1.71E+00	4.50E+00
1.75E+00	4.55E+00
1.80E+00	4.62E+00
1.85E+00	4.68E+00
1.90E+00	4.74E+00
1.96E+00	4.84E+00
2.06E+00	4.89E+00
2.11E+00	4.93E+00
2.17E+00	5.00E+00
2.24E+00	5.07E+00
2.31E+00	5.13E+00
2.38E+00	5.20E+00
2.47E+00	5.26E+00
2.52E+00	5.31E+00
2.57E+00	5.37E+00
2.62E+00	5.45E+00
2.68E+00	5.51E+00
2.75E+00	5.56E+00
2.80E+00	5.63E+00
2.84E+00	5.68E+00
2.88E+00	5.73E+00
2.95E+00	5.79E+00
3.04E+00	5.84E+00
3.11E+00	5.89E+00
3.15E+00	5.94E+00
3.21E+00	6.04E+00
3.26E+00	6.12E+00

6.20E+00	2.00E+06
6.27E+00	2.57E+06
6.34E+00	3.19E+06
6.42E+00	3.86E+06
6.50E+00	4.33E+06
6.56E+00	3.96E+06
6.66E+00	3.40E+06
6.74E+00	2.71E+06
6.80E+00	2.00E+06
6.89E+00	1.55E+06
6.95E+00	1.22E+06
7.03E+00	9.69E+05
7.14E+00	6.97E+05
7.24E+00	5.54E+05
7.34E+00	4.25E+05
7.41E+00	3.34E+05
7.50E+00	2.87E+05
7.60E+00	2.76E+05
7.69E+00	3.17E+05
7.79E+00	3.89E+05
7.90E+00	4.64E+05
8.02E+00	5.83E+05
8.16E+00	6.79E+05
8.29E+00	7.52E+05
8.46E+00	7.24E+05
8.64E+00	6.14E+05
8.67E+00	4.95E+05
8.87E+00	3.51E+05
9.10E+00	2.46E+05
9.34E+00	1.96E+05
9.55E+00	1.54E+05
9.74E+00	1.19E+05
9.84E+00	8.81E+04
SP1 d 0	7.28E+04
4.36E+05	6.02E+04
3.51E+05	4.85E+04
2.31E+05	3.91E+04
1.82E+05	3.27E+04
1.50E+05	2.85E+04
1.27E+05	3.11E+04
1.43E+05	3.72E+04
1.79E+05	4.38E+04
2.31E+05	5.10E+04
3.09E+05	5.44E+04
4.19E+05	5.17E+04
5.76E+05	4.27E+04
7.61E+05	3.58E+04
1.09E+06	3.11E+04
1.53E+06	3.11E+04

3.58E+04
4.50E+04
5.51E+04
8.16E+04
1.07E+05
1.56E+05
2.37E+05
3.56E+05
5.27E+05
8.21E+05
1.06E+06
1.23E+06
1.33E+06
1.23E+06
1.01E+06
7.61E+05
4.82E+05
3.65E+05
2.34E+05
1.34E+05
7.10E+04
4.33E+04
2.64E+04
1.95E+04
1.40E+04
1.19E+04
1.03E+04
1.02E+04
1.17E+04
1.45E+04
2.15E+04
3.45E+04
5.58E+04
9.27E+04
1.19E+05
1.54E+05
1.75E+05
1.70E+05
1.46E+05
1.26E+05
9.15E+04
7.10E+04
4.98E+04
3.72E+04
3.36E+04
3.19E+04
3.72E+04
4.91E+04
6.75E+04

9.87E+04
1.37E+05
1.84E+05
2.34E+05
2.69E+05
2.87E+05
2.56E+05
2.03E+05
1.43E+05
1.00E+05
8.06E+04
7.10E+04
6.02E+04
4.91E+04
3.86E+04
2.96E+04
2.30E+04
1.80E+04
1.61E+04
1.59E+04
1.74E+04
2.00E+04
2.21E+04
2.27E+04
2.15E+04
2.18E+04
2.18E+04
2.07E+04
2.02E+04
2.05E+04
1.95E+04
1.78E+04
1.63E+04
c -----
c SIM DESCRIPTION
c -----
MODE n
NPS 10e8
PHYS:n J 20 \$ implicit capture off
c -----
c POLIIMI OPTIONS
c -----
IPOL 0 0 0 0 2J 1 1 \$ standard MCNPX +
collision infos cell 1
RPOL 0.001 0.001 \$ n,g energy deposition > 1
keV
FILES 21 lvr15.txt
c -----

C.3 LR-0

For the simulations of the LR-0 response, a stilbene crystal of $\varnothing 10 \text{ mm} \times 10 \text{ mm}$ was used, since the experimental results with the $\varnothing 25 \text{ mm} \times 25 \text{ mm}$ one were not completely correct (see 7.4.1), meanwhile several experimental measurements with the smaller m-g stilbene were available and verified at Rez. The neutron spectrum used is represented in Figure C.4.

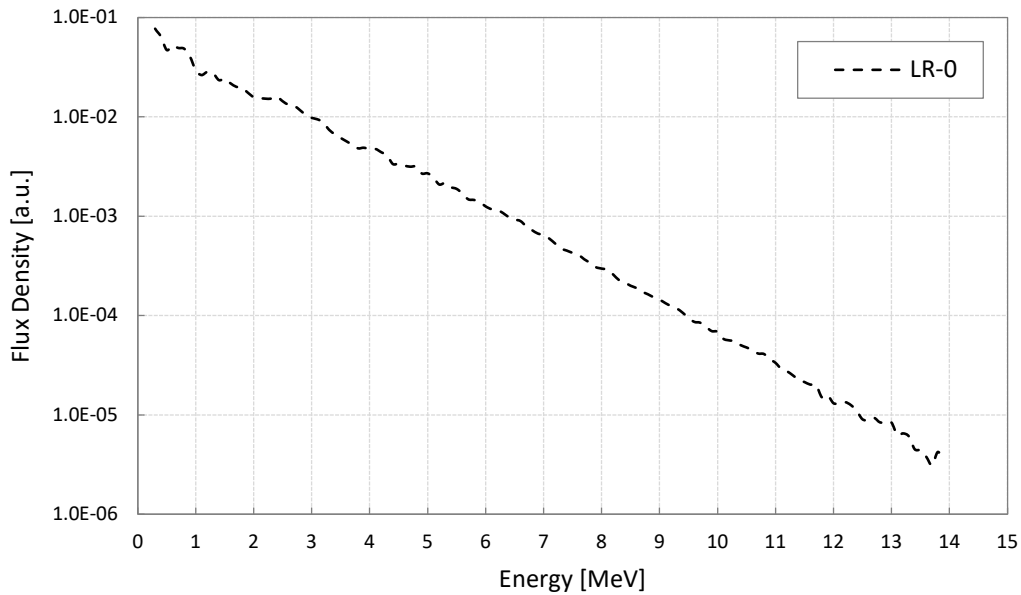


Figure C.4. LR-0 neutron spectrum used for the simulation.

```

c -----
c          stilbene 10x20 + LR-0
c -----
c -----
c CELL DESCRIPTION
c -----
1 1 -1.15 -1    IMP:n,p=1 $ Stilbene InradOptics
2 0   1 -2     IMP:n,p=1 $ Void
3 0   2       IMP:n,p=0 $ Outside Univ

c -----
c SURF DESCRIPTION
c -----
c Stilbene

1 RCC 0 0 0 0 0 1 0.5
c Void
2 SO 50

c -----
c MAT DESCRIPTION
c -----
c Stilbene
M1 1001 12
6012 14

c -----
c SOURCE DESCRIPTION
c -----
SDEF par=1 pos=0 0 0.5 erg=d1

```

SI1 h 1.00E-01	5.00E+00
2.00E-01	5.10E+00
3.00E-01	5.20E+00
4.00E-01	5.30E+00
5.00E-01	5.40E+00
6.00E-01	5.50E+00
7.00E-01	5.60E+00
8.00E-01	5.70E+00
9.00E-01	5.80E+00
1.00E+00	5.90E+00
1.10E+00	6.00E+00
1.20E+00	6.10E+00
1.30E+00	6.20E+00
1.40E+00	6.30E+00
1.50E+00	6.40E+00
1.60E+00	6.50E+00
1.70E+00	6.60E+00
1.80E+00	6.70E+00
1.90E+00	6.80E+00
2.00E+00	6.90E+00
2.10E+00	7.00E+00
2.20E+00	7.10E+00
2.30E+00	7.20E+00
2.40E+00	7.30E+00
2.50E+00	7.40E+00
2.60E+00	7.50E+00
2.70E+00	7.60E+00
2.80E+00	7.70E+00
2.90E+00	7.80E+00
3.00E+00	7.90E+00
3.10E+00	8.00E+00
3.20E+00	8.10E+00
3.30E+00	8.20E+00
3.40E+00	8.30E+00
3.50E+00	8.40E+00
3.60E+00	8.50E+00
3.70E+00	8.60E+00
3.80E+00	8.70E+00
3.90E+00	8.80E+00
4.00E+00	8.90E+00
4.10E+00	9.00E+00
4.20E+00	9.10E+00
4.30E+00	9.20E+00
4.40E+00	9.30E+00
4.50E+00	9.40E+00
4.60E+00	9.50E+00
4.70E+00	9.60E+00
4.80E+00	9.70E+00
4.90E+00	9.80E+00

9.90E+00	4.40E+05
1.00E+01	4.33E+05
1.01E+01	3.62E+05
1.02E+01	2.63E+05
1.03E+01	2.35E+05
1.04E+01	2.53E+05
1.05E+01	2.45E+05
1.06E+01	2.09E+05
1.07E+01	2.15E+05
1.08E+01	1.94E+05
1.09E+01	1.79E+05
1.10E+01	1.75E+05
1.11E+01	1.56E+05
1.12E+01	1.41E+05
1.13E+01	1.38E+05
1.14E+01	1.36E+05
1.15E+01	1.36E+05
1.16E+01	1.42E+05
1.17E+01	1.28E+05
1.18E+01	1.18E+05
1.19E+01	1.15E+05
1.20E+01	1.04E+05
1.21E+01	9.33E+04
1.22E+01	8.72E+04
1.23E+01	8.42E+04
1.24E+01	7.84E+04
1.25E+01	6.61E+04
1.26E+01	5.96E+04
1.27E+01	5.47E+04
1.28E+01	5.06E+04
1.29E+01	4.67E+04
1.30E+01	4.30E+04
1.31E+01	4.36E+04
1.32E+01	4.20E+04
1.33E+01	4.24E+04
1.34E+01	3.93E+04
1.35E+01	3.65E+04
1.36E+01	2.99E+04
1.37E+01	3.01E+04
1.38E+01	2.88E+04
1.39E+01	2.81E+04
1.40E+01	2.81E+04
1.00E+04	2.40E+04
SP1 d 0	2.41E+04
8.97E+05	2.18E+04
6.88E+05	1.86E+04
5.73E+05	1.92E+04
4.20E+05	1.75E+04
4.64E+05	1.68E+04

1.51E+04	4.26E+02	
1.32E+04	4.00E+02	
1.30E+04	3.70E+02	
1.24E+04	3.66E+02	
1.12E+04	3.25E+02	
1.05E+04	2.98E+02	
1.03E+04	2.59E+02	
9.60E+03	2.45E+02	
8.72E+03	2.23E+02	
8.26E+03	2.02E+02	
7.98E+03	1.91E+02	
7.07E+03	1.80E+02	
6.46E+03	1.78E+02	
5.97E+03	1.34E+02	
5.78E+03	1.40E+02	
5.30E+03	1.17E+02	
4.73E+03	1.17E+02	
4.23E+03	1.20E+02	
4.02E+03	1.12E+02	
3.81E+03	9.79E+01	
3.65E+03	8.06E+01	
3.29E+03	7.93E+01	
3.03E+03	8.33E+01	
2.74E+03	7.51E+01	
2.65E+03	7.54E+01	
2.58E+03	7.47E+01	
2.31E+03	5.61E+01	
2.03E+03	5.81E+01	
1.92E+03	5.42E+01	
1.78E+03	4.03E+01	
1.69E+03	3.92E+01	
1.55E+03	3.38E+01	
1.46E+03	2.78E+01	
1.36E+03	3.78E+01	
1.29E+03	3.04E+01	
1.19E+03	2.99E+01	
1.11E+03	0.00E+00	
1.05E+03	c -----	
9.51E+02	c SIM DESCRIPTION	
8.47E+02	c -----	
7.70E+02	MODE n	
7.56E+02	NPS 10e8	
6.87E+02	PHYS:n J 20	\$ implicit capture off
6.22E+02	c -----	
6.13E+02	c POLIIMI OPTIONS	
5.21E+02	c -----	
5.02E+02	IPOL 0 0 0 0 2J 1 1	\$ standard MCNPX +
4.92E+02	collision infos cell 1	
4.49E+02		

RPOL 0.001 0.001
1 keV

\$ n,g energy deposition >

FILES 21 lr0.txt

c -----

C.4 MASURCA

The simulation related to MASURCA is presented in the following. The chosen MASURCA spectrum (Figure C.5) is the one at the beginning of the radial channel, REF model (see **APPENDIX A**).

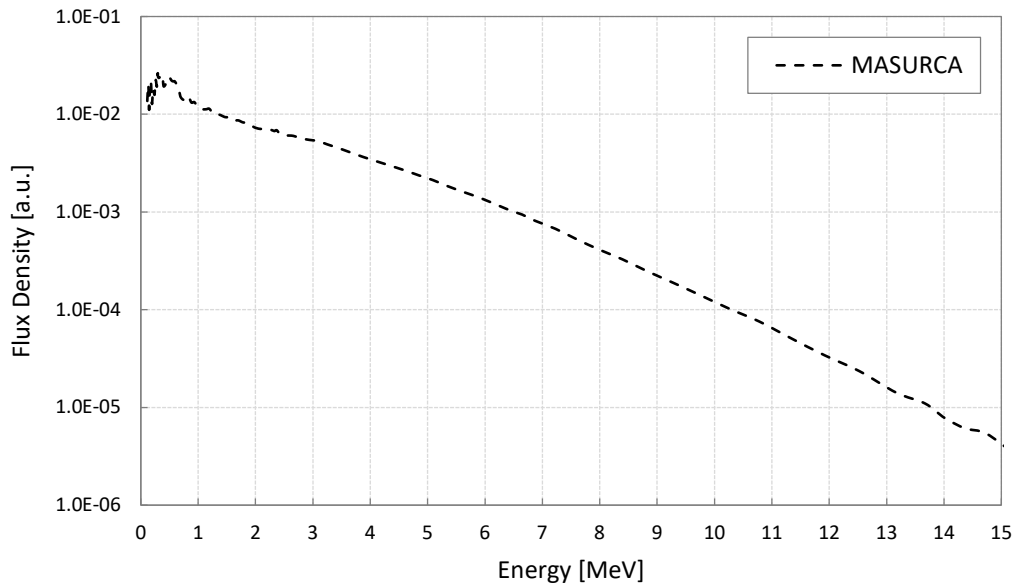


Figure C.5. MASURCA neutron spectrum used for the simulation.

```

c -----
c      stilbene 25x25 + MASURCA
c -----
c -----
c CELL DESCRIPTION
c -----
1 1 -1.15 -1    IMP:n,p=1 $ Stilbene InradOptics
2 0   1 -2     IMP:n,p=1 $ Void
3 0   2   1    MP:n,p=0  $ Outside Univ
c -----

```

```

c SURF DESCRIPTION
c -----
c Stilbene
1 RCC 0 0 0 0 0 2.54 1.27
c Void
2 SO 50
c -----
c MAT DESCRIPTION
c -----
c Stilbene

```

M1 1001 12	1.056
6012 14	1.137
c -----	1.195
c SOURCE DESCRIPTION	1.256
c -----	1.320
SDEF par=1 pos=0 0 1.27 erg=d1	1.388
SI1 h 0.092	1.460
0.105	1.534
0.114	1.613
0.120	1.696
0.126	1.783
0.132	1.874
0.139	1.970
0.146	2.071
0.154	2.177
0.162	2.269
0.170	2.327
0.179	2.356
0.188	2.375
0.197	2.426
0.208	2.529
0.218	2.659
0.229	2.795
0.241	2.939
0.260	3.089
0.280	3.248
0.291	3.504
0.296	3.873
0.298	4.280
0.300	4.609
0.318	4.845
0.351	5.093
0.378	5.354
0.398	5.629
0.429	5.917
0.487	6.221
0.537	6.484
0.564	6.648
0.593	6.875
0.624	7.228
0.656	7.598
0.689	7.988
0.725	8.397
0.762	8.828
0.801	9.280
0.842	9.756
0.885	10.255
0.934	10.780
0.982	11.335

11.915	5.39E+11
12.525	5.18E+11
13.170	5.66E+11
13.670	5.10E+11
14.015	5.16E+11
14.370	4.71E+11
14.735	4.38E+11
15.300	4.36E+11
16.085	4.41E+11
16.700	3.96E+11
17.120	3.91E+11
18.485	3.81E+11
SP1 d 0	3.64E+11
4.11E+11	3.58E+11
5.30E+11	3.32E+11
6.20E+11	3.36E+11
7.04E+11	3.20E+11
7.78E+11	3.16E+11
6.31E+11	2.87E+11
4.30E+11	2.75E+11
6.26E+11	2.73E+11
6.79E+11	2.69E+11
6.55E+11	2.61E+11
8.31E+11	2.66E+11
5.83E+11	2.65E+11
4.94E+11	2.45E+11
6.23E+11	2.36E+11
7.01E+11	2.33E+11
6.46E+11	2.20E+11
6.16E+11	2.12E+11
8.66E+11	2.06E+11
7.42E+11	1.91E+11
8.79E+11	1.70E+11
1.01E+12	1.42E+11
1.02E+12	1.19E+11
9.45E+11	1.03E+11
9.11E+11	9.20E+10
9.60E+11	8.22E+10
9.79E+11	7.11E+10
7.51E+11	6.20E+10
7.77E+11	5.40E+10
9.31E+11	4.55E+10
8.58E+11	3.93E+10
8.42E+11	3.65E+10
8.42E+11	3.15E+10
7.86E+11	2.61E+10
7.35E+11	2.04E+10
5.95E+11	1.60E+10
5.53E+11	1.27E+10

9.60E+09
7.32E+09
5.45E+09
3.98E+09
2.94E+09
1.98E+09
1.33E+09
9.13E+08
5.49E+08
4.26E+08
3.02E+08
2.37E+08
2.10E+08
1.24E+08
6.98E+07
3.54E+07
3.47E+07

1.59E+07
c -----
c SIM DESCRIPTION
c -----
MODE n
NPS 10e8
PHYS:n J 20 \$ implicit capture off
c -----
c POLIIMI OPTIONS
c -----
IPOL 0 0 0 0 2J 1 1 \$ standard MCNPX +
collision infos cell 1
RPOL 0.001 0.001 \$ n,g energy deposition > 1
keV
FILES 21 masurca_25_c.txt
c -----

APPENDIX D

Contribution

L. Dioni, R. Jacqmin, B. Stout, M. Sumini. "A Multipurpose Fast Neutron Beam Capability at the MASURCA Facility." *ANIMMA 2015: International Conference on Advancements in Nuclear Instrumentation Measurement Methods and their Applications* (2016)

Abstract: In this paper we investigate the possible future use of the CEA Cadarache MASURCA experimental fast reactor to generate a fairly high-intensity continuous beam of fast neutrons, having energies distributed in the 1 KeV to 5 MeV range. Such an extracted beam of fast neutrons, tailorable in intensity, size and energy, would be rather unique; it would be of interest to neutron-based research and could open a range of new applications at MASURCA. We report the results of numerical simulations which have been performed to evaluate the feasibility of such a beam port and to characterize it spectrally.

L. Dioni, R. Jacqmin, B. Stout, M. Sumini. "Developing a Fast Neutron Beam Capability in the MASURCA Facility: Spectrum and Intensity Evaluation." *PHYSOR 2016: Unifying Theory and Experiments in the 21st Century* (2016)

Abstract: In this paper, we investigate the possibility of using the CEA Cadarache MASURCA experimental reactor to deliver a well-characterized, fairly-intense beam of intermediate-to-fast energy neutrons. We report the results of numerical simulations which have been performed to establish the feasibility of such a beam. We show that it is possible to achieve a beam intensity of more than 10^8 neutrons $\text{cm}^{-2} \text{s}^{-1}$ in the experimental room past the reactor biological shield, ~80% of the neutrons having energies above 100 keV, and 96% above 10 keV. The characteristics of this MASURCA extracted beam are compared with those of other neutron physics facilities designed to produce continuous beams of fast neutrons. The analysis shows that the MASURCA setup would have several distinctive advantages.

Key Words: MASURCA, research reactor, fast neutron beam, fast neutron detection.

L. Dioni, R. Jacqmin, B. Stout, M. Sumini. "On the Possible Use of the MASURCA Reactor as a Flexible, High-intensity, Fast Neutron Beam Facility." *ND 2016: International Conference on Nuclear Data for Science and Technology* (2017)

Abstract: In recent works [1,2], we have shown that the MASURCA research reactor could be used to deliver a fairly-intense continuous fast neutron beam to an experimental room located next to the reactor core. As a consequence of the MASURCA favorable characteristics and diverse material inventories, the neutron beam intensity and spectrum can be further tailored to meet the users' needs, which could be of interest for several applications. Monte Carlo simulations have been performed to characterize in detail the extracted neutron (and photon) beam entering the experimental room. These numerical simulations were done for two different bare cores: A uranium metallic core (~30% ^{235}U enriched) and a plutonium oxide core (~25% Pu fraction, ~78% ^{239}Pu). The results show that the distinctive resonance energy structures of the two core leakage spectra are preserved at the channel exit. As the experimental room is large enough to house a dedicated set of neutron spectrometry instruments, we have investigated several candidate neutron spectrum measurement techniques, which could be implemented to guarantee well-defined, repeatable beam conditions to users. Our investigation also includes considerations regarding the photons in the beams.

L. Dioni, V. Gressier, G. Nardin, R. Jacqmin, B. Stout, M. Sumini. "Test of a Solution-grown Stilbene Scintillator in Mono-energetic Neutron Beams of 565 keV and 5 MeV." *Nuclear Instrumentation and Methods in Physics Research A* (2017): accepted

Abstract: The results of measurements performed with a solution-grown stilbene scintillator placed in reference mono-energetic neutron fields are presented. The \varnothing 25 mm organic scintillator was positioned in 5 MeV and 565 keV neutron fields delivered by the AIFIRA facility at CENBG. The goal of the experiment was to assess the performance of the solution-grown stilbene crystal (n - γ discrimination, response, anisotropy, sensitivity) relative to that of a BC501A liquid scintillator of larger size. Neutron pulse height spectra after gamma discrimination are compared. The results show that the stilbene crystal not only has a better discrimination capability than the BC501A (35 % higher FoM) at 5 MeV, but is also able to separate neutrons from gamma-rays at 565 keV and below, a range where the BC501A is inoperative. This study also confirms the anisotropy of the crystal response, as already observed by other groups at different energies.

Keywords: Organic Scintillators, Solution-grown Stilbene, Mono-energetic Neutrons, PSD, Scintillation Anisotropy.

Acknowledgements

This work has been carried out thanks to the support of the A*MIDEX grant (n° ANR-11-IDEX-0001-02) funded by the French Government «Investissements d'Avenir» program and to the support of the SPECTRAL project funded by the French NEEDS (Nuclear Energy, Environment, Waste and Society) interdisciplinary research challenge.

